

Fast to Slow Megathrust Slip and Fault Strength at Seismogenic Depths of the Cascadia Subduction Zone

Duo Li

Doctor of Philosophy

Department of Earth and Planetary Sciences

McGill University

Montreal, Quebec, Canada

Feb-23-2018

A thesis submitted to McGill University for the degree of Doctor of Philosophy

©Duo Li, 2018
All rights reserved

ACKNOWLEDGEMENTS

In my fifth year at McGill, I am engaged in writing my Ph.D. thesis and preparing for the graduation. I realized that in my four-year study I have owed my gratitude to many people.

First and foremost, I thank my advisor Prof. Yajing Liu for introducing me to the field of subduction zones and slow slip events, for guiding me through every stage of my Ph.D study, for providing continuous encouragements and supports, and for sending me to visit Woods Hole Oceanographic Institution (WHOI) which is among the best places in ocean sciences around the world. I also thank my advisor at WHOI, Dr. Jeffrey McGuire, for all the tutorials in the OBS data process and guiding me through the entire research of Mendocino. His creativeness and preciseness is significant for the project. The patience of Yajing and Jeff helps me survive through all the difficulties. My deep gratitude also goes to my committee members, Prof. Christie Rowe and Prof. Rebecca Harrington. The discussions and suggestions from them always broaden my perspectives in seismology and geology. I benefit a lot from the course of numerical modeling taught by Dr. Jian Lin, Dr. Mark Behn, and Dr. Olivier Marchal at WHOI.

I thank my co-authors Dr. Jeanne Hardebeck and Dr. Matt Wei for their inspiring ideas and suggestions in my research. I am grateful to the professors in the Department of Earth and Planetary Sciences at McGill for teaching me during the four years. I thank every member of the seismology group: Dr. Hongyu Yu, Bei Wang, Ge Li, Andres Pena Castro, John Onwuemeka and Dr. Kai Deng, for the helpful discussions from day to day. I also benefit a lot from the discussions with Dr. Takanori Matsuzawa, Dr. Bunichiro Shibazaki, Dr. Kelin Wang, Dr. Kang Wang, Dr. Shuoshuo Han and Dr. Han Yue.

I especially thank my parents and my boyfriend, Shihao, for understanding and encouraging me through all the difficulties in these years. The unconditional love from my families help me to fight my way all these years.

ABSTRACT

The Cascadia subduction zone is short of modern seismological records of megathrust earthquakes, which makes it difficult to investigate the potential of fault ruptures directly. At the very beginning of the 21st century, a type of quasi-static fault deformation was observed around the downdip end of seismogenic zones. These aseismic transient events are called slow slip events (SSEs). SSEs accommodate a fraction of the plate convergence and may affect the stress loading at the megathrust depths. The discovery of SSEs sheds light on our knowledge of megathrust faults. This thesis aims to investigate physical constraints for subducting faults at depths of both megathrust earthquakes and slow slip events.

Chapter 1 gives an introduction of the Cascadia megathrust fault and the current understanding of the physics of SSEs.

In Chapter 2, I study the physics of the deep SSEs by investigating the effects of the megathrust fault geometry and overlying continental plate. I incorporate a realistic fault geometry of the northern Cascadia in the framework of rate- and state-dependent friction law, to simulate the spatiotemporal evolution of SSEs on a non-planar subduction fault. The modeled SSEs capture the major characteristics revealed by GPS observations. The along-strike distribution of SSE is inversely related to the fault local dip and strike angle of the SSE zone, suggesting a strong geometrical influence. Besides the GPS-detectable fast-spreading phase, I find that each SSE cycle consists of a deep pre-SSE preparation (nucleation) and a post-SSE relaxation (healing) phase, which may be the driving mechanism for the inter-ETS (Episodic Tremor and Slip) tremor activity that is discovered in Cascadia.

In Chapter 3, I develop a 3-D episodic SSE model for the northern and the central

Cascadia, incorporating both seismic and geodetic observations to constrain heterogeneous megathrust fault properties. The segmentation of SSE recurrence intervals from models that are constrained by Free-air and Bouguer gravity anomalies is equally comparable to GPS observations. However, the model constrained by Free-air anomaly does a better job in reproducing the cumulative slip as well as more consistent surface displacements with GPS observations. The modeled along-strike segmentation only represents the averaged slip release over many SSE cycles, rather than acting as permanent barriers. Individual SSE can still propagate across the segment boundaries, which may cause interactions between adjacent SSEs, as observed in the time-dependent GPS inversions.

In Chapter 4, I study the fault shear strength at the seismogenic depths by inverting fault strength from tectonic stress tensors in the continental crust and oceanic mantle in Mendocino Triple Junction, the southern end of the Cascadia subduction zone. I obtain the fault strength for the megathrust fault in Mendocino. I use Cascadia Initiative (CI) expedition OBS data to resolve the focal mechanisms for small-to-intermediate earthquakes from 2014 to 2015. The stress orientations are obtained by combining the CI OBS resolved earthquake focal mechanisms with those reported by the Northern California Earthquake Data Center between 1980 and 2016. The fault shear strength scales with a subjective mantle strength assumed in the inversion. When the mantle strength is in the range of 50~400 MPa, the megathrust fault shear strength can be no higher than 50 MPa. The resolved friction coefficients are in the range of 0 to 0.2.

In Chapter 5, I use a planar fault model with rate and state friction parameters constrained by geodetic fault locking coefficients to study megathrust earthquake cycles. The modeled coseismic fault slip can reproduce the historical coastal subsidence observations. The along-strike variation of coseismic rupture is affected by both the

width of seismogenic zone and heterogeneous frictional properties (e.g., nucleation size) in Cascadia.

Chapter 6 contains conclusions and future scopes.

ABRÉGÉ

La Cascadia subduction zone manque d'un enregistrement sismologique moderne du tremblement de terre de mégathrust, ce qui rend difficile l'enquête directe sur la faute. Au début du XXI^e siècle, un type de déformation de panne quasi statique est observé autour de la limite descendante de la zone sismogénique, appelée événement à glissement lent (SSEs). Les SSEs accueillent une fraction de la convergence des plaques et peuvent déclencher des tremblements de terre de mégathrust. La découverte des SSE met en lumière les études sur les propriétés de la faute. Cette thèse vise à étudier la physique du défaut de subduction par la rotation du stress dans la zone sismogénique peu profonde et les caractéristiques des SSE descendantes.

Le chapitre 1 résume la faille de la mégathrust de Cascadia et la compréhension actuelle de la physique des SSEs.

Dans le chapitre 2, j'étudie la physique du glissement lent asismique profond quasi-épisodique en étudiant l'effet de la géométrie et de la plaque continentale recouvrante. J'invente une géométrie de faiblesse réaliste du nord de Cascadia dans le cadre du droit de friction dépend du taux et de l'état, pour simuler l'évolution spatiotemporelle des événements à glissement lent sur un défaut de subduction non planaire. Les SSEs modélisés captent les principales caractéristiques révélées par les observations GPS. La segmentation du glissement lent à la suite de la grève est inversement liée à la trempe moyenne et à la trempe différentielle de la zone à glissement lent, ce qui suggère une forte régulation géométrique du processus de glissement lent. En plus de la phase de "propagation rapide" détectable par GPS, je trouve que chaque cycle SSE consiste en phases profondes "pre-SSE" et "post-SSE", ce qui peut être le mécanisme de conduite pour l'activité de tremblement inter-ETS plus profond découverte en Cascadia.

Dans le chapitre 3, Je développe un modèle épidémique SSE 3-D pour Cascadia au nord et au centre, en incorporant à la fois des observations sismiques et géodésiques pour contraindre les hétérogénéités dans les propriétés de défaut de méga-crotte. Les segmentations des intervalles de récurrence des modèles contraints par les deux types d'anomalies de gravité sont également comparables aux observations GPS. Cependant, le modèle contraint par l'anomalie de l'air libre permet de mieux reproduire le glissement cumulatif ainsi que des déplacements de surface plus cohérents avec des observations GPS. La segmentation modélisée du long de la grève ne représente que la libération de glisse en moyenne pendant de nombreux cycles SSE, plutôt que des barrières permanentes. Les événements de glissement lent individuel peuvent encore se propager dans les limites, ce qui peut provoquer des interactions entre les SSE adjacentes, comme cela a été observé dans les inversions de GPS dépendant du temps.

Dans le chapitre 4, la contrainte directe de la résistance aux pannes est difficile. J'étudie la résistance au cisaillement par défaut dans la zone sismogénique peu profonde en inversant la résistance aux défauts des tensorètes tectoniques dans la croûte continentale et le manteau océanique. J'obtiens la résistance à la défektivité pour les défauts intra-plaques et intercalaires dans Mendocino, l'extrémité sud de la Cascadia subduction zone. J'utilise les données d'expédition de l'Initiative Cascadia pour inverser les mécanismes focaux. Le tenseur de contrainte tectonique est obtenu à partir de mécanismes focaux historiques. La résistance à la cisaillement de la charge augmente avec une résistance subjective du manteau utilisée dans l'inversion. Dans la gamme de 50 ~400 MPa, la résistance à la défektivité peut être aussi petite que 50 MPa, ce qui est beaucoup plus bas que la croûte et le manteau.

Dans le chapitre 5, J'ai configuré un modèle de défaut planaire avec la contrainte des coefficients de verrouillage de défaut géodésiques. Le glissement de faille coseismique modéré peut reproduire les observations historiques de l'affaissement côtier. La

variation de la rupture coseismique à long terme est affectée à la fois par la largeur de la zone sismogénique et par des propriétés de frottement hétérogènes (par exemple, la taille de la nucléation) dans Cascadia.

Le chapitre 6 contient des conclusions et des périmètres futurs.

CONTRIBUTIONS

Chapter 2 has been published as: D. Li and Y. Liu (2016), Spatiotemporal evolution of slow slip events in a nonplanar fault model for northern Cascadia subduction zone, *J. Geophys. Res. Solid Earth*, 121, 6828–6845, doi:10.1002/2016JB012857. D. Li is responsible for running the simulations, making figures and analysing results. D. Li and Y. Liu participate in discussions and revisions.

Chapter 3 has been published as: D. Li and Y. Liu (2017), Modeling slow-slip segmentation in Cascadia subduction zone constrained by tremor locations and gravity anomalies, *J. Geophys. Res. Solid Earth*, 122, 31383157, doi:10.1002/2016JB013778. D. Li is responsible for running the simulations, making figures and analysing results. D. Li and Y. Liu participate in discussions and revisions.

Chapter 4 has been published as: D. Li, J. J. McGuire, Y. Liu and H. L. Hardebeck, Stress rotation across the Cascadia megathrust requires a weak subduction plate boundary at seismogenic depths. D. Li is responsible for data processing, focal mechanism solutions and running principle stress inversion. D. Li and J. McGuire together make the Matlab scripts for absolute stress magnitude inversion and analyse the results. All participate in the discussion and revisions.

In chapter 5, D. Li is responsible for designing and running the simulations and making figures and tables. Y. Liu and D. Li participate in the discussions.

TABLE OF CONTENTS

ACKNOWLEDGEMENTS	ii
ABSTRACT	iv
ABRÉGÉ	vii
CONTRIBUTIONS	x
LIST OF TABLES	xiv
LIST OF FIGURES	xv
1 Introduction	1
1.1 Cascadia Megathrust Fault	2
1.2 Current Understanding of SSEs	5
1.2.1 SSEs in Cascadia	6
1.2.2 Physics of SSEs	6
1.2.3 Relation with Megathrust Earthquakes	8
1.2.4 Numerical Models of SSEs	9
1.3 Thesis Outline	10
2 Spatiotemporal Evolution of Slow Slip Events in A Non-planar Fault Model for Northern Cascadia Subduction Zone	12
2.1 Introduction	12
2.2 Method	15
2.2.1 Laboratory-derived Rate- and State- Friction Law	15
2.2.2 Fault Geometry	17
2.2.3 Governing Equations	20
2.2.4 Model 1: Isothermal SSE Depths	21
2.2.5 Model 2: Uniform SSE Depths	23
2.2.6 Parameter Exploration	23
2.3 Results	25
2.3.1 Slow Slip Segments	27
2.3.2 Effect of Fault Geometry	33
2.3.3 Slow Slip Phases and Scaling Relations	36
2.4 Discussions	41

2.4.1	Geometric Effect	41
2.4.2	Inter-SSE Slip and Tremor Activity	44
2.5	Conclusions	46
Appendix A: “Aging” law vs. “Slip” law		47
3	Modeling Slow-slip Segmentation in Cascadia Subduction Zone Constrained by Tremor Epicenters and Gravity Anomalies	50
3.1	Introduction	50
3.2	Method	53
3.2.1	Governing Equations	53
3.2.2	Fault Geometry	55
3.2.3	Model Parameters	56
3.3	Results	61
3.3.1	Cumulative Slip Constrained by Gravity Anomalies	62
3.3.2	Slip in Central Oregon	65
3.3.3	Segmentation of Recurrence Interval	67
3.3.4	Synthetic GPS Vectors	69
3.3.5	Along-strike Migration	73
3.3.6	Source Parameter Scaling Relations	76
3.4	Discussion	79
3.4.1	Effects of the Overlying Continental Lithosphere	79
3.4.2	Creeping in Oregon	84
3.4.3	Tremorless Slip	85
3.5	Conclusions	86
Appendix A: A Hybrid Fitting of Bouguer Anomaly:		88
4	Stress Rotation Across the Cascadia Megathrust Requires a Weak Subduc- tion Plate Boundary at Seismogenic Depths	91
4.1	Introduction	91
4.2	Focal Mechanisms and Principal Stress Inversion	95
4.2.1	Catalogue	95
4.2.2	Focal Mechanism	96
4.2.3	Principal Stress Inversion	98
4.2.4	Binning Strategy	101
4.2.5	Stress Orientations in Overlying Crust and Subducting Mantle	104
4.3	Stress Inversion for PBZ	107
4.3.1	Method	107
4.3.2	Results	114
4.4	Discussions	118
4.4.1	Stress Rotation across PBZ	118
4.4.2	Weak Thrust Fault	120

4.5	Conclusions	123
	Appendix A: Tests on Depth Group	127
	Appendix B: LMI Inversion Matrix	128
5	Modeling Megathrust Earthquake Cycles Constrained by Geodetic Inversion of Fault Locking	132
5.1	Introduction	132
5.2	Method	134
	5.2.1 Planar Fault	134
	5.2.2 Parameter Choice	136
	5.2.3 Coastal Subsidence Data	137
5.3	Results	139
	5.3.1 Modeled coseismic slip in northern Cascadia	139
	5.3.2 Synthetic coastal subsidence	140
	5.3.3 Aseismic slip in central Cascadia: uniform h^*	141
	5.3.4 Coseismic slip in central Cascadia: heterogeneous h^*	142
5.4	Discussions	143
	5.4.1 Various Nucleation Sizes	143
	5.4.2 Current Fault Locking Models	147
5.5	Conclusions	148
6	Conclusions and Perspectives	150
6.1	Thesis Conclusions	150
6.2	Scope for Future Work	154

LIST OF TABLES

<u>Table</u>	<u>page</u>
4-1 The cutoff tolerance at each mantle S^M from 50 to 400 MPa.	113
4-2 Test 1-9 for the depth and thickness of plate boundary zone (PBZ). The number of earthquakes in each group are shown. D: perpendicular distance to slab interface given by McCrory et al. [2012]. H: thickness of slab interface group.	125
4-3 List of focal mechanisms: event, latitude, longitude, depth, M_L magnitude	126
5-1 Recurrence intervals T and slips δ of coseismic ruptures in Model I and Model II	140

LIST OF FIGURES

<u>Figure</u>	<u>page</u>
1–1 Map showing the geography of the Cascadia subduction zone. Earthquakes of $M_L > 1$ from 1980 to 2016, based on USGS catalogue (https://earthquake.usgs.gov/earthquakes/search/) (red dots). JdF: Juan de Fuca Plate. PA: Pacific Plate. NA: North American Plate. . . .	3
2–1 (a) The 3-D non-planar northern Cascadia subduction zone fault model with triangular mesh on the fault (element size is ~ 20 km for illustration purpose while spacing of ~ 1 km is used in simulations). Top red Cartesian coordinates X-Y: X is trench-parallel direction and Y is trench-normal direction, after rotating 30° from original X'-Y' coordinates. Depth 0 km is at sea level. Trench is at 5 km depth. Frictional stability transition from velocity-weakening ($a - b < 0$) to velocity-strengthening ($a - b > 0$) is at 46 km (blue line). Effective normal stress $\bar{\sigma} = 1.5$ MPa is between 33 and 50 km (pink lines). PA: Port Angeles and SEA: Seattle. Coastline is on the top surface. . . .	18
2–2 Graphs showing parameter $a - b$ and $\bar{\sigma}$ in Model 1. (a) Friction parameter $a - b$ versus downdip distance along a cross-section shown by the black dashed line in Figure 2–1. Top axis shows the depth in km from 5 km at the trench. Gray shaded region (W) is velocity-weakening under $\bar{\sigma} = 1.5$ MPa. (b) Mapview of $\bar{\sigma}$ on the fault. The locked fault from 5 km to 28 km is not shown. Blue shows $\bar{\sigma} = 1.5$ MPa while red is 50 MPa. Dot-Dashed lines are depth contours of 20-50 km. PA: Port Angeles.	22
2–3 Graphs showing parameter $a - b$ and $\bar{\sigma}$ in Model 2. (a) Effective normal stress $\bar{\sigma} = 1.5$ MPa in the SSE zone (dark blue) and 50 MPa elsewhere. Cross-sections A and B are chosen to demonstrate the $a - b$ distribution along downdip distance. (b) Solid and dashed lines represent $a - b$ distributions in Model 1 and Model 2, respectively. Grey shaded area shows the range of velocity-weakening under low effective normal stress ($W = 70$ km) for Model 2 set up.	24

- 2-4 Graphs showing (a) recurrence interval T_{cyc} scaled with d_c , (b) maximum slip velocity $\log_{10}(V_{max})$, and (c) cumulative slip δ scaled with d_c of simulation cases with parameters: (1) Yellow: $W = 79\text{km}$, $d_c = 1.4\text{mm}$, $\bar{\sigma} = 1.0 \text{ MPa}$, (2) Cyan: $W = 79\text{km}$, $d_c = 0.7\text{mm}$, $\bar{\sigma} = 1.0 \text{ MPa}$, (3) Blue: $W = 79\text{km}$, $d_c = 0.7\text{mm}$, $\bar{\sigma} = 1.5 \text{ MPa}$, (4) Green: $W = 64\text{km}$, $d_c = 0.7\text{mm}$, $\bar{\sigma} = 1.5 \text{ MPa}$, (5) Red: $W = 72\text{km}$, $d_c = 0.7\text{mm}$, $\bar{\sigma} = 1.5 \text{ MPa}$, (6) Black: $W = 76\text{km}$, $d_c = 0.7\text{mm}$, $\bar{\sigma} = 1.5 \text{ MPa}$. Error bars show the standard deviations in each case. 26
- 2-5 Fault slip velocity beneath Port Angeles during a 120-year simulation period (Model 1), with parameter setup of the red diamonds in Figure 2-4. Red dashed line is 41 mm/yr or $1.3 \times 10^{-9} \text{ m/s}$. Shaded region are the 13-year time period, during which we calculate the average cumulative slip in Figure 2-8. 27
- 2-6 (a) Moment rate of the three slip patches (shown in Figure 2-8a): central, northern and southern, during a 13-year simulation period (Model 1). Horizontal dot-dashed line at $4 \times 10^{11} \text{ Nm/s}$ is the cutoff threshold for defining slow slip on the central patch. (b) Top: Detrended east component of daily GPS time series of from 1997 to 2010 (13 years) station ALBH (from Pacific Northwest Geodetic Array: <http://www.geodesy.cwu.edu/>). Bottom: The modeled cumulative slip of three patches during the same period. The position of each line is shown by colored diamond in Figure 2-8b. 28
- 2-7 (a) Graphs showing spatiotemporal evolution of slip velocity at depth 35 km depth for a 13-year simulation period (Model 1). Green, blue and red dashed lines mark the boundaries of northern patch, central patch and southern patch, respectively. White arrows illustrate the bilateral propagation of $\sim 2 \text{ km/day}$ during ~ 20 days in one episode. (b) Cumulative slip at 35 km depth contour of three patches during the same period. The position of each line is shown by colored diamond in Figure 2-8b. 30

2–8	<p>Maps showing (a) cumulative slip averaged of 8 SSE episodes over 13 years shows in Figure 2–6. Three distinctive slip patches are marked by bold white dashed lines. Slip is calculated when moment rate exceeds 4×10^{11} Nm/s (equivalent to an average slip rate V_{pl}) on the central patch (CP), and 2×10^{11} Nm/s ($V_{pl}/2$) on the northern and southern patches (NP and SP). Maximum cumulative slip values on northern, central and southern are 1, 2.5 and 2.0 cm, respectively. PA: Port Angeles. (b) Slip released during SSEs as a percentage of plate convergence ($V_{pl} = 41$ mm/yr) over 13 years. The maximum percentage is $\sim 50\%$ beneath Port Angeles. The maximum in northern and southern slip patch is less than 30%. Dashed white contour marks the position of 35 km depth. Diamonds denote the position of the cumulative slip in Figure 2–6 and 2–7.</p>	32
2–9	<p>Subduction fault geometry represented by (a) local dip angle and (b) local strike angle of each element on the fault. Dot-dashed lines show depth contours of 20-50 km depth in (a) and 35 km in (b), where shear stress evolution is shown in Figure 2–10.</p>	34
2–10	<p>Along-strike variations of fault geometry and cumulative slip. (a) Model 1: cumulative slip of three patches are shown by diamonds (green: northern; blue: central; red: southern). Vertical and horizontal bars show the along-strike range and standard deviation, respectively. Fault local dip angle (red dashed line) and local strike angle (blue dashed line) are averaged over SSE depths. Black solid line shows W/h^*. (b) Model 2: Maximum cumulative slip at along-strike 150, 50, -50, -125, -200 km (red diamonds). Solid line is at the uniform $W/h^* \approx 1.5$. Red and blue dashed lines show fault local dip and strike angles, respectively.</p>	35
2–11	<p>Graphs showing (a) spatiotemporal evolution of slip velocity at $a - b = -0.0025$ contour for a 10-year simulation period of Model 2. Black and red diamonds in (a) show the along-strike positions where (b) cumulative slip is plotted.</p>	36

2–12 (a) Northern Cascadia tremor activity hours per day from 2007/4 to 2008/7 is shown [Wech and Creager, 2008]. The major ETS events in the time period from May 4 to May 24 is highlighted in red [Wech and Creager, 2008]. This time period is aligned with the first 33 days in the modeled fast-spreading phase. Gray shadow shows the 110 days before the 2008 ETS event, aligned with the pre-SSE phase. (b) Graph showing cumulative moment (black) and moment rate (red) of 547 days in one episode defined on the central slip patch. Three phases are defined by moment rate: a pre-SSE preparation (day 260-370) and post-SSE relaxation (day 431-473) phase $\sim 2-4 \times 10^{11}$ Nm/s and fast-spreading phase (day 370-431) $> 4 \times 10^{11}$ Nm/s. Widths of vertical shaded bars show the four periods of snapshots in Figure 2–13.	38
2–13 Four snapshots of cumulative slip (a) day 330 to 370, pre-SSE preparation, (b) day 370-383 and (c) day 383-403, fast-spreading, (d) day 433-470, post-SSE relaxation. These four time windows are corresponding to shaded bars of (b)-(e) in Figure 2–12b.	39
2–14 (a) Moment-area scaling relation of 79 SSEs in central (blue), northern (green) and southern (red) patches. Moment is calculated within the fast-spreading phase of each episode. Only the elements with slip greater than 0.5 mm are accounted in calculating the moment and area, the same criterion as in Schmidt and Gao [2010]. (b) Moment-duration scaling of all SSEs on three patches. Dot-dashed lines show the scaling of $M \sim T$	40
2–15 Shear stress at 35 km depth contour is plotted every 5 days during a central patch SSE (black line) from day 370 to 390 (fast-spreading phase in Figure 2–12b). Dashed red and black lines are the local dip and strike angles along the strike, respectively. SSE nucleation zone is denoted by blue arrows. Grey bars denote the segmentation boundaries.	42
2–16 Graphs showing (a) maximum cumulative slip, (b) equivalent moment magnitude, (c) recurrence interval, and (d) duration, versus average fault dip angle at SSE depths. Southwest Japan (light blue): short-term (square) and long-term (diamond) in Shikoku, short-term in Ryuku Trench (circle) and short-term in northeast Kii Island and Tokai (triangle). Cascadia (red): Vancouver Island and northern Washington (square), northern Oregon (diamond) (no slip inversion is available for northern California). Mexico (yellow): Guerrero (square) and Oaxaca (diamond). New Zealand (dark blue): northern Hikurangi (diamond) and Manawatu (square). Alaska (purple): Upper (square) and Lower Cook Inlet (diamond). Costa Rica: Nicoya Peninsula (green square).	43

2–17	(a) Slip rate during 2 years is shown for both “aging” (black) and “slip” (red) law. (b) Slip rate along the strike of every 0.84 hour is shown, modeled with “slip” law. The maximum slip rate is 0.01 mm/s. (c) Slip rate along the strike of every 10 day is shown, modeled with “aging” law. The maximum slip rate is 1.1^{-8} m/s.	49
3–1	Graphs showing fault geometry and meshing of Cascadia subduction zone. The meshed grid sizes on the fault are ~ 10 km for illustration while ~ 1 km in the simulation. Depth contours of 10-50 km are from the study of McCrory et al. [2012]. Black vector shows the representative plate convergence direction. Gray vectors shows the X-(trench-normal) and Y-(trench-parallel) axes. Coastlines are shown by black lines. B.C.: British Columbia; WA: Washington; OR:Oregon; PA: Port Angeles; SEA: Seattle.	57
3–2	(a) Fault locking fraction ϕ of Gamma decade-scale model from the GPS inversion study of Schmalzle et al. [2014]. White circles mark their downdip 20% locked contour. Red dots show 6-year PNSN tremor epicenters catalog (2009/8-2015/4, http://pnsn.org/tremor). Gray polygons represent the block model from the study of McCaffrey et al. [2007]. (b) Non-dimensional rate-state friction parameter $a - b$. The upper- (white) and lower-limits (black) of the SSE depths in our model are obtained from outlining the tremor epicenters in (a). Within these lines, $a - b$ changes linearly from -0.003 to 0 with depth. $a - b = -0.003$ for further updip and velocity-strengthening ($a - b > 0$) for further downdip. Hatched lines represent the shallow locked fault (5-20km, depth referred to the sea-level). The plate convergence direction is 60° from north. Plate convergence rate changes linearly along the strike (black arrows) [McCaffrey et al., 2007].	59
3–3	Maps showing (a) Bouguer anomaly (onshore) and free-air (offshore) and (b) free-air anomaly in Cascadia. Color scales are in different. Data sources are from U.S. Geological Survey (USGS, http://mrdata.usgs.gov/gravity/isostatic/) and Natural Resources Canada (http://www.nrcan.gc.ca/home). The gravity anomalies along the 35km-depth contour (white lines) are used to constrain $\bar{\sigma}$ along the strike in our model.	61

3–4	Graph showing (a) cumulative slip of the reference model with uniform $\bar{\sigma}=1.0$ MPa. Five patches are defined as P1-P5 in (b). PA: Port Angeles and SEA: Seattle. (b) Cumulative slip along the contour of $a - b=-0.0025$. The maximum cumulative slip in each of the five segments is 1.7, 1.7, 2.1, 2.0 and 1.5 cm, respectively. (c) The width of downdip distance of velocity-weakening in SSE depths, W , along the strike, which is constrained by the tremor locations in Figure 3–2a. Local maxima of W in each segments are 85, 95, 85, 108 and 60 km.	63
3–5	(a) Cumulative slip of the model with $\bar{\sigma}$ constrained by Bouguer anomaly. PA: Port Angeles and SEA: Seattle. (b) Cumulative slip along the contour of $a - b=-0.0025$. Maximum cumulative slips of the five segments are 2.7, 3.2, 4.6, 3.2 and 2.9 cm. (c) Bouguer anomaly of 35 km depth contour (blue) and its multi-segment linear fit (black).	64
3–6	(a) Cumulative slip of the model with $\bar{\sigma}$ constrained by free-air anomaly. PA: Port Angeles and SEA: Seattle. (b) Cumulative slip along the contour of $a - b=-0.0025$. Maximum cumulative slips of five segments are 2.2, 3.3, 2.2, 2.5 and 2.2 cm. (c) Free-air anomaly of 35 km depth contour (blue) and its polynomial fit (black).	66
3–7	Recurrence intervals of models with (a) uniform $\bar{\sigma}$ (black bars), (b) $\bar{\sigma}$ constrained by Bouguer anomaly (red bars) and (c) $\bar{\sigma}$ constrained by free-air anomaly (blue bars). Dashed lines represent the effective normal stress used in each model. Error bars show the standard deviations. Recurrence intervals observed by Brudzinski and Allen [2007] are shown as gray bars in (a-c).	68
3–8	Segmentation of slow slip events from Schmalzle et al. [2014]. Black and green dots shows non-volcanic tremors from Pacific Northwest Seismic Network (PNSN) and Miami University(MU) catalog, respectively. Red dots are east components of GPS series from stations ALBH, KTKA, CPXX, DDSN and P376. Gray bars denote episodic slow slip events detected by Schmalzle et al. [2014]. The average recurrence intervals of two segments, 44°-50°N (red) and 42°-47°N (blue), are 280 and 180 days, respectively. Hatched lines show the overlapping region between these two segments, where occasionally ruptured by SSEs from both sides.	70

3–9	(a) GPS displacements calculated from the slip distribution of the July 1998 SSE in northern Washington (Mw 6.6) [Schmidt and Gao, 2010] (black vectors). White contours denotes the cumulative slip contours of 1-3 cm. Modeled GPS vectors (gray) are calculated from our modeled cumulative slip of the model with $\bar{\sigma}$ constrained by free-air anomaly, which has an equivalent magnitude of Mw 6.7 (shear modulus of 30 GPa). The reduced chi-square is defined by Equation 3.7. Dotted lines are depth contours from 20 to 40 km. PA: Port Angeles. SEA: Seattle. (b) shows the same results as (a), except for that the modeled cumulative slip is of the model with $\bar{\sigma}$ constrained by Bouguer anomaly.	71
3–10	(a) GPS displacements calculated from the slip distribution of the May 2004 SSE in southern Washington (Mw 6.2) (black vectors). White contours are the cumulative slip contours of 1-2 cm. Modeled GPS vectors (gray) are calculated from our modeled cumulative slip of the model with $\bar{\sigma}$ constrained by free-air anomaly, which has an equivalent magnitude of Mw 6.2. SEA: Seattle. PORT: Portland. (b) show the same results as (a), except for that the modeled cumulative slip is of the model with $\bar{\sigma}$ constrained by Bouguer anomaly.	72
3–11	Snapshots of two sequential SSEs of the model with $\bar{\sigma}$ constrained by free-air anomaly. The first event initiates at 45°N and then propagates northward at a speed of ~ 2 km/day (a-d). The event lasts for 41 days. The second event starts between 47.5°N at day 63 and extends in the range 47°N -48°N (g-h). The final cumulative slip is ~ 3.0 cm beneath Port Angeles. In the gap between the two SSEs, from day 41 to 63, the slip front migrates from 46°N to 47°N at a very low rate (e-f). VAN: Vancouver. PA: Port Angeles. SEA: Seattle. PORT: Portland.	74
3–12	Snapshots of two sequential SSE adjacent to each other of the model with $\bar{\sigma}$ constrained by free-air anomaly. The first SSE initially appears beneath Port Angeles and propagates bilaterally for 30 days (a-c). Later at day 41, the second SSE occurs beneath southern Vancouver Island, migrates southward and finally stops at where the first SSE terminates (d-h). The maximum cumulative slips of these two episodes are about 2.5 and 3.0 cm. VAN: Vancouver. PA: Port Angeles. SEA: Seattle. PORT: Portland.	76

3–13	(a) Average slip velocity over the entire segments of P2 in 7 years. (b) Duration defined with velocity criterion $V_{ave} > V_{pl}$. The duration is ~ 20 days. (c) Maximum slip velocity of segment P2. (d) Duration defined with velocity criterion $V_{max} > 3V_{pl}$. The duration is ~ 200 days. (e) Cumulative moment rate (Nm/s) of slip patch P2. Each peak represents one episodic SSEs and well correlates to average slip velocity in (a). Dot-dashed lines are $3V_{pl}$, V_{pl} and $0.5V_{pl}$	78
3–14	(a) Moment-area and (b) moment-duration scaling of 75 events in the three models with velocity criteria $V_{ave} > V_{pl}$. (c) Moment-area and (d) moment-duration scaling with velocity criteria $V_{ave} > 0.5V_{pl}$. Different triangles represent results from different models: Blue, uniform $\bar{\sigma} = 1.0$ MPa; Red: $\bar{\sigma}$ constrained by free-air anomaly and Black, $\bar{\sigma}$ constrained by Bouguer anomaly. Constant stress drops of 0.01 and 0.1 MPa are calculated with circular rupture model and also represent the range of stress drops estimated for Cascadia SSEs [Gao and Schmidt, 2012]. The dot-dashed lines in (b) and (d) shows the inferred linear scaling $M \sim T$ for slow earthquakes [Ide et al., 2007], while our modeling results show deviations from the linear trend at $M \sim T^{1.75}$ and $M \sim T^{1.47}$, respectively.	80
3–15	(a) Cumulative slip of model (4) with $\bar{\sigma}$ approximating a hybrid-fit of Bouguer anomaly. Five patches are defined as P1-P5 in (b). (b) Cumulative slip along the contour of $a - b = -0.0025$. The maximum cumulative slip in each of the five segments is 1.9, 3.0, 4.0, 2.0 and 1.8 cm, respectively. The dashed line is cumulative slip profile of segmented-line fit of Bouguer anomaly (c) Bouguer anomaly of 35 km depth contour (blue) and its hybrid-fit (solid black line). The dashed line is the segmented-line fit.	90
4–1	Map showing topography and seismicity distribution (insert) in Mendocino Triple Junction (MTJ). Historical events with magnitude Mw6.5+ from US Geological Surveys (USGS) catalogue are shown in red. Plate boundaries, including the ridge of Gorda Plate, the Mendocino transform fault and the San Andreas Fault, are from the USGS. Relative plate motions are shown in arrows (N27.5°W between PA and NA). The only thrust event that has been recorded by the seismometers is the 1992 Mw7.1 Cape Mendocino earthquake. Beachball in black shows the Jan 28th, 2015 Mw5.7 earthquake that has been captured by the Cascadia Initiative OBS array. White box shows the study region.	94

4-2	Map showing seismic stations used in this study and the aftershock sequences. The Cascadia Initiative expedition (CI) OBS array is shown in blue triangles. Inland seismic networks include the NCSN (red), PBO (green) and PASCAL (black). Coulomb stress changes of the Mw5.7 mainshock on a 13° dipping thrust fault at 20km-depth is shown in contours (200 kPa interval), ranging from 0 to 400 kPa. Beachballs show focal mechanism of 40 earthquakes from January 29th, 2015 to July, 2015. The size of each earthquake is scaled by the upper-right focal mechanism of M_L 5.0. Quaternary faults in northern California are from USGS (https://earthquake.usgs.gov/hazards/qfaults/). Black dashed lines are depth contours from 5 km to 20 km.	96
4-3	Graphs showing histogram of (a) station coverage index <i>stdr</i> and (b) fraction of misfit <i>mfrac</i> of the 91 earthquakes that are obtained in CI year 2 and year 4	98
4-4	Graphs showing focal mechanisms from (a) NCEDC catalogue and (b) our OBS obtained catalogue, respectively. The Richter magnitude (M_L) is attached to each ball. The event list is shown in Table 4-3.	99
4-5	West-to-east cross-section of the hypocenters and assigned depth groups. The earthquake hypocenters are from NCEDC catalogue (1980-2015) and that obtained from OBS arrays (2012-2013 and 2014-2015). Events in the continental crust (green), plate boundary (blue) and oceanic mantle (red) are distinguished by perpendicular distances to the fault interface given by McCrory et al. [2012]. The dashed line is the assumed fault plate for the 1992 Mw7.1 Cape Mendocino event.	100
4-6	Mapview of distribution of focal mechanisms in (a) shallow crust, (b) PBZ and (c) deep mantle group, which are shown in Figure 4-5. Polar histogram shows the strike orientations of focal mechanisms.	101
4-7	Stress inversion results for (a) shallow crust, (b) PBZ and (c) deep mantle are shown in lower-hemisphere projection. The cloud of dots shows the distribution of bootstrap resampling results. Red: σ_1 , green: σ_2 and blue: σ_3 . Subregion (1)-(4) are shown in Figure 4-6a. Blue arc is the subducting fault plane dipping at 13°. P-(red) and T-(blue) axes for focal mechanisms in (d) crust, (e) PBZ and (f) mantle are shown in lower-hemisphere projection.	103

4–8	(a) Map showing grid-search test for the north-south trend boundary in each depth group. The position of north-south trend boundary is moving from 124.5W to 124.1W (red dashed lines). The solid red line separates the Mendocino transform fault and other intraplate earthquakes. Subfigure (b)-(f) show the inversion results of 1000 bootstraps for north-south boundary in (a). Black dashed lines are depth contours from 5 km to 20 km	105
4–9	(a) Graph showing normalized distribution of the trend of σ_1 . Graphs of standard deviations of (b) trend and (c) plunge of σ_1 for the four sub-regions (1)-(4) in each test. X-axes shows the grid-search test for north-south boundary moving from b to f in Figure 4–8a. The preferred result has the smallest overall deviation (gray shaded bars).	106
4–10	Graphs showing histograms of bootstrap inversion results of (a) R_{MSATSI}^C in crust and (b) R_{MSATSI}^M in mantle. The best estimations of R_{MSATSI}^C and R_{MSATSI}^M are 0.25 and 0.5, respectively. The standard deviations are ~ 0.1 and 0.04, respectively.	107
4–11	Schematic Diagram of the three-layer subduction zone model. PBZ represents the relatively weak region around the subduction fault interface. B1 and B2 denote the PBZ-mantle and crust-PBZ boundaries respectively. Normal- and dip-vector are shown in arrows and strike-vector in cross. The dip angle is 13°	108
4–12	(a) Results with the subjective mantle strength $S^M = 150$ MPa under different tolerances ranging from 1 to 50 MPa are shown. Differential stress of mantle (red), crust (green) and PBZ (blue). (b) R-ratio residual is defined as $\hat{R}^i - R_{MSTASI}^i$ (left-axis). The averaged residuals in the traction continuity equations, $RESD$, are shown in right-axis. Gray shadowed bars denote the cut-off tolerance.	112
4–13	Same as Figure 4–12 except for $S^M = 200$ MPa.	113
4–14	Graph showing the strength of PBZ (blue) and crust (green) at each pair of assumed mantle (S^M) from 50 to 400 MPa and tolerance when minimizing the assumed mantle strength $\ (\sigma_1^{PBZ} - \sigma_3^{PBZ}) - S^M\ $ (Version 1). The line shows the averaged of the bootstrap results (dots). The cutoff tolerance at each mantle strength is shown in Table 4–1.	116

4–15	Graphs showing the range of the strength of PBZ (blue) and crust (green) at each pair of assumed mantle (S^M) from 50 to 400 MPa and tolerance when maximizing (Version 2) and minimizing (Version 3) $ \sigma_1^{PBZ} - \sigma_3^{PBZ} $. Blue circles and dots are differential stress in PBZ using version 2 and version 3, respectively. Differential stress in the crust is reversely related with that in the PBZ in the maximization (green circles) and minimization (green dots).	117
4–16	Effective friction coefficients at each pair of mantle and tolerance. Green circles are results when minimizing $ (\sigma_1^M - \sigma_3^M) - S^M $ (Version 1) in the convex optimization LMIs. Red circles and blue dots are maximizing (Version 2) and minimizing (Version 3) $ \sigma_1^{PBZ} - \sigma_3^{PBZ} $, respectively.	118
4–17	Histograms of bootstrap results of effective friction coefficient μ . μ is calculated as the ratio of shear/normal. The assumed mantle strength S^M is (a) 150, (b) 200, (c) 300 and (d) 400 MPa, respectively. Gaussian distributions are shown in red.	119
4–18	Graphs showing inverted stress orientation in PBZ in lower-hemispheric projection. Red: σ_1 , green: σ_2 , blue: σ_3 . The assumed mantle strength S^M is (a) 150, (b) 200, (c) 300 and (d) 400 MPa. σ_1 (compression) makes a high angle $\sim 75\text{-}80^\circ$ to the horizontal surface.	121
4–19	Test on the depth and thickness of PBZ earthquakes in Table S1. (a) Trend and (b) plunge of σ_1 of two lateral sub-regions in different Test 3-9. Test 9 has the distinction in trend and plunge of compression. Stress tensor of (c) test 9 and (d) test 7. Red: σ_1 , green: σ_2 and blue: σ_3	130
4–20	(a) Three depth groups are defined as the continental crust (green), the plate boundary zone (blue) and the oceanic mantle (red). The perpendicular distance to the interface of top and bottom of slab interface is shown in arrows. (b) Distributions of focal mechanisms in three depth groups. Four sub-areas (1)-(4) are shown in red. (c) Stress inversion results of each depth group are shown in lower-hemisphere projection. Red: σ_1 , green: σ_2 and blue: σ_3	131
5–1	Maps showing fault locking coefficients ϕ of Model I: study of Schmalzle et al. [2014] and Model II: study of Burgette et al. [2009]. Red dashed lines are 50% fault locking contours. PORT: Portland, SEA: Seattle, PA: Port Angeles. VAN: Vancouver.	135

5–2	Maps showing non-dimensional frictional parameter $a - b$ of (a) Model I and (b) Model II. Parameter $a - b$ is linearly decreasing from -0.0035 to 0 from trench to downdip. 50% fault locking contours are shown by red dashed lines. (c) Along-strike length of velocity-weakening portion, W , on the fault interface. The range of the northern, central and southern Cascadia are denoted by gray bars.	137
5–3	Maps showing coseismic fault slip in Model I and Model II. The cumulative slip is averaged over 1500 years with 3 or 4 earthquake cycles. The seismic moment magnitudes of the northern Cascadia slip patches in Model I and Model II are Mw8.7 and Mw8.6, respectively. Red triangles are sites of coastal sediment measurements that are shown in the study of Leonard et al. [2010].	140
5–4	Graphs showing synthetic subsidence records of Model I (blue) and Model II (red). The paleoseismic subsidence data of the study of Wang et al. [2013] are shown in black. The error bars are uncertainty range estimated by Wang et al. [2013].	141
5–5	Graphs of downdip distance of velocity-weakening, W (blue), and the modeled coseismic/aseismic slip (red) in Model II, with uniform h^* along the strike. Coseismic slip appears in the northern and southern while aseismic in the central Cascadia. The range of three segments are shown in gray.	142
5–6	Modeled coseismic rupture on the fault for (a) northern, (b) southern and (c) central Cascadia in Model II, using heterogeneous h^* along the strike. The seismic moment magnitudes of the three patches are Mw8.7, Mw8.1 and Mw7.8, respectively. Red triangles show the sites of coastal sediment measurements.	144
5–7	Graphs showing (a) synthetic subsidence records from three coseismic segments: northern (red), central (blue) and southern (magenta) and (b) sum of synthetic subsidences of three segments (green). Observational data from Wang et al. [2013] is in black.	145

CHAPTER 1

Introduction

Since 2001, over ten M8+ earthquakes have struck global subduction margins. Two of them, the 2004 Sumatra-Andaman and the 2011 Tohoku-Oki earthquake, were M9+ and caused devastating damage to the coastal communities. The 2011 Mw9.0 Tohoku-Oki earthquake slipped more than 50 m within 40 km landward from the trench [Lay et al., 2011; Yue and Lay, 2011; Sun et al., 2017] and generated disaster tsunami waves that killed thousands of people and disabled the Fukushima nuclear plant with lasting contamination effects. Geophysicists were surprised that the epicenter of the Tohoku-oki event was located about 50 km landward of the trench [Simons et al., 2011], where no strong coupling was inferred from the GPS inversion study of Hashimoto et al. [2009]. Presently, we still have very little knowledge of how the stress status on the fault is related to the nucleation of megathrust earthquakes.

For a long time, the subduction convergence was thought to be accommodated through coseismic slip, afterslip or continuous creeping. This assumption is challenged by the discovery of a type of quasi-static fault deformation using onshore GPS arrays in the Vancouver Island and the Washington state. This type of quasi-static deformation, which is called slow slip event (SSE), is identified occurring near or downdip of seismogenic portions [Dragert et al., 2001; Schwartz and Rokosky, 2007; Peng and Gomberg, 2010]. On average SSEs have slip rates of 10-100 times higher than plate convergences and last for days to months [Dragert et al., 2001; Rogers and Dragert, 2003; Schwartz and Rokosky, 2007]. Although SSEs have low slip rates, they can release elastic energy equivalent to Mw6.0 earthquakes in Cascadia [Dragert et al., 2001]. SSEs have been

observed in other circum-Pacific subduction zones, e.g., the southwest Japan [Obara, 2002] and the Hawaii volcanic island [Segall et al., 2006]. Almost all SSEs are inferred to appear around the frictional transition portion from unstable to stable fault slip [e.g., Schwartz and Rokosky, 2007; Peng and Gomberg, 2010]. The fault slip spectrum from slow to fast earthquakes may reflect the inherent characteristics of faults, e.g., frictional properties [Peng and Gomberg, 2010] or brittle-to-ductile rheological changes [Gao and Wang, 2017].

As adjacent to or partially overlapping with the shallow seismogenic zone, SSEs have the potential to facilitate deep-to-shallow stress transfer [Liu et al., 2007] or affect the initiation of megathrust earthquakes [Kato et al., 2012]. Investigating the distribution and interaction of SSEs and megathrust earthquakes may help us to understand the physical properties of megathrust faults. In this thesis, I aim to investigate the physical properties of subduction faults through the characteristics of the deep SSEs and the stress state of the shallow seismogenic zone. I study the influence of fault geometry and heterogeneity of the overlying plates on the source parameters of SSEs. My study shows that fault geometry and overlying plates play significant roles in the nucleations and distributions of SSEs. I also study shear strength on the megathrust fault in Cascadia. My research focus is important for understanding the seismic hazard in Cascadia and other subduction zones.

1.1 Cascadia Megathrust Fault

The Cascadia subduction zone marks the convergence boundary where the Juan de Fuca Plate is descending beneath the North American Plate at $\sim 3\text{-}4$ cm/yr [McCaffrey et al., 2007]. The margin extends ~ 1100 km from Vancouver Island to the northern California and is terminated by the Nootka and Mendocino Transform Tault at the northern and southern edges, respectively. According to marine turbidite sediment

records, a number of megathrust earthquakes have struck the entire 1100 km long margin at an interval of ~ 300 -500 yr over the past $\sim 10,000$ years [Goldfinger et al., 2012]. The magnitudes of these earthquakes are up to $M9+$ [Leonard et al., 2010]. The latest megathrust earthquake occurred in \sim A.D. 1700 and generated tsunami waves, which are recorded in Japanese historical documents [Satake et al., 1996, 2003]. However, no significant megathrust earthquake has been recorded by the modern seismic networks.

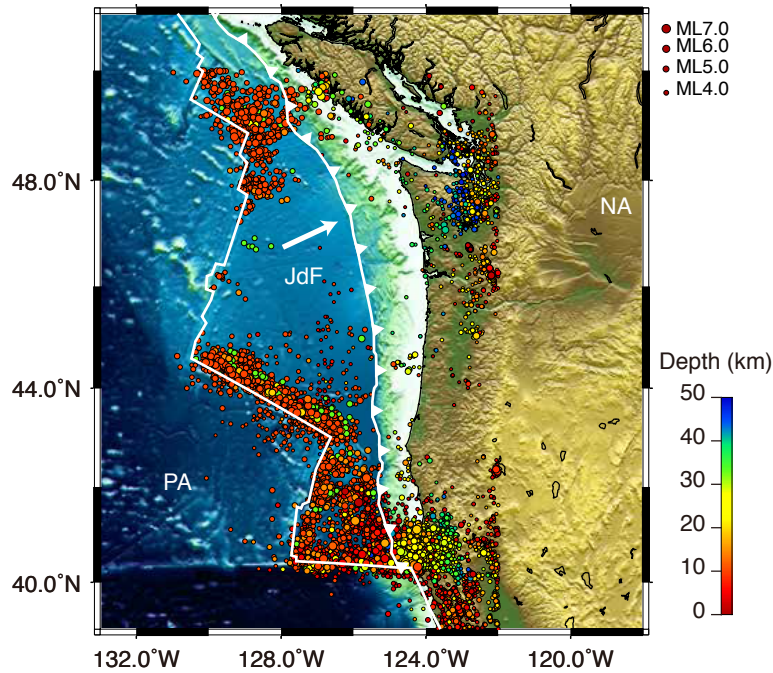


Figure 1–1: Map showing the geography of the Cascadia subduction zone. Earthquakes of $M_L > 1$ from 1980 to 2016, based on USGS catalogue (<https://earthquake.usgs.gov/earthquakes/search/>) (red dots). JdF: Juan de Fuca Plate. PA: Pacific Plate. NA: North American Plate.

The Cascadia subduction zone has a lower rate of interplate seismicity, in comparison with other subduction zones, e.g., the Japan or Peru-Chile Trench [Tréhu et al., 2015]. The thrust interface is seismologically “quiet” since the installation of modern seismic networks. The two most seismically-active regions appear at both ends of the

margin: the Mendocino Triple Junction (MTJ) and the Nootka Transform Fault [McCrary, 2000] (Figure 1–1). The MTJ marks the southern end of the Cascadia, where the Pacific Plate, the Gorda Plate and the North American Plate meet. In the MTJ, many strike-slip earthquakes appear either on the transform fault or within the Gorda lithosphere. Some of the earthquakes between 1989 and 2014 located off Oregon coast were close to the fault interface and had thrust focal mechanisms [Tréhu et al., 2015]. These thrust earthquakes appear in two clusters, which may be attributed to the subducted seamounts on the fault interface, but none of them are larger than Mw5.0 [Tréhu et al., 2015]. So far the only significant thrust event, a Mw7.1 earthquake, occurred on April 1992 at the Cape Mendocino [Oppenheimer et al., 1993]. However, the mainshock occurred at less than 10 km depth [Oppenheimer et al., 1993], which makes it hard to distinguish whether this earthquake ruptured the megathrust interface or a shallow dipping fault within the continental crust [Wang and Rogers, 1994; McCrary et al., 2012].

The nature of the “silent” subduction interface is still enigmatic to geophysicists. The absence of inter-plate seismicity may indicate complete healing and locking of the megathrust fault over the three centuries after the great earthquake of A.D. 1700 and somewhat lower degree of structure heterogeneity [Obana et al., 2015]. The absence of earthquakes may also result from a (partially) creeping fault in Cascadia, as indicated by the GPS inversion in central Oregon [Schmalzle et al., 2014]. However, the geodetic observations show that the current fault is firmly locked to 20 km depth [Burgette et al., 2009; Schmalzle et al., 2014]. The existence of historical megathrust earthquakes inferred from marine sediment records also suggests the capability of coseismic fault energy release [Satake et al., 2003; Leonard et al., 2010]. Even the creeping segment of the San Andreas Fault produces $M < 3$ seismicity at the depth of seismogenic zone [Shelly and Hardebeck, 2010].

1.2 Current Understanding of SSEs

The discovery of SSEs sheds lights on the researches of megathrust faults. SSEs are first identified as the quasi-static slip appearing near or at some distance below seismogenic zone, where the fault is previously thought to be continuous creeping in Cascadia [Dragert et al., 2001; Schwartz and Rokosky, 2007; Peng and Gomberg, 2010]. Now SSEs are widely distributed in six circum-Pacific margins [e.g., Hirose et al., 1999; Dragert et al., 2001; Rogers and Dragert, 2003; McGuire and Segall, 2003; Ohta et al., 2006; McCaffrey et al., 2008; Szeliga et al., 2008; Outerbridge et al., 2010; Schmidt and Gao, 2010; Wallace et al., 2012; Wei et al., 2012; Schmalzle et al., 2014; Fu et al., 2015]. Sometimes SSEs are accompanied by seismic radiations in the form of non-volcanic tremors (NVTs), low-frequency earthquakes (LFEs), and very low-frequency earthquakes (VLFs) [Miller, 2002; Rogers and Dragert, 2003; Peterson and Christensen, 2009; Wech et al., 2009; Obara, 2010; Gao et al., 2012; Frank et al., 2015b; Ghosh et al., 2015; Peng and Rubin, 2017]. Combining source parameters of both seismic and geodetic observations around the world, Ide et al. [2007] defined a distinctive slip mode other than the conventional fast earthquakes and called it slow earthquakes. The occasionally synchronized SSEs and low-frequency seismic energy release are hypothesized to be different manifestations of the same fault shearing process [Ide et al., 2007]. In contrast to the moment-duration scaling, $M \sim T^3$, of fast earthquakes, the moment-duration scaling of slow earthquakes has an index between 1 and 2 [Ide et al., 2008; Gao et al., 2012; Liu, 2014]. This distinctive moment-duration scaling suggests a new category besides traditional fast earthquakes [Ide et al., 2007]. Later, Peng and Gomberg [2010] proposed a continuous spectrum of slip mode between fast and slow earthquakes by supplementing the slow slip phenomena dataset with geodetic observations of other

types of slip mode, such as afterslip and landslides. Previous “gap” in the moment-duration diagram between fast and slow earthquakes, as shown in the study of Ide et al. [2007], may be due to the limitation of current observation capacity.

1.2.1 SSEs in Cascadia

Episodic SSEs are observed along the entire margin of the Cascadia subduction zone. Most episodic SSEs are accompanied with non-volcanic tremors, which are called episodic slips and tremors (ETs) in Cascadia [Rogers and Dragert, 2003]. Thus tremors have been used as a proxy for SSEs in Cascadia [Wech et al., 2009]. SSEs here normally last for ~ 15 -20 days and thus are usually called short-term SSEs in Nankai, Japan, in order to be distinguished from the long-term SSEs that last for years [Obara, 2011]. Non-volcanic tremors do not have impulsive P- or S-picks and have low-frequency (1-10 Hz) energy in seismographs, which makes them difficult to locate precisely [Obara, 2002]. At first there seems a wide depth distribution (up to ~ 40 km) within the overlying plate [Kao et al., 2005]. Relocating tremors with a cross-correlation technique shows that they appear near to the subduction interface at a depth of 30-50 km [McCausland et al., 2005; Wech and Creager, 2008]. Locations obtained by the multibeam back projection (MBBP) technique with small-scale seismic arrays in the Olympic Peninsula also support that tremors are close to the subduction interface [Ghosh et al., 2012]. Centroid moment tensor resolutions of LFEs and VLFs observed in Nankai and Cascadia prove that they occur as fault shear slip on the megathrust interfaces [Shelly et al., 2007; Ghosh et al., 2015; Hutchison and Ghosh, 2016].

1.2.2 Physics of SSEs

Based on the observations, the appearance of SSEs is closely related with the existence of high pore fluid near the subduction fault [Obara, 2002]. It is hypothesized that the near-lithostatic pore fluid reduces the normal stress loading on the fault and

promotes fault shear slip [Obara, 2002]. The importance of the high fluid pressure in generating slow earthquakes is supported by several observational pieces of evidence:

Firstly, the recurrence of slow slips or slow earthquakes is modulated by small stress perturbations of a few kPa, such as tidal stressing [Hawthorne and Rubin, 2013] or passing-by surface waves [Rubinstein et al., 2007; Peng et al., 2009]. The sensitivity to small stress perturbations suggests the fault is critically stressed. For example, triggered tremors have been observed during the passing-by Love waves in Cascadia [Rubinstein et al., 2007], the San Andreas Fault [Peng et al., 2009] and the Central Range in Taiwan [Peng and Chao, 2008]. The amplitude of the Coulomb stress changes generated by the passing waves is only a few tens of kPa.

Secondly, a high V_p/V_s (or high Poisson's ratio) layer located near the subduction fault interface is observed in six circum-Pacific subduction zones. Beneath Vancouver Island, a layer of high Poisson's ratio is found at a depth of 30-50 km [Audet et al., 2009]. Similarly, in Shikoku, Japan, a thin layer of high V_p/V_s ratio is detected near the slab interface at a depth of 30-50 km [Shelly et al., 2006]. A bunch of low-frequency earthquakes (LFEs), which is buried in the non-volcanic tremor signals, is located in the layer of high V_p/V_s ratio [Shelly et al., 2006].

Last but not least, the metamorphic dehydration of oceanic slab can appear at shallow depths (at $\sim 350-500^\circ\text{C}$) in warm and young subduction zones [Peacock et al., 2002], where most short-period slow earthquakes are observed. The depth of ETS zone is correlated with the forearc mantle wedge in Cascadia [McCrory et al., 2014]. It is hypothesized that serpentized mantle wedges has a lower slab-normal permeability and thus can trap the pore fluid within the oceanic crust and subduction shear zone around the mantle wedge corner [McCrory et al., 2014; Hyndman et al., 2015; Gao and Wang, 2017]. This is also supported by the observations of an increasing forearc V_p/V_s

ratio with depths, which is affected by the concentration of quartz-rich silica deposit evolution through permeability [Audet and Burgmann, 2014].

Rock experiments have found that the frictional stability is significant in the mechanism of SSEs. Leeman et al. [2016, and references therein] conducted experiments to investigate how the nucleations of SSEs are related with rock friction properties. A spectrum of slow-slip behaviors occurs near the threshold between stable and unstable failure. The behavior is governed by frictional dynamics via the interplay of fault frictional properties, effective normal stress and elastic stiffness of surrounding materials. In a recent experiment, faults can alternatively switch between fast and slow slip as a result of different loading rates, when the sample length is comparable to the critical nucleation size [McLaskey and Yamashita, 2017]. These laboratory findings may explain some field observations. For example, many regions of the fault that slipped seismically in the 2011 Tohoku-Oki earthquake slipped aseismically before and after it [Uchida and Matsuzawa, 2013; Ito et al., 2013].

1.2.3 Relation with Megathrust Earthquakes

It is still an open question whether SSEs can trigger megathrust earthquakes. SSEs can promote the nucleation of megathrust earthquakes, due to the stress loading to updip seismogenic zone [Dragert et al., 2001]. Before the 2011 Mw9.0 Tohoku-Oki earthquake, a series of foreshocks migrated towards the epicenter [Kato et al., 2012]. The migrating earthquakes are attributed to an offshore SSE [Kato et al., 2012]. The seismicity migration may represent the stress loading process which leads to the nucleation of the megathrust earthquake and may promote the dynamic rupture [Kato et al., 2012]. In Guerrero, Mexico, the 2014 Mw7.3 Papanoa earthquake was suggested to be triggered by a preceding SSE [Radiguet et al., 2016]. The epicenter of Papanoa earthquake is spatially adjacent to a region of +40 kPa Coulomb stress generated by

the preceding SSE [Radiguet et al., 2016]. This possibly indicates a threshold for the static triggering of earthquakes by slow slip process.

1.2.4 Numerical Models of SSEs

There are several physical models of SSEs. Firstly, the “cut-off ” slip rate friction law assumes that the frictional strength of the fault is velocity-weakening (VW) at a low slip rate and velocity-strengthening (VS) at a high slip rate, as inferred from experiments of halite samples [Shimamoto, 1986]. The cut-off velocity from VW to VS is about $10^{-7} - 10^{-5}$ m/s based on experiment data [Shimamoto, 1986]. Shibazaki and Iio [2003] reproduced transient slip events for a planar fault geometry with this “cut-off” friction law. By assuming the near-lithostatic pore fluid pressure at the frictional weakening portion on the fault, episodic SSEs occur spontaneously with a slip rate 10-100 times higher than the plate convergence rate [Shibazaki and Iio, 2003].

Secondly, Liu and Rice [2005] build the numerical model in the framework of laboratory-derived rate-and-state friction law, in which the fault strength depends not only on the slip rate but also on the contact history, i.e., state [Dieterich, 1979; Ruina, 1983]. In this framework, frictional parameters from both wet granite [Blanpied et al., 1998] and gabbro gauges [He et al., 2007] sliding experiments are tested [Liu and Rice, 2009]. The source parameters (e.g., recurrence interval and magnitude) roughly scales with the downdip width of velocity-weakening portion on the fault [Liu and Rice, 2009]. Thus the diverse slip phenomena around the world can be attributed to the various frictional properties on the fault [Liu and Rice, 2009]. The pore pressure level, which affects the effective normal stress on the fault, can modulate the recurrence intervals of episodic SSEs [Liu and Rice, 2007]. For example, the 14-month recurrence interval of SSEs in Cascadia requires an effective normal stress of 2-3 MPa [Liu and Rice, 2007].

The third class of numerical models incorporates the effect of dilatancy-strengthening which is derived from frictional experiments of porous rocks [Liu and Rubin, 2010;

Segall et al., 2010]. The dilatant-strengthening has been proposed to be important in preventing rapid deformation of landslides [Marone et al., 1990; Iverson et al., 2000] and glacier basal sediments [Clarke, 1987]. During the increasing fault slip, the rapid porosity growth could temporally suppress the pore pressure level and thus inhibit the slip rate and terminate further fault ruptures [Liu and Rubin, 2010; Segall et al., 2010]. The high effective dilatant-strengthening affects the slip budget at the downdip of seismogenic zones by stopping the seismic ruptures and increasing the afterslip and aseismic slip [Liu, 2013].

1.3 Thesis Outline

This thesis aims to investigate the physical mechanism of episodic SSEs in subduction zones and the shear strength of megathrust faults at seismogenic depths.

In Chapter 2, I study the physics of the deep SSEs by investigating the effect of subduction geometry. I incorporate a realistic fault geometry of the northern Cascadia in the framework of rate- and state-dependent friction law, to simulate the spatiotemporal evolution of SSE on a non-planar subduction fault. The modeled SSEs capture the major characteristics revealed by GPS observations. The along-strike distribution of SSE is inversely related to the local dip angle of SSE zone, suggesting strong geometrical control on the slow slip process. Besides the GPS-detectable "fast-spreading" phase, I find that each SSE cycle consists of a deep "pre-SSE" preparation (nucleation) and a "post-SSE" relaxation (healing) phase, which may be the driving mechanism for the deeper inter-ETS tremor activity discovered in Cascadia.

In Chapter 3, I investigate how the fault heterogeneities of the overlying continental lithosphere affect the source process of SSEs. I develop a 3-D episodic SSE model for the northern and central Cascadia, incorporating both seismic and geodetic observations to constrain the heterogeneities in the megathrust fault properties. The

segmentation of recurrence intervals that is constrained by Free-air and Bouguer gravity anomalies is equally comparable to GPS observations. However, the model that is constrained by Free-air anomaly does a better job in reproducing the cumulative slip as well as more consistent surface displacements with GPS observations. The modeled along-strike segmentation only represents the averaged slip release over many SSE cycles, rather than permanent barriers.

In Chapter 4, I study the shear strength of megathrust faults in the shallow seismogenic zone. I use Cascadia Initiative expedition OBS data to obtain the focal mechanisms of small-to-intermediate earthquakes. The tectonic stress tensors in the continent and mantle are obtained from both the historical focal mechanisms between 1980 and 2015 and earthquake focal mechanisms resolved by OBS data. I setup an inversion algorithm for the fault shear strength using a convex optimization technique. The shear strength of the plate boundary fault scales with the assumed mantle strength used in the inversion. When the mantle strength is in the range of 50 to 400 MPa, the fault shear strength can be no higher than 50 MPa. The resolved effective friction coefficients are between 0 and 0.2.

In Chapter 5, I model the earthquake cycle with the seismogenic zone constrained by different fault locking patterns in the Cascadia margin. The frictional parameter $a - b$ is assumed to be proportional to the fault locking coefficients. To match up the coastal surface subsidence measurements, heterogeneous along-strike nucleation sizes are needed in reproducing coseismic fault slip in the model. The nucleation size in the central Cascadia needs to be about half the size of that in northern Cascadia.

Chapter 6 contains the thesis conclusions and scope for future works.

CHAPTER 2

Spatiotemporal Evolution of Slow Slip Events in A Non-planar Fault Model for Northern Cascadia Subduction Zone

2.1 Introduction

Episodic slow slip events (SSEs) fill in the fault sliding spectrum between stable creep and dynamic earthquakes and accommodate a fraction of the cumulative slip on plate boundary faults [Ide et al., 2007; Peng and Gomberg, 2010]. In subduction zones, such transient quasi-stable slip occurs near the downdip limit of the megathrust seismogenic zone with slip velocities several orders of magnitude faster than plate convergent rates, durations of several days-to-years, and quasi-periodic recurrence intervals of months-to-years [e.g., Hirose et al., 1999; Dragert et al., 2001; Ohta et al., 2006; McCaffrey et al., 2008; Outerbridge et al., 2010; Schmidt and Gao, 2010; Wallace et al., 2012; Wei et al., 2012; Fu et al., 2015]. Seismic radiations in the form of non-volcanic tremors, low-frequency earthquakes (LFEs), and very low-frequency earthquakes (VLFs) are found accompanying the migration of SSEs in southwest Japan [Shelly et al., 2006; Obara, 2010], Cascadia [Rogers and Dragert, 2003; Wech et al., 2009], and possibly in south central Alaska [Peterson and Christensen, 2009].

Numerical simulations in SSE source mechanism have shown that SSEs can be modeled as shear sliding on faults at depths of unstable to stable transitional frictional behavior [e.g., Liu and Rice, 2005; Shibazaki and Shimamoto, 2007; Rubin, 2008] or a mixture of alternating stability properties [e.g., Skarbek et al., 2012], effective dilatancy strengthening under high pore pressure conditions [Liu and Rubin, 2010; Segall et al., 2010; Liu, 2013], or through a combination of brittle and viscous material rheology [Reber et al., 2015]. Most of the friction-based models involve near-lithostatic

pore pressure condition at SSE source depths in order to modulate SSE durations and recurrence intervals. The presence of high pore pressure, often corresponding to an effective normal stress of a few MPa, is likely due to the fluids released from metamorphic dehydration of oceanic slab at or below the SSE depths and is supported by seismic imaging results of high V_p/V_s structures in northern Cascadia and southwest Japan [Shelly et al., 2006; Audet et al., 2009], as well as the observations of low stress drops [Gao et al., 2012] and tremor sensitivity to small-amplitude tidal stressing [Hawthorne and Rubin, 2010; Houston, 2015].

The Cascadia subduction zone is one of the best-instrumented subduction margins, where two decades of continuous GPS and seismic monitoring has revealed heterogeneous distributions of slow slip and tremor activity along the plate boundary [e.g., Dragert et al., 2001; Rogers and Dragert, 2003; Kao et al., 2009; Wech and Creager, 2011]. GPS inversion studies have found slow slip patches that repeat quasi-periodically at intervals of ~ 14 , 19 and 10 months from north to south along the margin [Brudzinski and Allen, 2007; Szeliga et al., 2008; Schmidt and Gao, 2010]. This along-strike variation may relate to the composition of the overlying continental lithosphere; the denser and stronger Siletzia terrane could accommodate more cumulative stress and result in longer recurrence interval [Brudzinski and Allen, 2007]. In addition to the three strongest segmentation boundaries, Boyarko et al. [2015] found minor boundaries between tremor activity coincide with offshore sedimentary basins that are related to paleo-megathrust asperities. Slow slip observations also vary along the downdip direction in Cascadia. Non-volcanic tremors occur more frequently with increasing depth, implying a downdip decrease in slow slip magnitude and periodicity [Wech and Creager, 2011], possibly due to the reduced fault gouge permeability during progressive silica enrichment with depth in the forearc crust [Audet and Burgmann, 2014]. The spatial

variations of slow slip phenomena along both the strike and downdip dimensions suggest that slab geometry may play an important role in controlling the observed SSE characteristics in Cascadia.

However, most SSE source models have adopted the planar fault approach while focusing on the effects of frictional and hydraulic conditions on the source parameters and along-strike segmentation of SSEs [e.g., Rubin, 2008; Segall et al., 2010; Colella et al., 2012; Liu, 2013, 2014]. Mitsui and Hirahara [2006] simulated slow slip on a fault consisting of three planar elements of varying dip angles to demonstrate the fault geometry effect on SSEs, although detailed slow slip evolution cannot be simulated due to their simplified conceptual model set up. Nonplanar slab geometry has been incorporated in the source model for SSEs in Kii Peninsula, Tokai, and Shikoku in southwest Japan [Shibazaki et al., 2012; Matsuzawa et al., 2013]. The plate configuration in Japan is thought to contribute to the appearance of the long-term SSEs in central Shikoku and their distinction from short-term counterparts, although the effects of geometric complexity have not been quantitatively explored.

In this chapter, I present a nonplanar subduction fault model for northern Cascadia, in the framework of rate- and state-dependent friction law, to investigate explicitly the effect of fault geometry on SSE source properties and their implication for megathrust earthquakes. I model episodic SSEs during the interseismic period, analyze the slow slip process based on the moment release rate, and calculate the SSE source parameters (recurrence interval, cumulative slip, duration, fault area, and equivalent magnitude). Without introducing small-scale frictional heterogeneities or fine-tuning model parameters, our numerical results show that the variation in fault geometry can result in the segmentation of three distinctive slip patches, with the central 150 km long segment beneath Port Angeles exhibiting a maximum slip of ~ 2.5 cm and repeating every ~ 1.5 years, comparable to GPS inversion results. Each slow slip episode evolves

in pre-SSE preparation, fast-spreading, and post-SSE relaxation phases defined by moment rates. In particular, slow slip during the preparation phase may be the driving mechanism for deeper inter-ETS (episodic tremor and slip) tremor activity [Wech and Creager, 2011], although the modeled slip rates are below current GPS detection limits for northern Cascadia. I emphasize that the goal of this work is to investigate the effect of fault geometry on SSE source properties. In the following sections, I do not intend to fine-tune model parameters to precisely reproduce all the SSE observations but rather focus on the general comparison of their observed and simulated spatial and temporal patterns.

2.2 Method

2.2.1 Laboratory-derived Rate- and State- Friction Law

Experiments. Extensive rock shearing experiments have been conducted to investigate the mechanism of faulting and earthquakes in the 1970s and 1980s. Several characteristics of friction are found by these experiments. Firstly, the static friction (μ_s) increases logarithmically with the hold time for both initially bare rock surfaces [Dieterich, 1972; Beeler et al., 1994] and granular fault gouges [Dieterich, 1981; Marone and Blanpied, 1994]. Secondly, the dynamic friction (μ_d) for rocks and gouges decreases with the slip velocity, which is called velocity-weakening [Scholz and Engelder, 1976; Dieterich, 1978]. Subsequent experimental work found that with higher velocity, the friction of rocks can exhibit a transition from velocity-weakening to velocity-strengthening [Blanpied et al., 1987]. Additionally, roughness, shearing distances, thickness of the gouge or dilatancy (porosity increase due to amplified fault slip rate) can also affect the friction coefficients in the experiments [e.g. Marone, 1998]. Scaling the experiment data directly to natural faults has not been proved yet, due to the limitation of current lab conditions. However, these rock experiments provide a quantitative method to understand the fault frictional instability.

Constitutive Friction Law. From lab experiments, frictional strength depends on not only the sliding rate but also the asperity contact properties [Dieterich, 1979, 1981; Ruina, 1983]. In the constitutive law, friction coefficient f is dependent on the fault slip rate V and slip history, formulated as a single state variable θ ,

$$\tau = \bar{\sigma} f = (\sigma - p) \left[f_0 + a \ln \left(\frac{V}{V_0} \right) + b \ln \left(\frac{V_0 \theta}{d_c} \right) \right]. \quad (2.1)$$

Here, a and b are non-dimensional friction parameters, d_c is the characteristic distance over which θ evolves to a new steady status, f_0 is the friction coefficient at a reference velocity V_0 at the steady state and $\bar{\sigma} = \sigma - p$ is the effective normal stress.

There are two commonly used evolution laws for describing the evolution of the state variable θ . The "aging" law allows friction to evolve on stationary asperity contacts as supported by the experiments of Beeler et al. [1996],

$$\frac{d\theta}{dt} = 1 - \frac{V\theta}{d_c}, \quad (2.2)$$

whereas the "slip" law argues that all changes in friction involve slip [Ruina, 1983],

$$\frac{d\theta}{dt} = -\frac{V\theta}{d_c} \ln \left(\frac{V\theta}{d_c} \right). \quad (2.3)$$

At a steady status θ_{ss} (where $\frac{d\theta}{dt} = 0$), $\theta_{ss} = \frac{d_c}{V_{ss}}$ and Eq 2.1 becomes $\tau_{ss} = \tau_0 + (a - b) \ln \left(\frac{V_{ss}}{V_0} \right)$. Thus $a - b = \frac{d\tau_{ss}}{d \ln(V)}$, when friction stability parameter $a - b$ is positive (velocity-strengthening, VS), slip remains stable and any slip perturbation evolves towards a steady state. Slip can be either unstable or conditionally stable when $a - b$ is negative (velocity-weakening, VW).

The “slip” law and the “aging” law. It is under debate which law is more “realistic” in representing the contact history from experimental data [Marone, 1998]. Unfortunately, neither of these two candidates can fit the experimental data perfectly.

The “aging” law can well approximate the time-dependent increase of shear strength but fails as the asymmetric displacements at increasing and decreasing slip rate steps [Ampuero and Rubin, 2008]. On the contrary, the “slip” law can fit the symmetric step changes at both increasing and decreasing slip rates but fails to reconcile the time-dependent increase of shear strength [Ampuero and Rubin, 2008].

In the framework of rate- and state- friction, both “slip” and “aging” law are used in simulating both coseismic earthquakes and aseismic slow slip cycles [Lapusta et al., 2000; Rubin and Ampuero, 2005; Liu and Rice, 2005]. However, at a large velocity step, the “slip” law requires a shorter distance for nucleations and transitions from aseismic to seismic slip and consequently a narrower range of W/h^* (the ratio of velocity-weakening distance W and nucleation size h^* which will be introduced in detail later) allowing self-sustained SSEs, in comparison with the “aging” law [Ampuero and Rubin, 2008]. The reason for this is that the dependence of shear stress on displacements during velocity jumps from V_1 to V_2 ($V_1 < V_2$) of “slip” law and ‘aging’ law are $-\delta/d_c$ and $\exp(-\delta/d_c)$, respectively (where δ is displacement and d_c is characteristic slip distance in rate-state friction) [Ampuero and Rubin, 2008]. This dependence results in a narrower band of VW portion for the ‘slip’ law to settle in a new steady status (V_2), compared with the “aging” law. The narrow range of frictional parameters for SSEs with the “slip” law calls for other mechanisms, such as dilatancy strengthening, to reproduce the worldwide SSE observations [Rubin, 2008]. The comparison of “slip” and “aging” law is shown in Appendix A.

2.2.2 Fault Geometry

The Cascadia subducting slab geometry is constrained by either seismic velocity structure images or by incorporating hypocenters and wide-angle reflection and refraction surveys [Fluck et al., 1997; McCrory et al., 2006; Audet et al., 2010; McCrory et al., 2012]. These studies use different datasets and assumptions in estimating the

location of the plate boundary. Here I construct a non-planar fault interface based on the most recent comprehensive Cascadia slab model by McCrory et al. [2012]. The slab geometry of McCrory et al. [2012] is updated from their previous version of McCrory et al., [2006] after incorporation of more recent seismicity relocations and regional seismic velocity structures along the Cascadia margin. To save up numerical consumption, I only use McCrory et al., [2012]. Our model domain extends 450 km along the margin from Vancouver Island to Washington state (between latitude 46°N and 50°N, Figure 2–1) which covers the most prominent geometric feature where a class of Mw6.0 SSEs spatially correlate with the slab bending beneath the northern Washington state [Schmidt and Gao, 2010].

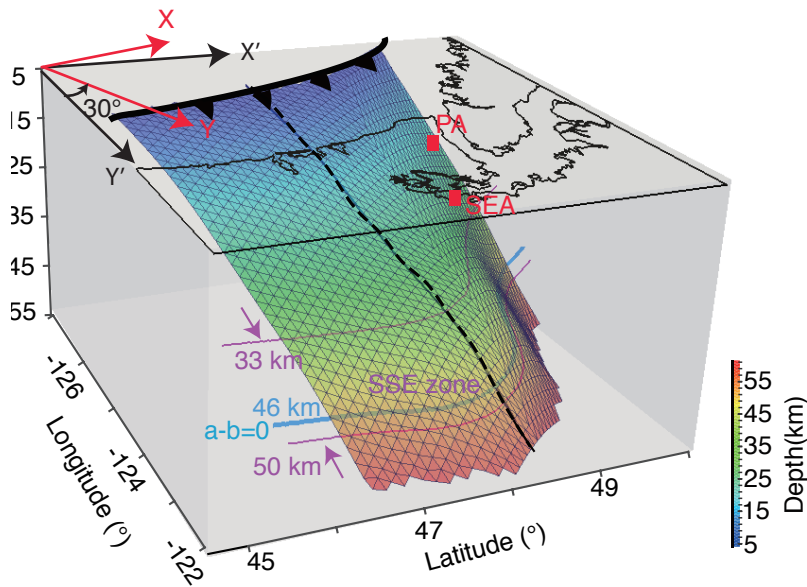


Figure 2–1: (a) The 3-D non-planar northern Cascadia subduction zone fault model with triangular mesh on the fault (element size is ~ 20 km for illustration purpose while spacing of ~ 1 km is used in simulations). Top red Cartesian coordinates X-Y: X is trench-parallel direction and Y is trench-normal direction, after rotating 30° from original X'-Y' coordinates. Depth 0 km is at sea level. Trench is at 5 km depth. Frictional stability transition from velocity-weakening ($a - b < 0$) to velocity-strengthening ($a - b > 0$) is at 46 km (blue line). Effective normal stress $\bar{\sigma} = 1.5$ MPa is between 33 and 50 km (pink lines). PA: Port Angeles and SEA: Seattle. Coastline is on the top surface.

The oblique subduction between the Juan de Fuca and North American Plates is dominant in southern Washington and Oregon but is largely offset by the northward translation of the Oregon forearc and becomes less significant in our modeling region [Miller et al., 2001; McCaffrey et al., 2007]. As the model mainly focuses on slow slip events in northern Cascadia (Vancouver Island and northern Washington), I apply a uniform convergence in the downdip direction and neglect any slip component along the strike direction. This effect of oblique subduction in northern Cascadia is also neglected in Schmidt and Gao [2010] with no obvious differences in GPS inversions. I note that a recent geodetic study in central Cascadia (43° to 46°N) reports considerable strike-parallel displacement in their SSE slip inversion [Schmalzle et al., 2014], which needs to be considered in future modeling studies for the entire Cascadia margin. In this study I set the plate convergence to be in the direction of 60° from the north at a rate of $V_{pl} = 41$ mm/yr, taken at the plate boundary location at (48°N, -127°W) based on the plate model of DeMets et al. [1994], which is also consistent with a more recent plate motion model by McCaffrey et al. [2013].

For the convenience of numerical simulation, I first convert the geographic coordinates of latitude-longitude into the Cartesian coordinates (X'-Y' in Figure 2-1) with origin at the reference point (48°N, -127°W). I then rotate X'-Y' 30° anticlockwise to the X-Y coordinates such that X-Y represent trench-parallel and trench-normal directions, respectively. After the conversion the fault is 450 km long along the strike and ~300 km in the downdip directions. The rotated X-Y plane is divided into a 1 km square grid, further diagonalized into triangular elements by using GMT command surface [Wessel and Bercovici, 1998] and projected onto the subduction fault plane. The triangular meshing is more advantageous for modeling slip on a curved fault as there is no overlap between adjacent elements. The resulted triangular element size on the fault

satisfies the grid resolution requirement dictated by the choice of frictional parameters [Day et al., 2005]. I consider the shallow 5-28 km as completely locked, representing the interseismic period and only allow fault slip in the dip direction between 28 and 55 km. In this model set up, a depth of 0 km represents the sea surface, and the trench is set to begin at depth 5 km. Thus, the subduction fault is effectively locked for the 23 km beneath the trench and is allowed to evolve under rate-state friction between 23 and 50 km, which sufficiently covers the observed SSE depth range of 30-45 km from the trench and is also consistent with long-term GPS inversion of fault coupling that shows locking down to approximately 20 km [McCaffrey, 2009; Schmalzle et al., 2014]. Assuming that the shallow part of the fault is completely locked also reduces computational resources needed for each simulation case, which allows us to achieve higher grid resolutions and explore a broader parameter space. The total number of elements for all the simulations presented in this chapter is on order of $\sim 100,000$, for which we use Compute Canada high-performance computing facility at McGill University to conduct the simulations.

2.2.3 Governing Equations

The evolution of fault shear stress is governed by the laboratory-derived rate and state-dependent friction law [Dieterich, 1979; Ruina, 1983], which has been shown in Chapter 2.2.1.

I adopt the quasi-dynamic relation between shear stress τ and fault slip δ following Rice [1993],

$$\tau_i(t) = - \sum_{j=1}^N K_{ij} (\delta_j(t) - V_{pl}t) - \eta \frac{d\delta_i(t)}{dt}, \quad (2.4)$$

where $\tau_i(t)$ and $\delta_i(t)$ are shear stress and slip on element i , respectively, and stiffness matrix K_{ij} represents the shear stress change on element i due to a unit

dislocation in dip direction on element j . This Green’s function K_{ij} is calculated in an elastic half-space medium [Okada, 1992], as first implemented for triangular dislocation elements by Stuart et al. [1997], and benchmarked here against a Matlab code developed by Meade [2007]. The radiation damping factor $\eta = \mu/2c_s$ (c_s is shear wave speed) is introduced to prevent the slip velocity from going unbounded during an earthquake [Rice, 1993]. This quasi-dynamic approach is appropriate for simulating slow slip processes with the updip seismogenic zone fully locked.

2.2.4 Model 1: Isothermal SSE Depths

The non-dimensional friction stability parameter $a - b$ depends on temperature, rock type, and normal stress in friction experiments [e.g., Blanpied et al., 1998]. The depth-dependent $a - b$ distribution (Figure 2–2a) is obtained by converting frictional parameters measured on gabbro gouge shear experiments under hydrothermal conditions [He et al., 2007] using a temperature profile of the northern Cascadia subduction fault [Peacock, 2009]. For model simplification, I treat the gabbro temperature dependent friction parameter by linear relations segmented by six pivot points at $(T, a - b) = (18.5, 0.001)$, $(100, -0.0035)$, $(416, -0.0035)$, $(442, -0.0035)$, $(510, 0)$, $(540, 0.001)$. Thus the frictional weakening portion follows the isothermal contours (Figure 2–2b). As shown in Figure 2–2a for a profile beneath Washington State, the subduction fault is under velocity-weakening conditions from nearly the trench to a depth of ~ 46 km, followed by velocity-strengthening condition. Here a depth of 0 km represents sea surface and the trench is set to start at depth 5 km.

The effective normal stress $\bar{\sigma}$ increases from the trench at a vertical gradient of 18 MPa/km up to depth ~ 7.7 km where $\bar{\sigma}$ reaches and remains at 50 MPa further downdip, although the specific gradient and values of effective normal stress updip have negligible effect on our simulation results as the fault is assumed to be locked at depths 5 to 28km. The depth range of locked zone is estimated based on the long-term GPS inversions

and the ETS depth [Schmidt and Gao, 2010; Hyndman, 2013]. Following previous SSE modeling studies, I assume pore pressure is near-lithostatic ($\bar{\sigma}$ of a few MPa) for a certain depth range around the velocity-weakening to strengthening stability transition [Liu and Rice, 2007]. I refer this range as SSE depths in this chapter. Within the SSE depth range, the fault under velocity-weakening condition has a downdip width of W (Figure 2–2a). The characteristic slip distance d_c is correspondingly reduced to the mm range to allow the appearance of spontaneous SSEs.

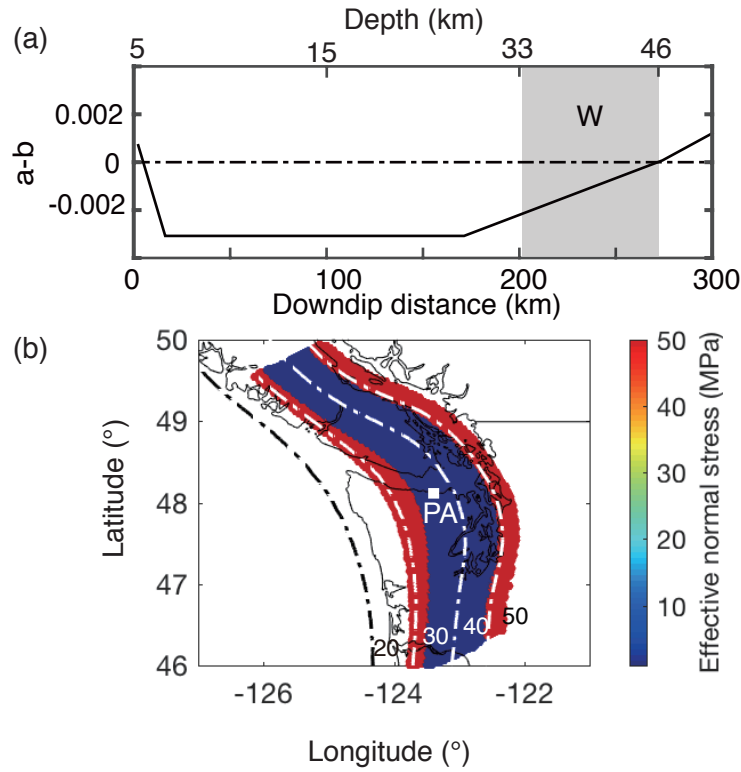


Figure 2–2: Graphs showing parameter $a - b$ and $\bar{\sigma}$ in Model 1. (a) Friction parameter $a - b$ versus downdip distance along a cross-section shown by the black dashed line in Figure 2–1. Top axis shows the depth in km from 5 km at the trench. Gray shaded region (W) is velocity-weakening under $\bar{\sigma} = 1.5$ MPa. (b) Mapview of $\bar{\sigma}$ on the fault. The locked fault from 5 km to 28 km is not shown. Blue shows $\bar{\sigma} = 1.5$ MPa while red shows 50 MPa. Dot-Dashed lines are depth contours of 20–50 km. PA: Port Angeles.

2.2.5 Model 2: Uniform SSE Depths

In the above model setup (referred in this chapter as Model 1), W is the along-dip distance of the velocity-weakening SSE zone defined between two isothermal (or depth) contours. Thus for any two fixed depth contours, for example, 33 to 46 km as shown in Figure 2-2a, W varies along the strike inversely proportional to the SSE zone average dip angle α , $W = 13 \text{ km}/\sin(\alpha)$. A shallower dipping section would result in a wider W and hence a larger W/h^* .

In order to separate the geometric effect from that of W/h^* , I design Model 2 where W/h^* is kept uniform along the strike. As illustrated in Figure 2-3, for all the cross-sections along the strike, W is uniformly 70 km updip from the friction stability transition. Within W , parameter $a - b$ increases linearly from -0.0035 to 0 , and $\bar{\sigma}$, d_c are kept as constant such that h^* , hence W/h^* , is always uniform along the strike. The major differences in Model 1 and Model 2 setup are evident for the central section of our model domain, where Model 1 would result in a much wider W if it follows the same $a - b$ linear increase from -0.0035 to 0 as in Model 2. In Section 2.3 I will present results primarily for the case $\bar{\sigma} = 1.5 \text{ MPa}$, $d_c = 0.7 \text{ mm}$, $W/h^* \approx 0.5$ to 0.8 (along-strike variation) of Model 1, and $\bar{\sigma} = 1.5 \text{ MPa}$, $d_c = 0.7 \text{ mm}$, $W/h^* \approx 1.5$ of Model 2, if not otherwise noted.

2.2.6 Parameter Exploration

Nucleation Size h^* . There is a critical stiffness in the spring-block system given by [Ruina, 1983]: $k_{cr} = \frac{\bar{\sigma}(b-a)}{D_c}$. The stiffness of the elastic material is proportional to $k_{elastic} = \mu' \frac{\delta}{L}$. Equalling the above two stiffness will give us $L = \frac{\mu' D_c}{\bar{\sigma}(b-a)}$, where $\mu' = \frac{\mu\pi}{2(1-\nu)}$ for in-plane type of slip and μ is shear modulus and ν is Poisson's ratio. L is regarded as the minimum discretized cell size [Rice, 1993].

A characteristic nucleation size, h^* , is defined as the minimum rupture radius. In numerical modeling, the usual definition of h^* is adopted as $h_{RR}^* = \frac{2\mu d_c}{\pi(1-\nu)(b-a)\bar{\sigma}}$,

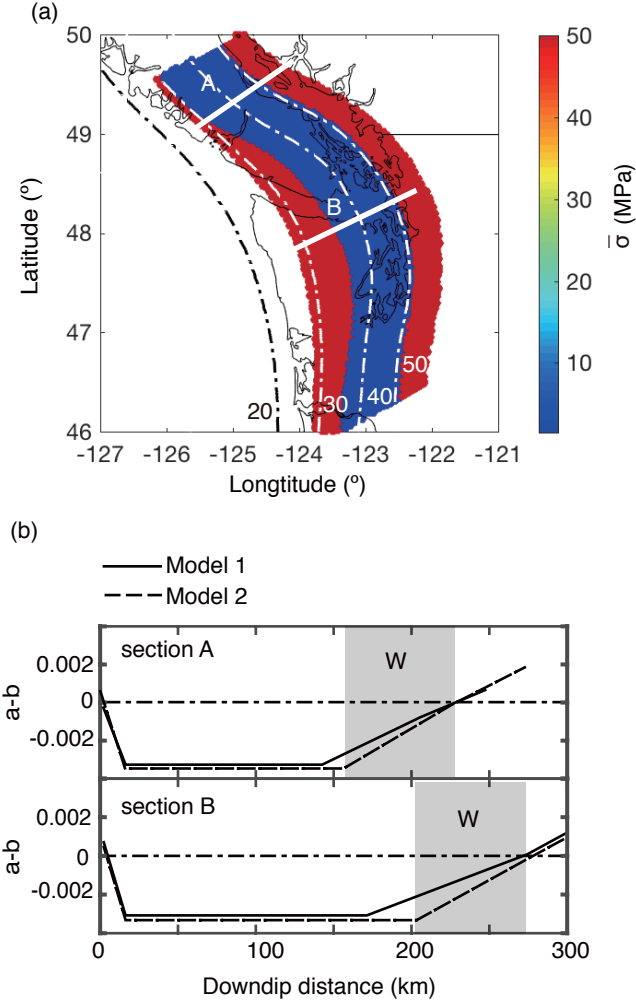


Figure 2-3: Graphs showing parameter $a - b$ and $\bar{\sigma}$ in Model 2. (a) Effective normal stress $\bar{\sigma} = 1.5$ MPa in the SSE zone (dark blue) and 50 MPa elsewhere. Cross-sections A and B are chosen to demonstrate the $a - b$ distribution along downdip distance. (b) Solid and dashed lines represent $a - b$ distributions in Model 1 and Model 2, respectively. Grey shaded area shows the range of velocity-weakening under low effective normal stress ($W = 70$ km) for Model 2 set up.

by equating the critical stiffness to the system stiffness [Rice and Ruina, 1983; Rice, 1993]. Rubin and Ampuero [2005] defined another $h_{RA}^* = \frac{2\mu b d_c}{\pi(1-\nu)(b-a)^2 \bar{\sigma}}$, by balancing the fracture energy balance at the crack tip [Rubin and Ampuero, 2005]. In essence, h_{RR}^* is the threshold for self-accelerating slip transients and h_{RA}^* is the threshold for

dynamic ruptures. Hence, the characteristic nucleation size for SSEs as in this study should be between h_{RR}^* and h_{RA}^* [Rubin, 2008].

In this study, I use the definition:

$$h^* = \frac{2\mu b d_c}{\pi(1-\nu)(b-a)^2 \bar{\sigma}}, \quad (2.5)$$

following Rubin and Ampuero [2005]. Here, shear modulus $\mu = 30$ GPa, and Poisson's ratio $\nu = 0.25$. The length ratio W/h^* has been found to be a key parameter in determining the occurrence of slow slip events in subduction zones [Liu and Rice, 2007] and aseismic creep events on continental strike-slip faults [Wei et al., 2013].

Parameter Space. In order to find the optimal set of $\bar{\sigma}$, d_c and W that best reproduces the GPS observations, I explore the parameter space by independently varying the above three parameters to achieve a broad range of W/h^* , which strongly influences SSE source properties [Liu and Rice, 2007; Rubin, 2008; Liu and Rice, 2009]. As shown in Figure 2–4, the three key source parameters (recurrence interval, maximum slip rate and cumulative slip in each episode), all increase with W/h^* , with considerable variations in each simulation case due to the stress evolution over multiple episodes. Figure 2–4 also shows that except for the case of $W/h^* \approx 0.25$, all other simulation cases produce SSEs of recurrence interval of 1-2 years, cumulative slip of 1.5-2.5 cm, which are generally consistent with GPS inferred SSE properties in Cascadia [Szeliga et al., 2008; Schmidt and Gao, 2010]. The parameter set used in this chapter is: $W = 72$ km, $d_c = 0.7$ mm, $\bar{\sigma} = 1.5$ MPa.

2.3 Results

With the parameter setting introduced in Section 2.2.4, I model the fault slip and stress history for a period that is sufficiently long to represent fault evolution in the interseismic period and to include many SSE episodes. As an example, I show in Figure 2–5 the 120 year history of slip rate on the fault beneath Port Angeles. In general,

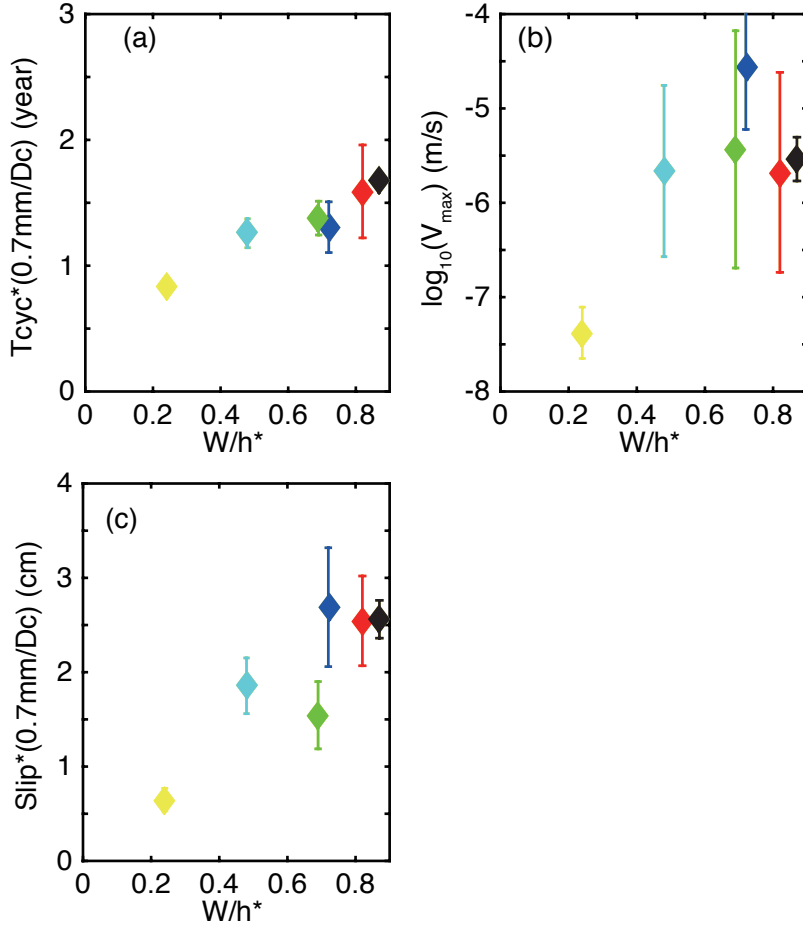


Figure 2-4: Graphs showing (a) recurrence interval T_{cyc} scaled with d_c , (b) maximum slip velocity $\log_{10}(V_{max})$, and (c) cumulative slip δ scaled with d_c of simulation cases with parameters: (1) Yellow: $W = 79\text{km}$, $d_c = 1.4\text{mm}$, $\bar{\sigma} = 1.0$ MPa, (2) Cyan: $W = 79\text{km}$, $d_c = 0.7\text{mm}$, $\bar{\sigma} = 1.0$ MPa, (3) Blue: $W = 79\text{km}$, $d_c = 0.7\text{mm}$, $\bar{\sigma} = 1.5$ MPa, (4) Green: $W = 64\text{km}$, $d_c = 0.7\text{mm}$, $\bar{\sigma} = 1.5$ MPa, (5) Red: $W = 72\text{km}$, $d_c = 0.7\text{mm}$, $\bar{\sigma} = 1.5$ MPa, (6) Black: $W = 76\text{km}$, $d_c = 0.7\text{mm}$, $\bar{\sigma} = 1.5$ MPa. Error bars show the standard deviations in each case.

the slip rate varies between ± 1 order of magnitude of the plate convergence rate, with SSEs appearing every 1-2 years. The moderate fluctuations in the maximum slip rate of each SSE episode are due to the stress evolution on the 3-D fault, including influence from SSEs elsewhere on the fault. In the following I select a representative 13 year

time period (Figure 2–6) to illustrate the slow slip source properties and comparison to GPS daily records of 1997-2009.

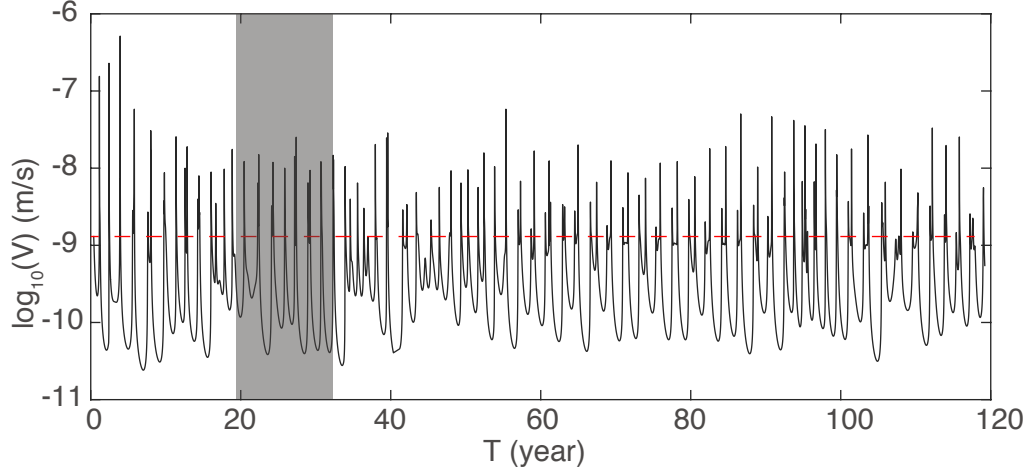


Figure 2–5: Fault slip velocity beneath Port Angeles during a 120-year simulation period (Model 1), with parameter setup of the red diamonds in Figure 2–4. Red dashed line is 41 mm/yr or 1.3×10^{-9} m/s. Shaded region are the 13-year time period, during which we calculate the average cumulative slip in Figure 2–8.

2.3.1 Slow Slip Segments

Figure 2–7 shows the spatio-temporal evolution of slip velocity and cumulative slip at 35 km depth for a selected 13-year simulation period from Model 1. Except for the along-strike boundaries where slip approaches the constant $V_{pl} \sim 10^{-9}$ m/s, the subduction fault experiences episodic SSEs of velocities 1-2 orders of magnitude higher than V_{pl} and recurrence intervals of 1 to 1.5 years. The along-strike propagation speed is in the range of 1 to 5 km/day, which is slightly lower than that inferred from GPS for northern Cascadia SSEs. As in previous numerical studies [Liu and Rice, 2007], the time scale of modeled SSEs, when other parameters are fixed, is controlled by the level of effective normal stress $\bar{\sigma}$; a smaller $\bar{\sigma}$ could result in shorter time scales and hence faster propagation speeds. Here $\bar{\sigma} = 1.5$ MPa is chosen, together with other frictional parameters such as $d_c = 0.7$ mm and the gabbro friction parameter $a - b$ (Figure 2–2) in order to satisfy the minimum model resolution.

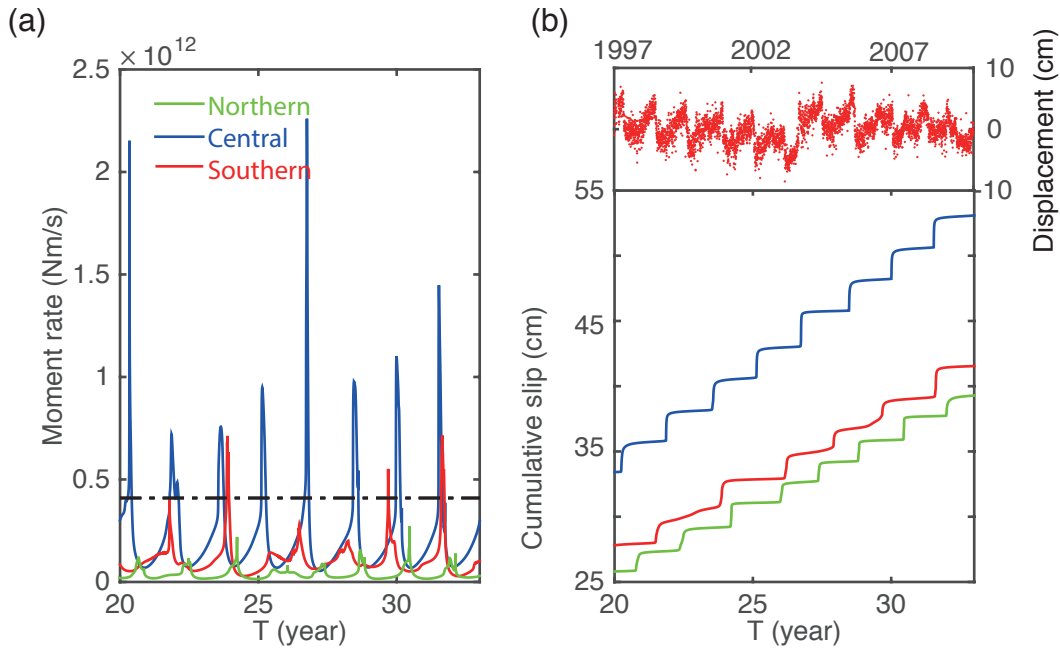


Figure 2-6: (a) Moment rate of the three slip patches (shown in Figure 2-8a): central, northern and southern, during a 13-year simulation period (Model 1). Horizontal dot-dashed line at 4×10^{11} Nm/s is the cutoff threshold for defining slow slip on the central patch. (b) Top: Detrended east component of daily GPS time series of from 1997 to 2010 (13 years) station ALBH (from Pacific Northwest Geodetic Array: <http://www.geodesy.cwu.edu/>). Bottom: The modeled cumulative slip of three patches during the same period. The position of each line is shown by colored diamond in Figure 2-8b.

For the short 13-year period shown here, there are already modest variations in the maximum slip rate reached during each SSE episode and their recurrence intervals, demonstrating the heterogeneous stress conditions on the fault. A major slip patch can be defined between along-strike -100 and 50 km (central), and two minor slip patches straddling the central patch at along-strike from -190 to -110 km (southern) and 75 to 125 km (northern) (Figure 2-8a). These segmentation boundaries are identified based on the slow slip rate and along-strike propagation speed between the three slip patches that are persistent over multiple SSE cycles.

Here I define the onset of SSE episodes based on the moment rate on the three distinctive slip patches. Compared to the maximum slip rate criteria commonly used in previous studies [Collela et al., 2011; Shibazaki et al., 2012], moment rate, equivalently average slip rate on a defined fault area, is a more appropriate representative of the energy release process [Liu, 2014]. The average fault width is ~ 70 km for the central patch, and ~ 65 km for the south patch and ~ 60 km for the north patches. The area of each patch is defined by their respective downdip fault width and along-strike lengths. The cumulative moment within each patch is calculated and a SSE is identified when its moment rate exceeds a cutoff value. As shown in Figure 2–6a, central patch slow slip is defined when moment rate exceeds 4×10^{11} Nm/s (equivalent to an average slip rate of V_{pl}). I also note that slip on the north and south patches is smaller, so they are defined when moment rate exceeds 2×10^{11} Nm/s (equivalent to an average slip rate of $0.5V_{pl}$).

SSEs on the central patch are regular in their recurrence interval and cumulative slip. A total of 8 SSE episodes occur on the central patch during a 13-year simulation period, resulting in an average recurrence interval of ~ 1.5 years (Figure 2–6a). This recurrence interval is comparable with that of GPS observations in the northern Washington. Top panel in Figure 2–6b is the detrended daily GPS series (east component) from 1997 to 2010 at the station of ALBH (Pacific Northwest Geodetic Array: <http://www.geodesy.cwu.edu/>). The recurrence interval of each slip reversal at ALBH is 14~2 months (~ 1.2 years). Our choices of $\bar{\sigma}$ and d_c values that are limited by the model grid size may primarily contribute to the slightly longer recurrence intervals from the model. The scaling of SSE interval and cumulative slip with d_c in Figure 2–4 demonstrates that the observed values can be more accurately reproduced if the mesh size is sufficiently small to allow choices of d_c close to lab values of tens of microns. In addition, the assumption of a uniform effective normal stress across all SSE depths,

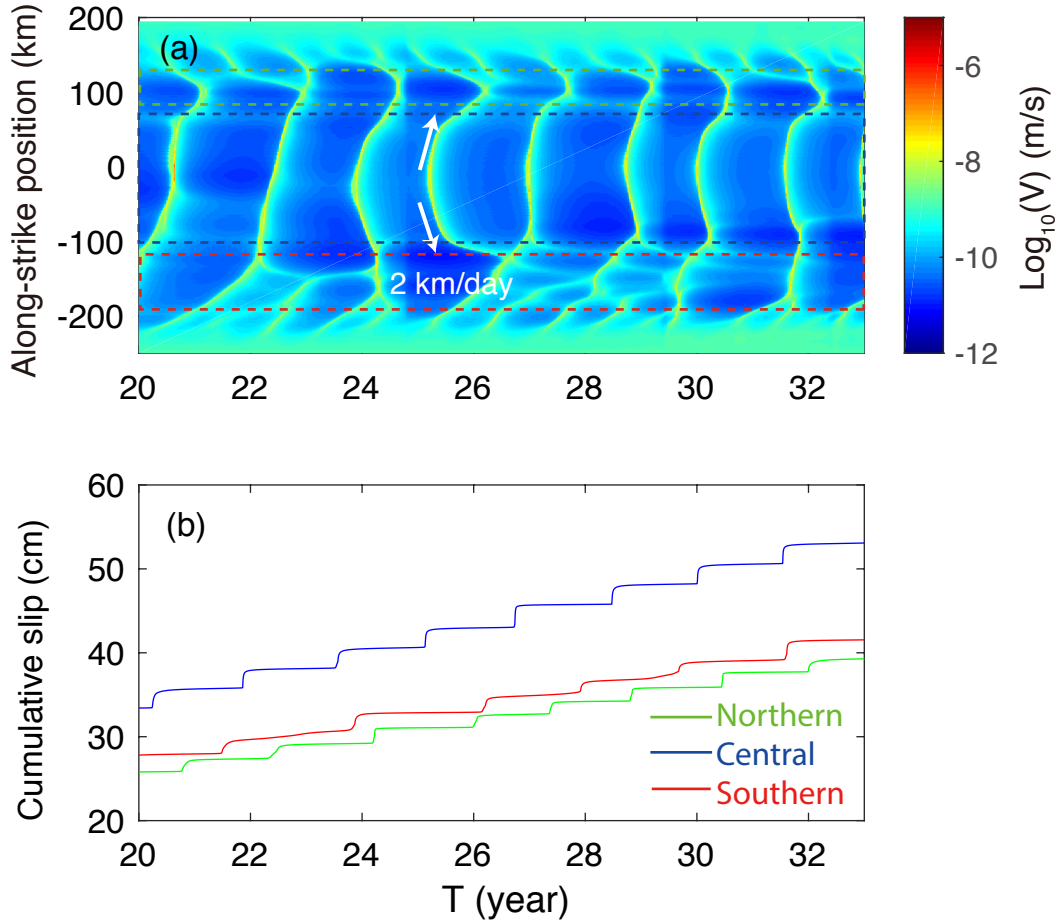


Figure 2-7: (a) Graphs showing spatiotemporal evolution of slip velocity at depth 35 km depth for a 13-year simulation period (Model 1). Green, blue and red dashed lines mark the boundaries of northern patch, central patch and southern patch, respectively. White arrows illustrate the bilateral propagation of ~ 2 km/day during ~ 20 days in one episode. (b) Cumulative slip at 35 km depth contour of three patches during the same period. The position of each line is shown by colored diamond in Figure 2-8b.

rather than a tapering distribution with depth, as suggested by the along-dip variation in tremor activity [Wech and Creager, 2011] may also contribute to the longer modeled recurrence interval. SSEs on the north and south patches are less regular in recurrence interval and amount of cumulative slip. The cumulative slow slip on each slip patch is

calculated when the moment rate criteria are satisfied, and then averaged by the total number of events on each patch during the simulation period (13 years) to construct the slip distribution map (Figure 2–8a).

The along-strike segmentation of modeled SSEs in Figure 2–8a provides a direct comparison to the slow slip distribution in northern Cascadia based on 10-year GPS inversion of Schmidt and Gao [2010]. The major slip patch is distributed ~ 150 km along the strike beneath Port Angeles, with a maximum slip of 2.5 cm between depths of 33 and 46 km. The model results are essentially consistent with the GPS observation that 11 out of a total of 16 slow slip events in northern Cascadia between 1998 and 2008 had the maximum slip of ~ 3 cm beneath Port Angeles [Schmidt and Gao, 2010]. The equivalent magnitude range of modeled SSEs on the central patch is $M_w 6.0$ to 6.7, also consistent with $M_w 6.1$ to 6.7 from their GPS inversion results.

Two minor slow slip patches, with an along-strike length of ~ 50 km and ~ 80 km respectively, arise to the north and south of the central patch. The maximum cumulative slip on the north patch and south patch is about 1 cm and 2 cm, respectively. Such minor slip in northern and southern patch may correspond to the smaller slow slip signals detected by GPS beneath northern Vancouver Island and southern Washington State [Schmidt and Gao, 2010]. Compared to the repeating $\sim M_w 6.0$ s beneath Port Angeles, these minor slip areas follow the slab curvature and are closer to the coastline where relatively sparse GPS coverage prior to 2006 may have contributed to the fewer detections and lower spatial resolution of these events [Szeliga et al., 2008; Schmidt and Gao, 2010].

I also note from Figure 2–7b that the total slip accumulated during the 13-year simulation period on the northern and southern patch is about two thirds of that on the central patch, indicating less strain energy is released in the form of slow slip events. The relative slip budget is important for earthquake hazard assessment in the

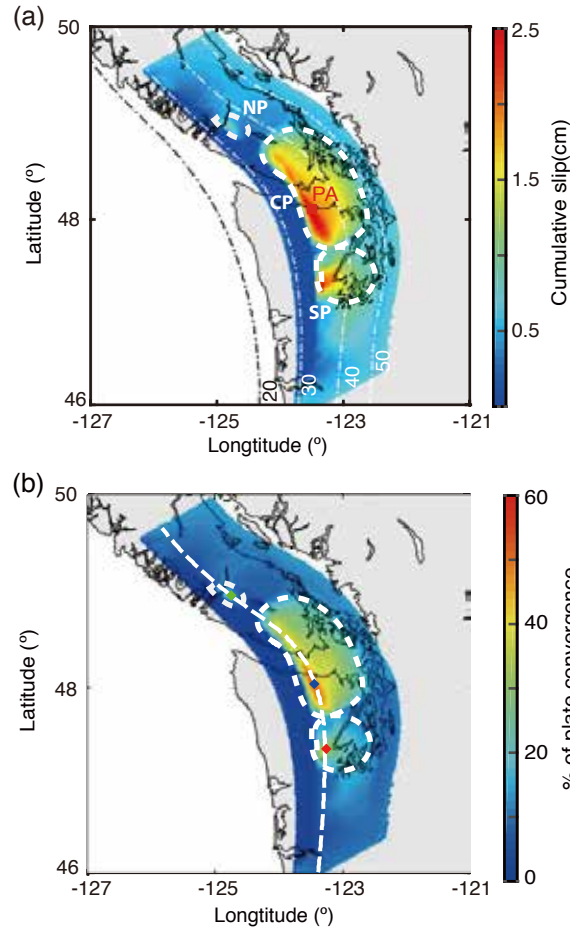


Figure 2–8: Maps showing (a) cumulative slip averaged of 8 SSE episodes over 13 years shows in Figure 2–6. Three distinctive slip patches are marked by bold white dashed lines. Slip is calculated when moment rate exceeds 4×10^{11} Nm/s (equivalent to an average slip rate V_{pl}) on the central patch (CP), and 2×10^{11} Nm/s ($V_{pl}/2$) on the northern and southern patches (NP and SP). Maximum cumulative slip values on northern, central and southern are 1, 2.5 and 2.0 cm, respectively. PA: Port Angeles. (b) Slip released during SSEs as a percentage of plate convergence ($V_{pl} = 41$ mm/yr) over 13 years. The maximum percentage is $\sim 50\%$ beneath Port Angeles. The maximum in northern and southern slip patch is less than 30%. Dashed white contour marks the position of 35 km depth. Diamonds denote the position of the cumulative slip in Figure 2–6 and 2–7.

Cascadia margin. By dividing the total slip amount released during SSE episodes to the slip accumulated by plate convergence rate during the same period, I construct a slip budget map for our model domain. As shown in Figure 2–8b, a maximum of \sim

50% of the slip accumulated by steady sliding at V_{pl} has been released during SSEs beneath southern Vancouver Island, which is consistent with the slip budget inferred from GPS inversions [Schmidt and Gao, 2010]. It also suggests $\sim 50\%$ of accumulated slip is still available for energy release in a combination of other forms of aseismic and seismic slip.

2.3.2 Effect of Fault Geometry

The correlation between the central slip patch and the subduction slab curvature suggests that fault geometry may play an important role in the along-strike segmentation of SSEs in northern Cascadia. In this section I use the local dip and local strike angles of elements at the SSE depths to represent the fault geometry effect; a small dip angle represents fault surface close to a horizontal plane and a small local strike means little deviation from the trench-parallel direction. Both geometry parameters (Figure 2–9) demonstrate the smallest dip and strike angles beneath Washington state corresponding to the central slip patch. The dip angle increases significantly below ~ 45 km and toward the northern and southern patches, while local strike also significantly deviates from the trench-parallel direction toward the northern and southern patches.

The along-strike distribution of the three slow slip patches approximately correlates with the variation of local fault dip and strike angles (Figure 2–8a). The central patch with the smallest dip and strike angles results in the largest average slip, while the northern and southern patches accumulate less slip with steeper dips and larger strikes. It appears that the cumulative slip values on the three patches are more closely correlated with the local strike than with the dip angle, which suggests that the along-strike variation of fault geometry may play an important role in influencing the segmentation patterns of Cascadia SSEs. Within the central patch, slip increases slightly from ~ 1.7 cm beneath the southern Vancouver Island to ~ 2.5 cm beneath Port

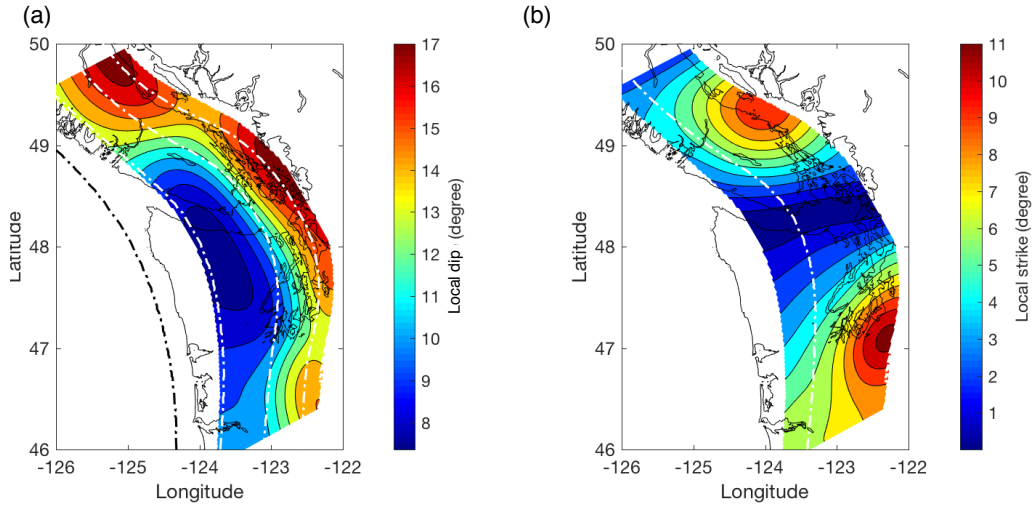


Figure 2-9: Subduction fault geometry represented by (a) local dip angle and (b) local strike angle of each element on the fault. Dot-dashed lines show depth contours of 20-50 km depth in (a) and 35 km in (b), where shear stress evolution is shown in Figure 2-10.

Angeles (Figure 2-10a), which also correlates with the decreasing dip angle toward the south. This correlation is partially due to the along-strike variation of W/h^* , the ratio of the SSE zone width under velocity-weakening and the characteristic nucleation size. For Model 1 cases where W is defined between depth contours, a smaller dip angle would lead to a wider SSE zone width which explains the peak of W/h^* at the location of the smallest dip angle.

However, W/h^* is not the only responsible factor influencing the along-strike slip distribution and the segmentation boundaries. As described in Section 2.2.5, in a slightly modified model setup (Model 2, Figure 2-3), I constrain the downdip distributions of parameters $a - b$, $\bar{\sigma}$ and d_c in the SSE zone such that both W and h^* are uniformly distributed along the strike. With a constant W/h^* , Model 2 allows us to explicitly quantify the effect of fault geometry on the distribution of slow slip. Compared to SSEs in Model 1 (Figure 2-7), along-strike SSE segments in Model 2 become

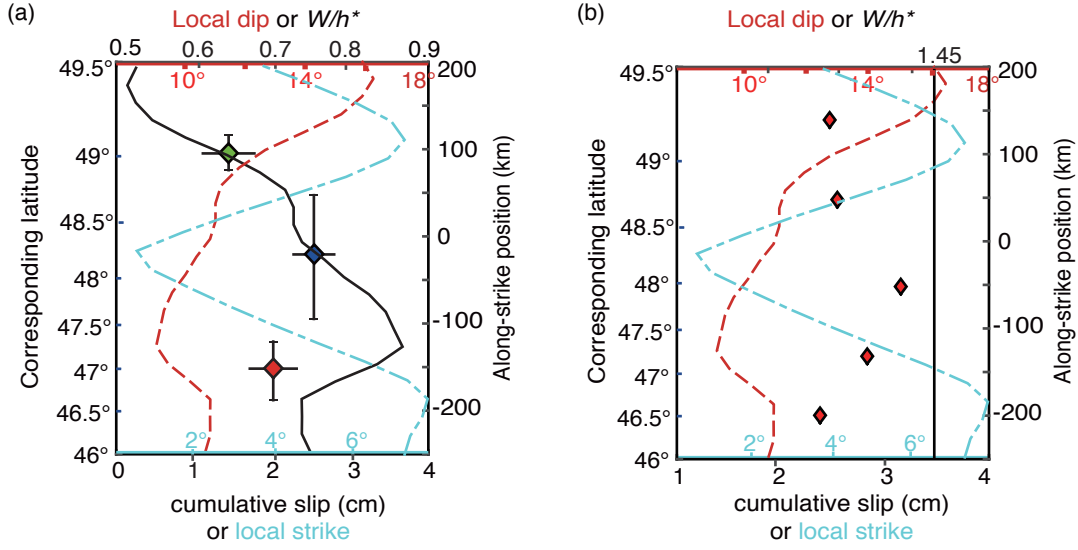


Figure 2–10: Along-strike variations of fault geometry and cumulative slip. (a) Model 1: cumulative slip of three patches are shown by diamonds (green: northern; blue: central; red: southern). Vertical and horizontal bars show the along-strike range and standard deviation, respectively. Fault local dip angle (red dashed line) and local strike angle (blue dashed line) are averaged over SSE depths. Black solid line shows W/h^* . (b) Model 2: Maximum cumulative slip at along-strike 150, 50, -50, -125, -200 km (red diamonds). Solid line is at the uniform $W/h^* \approx 1.5$. Red and blue dashed lines show fault local dip and strike angles, respectively.

less regular. As shown in Figure 2–11, for a fixed along-strike location the SSE recurrence interval and cumulative slow slip amount can vary considerably from episode to episode, which makes it difficult to construct an averaged slow slip distribution as in Figure 2–8a for distinctive slip patches. Rather, I present the average slow slip at five representative locations at along-strike (from south to north) -200, -125, -50, 50 and 150 km. The average cumulative slip within each segment is 2.5 to 3.5 cm, slightly larger than those in Model 1 because of a larger W/h^* ratio determined by the parameters in Model 2. Nevertheless, Figure 2–10 shows that with an along-strike uniform W/h^* there is still an inverse correlation between the cumulative slip and the local fault dip and strike angles. In particular, the maximum slip arises at along-strike distance -50 km, beneath Port Angeles, where the local strike is the smallest. Our

results confirm that the fault geometry alone can influence SSE process, in addition to the previously recognized controlling parameter W/h^* .

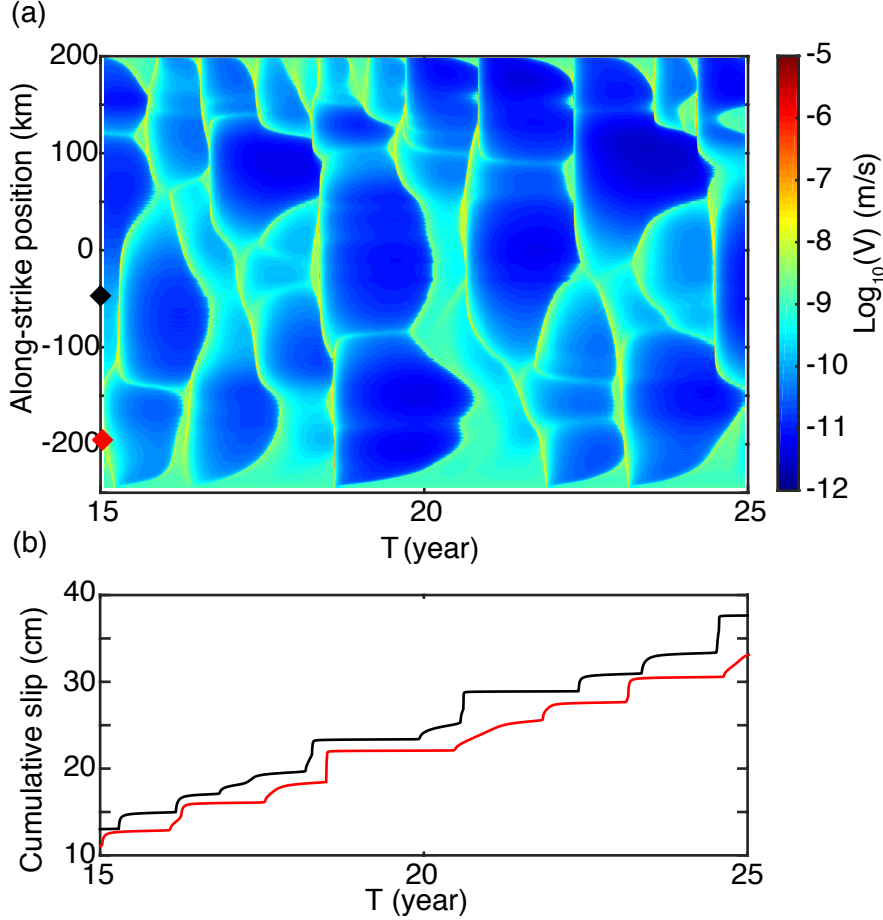


Figure 2-11: Graphs showing (a) spatiotemporal evolution of slip velocity at $a - b = -0.0025$ contour for a 10-year simulation period of Model 2. Black and red diamonds in (a) show the along-strike positions where (b) cumulative slip is plotted.

2.3.3 Slow Slip Phases and Scaling Relations

Our simulation results also reveal that similar to their seismic counterparts, slow slip events consist of pre-SSE preparation, fast-spreading, and post-SSE relaxation phases with distinctive moment release rates (Figure 2-12). For example, the moment rate of the central 150 km-long SSE patch increases during the "pre-SSE" phase from 2×10^{11} to 4×10^{11} Nm/s, which is approximately equivalent to an average slip rate

of $V_{pl}/2$ and V_{pl} , respectively. Slip accumulates slowly from the frictional stability transition (depth 46 km) while propagating updip in the preparation phase (Figure 2–13a). Once the slow slip front reaches the updip limit of the SSE zone (depth 33 km), slip propagation reverses toward the downdip direction and also spread fast along the strike (Figure 2–13a-d). Slip propagates bilaterally along the strike at an average speed of ~ 2 km/day, which as previously discussed for the slightly longer recurrence interval is also related to the choices of $\bar{\sigma}$ and d_c . Moment rate reaches a maximum of 9.5×10^{11} Nm/s, due to the high slip rate on the entire patch. Majority of the slip is accumulated during ~ 60 days, accounting for about 10% of the SSE cycle. After the fast-spreading phase, the moment rate rapidly falls down to 2×10^{11} , which defines the relaxation "post-SSE" stage (Figure 2–13d).

To compare the three SSE phases to nonvolcanic tremor activity, I plot the automatic tremor detection catalog between April 2007 and July 2008 in northern Cascadia [Wech and Creager, 2008], at the same time scale as the SSE moment rate. The major tremor burst from 4 to 24 May 2008 corresponds to the period of increasing moment rate in the fast-spreading phase, while there is also minor tremor activity a couple of months before the 2008 ETS event and during the inter-ETS period. I will discuss the potential relation between the minor tremor activity and the preparation phase slow slip in Section 2.4.2.

After the slow slip phases are defined, I calculate the source parameters (equivalent moment, duration and slow slip area) of each episode and summarize their scaling relations in Figure 2–14. In each of the three slip patches of Model 1, the equivalent slow slip area and moment are summed up for all triangular elements on which slip is greater than 0.5 mm (Eq. 2.6), which is the same criterion used in Cascadia slow slip inversion [Schmidt and Gao, 2010]. The dataset presented in Figure 2–14 include 79 SSEs from a total simulation period of 120 years. The calculated moment-area scaling

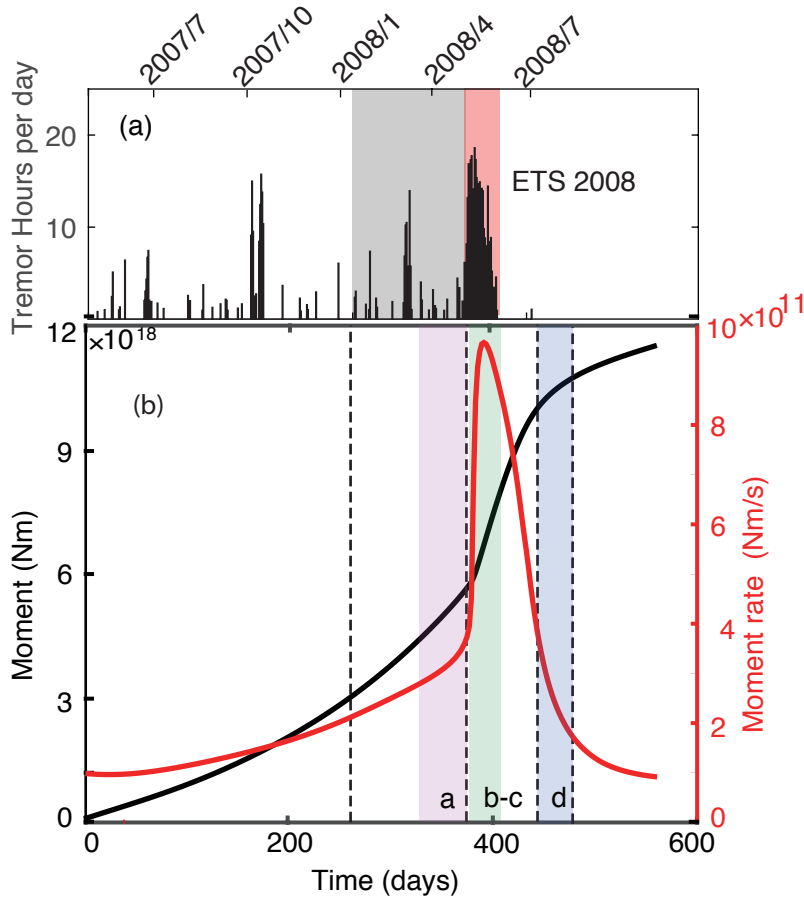


Figure 2–12: (a) Northern Cascadia tremor activity hours per day from 2007/4 to 2008/7 is shown [Wech and Creager, 2008]. The major ETS events in the time period from May 4 to May 24 is highlighted in red [Wech and Creager, 2008]. This time period is aligned with the first 33 days in the modeled fast-spreading phase. Gray shadow shows the 110 days before the 2008 ETS event, aligned with the pre-SSE phase. (b) Graph showing cumulative moment (black) and moment rate (red) of 547 days in one episode defined on the central slip patch. Three phases are defined by moment rate: a pre-SSE preparation (day 260-370) and post-SSE relaxation (day 431-473) phase $\sim 2\text{--}4 \times 10^{11}$ Nm/s and fast-spreading phase (day 370-431) $> 4 \times 10^{11}$ Nm/s. Widths of vertical shaded bars show the four periods of snapshots in Figure 2–13.

shows a constant stress drop around 0.01 MPa (Figure 2–14a), which is consistent with the stress drops of 0.01 to 0.1 MPa for most subduction zone SSEs [Ide et al., 2007; Gao et al., 2012] and with theoretical and numerical estimates [Rubin, 2008; Colella

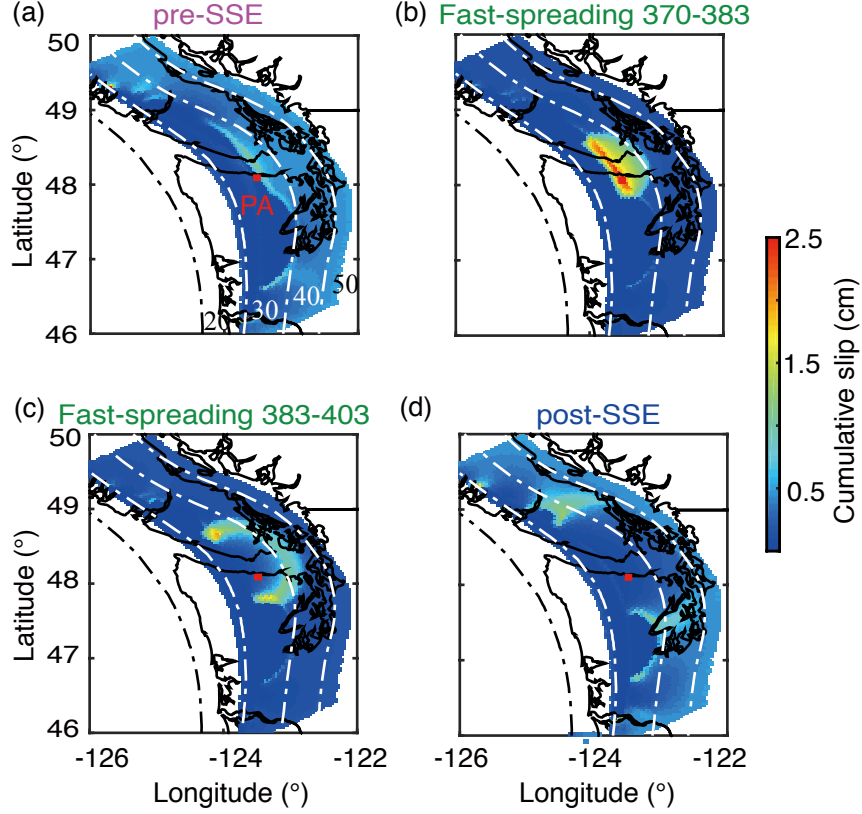


Figure 2–13: Four snapshots of cumulative slip (a) day 330 to 370, pre-SSE preparation, (b) day 370-383 and (c) day 383-403, fast-spreading, (d) day 433-470, post-SSE relaxation. These four time windows are corresponding to shaded bars of (b)-(e) in Figure 2–12b.

et al., 2012; Liu, 2014]. The stress drops are 2-3 orders of magnitude lower than regular earthquakes of equivalent magnitude, which constitute another line of evidence for the near-lithostatic pore pressure condition at SSE depths.

$$M = \sum_{j=1}^N \mu \delta_j A_j \quad (2.6)$$

where $\mu = 40\text{GPa}$ and $\delta_j > 0.5\text{mm}$.

Most of the modeled events have durations between 0.1 to 0.5 years and equivalent moment between 10^{17} and 10^{19} Nm (Figure 2–14b). The small range in duration limits

the ability to clearly define a scaling between moment and duration, although the larger magnitude events seem to follow the linear relation as proposed by Ide et al. [2007]. I also note that majority of events that clearly deviate from the linear relation are from the northern patch (green symbols) with the smallest slip amount and probably least constraint from geodetic observations. Although the central patch still hosts the largest SSEs in terms of moment, some northern and southern SSEs have similar equivalent moments instead of being at least one order of magnitude smaller than those from a 13-year period in Figures 2–6 and 2–8. This indicates potential evolution of the three-patch segmentation over a longer period, and the current Cascadia SSE distribution based on two decades of GPS observation may just represent a snapshot of the spatio-temporal evolution of SSEs in a subduction earthquake cycle.

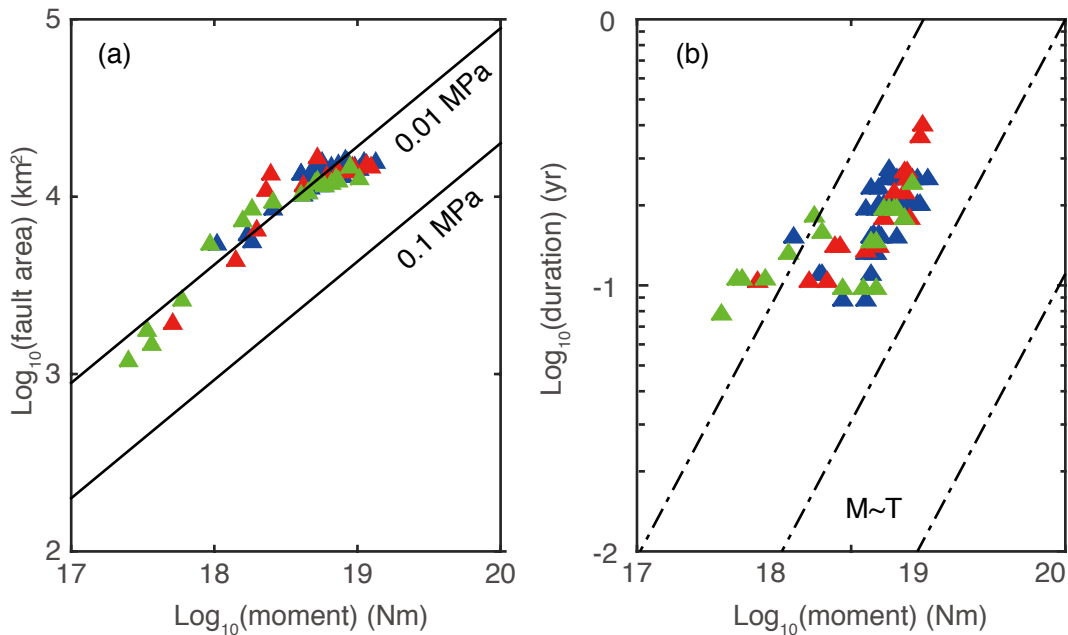


Figure 2–14: (a) Moment-area scaling relation of 79 SSEs in central (blue), northern (green) and southern (red) patches. Moment is calculated within the fast-spreading phase of each episode. Only the elements with slip greater than 0.5 mm are accounted in calculating the moment and area, the same criterion as in Schmidt and Gao [2010]. (b) Moment-duration scaling of all SSEs on three patches. Dot-dashed lines show the scaling of $M \sim T$.

2.4 Discussions

2.4.1 Geometric Effect

The appearance of three distinct slip patches in our model does not require the introduction of additional along-strike heterogeneities in frictional parameters or changes in the level of effective normal stress. The fact that a major slip patch arises beneath Port Angeles and is limited to ~ 150 km along the strike strongly suggests fault geometry plays a key role. These effects are further illustrated in Figure 2–15 by the shear stress history during the propagation of a central patch slip event. The nucleation of the slow slip event coincides with the along-strike range (-40 to -10 km) where the local strike angle is the smallest. A zero local strike angle indicates the element on the fault exactly follows the trench-parallel direction hence the direction to maximize the downdip loading due to plate convergence.

In addition to the first-order spatial correlation between the fault local dip/strike and cumulative slip shown in Figure 2–10, I also note that the segmentation boundaries are located where along-strike gradient in the local dip angle reaches a local maximum or shear stress is at a local minimum level such that further along-strike propagation is inhibited. Toward the northern boundary of the central slip patch at about 80 km, the local dip angle changes from $\sim 12^\circ$ to 1° over an along-strike distance less than 50 km, which is the most rapid change along the entire model domain. The steepening of fault may have also contributed to the eventual stop of the slow slip. Toward the southern boundary at about -90 km, the central patch slip gradually slows down as it approaches a local shear stress low. Hence, our modeling results demonstrate that local heterogeneities in either fault geometry or stress field can cause along-strike segmentations of slow slip events. The shear stress evolution in Figure 2–15 also shows the stress drop is 0.03-0.04 MPa within ~ 50 km from the nucleation point. This direct measurement is slightly higher than the average of 0.01 MPa based on the relation

between total slip area and equivalent moment (Figure 2–14a), as the latter estimate also includes slip at times of decreasing moment rate.

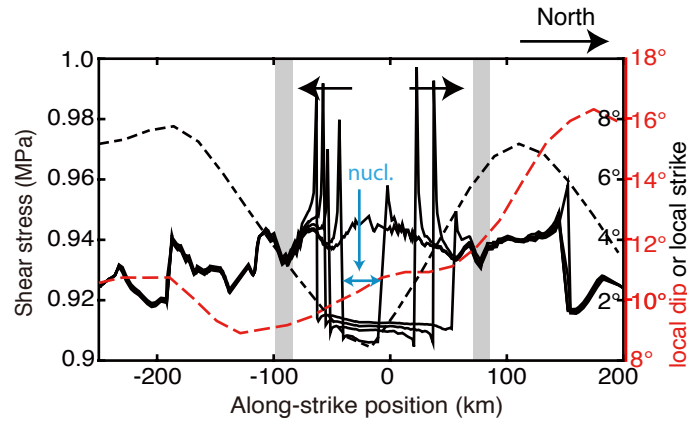


Figure 2–15: Shear stress at 35 km depth contour is plotted every 5 days during a central patch SSE (black line) from day 370 to 390 (fast-spreading phase in Figure 2–12b). Dashed red and black lines are the local dip and strike angles along the strike, respectively. SSE nucleation zone is denoted by blue arrows. Grey bars denote the segmentation boundaries.

Fault geometry may also play an important role in controlling slow slip source parameters in other subduction zones. For the purpose of discussion, in Figure 2–16 I compile four source parameters (maximum slip, equivalent moment magnitude, recurrence interval and duration) of six circum-Pacific subductions with SSE observations. Although there is no obvious trend between these source parameters and the average dip angle on the global scale, I notice that the slow slip events in Upper Cook Inlet, Alaska, have the longest recurrence intervals and durations, while the average dip angle (average dip angle $\sim 12^\circ$) is the shallowest among all subduction zones. In a recent modeling study of the south central Alaska SSEs, the SSE along-strike segmentation has been suggested to be related to the subducted Yakutat Plateau, inferred from seafloor topography and verified [Wei et al., 2017]. SSE parameters for the four regions in the southwest Japan also generally follow a decreasing trend with the dip angle.

Matsuzawa et al. [2013] also found that shallower-dipping fault can lead to larger slow slip, which agrees with geodetic observations in Shikoku.

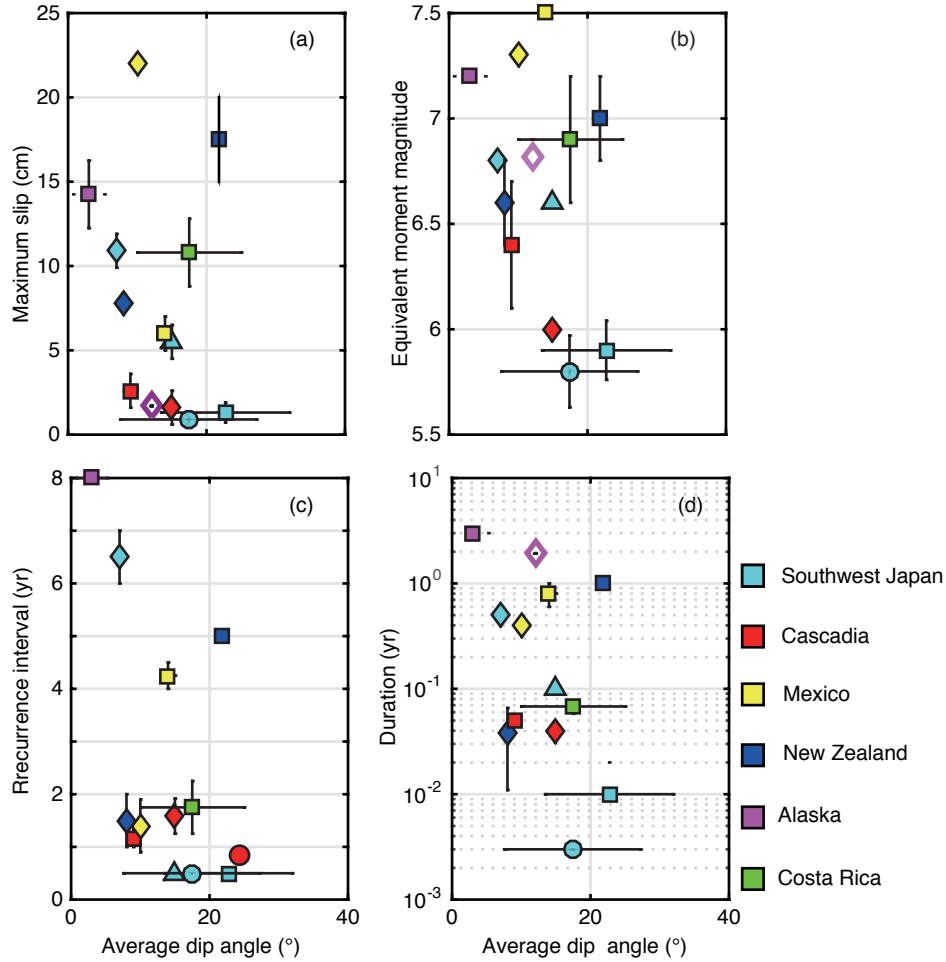


Figure 2-16: Graphs showing (a) maximum cumulative slip, (b) equivalent moment magnitude, (c) recurrence interval, and (d) duration, versus average fault dip angle at SSE depths. Southwest Japan (light blue): short-term (square) and long-term (diamond) in Shikoku, short-term in Ryuku Trench (circle) and short-term in northeast Kii Island and Tokai (triangle). Cascadia (red): Vancouver Island and northern Washington (square), northern Oregon (diamond) (no slip inversion is available for northern California). Mexico (yellow): Guerrero (square) and Oaxaca (diamond). New Zealand (dark blue): northern Hikurangi (diamond) and Manawatu (square). Alaska (purple): Upper (square) and Lower Cook Inlet (diamond). Costa Rica: Nicoya Peninsula (green square).

The relation between SSE parameters and fault dip angle appear different in other subduction zones (Figure 2–16). In Hikurangi, New Zealand, the SSE distribution, in general, follows the geodetically inferred plate coupling extent [Wallace and Beavan, 2010; Wallace et al., 2012]. In northern Hikurangi and Costa Rica where slow slip events occur near the trench, compositional and geometrical heterogeneities of the plate interface are also suggested to be the additional control on shallow slow earthquakes [Saffer and Wallace, 2015]. Finally, differences in instrumentation and data processing methods could also contribute to the apparent regional variations [Peng and Gombert, 2010].

Our model does not rule out other possible environmental effects on the slow slip process. Progressive silica enrichment in the forearc crust [Audet and Burgmann, 2014], hydraulic conductivity changes along the subduction fault, and mixture of stable and unstable behaviors due to mineral phase changes or velocity-dependence of friction stability could all contribute to the compositional heterogeneities that influences slow slip zone architecture [Saffer and Wallace, 2015]. The slow slip depth range in our model is largely controlled by thermal models for the northern Cascadia subduction zone, although temperature may not be the key controlling factor in the shallow slow slip behavior in subduction zones such as Hikurangi, New Zealand and Costa Rica. Therefore, instead of relying solely on fault zone temperature and rate-state friction data from a particular type of fault gouge, future development in the non-planar subduction fault model may use non-volcanic tremor locations to define the slow slip depth ranges [Wech and Bartlow, 2014] and infer fault effective normal stress conditions from along-strike gravity anomalies [Brudzinski and Allen, 2007]

2.4.2 Inter-SSE Slip and Tremor Activity

In Cascadia, inter-ETS (episodic tremor and slip) tremors have recently been reported without obvious spatio-temporal linkage to geodetically-observable slow slip

signals [Wech and Creager, 2011]. For example, inter-ETS tremor activity is detected between February 2007 and April 2008 beneath north Washington state, accounting for $\sim 45\%$ of the total tremor duration of an entire ETS cycle [Wech and Creager, 2008]. This is just before the May 2008 ETS event. The spacial distribution shows that the peak activity of inter-ETS tremors is deeper (40-45 km) than during the major ETS events (33-38km) [Wech and Creager, 2008]. In our model, the pre-SSE stage arises from 46 km, the frictional stability transition zone, just downdip of the major cumulative slip of each episode (Figure 2–13a). The temporal evolution of inter-ETS tremor could also be related to the pre-SS stage our modeled SSEs. The increasing inter-ETS tremor activity is correlated with the increasing moment release during the pre-SSE stage in our model (Figure 2–12a). The average slip rate is below 1.3×10^{-9} m/s (or, 0.11 mm/d), based on the moment rate threshold in Figure 2–12b, which is below the GPS detection threshold of 0.25-0.5 mm/d inferred from GPS slip inversion models for central and northern Cascadia [Wech and Bartlow, 2014]. In addition, the combined duration of pre-SSE stage is ~ 120 days, about 20% of the entire SSE cycle period. The above similarities suggest that inter-ETS tremors may be associated with slow slip during the pre-SSE stage below current GPS detection threshold. Compared to the preparation phase (~ 110 days), moment rate in the post-SSE relaxation phase decreases to below 2×10^{11} Nm/s (equivalent to 0.5Vpl) over a much shorter period (~ 40 days), which may be related to the lack of minor tremor activity immediately following the 2008 major ETS event. The potential relation between inter-ETS slow slip and tremor is thus consistent with the hypothesis that a downdip variation in tremor activity is the seismic manifestation of a continuum of fault slip and strength in northern Cascadia [Wech and Creager, 2011; Audet and Burgmann, 2014].

2.5 Conclusions

In this study I use a non-planar fault model in the framework of rate- and state-dependent friction to simulate the spatiotemporal evolution of episodic slow slip events in the northern Cascadia subduction zone. The major findings in this chapter are:

1) Here I incorporate a realistic fault geometry of northern Cascadia in the framework of rate- and state-dependent friction law, to simulate the spatiotemporal evolution of SSEs. The central 150-km-long fault segment beneath Port Angeles acts as a repetitive slip patch, where SSEs appear every ~ 1.5 years with a maximum slip of ~ 2.5 cm. Two minor slip patches with smaller area and cumulative slip straddle this central slip patch. The modeled SSEs have captured the major characteristics revealed by GPS observations.

2) The along-strike segmentation of SSE is inversely related to the local dip and strike angles of the SSE zone, suggesting strong geometrical control on the slow slip process. This correlation holds even after removing the effect of W/h^* , ratio between velocity-weakening SSE fault width and characteristic nucleation size. Such geometrical control on SSE source properties may also be significant in other subduction zones.

3) Our modeling results also demonstrate that the spatiotemporal evolution of SSEs may be more complex than currently captured by geodetic surveys along subduction zones. Besides the GPS-detectable fast-spreading phase, I find that each SSE cycle consists of deep pre-SSE and post-SS phases. The fast-spreading phase is distinguished by the high moment rate release. The pre-SSE is likely correlated with the inter-ETS tremor appearance observed in Cascadia.

Appendix A: “Aging” law vs. “Slip” law

Here I make a test model applying both the “slip” and “aging” law to represent the fault strength in rate-state friction. Figure 2–1 exhibits the fault model with 450 km length along the strike. Frictional parameter $a - b$ is projected onto the fault through temperature profile in Cascadia [Hyndman and Wang, 1993]. The only difference is that I use a coarse grid spacing (1.5 km) here, to decrease the simulation time.

Figure 2–17 shows the slip rate of 2 years at Port Angeles (-125.43°W,48.11°N), with “slip” law (red) and “aging” law (black), respectively. One earthquake occurs with “slip” law when two SSEs occur with “aging” law. The slip rate evolution in both “slip” and “aging” law is shown in Figure 2–17a, respectively. The earthquake with “slip” law has a maximum slip rate of 0.01 mm/s. The maximum slip rate in “aging” law is only 1.1^{-8} m/s, which is 6 orders of magnitude smaller than the earthquake. The propagation patterns are also quite different: the earthquake propagates at 150 km/day while SSEs 10 km/day.

I has shown that with a proper frictional parameter choice with “aging” law could reproduce episodic SSE as shown in Figure 2–5. In this test model, however, under the same conditions, “slip” law is not able to do that. For the same width of velocity-weakening portion on the fault, “slip” law produces 2 orders of magnitudes higher slip rate (~ 0.01 mm/s) than the SSE slip rate in the ‘aging’ law.

Empirically, the slip rate is reduced accordingly with W/h^* ratio Liu and Rice [2007]; Rubin [2008], where W is the width of downdip distance of velocity-weakening and h^* is critical nucleation size. The range of W can be roughly constrained by slow slip patterns in GPS inversions [Li and Liu, 2016]. The size of h^* does not have a solid observational support yet, even though several theoretical definition is used in

the modeling [Rice, 1993; Liu and Rice, 2007; Rubin, 2008]. I obtain $h_R^* = 5.3$ km in the definition of Rice [1993], where $d_c = 1.4$ mm, $\mu = 30$ GPa, $\nu = 0.25$, $\bar{\sigma} = 1.5$ MPa, and averaged $\overline{(b - a)} = 0.0015$. In the model of “aging” law, there are three SSE patches occurring along the strike (Figure 2-8). However, in the case of “slip” law, the seismic slip ruptures the entire fault (Figure 2-17b). This means that when the h^* is increased, the fault will fail to generate SSE patches. Therefore, I propose that the model of “aging” law is more appropriate to reproduce the episodic SSEs observed in Cascadia.

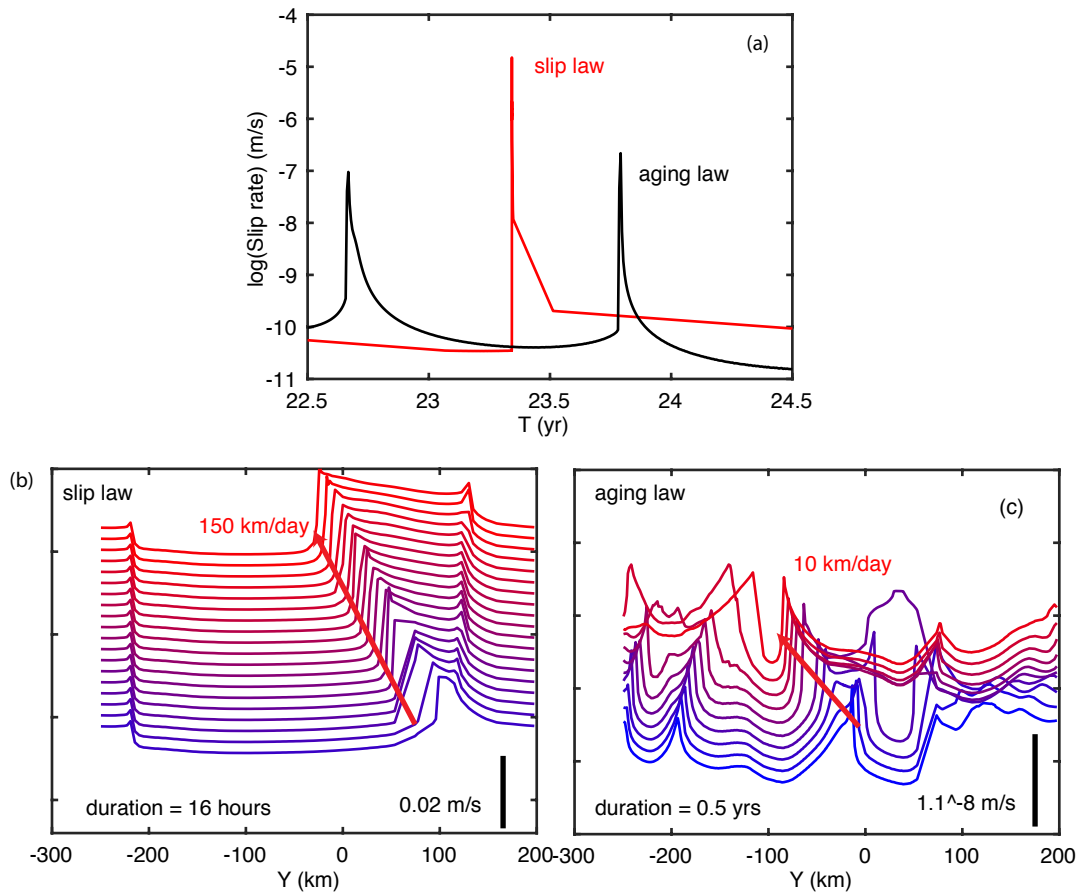


Figure 2-17: (a) Slip rate during 2 years is shown for both “aging” (black) and “slip” (red) law. (b) Slip rate along the strike of every 0.84 hour is shown, modeled with “slip” law. The maximum slip rate is 0.01 mm/s. (c) Slip rate along the strike of every 10 day is shown, modeled with “aging” law. The maximum slip rate is 1.1×10^{-8} m/s.

CHAPTER 3

Modeling Slow-slip Segmentation in Cascadia Subduction Zone Constrained by Tremor Epicenters and Gravity Anomalies

3.1 Introduction

Slow slip events (SSEs) are identified as quasi-static slip occurring on the conditionally stable fault, near or downdip of the seismogenic zone [Dragert et al., 2001; Obara, 2002]. They have been observed worldwide with diverse source parameters and seismic radiation characteristics in different tectonic settings [Rogers and Dragert, 2003; Segall et al., 2006; Peterson and Christensen, 2009; Obara, 2010; Peng and Gomberg, 2010; Obara, 2011; Gao et al., 2012; Bartlow et al., 2014; Frank et al., 2015b]. Adjacent to or partially overlapping with the shallow seismogenic zone, SSEs have been hypothesized to facilitate the deep-to-shallow stress transfer [Liu et al., 2007] or affect the megathrust initiation [Kato et al., 2012]. Shallow SSEs that are observed within ~ 50 km landward of the subduction trench may have potential to trigger tsunamis [Saffer and Wallace, 2015]. On the other hand, SSEs might be postponed or advanced by the occurrence of nearby large earthquakes [Hirose et al., 2012]. Peng and Gomberg [2010] have proposed an integrated physical model for all these diverse phenomena of slow and fast earthquakes, and attribute this physics to the inherent characteristics of the fault, such as the frictional properties.

In Cascadia, both geodetic and seismic observations suggest that episodic tremor and slip events (ETs) have various characteristics in their source parameters on the fault [Brudzinski and Allen, 2007; Boyarko et al., 2015]. Three ET segments that recur at ~ 14 , 19 and 10 months from Vancouver Island to the northern California [Brudzinski and Allen, 2007; Szeliga et al., 2008], but the nature of this segmentation

is not fully understood. The along-strike segmentation in ETS has been suggested to be related to the variation of gravity anomalies along the margin, which may indicate the influence of the overlying continental plate on the source parameters of ETS [Brudzinski and Allen, 2007]. The along-strike tremor segmentation in Cascadia has been reported to correspond with offshore paleo-earthquakes "patches" [Boyarko et al., 2015], which are inferred from the studies of marine sediments in fore-arc basins [Wells et al., 2003; Goldfinger et al., 2008]. These observations suggest a relation between shallow and deep fault rupture, which may help to investigate the faulting mechanism in subduction zone. On the other hand, Audet and Burgmann [2014] reported that the fore-arc V_p/V_s ratio in the overlying continent decreases with increasing depth, as well as the along-dip decreasing recurrence interval of ETS tremors. They proposed that the decreasing V_p/V_s structure may be controlled by permeability reduction via the temperature-dependent silica solubility, which suggests influence of the continental rock composition on the ETS source process. The heterogeneities of ETSs and their relation with overlying plate may be important to the hazard estimation in Cascadia margin.

The diverse source parameters and segmentation of SSEs have been reproduced in the numerical models using the framework the laboratory-derived rate-and-state friction, under the condition of near-lithostatic pore pressure [Liu and Rice, 2007; Rubin, 2008; Colella et al., 2012; Shibazaki et al., 2012], or dilatancy stabilization [Liu and Rubin, 2010; Segall et al., 2010; Liu, 2013] on the fault further downdip from the geodetically inferred "locked" portion, or dehydration-induced porosity wave [Skarbek and Rempel, 2016]. The recurrence of SSEs can be modulated by the level of pore pressure or the effectiveness of dilatancy [Liu and Rubin, 2010; Segall et al., 2010]. In addition, the variation of the plate convergence rate can also affect the recurrence interval of the spontaneous SSEs in the Nankai model as shown by Shibazaki et al. [2010]. The subduction fault curvature in northern Cascadia may also contribute to

the regular slip patches in a numerical model incorporating the 3-D fault geometry [Li and Liu, 2016].

In this study, I intend to examine the relationship between the heterogeneities of the fault physical properties and the along-strike segmentation of SSEs, in the framework of rate and state-dependent friction. The subduction fault geometry is constrained by updated seismicity relocations and regional velocity structures inversion studies [McCrorry et al., 2012]. My model extends from the southern British Columbia to Oregon, where slow slip inversions have been obtained from more than a decade of continuous GPS monitoring [Schmidt and Gao, 2010]. I use the recent 6-year (from 2009-8 to 2015-4) tremor catalogue from the Pacific Northwest Seismic Network (PNSN, <http://pnsn.org/tremor>) to constrain the depth range of SSEs. Both the free-air and Bouguer gravity anomalies are used to constrain the along-strike distribution of the level of effective normal stress (lithostatic stress minus pore pressure) within the SSE depths. Finally, the decreasing plate convergence rate along the Cascadia margin is taken into account to represent the realistic relative plate motion [McCaffrey et al., 2007].

I present modeling results from three scenarios where the along-strike distribution of the effective normal stress is assumed to be (1) uniform, (2) constrained by the Bouguer anomaly and (3) constrained by the free-air anomaly observed along the margin. I calculate the recurrence interval and cumulative slip of the modeled SSEs in each scenario, and compare the modeled segmentation patterns of SSE recurrence interval and cumulative slip to GPS inversions. Snapshots of individual SSE episode exhibit the along-strike propagation that is similar to time-dependent GPS observation. I also show the along-strike migration pattern between adjacent SSEs and the source parameter scaling relations with different selection criteria. In Discussion, I analyse

the influence of the heterogeneities of the overlying continent and the potential central Oregon creeping section on the source parameters of SSEs.

3.2 Method

3.2.1 Governing Equations

The shear stress on the subduction fault is governed by the laboratory-derived rate and state-dependent friction law [Dieterich, 1979; Ruina, 1983]. The friction coefficient f is dependent on the fault slip rate V and a single state variable θ ,

$$\tau = \bar{\sigma} f = (\sigma - p) \left[f_0 + a \ln \left(\frac{V}{V_0} \right) + b \ln \left(\frac{V_0 \theta}{d_c} \right) \right]. \quad (3.1)$$

Here, a and b are non-dimensional friction parameters, d_c is the characteristic distance over which θ evolves following velocity steps, f_0 is the friction coefficient at a reference velocity V_0 at steady state, and $\bar{\sigma} = \sigma - p$ is the effective normal stress, difference between normal stress and pore pressure.

There are two commonly used evolution laws, “aging” law and “slip” law, for describing the evolution of the state variable.

$$\frac{d\theta}{dt} = 1 - \frac{V\theta}{d_c}, \quad (3.2)$$

$$\frac{d\theta}{dt} = -\frac{V\theta}{d_c} \ln \left(\frac{V\theta}{d_c} \right). \quad (3.3)$$

The “aging” law allows friction to evolve on stationary asperity contacts as supported by laboratory experiments [Beeler et al., 1996]. The “slip” law requires non-zero slip for friction evolution and has been shown to better represent the friction evolution during earthquake nucleation especially at large velocity steps [Ampuero and Rubin, 2008]. At steady state $\theta = \theta_{ss} = d_c/V$, frictional coefficient becomes the same $f_{ss} = f_0 + (a-b) \ln \frac{V}{V_0}$, for both “slip” and “aging” laws. Slip remains stable and any slip perturbation evolves towards the steady state, when the friction stability parameter

$a - b$ is positive (velocity-strengthening, VS). Slip can be either unstable or conditionally stable when $a - b$ is negative (velocity-weakening, VW). The conditionally stable slip mode appears when the fault width under velocity-weakening W is comparable to but less than the minimum size for unstable slip, namely the characteristic nucleation size, h^* , which is related to the rate-state friction parameters a , b , D_c and $\bar{\sigma}$, as formulated by Rice and Ruina [1983]; Rice [1993] and more recently by Rubin and Ampuero [2005]. I will further discuss the definition of nucleation size h^* and parameter choice of a , b and d_c in detail in Section 3.2.3.

There are different definitions of the critical length, or characteristic nucleation size, in the frictional unstable displacement. Rice [1993] defined the nucleation size based the critical stiffness in a continuum requirement.

$$h_R^* = \frac{2\mu d_c}{\pi(1-\nu)(b-a)\bar{\sigma}}, \quad (3.4)$$

Here, shear modulus $\mu = 30$ GPa and Poisson's ratio $\nu = 0.25$. The length ratio W/h^* has been found to be a key parameter in determining the occurrence of slow slip events in subduction zones [Liu and Rice, 2007] and aseismic creep events on the continental strike-slip faults [Wei et al., 2013].

Rubin and Ampuero [2005] gave a definition based on the fracture energy balance for the slip to continue.

$$h_{RA}^* = \frac{2\mu b d_c}{\pi(1-\nu)(b-a)^2\bar{\sigma}}, \quad (3.5)$$

h_{RA}^* describes the frictional crack expanding during the rupture, and thus is more physically meaningful [Rubin and Ampuero, 2005].

The quasi-dynamic relation between the shear stress and fault slip is introduced by Rice [1993],

$$\tau_i(t) = - \sum_{j=1}^N K_{i,j} (\delta_j(t) - V_{pl}t) - \eta \frac{d\delta_i(t)}{dt} \quad (3.6)$$

$\tau_i(t)$ and $\delta_i(t)$ are shear stress and displacement of i th element on the fault, respectively. Stiffness kernel $K_{i,j}$ is the shear stress change on element i from a unit dislocation in the dip direction on element j , and thus has the unit of stress/distance (bar/mm in our model). $K_{i,j}$ is calculated using dislocations on triangular elements as first introduced by Stuart et al. [1997] for modeling earthquake cycles under regional stress loading. The radiation damping factor $\eta = \mu/2c_s$ (μ is the shear modulus and c_s is the shear wave speed) is introduced to prevent the slip velocity from going unbounded during an earthquake [Rice, 1993]. Plate convergence rate V_{pl} is constant with time but its amplitude varies along the strike.

Compared with the full dynamic simulation, the quasi-dynamic approach can produce similar seismic cycles but with lower seismic rupture propagation speeds and longer co-seismic durations [Lapusta and Rice, 2003; Lapusta and Liu, 2009]. As the slip velocity in SSE is several orders of magnitudes smaller than that during seismic slip, I do not expect the difference between the quasi-dynamic and full-dynamic approaches to affect the source properties of the modeled SSEs in our study. The quasi-dynamic approach is a good approximation for simulating slow slip events as long as the seismogenic zone is not allowed to slip.

3.2.2 Fault Geometry

I use the Cascadia slab model of McCrory et al. [2012] to constrain the 3-D fault geometry. This updated slab model is built on relocated seismicity and regional velocity structure from Vancouver Island to Oregon. For the convenience of simulation, I convert the geographic coordinates of latitude-longitude into Cartesian coordinates, in which x- and y-axis represent the trench-parallel and trench-normal axis, respectively (Figure 3–1; also see [Li and Liu, 2016]). After the conversion the fault is 800 km along the strike and ~ 300 km in the downdip direction.

The triangular meshing of the thrust fault is achieved by diagonalizing the rectangular grids using command *surface* in *Generic Mapping Tools* [Wessel and Smith, 1998]. Triangular meshing is more suitable for modeling the fault curvature as it prevents overlapping between the adjacent elements (Figure 3–1). The fault starts from the trench (5 km depth, referred to the sea-level) and is locked downdip to 20 km (that is, no slip is allowed at 5-20 km during the simulation). I let the fault to slip in the dip direction only at 20-55 km ($\sim 100,000$ triangular elements) to save computation time on Computer Canada HPC cluster *Guillimin* (at McGill University). The distance between the adjoining nodes in the triangular elements is ~ 1 km. The grid resolution is dictated by the choices of frictional parameters as will be introduced in section 2.3.

I set the plate convergence rate to linearly decrease from 45 mm/year in the north to 34 mm/year in the south, over the 800-km long fault segment (Figure 3–2b), based on the plate motion model of McCaffrey et al. [2007].

3.2.3 Model Parameters

Frictional Stability $a - b$. In the rate- and state-dependent friction framework, parameters a , b and characteristic displacement d_c depend on many factors, such as the rock composition, temperature and confining stress [Blanpied et al., 1998]. The extrapolation of frictional properties from the laboratory to tectonic faults is adopted by many numerical studies on the fault deformation in earthquake cycles [e.g. Lapusta and Rice, 2003; Liu and Rice, 2007, 2009]. In previous studies, the temperature-dependent friction stability parameter $a - b$ has been adopted from sliding experiments with wet gabbro [He et al., 2006] or granite gouges [Blanpied et al., 1998] in reproducing a wide range of fast and slow slip behaviors [Lapusta and Rice, 2003; Liu and Rice, 2007, 2009; Kaneko et al., 2010; Wei et al., 2013; Li and Liu, 2016; Veedu and Barbot, 2016].

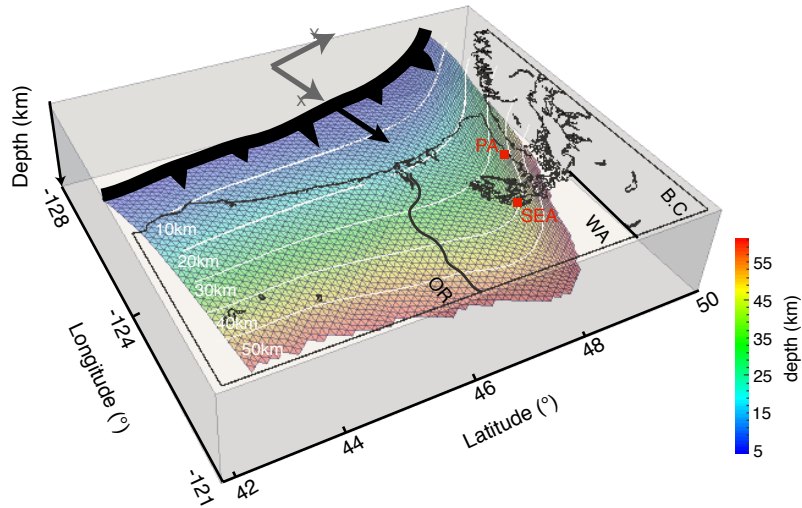


Figure 3–1: Graphs showing fault geometry and meshing of Cascadia subduction zone. The meshed grid sizes on the fault are ~ 10 km for illustration while ~ 1 km in the simulation. Depth contours of 10-50 km are from the study of McCrory et al. [2012]. Black vector shows the representative plate convergence direction. Gray vectors shows the X-(trench-normal) and Y-(trench-parallel) axes. Coastlines are shown by black lines. B.C.: British Columbia; WA: Washington; OR:Oregon; PA: Port Angeles; SEA: Seattle.

In order to realistically represent subduction fault heterogeneities, I introduce along-strike variation in the frictional stability parameter $a - b$ constrained by the epicentral distribution of non-volcanic tremors along the northern and central Cascadia. I use a 6-year tremor catalogue (from 2009.8 to 2015.4) from the Pacific Northwest Seismic Network (PNSN, <http://pnsn.org/tremor>), which is shown in Figure 3–2a. I assume that all non-volcanic tremors appear on the slab interface. The reason for this setup is that in Cascadia, episodic tremor and slow slip events in general spatio-temporally accompany each other as evidenced by seismic and geodetic observations [e.g. Rogers and Dragert, 2003; Wech et al., 2009]. The similar strategy of introducing frictional heterogeneities has been adopted by Matsuzawa et al. [2013] in modeling

short-term slow slip that synchronized with non-volcanic tremors in Shikoku, southwest Japan.

I outline the upper- and lower-limit for tremor epicenters, shown in Figure 3–2a, and set this region on the fault to be the transition zone. The range of tremors moves gradually from 35–50 km beneath Washington to 30–40 km beneath Oregon. I assign the up-dip limit of the transition zone to have the average value of velocity-weakening in the gabbro gouges sliding experiments, $a - b = -0.003$ [He et al., 2006], and the down-dip limit have $a - b = 0$. Within the transition zone, $a - b$ follows a linear increase with depth. Further updip to the locked zone, $a - b$ remains a constant of -0.003 . Figure 3–2b shows the mapview of the distribution of $a - b$ on the fault.

Characteristic Slip Distance d_c . The characteristic distance d_c is in the range of μm from lab experiments [Marone et al., 1990]. In numerical models, the characteristic nucleation size h^* scales with d_c . The definition of h^* is usually adopted as either $h_{RR}^* = \frac{2\mu d_c}{\pi(1-\nu)(b-a)\bar{\sigma}}$, by equating the critical stiffness to the system stiffness [Rice and Ruina, 1983; Rice, 1993], or $h_{RA}^* = \frac{2\mu b d_c}{\pi(1-\nu)(b-a)^2\bar{\sigma}}$, by balancing the fracture energy balance at the crack tip [Rubin and Ampuero, 2005]. In essence, h_{RR}^* is the threshold for self-accelerating slip transients and h_{RA}^* is the threshold for dynamic ruptures. Hence, the characteristic nucleation size for slow slip events as in this study should be between h_{RR}^* and h_{RA}^* [Rubin, 2008].

My choice of $d_c = 0.7$ mm results in $h_R^* = 11$ km and $h_{RA}^* = 92$ km, where $\mu = 30$ GPa, $\nu = 0.25$, $\bar{\sigma} = 1.0$ MPa, and averaged $\overline{(b-a)} = 0.0015$ and $\bar{b} = 0.0117$. Given the defined SSE downdip width W of 30–108 km, our h_R^* is much smaller than the minimum while h_{RA}^* approximates the maximum value of W . These above values of h^* result in a range of W/h^* that would lead to episodic slow slip events, as shown by the parameter space exploration in our previous SSE modeling [Li and Liu, 2016].

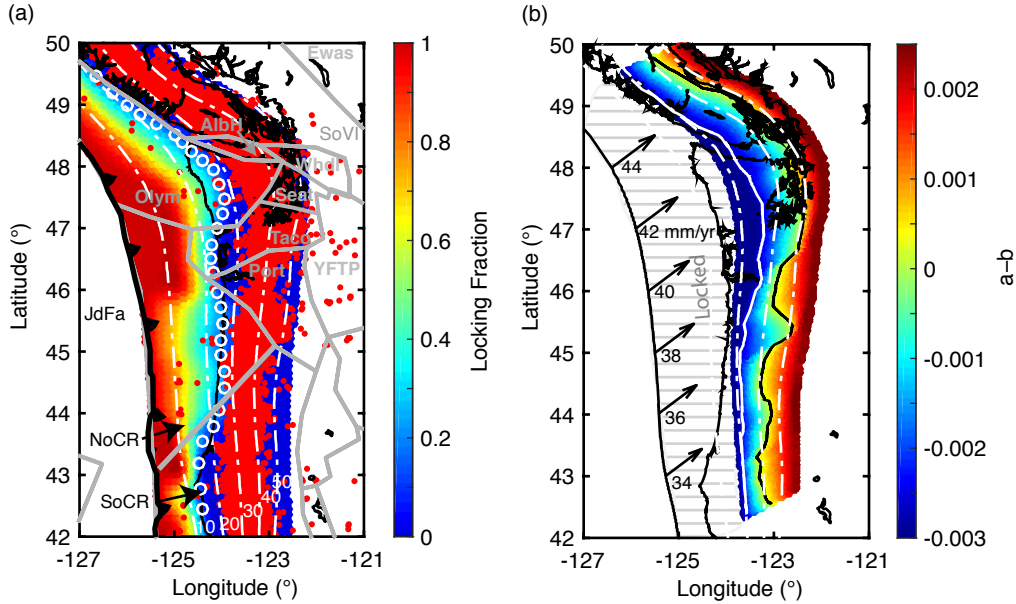


Figure 3-2: (a) Fault locking fraction ϕ of Gamma decade-scale model from the GPS inversion study of Schmalzle et al. [2014]. White circles mark their downdip 20% locked contour. Red dots show 6-year PNSN tremor epicenters catalog (2009/8-2015/4, <http://pnsn.org/tremor>). Gray polygons represent the block model from the study of McCaffrey et al. [2007]. (b) Non-dimensional rate-state friction parameter $a - b$. The upper- (white) and lower-limits (black) of the SSE depths in our model are obtained from outlining the tremor epicenters in (a). Within these lines, $a - b$ changes linearly from -0.003 to 0 with depth. $a - b = -0.003$ for further updip and velocity-strengthening ($a - b > 0$) for further downdip. Hatched lines represent the shallow locked fault (5-20km, depth referred to the sea-level). The plate convergence direction is 60° from north. Plate convergence rate changes linearly along the strike (black arrows) [McCaffrey et al., 2007].

Effective Normal Stress $\bar{\sigma}$. It has been hypothesized that high pore fluid plays an important role in promoting fault shear failure, by reducing the fault strength [Obara, 2002; Shelly et al., 2006]. In numerical studies, the level of effective normal stress ($\bar{\sigma}$) at the depth of ETS also modulates the magnitude of slip and recurrence interval of SSEs [Liu and Rice, 2007, 2009; Matsuzawa et al., 2013]. It has been shown that the along-strike segmentation of $\bar{\sigma}$ can lead to SSE segmentations in a Cascadia-like subduction fault model [Liu, 2014].

The along-strike segmentation of SSEs in Cascadia has been attributed to the varying gravity anomalies along the margin, which may reflect the material heterogeneity of the overlying continental plate [Brudzinski and Allen, 2007, and reference therein]. They argued that the density of continental lithosphere, which is reflected in the Bouguer anomalies, plays an important role in affecting the along-strike variation of SSE recurrence intervals. Here I incorporate two types of gravity anomalies, free-air and Bouguer, to represent the heterogeneity of the upper plate loading in our model. The application of both types of gravity anomalies allows me to test what properties of overlying continents affect the physics of SSEs. Free-air anomaly corrects the elevation of the measurement, and reflects the entire difference below that. Bouguer anomaly further corrects the plate thickness (including topography), by assuming uniform density below a isostatic depth, and thus mainly reflects the lithospheric density variation. The mapviews of these two gravity anomalies are shown in Figure 3–3 (data sources: USGS and Natural Resources Canada). Specifically, We use the gravity anomaly along the 35 km depth contour, representative of the average SSE depth, to approximate the along-strike variation of $\bar{\sigma}$. The profiles of both types of gravity anomalies are shown in Figure 3–5c and 3–6c.

In this study, I setup three models with different $\bar{\sigma}$ along the strike: (1) uniform 1.0 MPa, (2) a multi-segment linear fit of the Bouguer anomaly and (3) a polynomial fit of free-air anomaly. The distributions of $\bar{\sigma}$ of model (2) and model (3) are shown in Figure 3–5c and 3–6c, respectively. In models (2) and (3), the effective normal stress is chosen to vary between 1.0 to 1.5 MPa, which has been shown to be the range to generate the recurrence intervals of 1-2 years, based on the parameter space exploration in our previous studies [Liu and Rice, 2007; Li and Liu, 2016] and theoretical parameter analysis [Rubin, 2008]. Except for effective normal stress, other parameters are same in the three models.

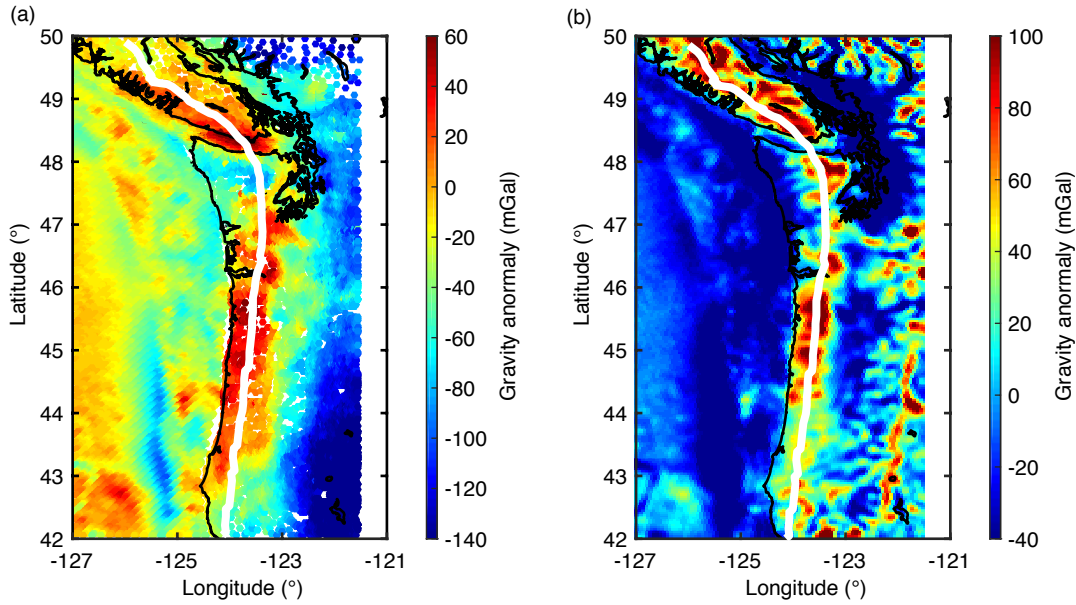


Figure 3-3: Maps showing (a) Bouguer anomaly (onshore) and free-air (offshore) and (b) free-air anomaly in Cascadia. Color scales are in different. Data sources are from U.S. Geological Survey (USGS, <http://mrddata.usgs.gov/gravity/isostatic/>) and Natural Resources Canada (<http://www.nrcan.gc.ca/home>). The gravity anomalies along the 35km-depth contour (white lines) are used to constrain $\bar{\sigma}$ along the strike in our model.

3.3 Results

I simulate SSEs for a history of 10-20 years, which generates ~ 20 episodes along the strike in each model. These episodic SSEs appear on several segments along the strike, with different recurrence intervals ranging from 1 to 2 years. I calculate the recurrence intervals and cumulative slips for each segment and analyse the characteristics of this along-strike segmentation. The segmentation reveals a combined influence of both the heterogeneities in fault frictional properties and the overlying effective normal stress. In this study, I focus on the effects of $\bar{\sigma}$ on the characteristic segmentation, which may reflect the along-strike heterogeneities of the overlying continental plate, by making quantitative comparisons to SSE source parameters from GPS inversions. In addition, I show two examples of time-dependent slip evolution, to illustrate the detailed slow slip release processes and interaction among multiple segments.

3.3.1 Cumulative Slip Constrained by Gravity Anomalies

I used the fault average slip rate as a criterion for defining slow slip events. SSEs are defined when $V_{ave} > V_{pl}$ occurs, where V_{ave} and V_{pl} are the slip rate and plate convergent rate averaged over each segment, respectively. After the starting and ending times of each SSE episode are determined, the cumulative slip is summed up and averaged over the total number of episodes.

As a reference model, the mapview of the average cumulative slip is shown in Figure 3-4a when the effective normal stress is assumed to be uniformly 1.5 MPa. Figure 3-4b shows the average cumulative slip at the contour of $a - b = -0.0025$. The cumulative slip is roughly the largest at this depth in each segment. Figure 3-4c shows the width of the velocity-weakening portion, W , which equals to the downdip distance between the upper- and lower-limit approximated from the tremor epicenters (Figure 3-2).

There are five consecutive slip segments identified from north to south, named as P1-P5 in Figure 3-4b. The along-strike lengths of these segments are 80, 120, 130, 170 and 100 km, respectively, which are fixed in order to simplify the calculation of average slip rate and cumulative slip.

The maximum slip on each segment is in the range of 1.7 to 2.3 cm. In the first order, the slip segmentation is an outcome of the heterogeneous distribution of W . The heterogeneity along the strike promotes the slip to initiate at the local maxima of W and accumulate large slip, which is evidenced by the along-strike correlation between the cumulative slip and the distribution of W profiles. It has been shown that both the SSE slip rate and recurrence interval are proportional to W/h^* , which is a key parameter in controlling SSE behaviors in both quasi- and fully-dynamic modeling [Rubin and Ampuero, 2005; Liu and Rice, 2007; Li and Liu, 2016; Veedu and Barbot,

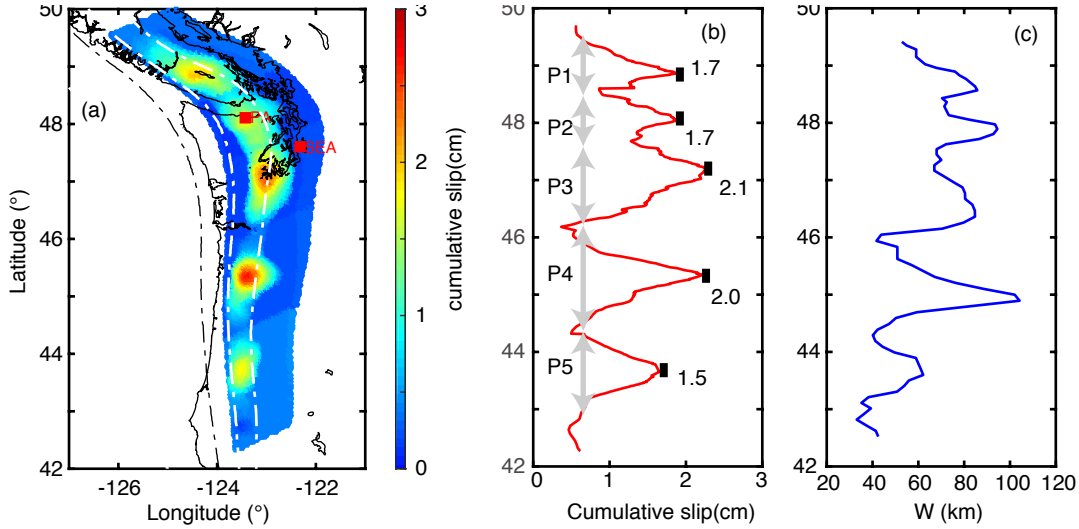


Figure 3-4: Graph showing (a) cumulative slip of the reference model with uniform $\bar{\sigma}=1.0$ MPa. Five patches are defined as P1-P5 in (b). PA: Port Angeles and SEA: Seattle. (b) Cumulative slip along the contour of $a - b = -0.0025$. The maximum cumulative slip in each of the five segments is 1.7, 1.7, 2.1, 2.0 and 1.5 cm, respectively. (c) The width of downdip distance of velocity-weakening in SSE depths, W , along the strike, which is constrained by the tremor locations in Figure 3-2a. Local maxima of W in each segments are 85, 95, 85, 108 and 60 km.

2016]. In our models, as characteristic nucleation size h^* is identical everywhere within SSE region, the distribution of W is thus equivalent to W/h^* .

The amount of cumulative slip in each segment is also affected by the varying plate convergence rate along the strike (Figure 2-1b). W in P4 (108 km) is almost 14% larger than that in P2 (95 km) (Figure 3-4c). However, this large increase in W is compensated by the decreasing plate convergence rate (from 40 to 37.7 mm/yr), hence the cumulative slip of P4 is only 8% larger than that of P2 (Figure 3-4b). This effect of varying plate convergent rate has also been shown in the SSE simulation in Nankai Trough [Shibazaki et al., 2012].

The segmentation in cumulative slip, as presented in Figure 3-4 and later in Figure 3-5 and 3-6, reflects the average intensity of energy release, but does not imply a permanent boundary for individual SSE episode. In each episode, the slip front can

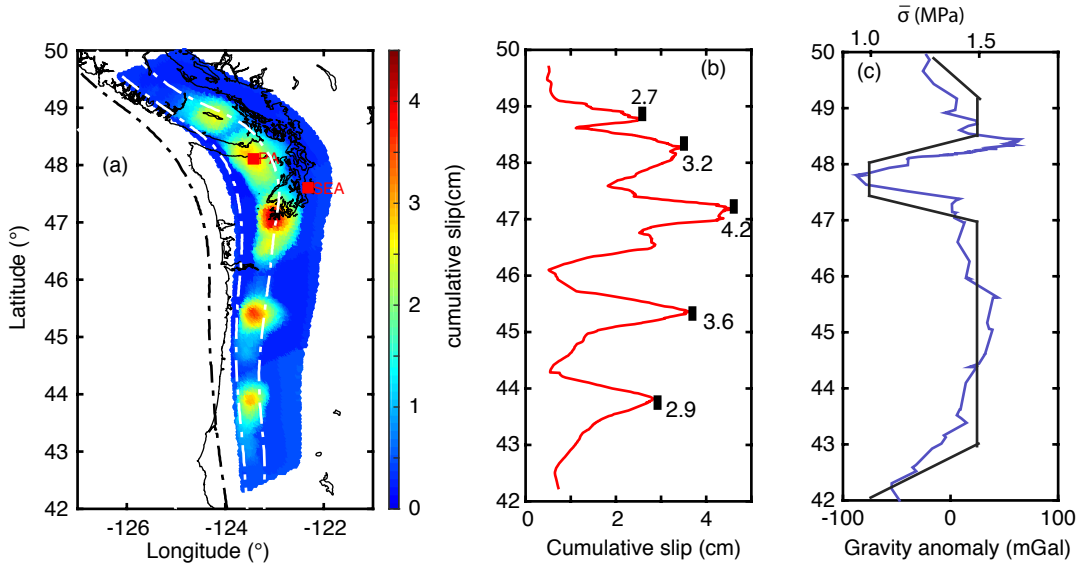


Figure 3–5: (a) Cumulative slip of the model with $\bar{\sigma}$ constrained by Bouguer anomaly. PA: Port Angeles and SEA: Seattle. (b) Cumulative slip along the contour of $a - b = -0.0025$. Maximum cumulative slips of the five segments are 2.7, 3.2, 4.6, 3.2 and 2.9 cm. (c) Bouguer anomaly of 35 km depth contour (blue) and its multi-segment linear fit (black).

propagate across the boundaries without making much contribution to the cumulative slip (see Section 3.3.5).

The average cumulative slip in mapview and along depth contour of $a - b = -0.0025$ as well as the corresponding along-strike $\bar{\sigma}$ constrained by gravity anomalies are shown in Figure 3–5 (Bouguer) and 3–6 (free-air), respectively. Both the models capture the segmentation pattern as shown in Figure 3–4 for the uniform $\bar{\sigma}$ case. The major differences are the amount of slip in northern Cascadia, which is directly caused by the along-strike distribution of $\bar{\sigma}$, as frictional parameters ($a - b$, W and d_c) and plate loading rate (V_{pl}) are identical in all three models. In the model of Bouguer anomaly, the cumulative slip per episode is 3.2 cm beneath Port Angeles and 4.2 cm in south Washington, as a result of $\bar{\sigma}$ increasing from 1.0 to 1.4 MPa (Figure 3–5b). On the other hand, in the model constrained by free-air anomaly, the cumulative slip decreases

from a maximum of 3.3 beneath Port Angeles to 2.2 cm in southern Vancouver Island and southern Washington, and is spatially related to the decreasing $\bar{\sigma}$ from 1.2 to 1.0 MPa (Figure 3–6b).

The spatial correlation between total slip amount and the level of effective normal stress is in general consistent with finding in previous numerical studies that variations in $\bar{\sigma}$ can cause complex SSE behaviors [Matsuzawa et al., 2013; Liu, 2014], and is also supported by seismic observations in natural subduction zones, such as the varying tremor recurrences along the interface observed in Cascadia [Audet and Burgmann, 2014] and pore pressure evolution with depth during adjacent LFEs in Guerrero, Mexico [Frank et al., 2015a]. However, the exact amount of slip can vary from model to model even with the same level of $\bar{\sigma}$. For example, the P4 segment beneath Oregon, with $\bar{\sigma} = 1.5$ MPa, has a cumulative slip of 2.5 and 3.6 cm in the models of free-air and Bouguer, respectively, which is probably due to the effect of the overall along-strike distribution of $\bar{\sigma}$.

The along-strike slip distribution from the model constrained by free-air anomaly appears more consistent with slow slip pattern inferred from GPS, in that the major regularly repetitive slip occurs beneath Port Angeles, with decreasing slip towards the Vancouver Island and northern Washington [Schmidt and Gao, 2010; Schmalzle et al., 2014]. Our previous model of the northern Cascadia, with frictional parameters constrained by isothermal contours, also shows that the slip pattern concentrates in Port Angeles, dominated by the slab curvature [Li and Liu, 2016].

3.3.2 Slip in Central Oregon

The cumulative slip varies from to 2.2 to 3.6 cm in Oregon (43°-44°N) in different models in my study. However, Schmalzle et al. [2014] shows that 14 SSEs occur in Oregon with a total cumulative slip of ~ 8 cm from 2005 to 2010, resulting in an

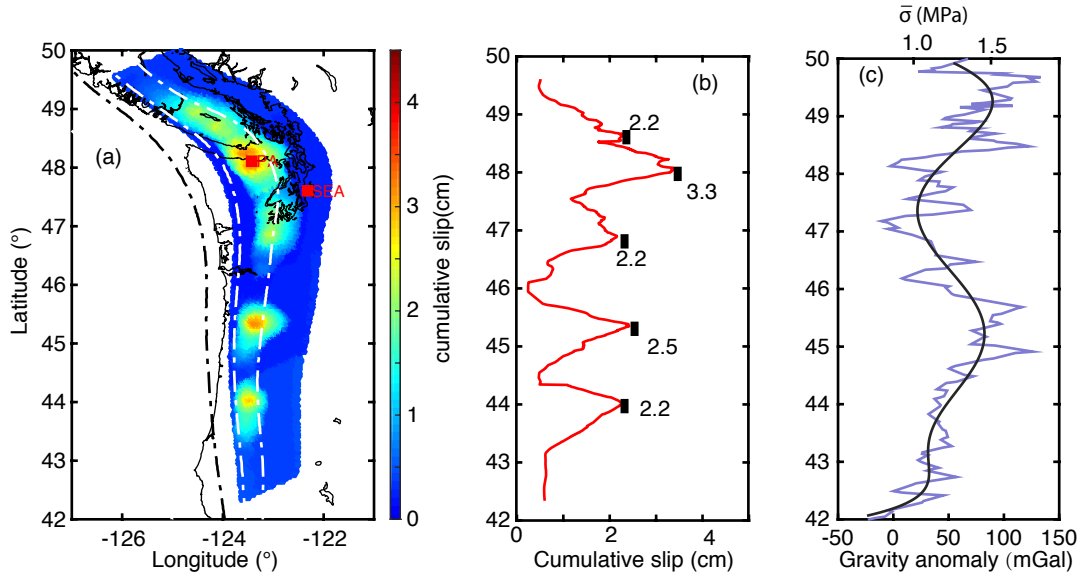


Figure 3-6: (a) Cumulative slip of the model with $\bar{\sigma}$ constrained by free-air anomaly. PA: Port Angeles and SEA: Seattle. (b) Cumulative slip along the contour of $a - b = -0.0025$. Maximum cumulative slips of five segments are 2.2, 3.3, 2.2, 2.5 and 2.2 cm. (c) Free-air anomaly of 35 km depth contour (blue) and its polynomial fit (black).

average slip of only ~ 0.6 cm, from 6-year GPS observations. In the following I further investigate this significant discrepancy.

With W, d_c and $\bar{\sigma}$ fixed, the episodic SSE behaviors depend on the parameter $a - b$, which directly affects h^* . I run a test by changing from $a - b = -0.003$ to $a - b = -0.0025$ (equivalently, $\sim 17\%$ reduction in the level of velocity-weakening) at the upper-limit of SSE depth, to examine how the amplitude of the cumulative slip is affected by $|a - b|$ in the segment of Oregon. With these parameters, the maximum cumulative slip in Oregon decreases from 3.6 cm to 3.4 cm, a reduction of $\sim 6\%$. Assume the relation between $|a - b|$ and cumulative slip can be extrapolated, a 85% decrease in $|a - b|$ would only lead to $\sim 30\%$ reduction in cumulative slip, which indicates that decreasing the effectiveness of velocity-weakening may not be sufficient to explain the small amount of SSE slip that observed in Oregon. I will discuss this in detail in Chapter 3.4.2.

3.3.3 Segmentation of Recurrence Interval

Continuous GPS records have revealed slow slip events recur at intervals of ~ 14 , 19 and 10 months from southern Vancouver Island to northern California along the Cascadia margin [Brudzinski and Allen, 2007]. In my simulations, the recurrence intervals of the modeled SSEs are highly affected by the variation of $\bar{\sigma}$. Here I present a quantitative comparison between the modeled and observed along-strike segmentation of SSE recurrence intervals from the three models presented in Figure 3–4, 3–5 and 3–6. Recurrence interval, T , is averaged over years in simulation or observation.

The recurrence intervals in the model of uniform $\bar{\sigma}$ vary between ~ 0.8 -1.1 years (Figure 3–7a). The relatively small along-strike variation is due to the uniform distribution of $\bar{\sigma}$. In the model with $\bar{\sigma}$ constrained by Bouguer anomaly, the recurrence interval reaches ~ 1.8 year between 44°N and 47°N and drops to ~ 1 year between 44°N and 43°N in the south and between 47° and 49°N in the north (Figure 3–7b). The standard deviations in the recurrence interval are large, especially beneath Oregon, probably due to the step-change in $\bar{\sigma}$ and the corresponding stress perturbations. The recurrence interval in the model with $\bar{\sigma}$ constrained by free-air anomaly increases from ~ 1 year to ~ 1.3 year from 48°N to 44°N and then decrease to 1 year further south (Figure 3–7c). Compared with Figure 3–7b, the recurrence intervals in Figure 3–7c show smaller deviations, probably due to the smoothness of the polynomial fitting.

To further quantify the comparison of modeled recurrence interval to segmentation observations reported by Brudzinski and Allen [2007], I define a weighted misfit function as following:

$$\chi^2 = \frac{\sum_{i=1}^M L_i * (T_i^{obv} - T_i^{mod})^2}{M}, \quad (3.7)$$

where T_i^{obv} and T_i^{mod} are the observed and modeled recurrence intervals at the i th segment, averaged over years. L_i is the length of the i th segment. M is the total

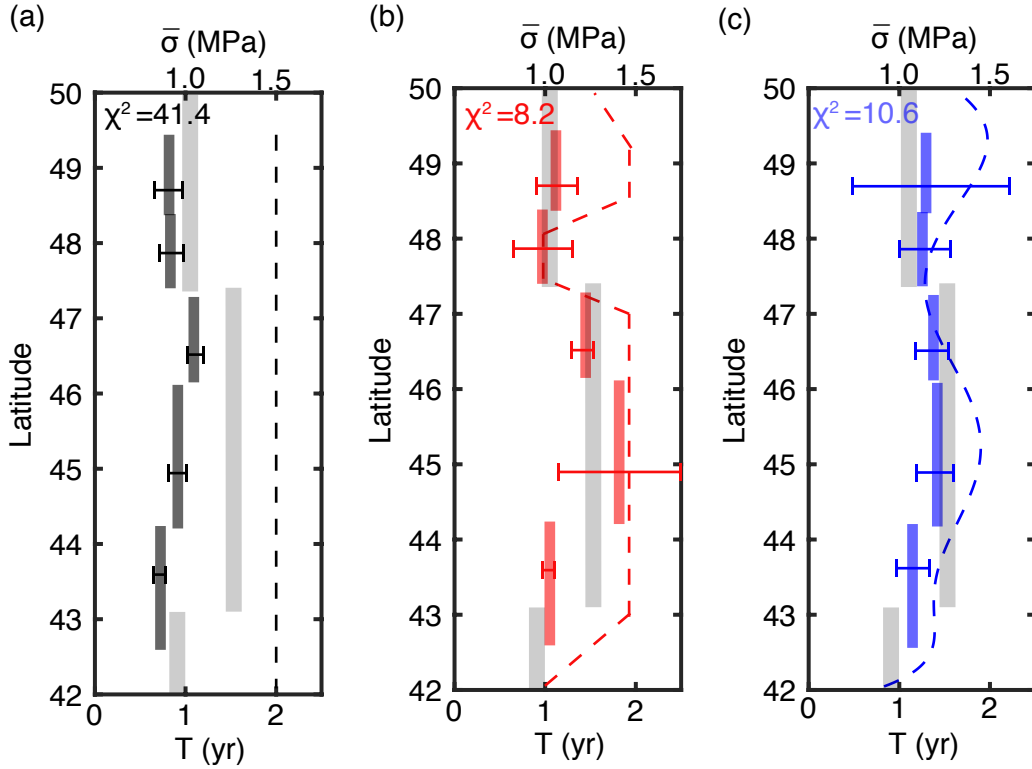


Figure 3–7: Recurrence intervals of models with (a) uniform $\bar{\sigma}$ (black bars), (b) $\bar{\sigma}$ constrained by Bouguer anomaly (red bars) and (c) $\bar{\sigma}$ constrained by free-air anomaly (blue bars). Dashed lines represent the effective normal stress used in each model. Error bars show the standard deviations. Recurrence intervals observed by Brudzinski and Allen [2007] are shown as gray bars in (a-c).

number of segments; $M = 5$ in all cases. This results in the misfits of 10.6 and 8.2, respectively, for the models with $\bar{\sigma}$ constrained by free-air and Bouguer, which are similar to each other but remarkably smaller than $\chi^2 = 41.4$ from the model with a uniform $\bar{\sigma}$.

The segmentation of recurrence intervals inferred from continuous GPS records of Brudzinski and Allen [2007] are shown by grey bars in Figure 3–7a-c. At each station, the recurrence interval is averaged over 5-16 years [Brudzinski and Allen, 2007]. Figure 3–8 shows the SSE segmentation obtained by Schmalzle et al. [2014] using stations from both the Pacific Northwest Geodetic Array (PANGA, <http://www.geodesy.cwu.edu/>)

and the Plate Boundary Observatory (PBO, <http://pbo.unavco.org/data/gps>), ranging from 42°N to 50°N. I divide these SSEs into two segments, one from 42°N to 47°N and the other from 44°N to 50°N. The recurrence intervals calculated for these segments are 180 and 280 days respectively (Figure 3–8), which are smaller than those of Brudzinski and Allen [2007], probably due to the different datasets and detection methods. Brudzinski and Allen [2007] focus on the spatio-temporally correlated GPS time series and non-volcanic tremors (ETS events), while Schmalzle et al. [2014] focus more on the coherent reversal signatures in GPS series.

There is a wide overlapped region between 44°N and 47°N (hatched lines in Figure 3–8), which is occasionally ruptured by SSEs from both sides. This overlapping in SSE appearance makes it difficult to define the segmentation from individual GPS record, as used in Brudzinski and Allen [2007]. The overlapping region of SSEs supports our results in Section 3.3.3 that there may be no permanent boundary along the strike for episodic SSEs. The tectonic implication of this overlapped region will be discussed in Section 3.4.2.

3.3.4 Synthetic GPS Vectors

Both models with $\bar{\sigma}$ constrained by free-air and Bouguer anomaly can reproduce the segmentation of recurrence intervals of SSEs, with minor differences in the detail (Figure 3–7). To further distinguish the effects of various gravity anomalies, the segmentation of cumulative slip should be accounted. In this section, I compare the modeled fault slip with the slip inferred from GPS. We also calculate the synthetic GPS displacements, calculated from the modeled cumulative slip, with the GPS observations reported by Schmidt and Gao [2010].

I calculate the synthetic GPS displacements from the modeled slip distributions, in a homogeneous half-space medium, characterized by shear modulus of 30 GPa and Poisson’s ratio of 0.25. The slip distributions are chosen from the results of both the

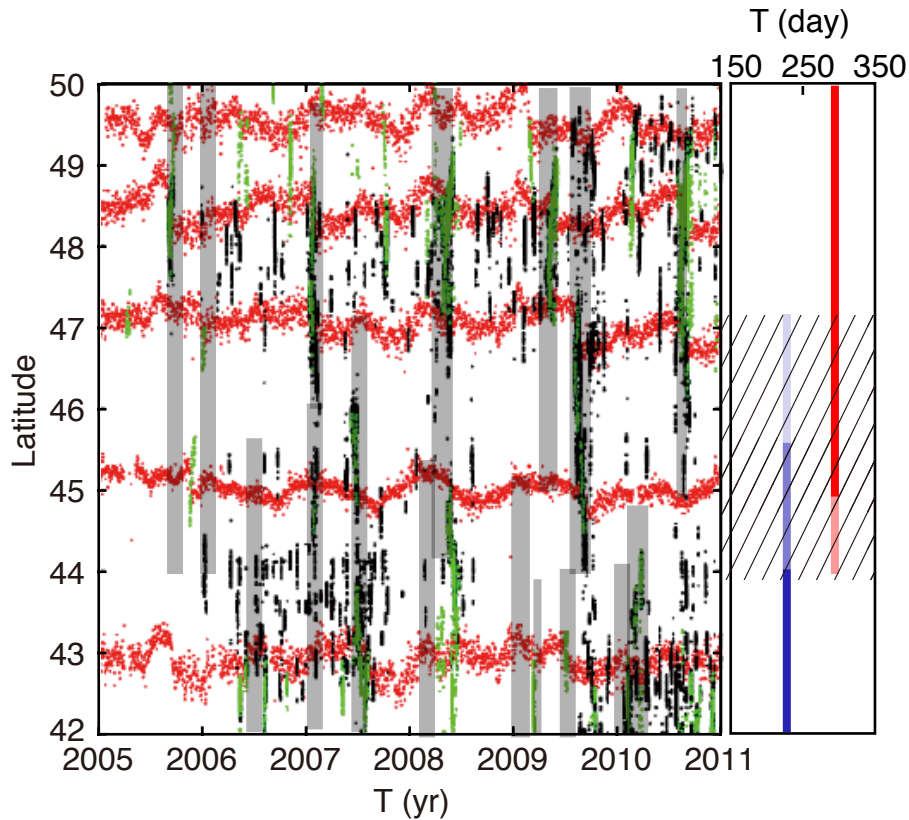


Figure 3–8: Segmentation of slow slip events from Schmalzle et al. [2014]. Black and green dots shows non-volcanic tremors from Pacific Northwest Seismic Network (PNSN) and Miami University(MU) catalog, respectively. Red dots are east components of GPS series from stations ALBH, KTKA, CPXX, DDSN and P376. Gray bars denote episodic slow slip events detected by Schmalzle et al. [2014]. The average recurrence intervals of two segments, 44°-50°N (red) and 42°-47°N (blue), are 280 and 180 days, respectively. Hatched lines show the overlapping region between these two segments, where occasionally ruptured by SSEs from both sides.

models with Bouguer and free-air anomalies, which have similar spatial slip patterns and equivalent magnitude to minimize bias in the comparison. We choose two SSE episodes in each model, one in northern Washington (Figure 3–9) and the other in the southern Washington (Figure 3–10), and compare the displacements with two SSE episodes in July 1998 and May 2004, respectively, with equivalent magnitudes of Mw6.7 and 6.6 [Schmidt and Gao, 2010]. The north- and east-components from both the GPS inversions and our forward models used in producing Figure 3–9 are all listed in Table

S1. As I model the SSEs using an updated Cascadia slab model [McCrorry et al., 2012] while the slip inversion in Schmidt and Gao [2010] was based on a previous version of the slab model [McCrorry et al., 2006], the moderate differences in the fault geometry may also contribute to the discrepancy as summarized in Figure 3–9 and 3–10.

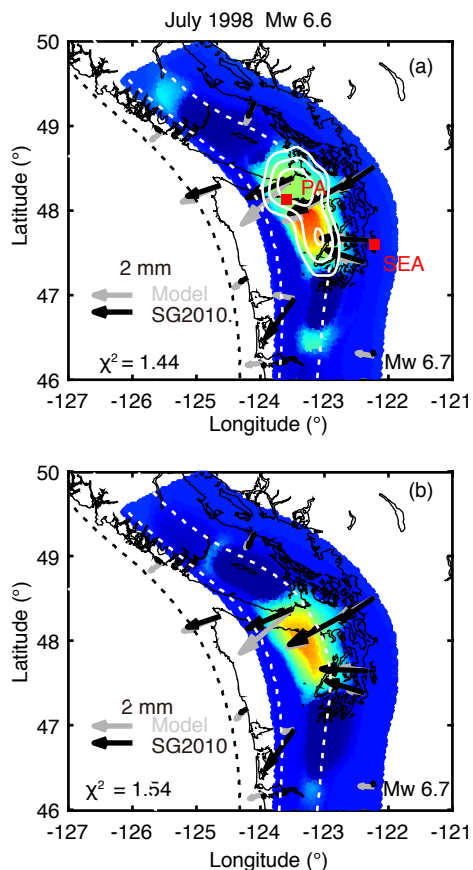


Figure 3–9: (a) GPS displacements calculated from the slip distribution of the July 1998 SSE in northern Washington (Mw 6.6) [Schmidt and Gao, 2010] (black vectors). White contours denotes the cumulative slip contours of 1-3 cm. Modeled GPS vectors (gray) are calculated from our modeled cumulative slip of the model with $\bar{\sigma}$ constrained by free-air anomaly, which has an equivalent magnitude of Mw 6.7 (shear modulus of 30 GPa). The reduced chi-square is defined by Equation 3.7. Dotted lines are depth contours from 20 to 40 km. PA: Port Angeles. SEA: Seattle. (b) shows the same results as (a), except for that the modeled cumulative slip is of the model with $\bar{\sigma}$ constrained by Bouguer anomaly.

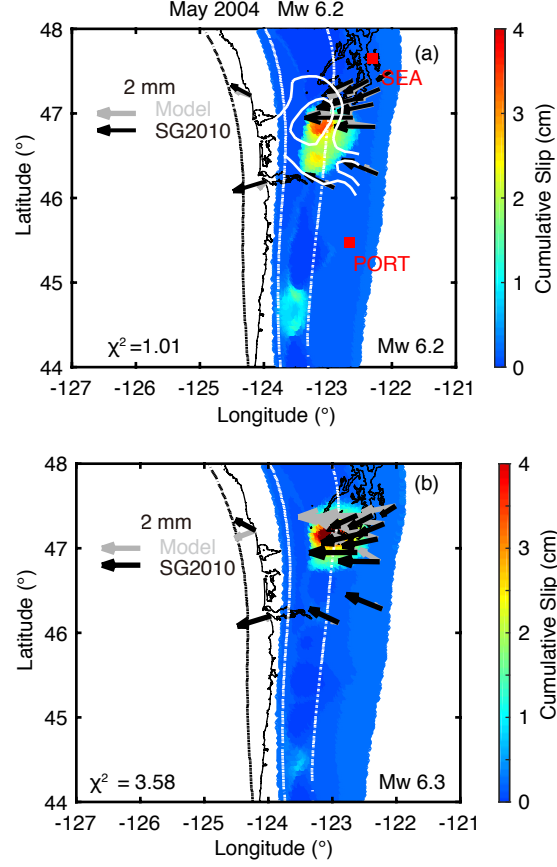


Figure 3–10: (a) GPS displacements calculated from the slip distribution of the May 2004 SSE in southern Washington (Mw 6.2) (black vectors). White contours are the cumulative slip contours of 1-2 cm. Modeled GPS vectors (gray) are calculated from our modeled cumulative slip of the model with $\bar{\sigma}$ constrained by free-air anomaly, which has an equivalent magnitude of Mw 6.2. SEA: Seattle. PORT: Portland. (b) show the same results as (a), except for that the modeled cumulative slip is of the model with $\bar{\sigma}$ constrained by Bouguer anomaly.

To quantify the misfit between modeled and observed surface displacement, I define the difference between observation and modeling as:

$$\chi^2 = \frac{\sum_{j=1}^N \left| \vec{S}_j^{obv} - \vec{S}_j^{mod} \right|^2}{N}, \quad (3.8)$$

where \vec{S}_j^{obv} and \vec{S}_j^{mod} are the observed and modeled GPS vectors at j th station. N is the total number of stations. During the July 1998 event, the major cumulative slip (~ 3.5

cm) appears in northern Washington, between Port Angeles and Seattle, inferred from GPS inversions. The GPS vectors (black arrows) show larger horizontal displacements around Port Angeles and decrease to the south. Almost all of the synthetic GPS vectors (gray arrows) are consistent with the observations, in terms of both direction and magnitude. Both models constrained by free-air and Bouguer anomalies can produce surface displacements with relatively small misfits, 1.44 and 1.54, respectively.

The May 2004 event occurred beneath southern Washington, between Seattle and Portland (Figure 3–10). The modeled maximum cumulative slip, which reaches ~ 3.4 cm south of Seattle, slightly larger than the maximum slip of ~ 2.7 cm from the GPS inversion [Schmidt and Gao, 2010]. Most of the modeled vectors (grey arrows), constrained by free-air anomaly agree with the observations (black arrows), with a misfit of 1.01. The modeled vectors with Bouguer anomaly, however, shows a significantly larger misfit, 3.58, due to an even larger cumulative slip of ~ 4.3 cm originating from the higher effective normal stress value used in this along-strike segment (Figure 3–5c).

3.3.5 Along-strike Migration

In this section, I show two examples of the time-dependent slip evolutions during two sequential SSEs from the model with $\bar{\sigma}$ constrained by free-air anomaly, which are similar to the spatio-temporal patterns of ETS episodes inferred from GPS inversion and automatic tremor detection.

Figure 3–11 shows the 10-day snapshots of two sequential SSEs extending from the south to north. The first event initiates around 45°N and then propagates northward at a speed of ~ 2 km/day (Figure 3–11a-d). The event lasts for 41 days with a final slip of ~ 3.2 cm. The second event starts around 47.5°N at day 63 and extends bilaterally between range 47° - 48°N (Figure 3–11g-h). The final cumulative slip is ~ 3.0 cm beneath Port Angeles. During the 22-day gap between these two SSEs, the slip front migrates

from 46°N to 47°N at a very low rate, and results in a tiny cumulative slip less than 1 cm (Figure 3–11e-f).

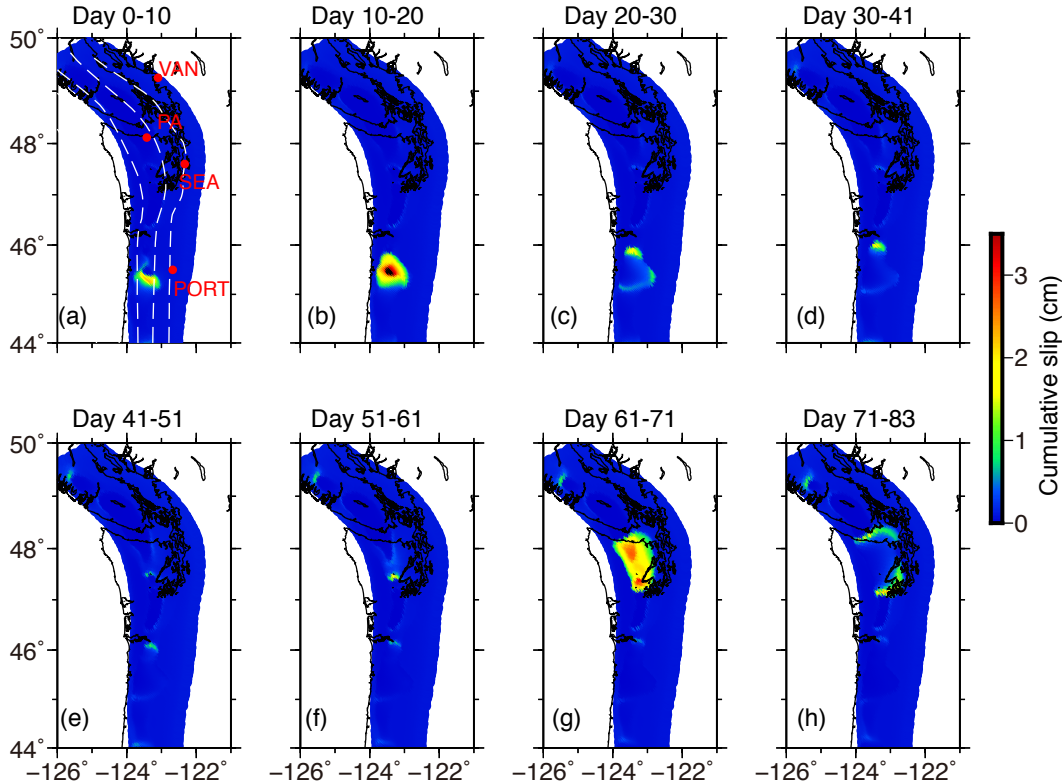


Figure 3–11: Snapshots of two sequential SSEs of the model with $\bar{\sigma}$ constrained by free-air anomaly. The first event initiates at 45°N and then propagates northward at a speed of ~ 2 km/day (a-d). The event lasts for 41 days. The second event starts between 47.5°N at day 63 and extends in the range 47°N -48°N (g-h). The final cumulative slip is ~ 3.0 cm beneath Port Angeles. In the gap between the two SSEs, from day 41 to 63, the slip front migrates from 46°N to 47°N at a very low rate (e-f). VAN: Vancouver. PA: Port Angeles. SEA: Seattle. PORT: Portland.

Figure 3–12 shows the 10-day snapshots of two successive SSEs in northern Cascadia. The first SSE initially appears beneath Port Angeles and propagates bilaterally for 30 days (Figure 3–12a-c). At day 41, the second SSE occurs beneath southern Vancouver Island, migrates southward and finally stops at where the first SSE terminates

(Figure 3–12d-h). The maximum cumulative slips of these two episodes are ~ 2.5 and 3.0 cm, respectively.

The SSE scenario shown in Figure 3–11 is similar to the time-dependent slip inversion of the 2011 ETS event reported by [Wech and Bartlow, 2014]. From June to August, 2011, two sequential ETS events occurred, which are spatio-temporally connected by a low-rate slow slip without tremor appearance. The first ETS initiated in June 2011 in northern Oregon and propagated to north for 30 days, stopped at central Oregon for 21 days before resuming propagation to Vancouver Island for another 42 days. The automatic detected tremors show a "gap" between $46.5\text{--}47^\circ\text{N}$, where low-rate slip is inferred from borehole strainmeter measurements in Oregon [Wech and Bartlow, 2014]. However, about 3 weeks after the first ETS, this gap is filled with south-migrating tremors of the second ETS event. The observation of tremorless slip may challenge the hypothesis that non-volcanic tremors and slow slips occur synchronized in Cascadia [Rogers and Dragert, 2003; Bartlow et al., 2011]. We will discuss the implication of the tremorless slip in Section 3.4.3.

Another modeled SSE scenario, as shown in Figure 3–12, is comparable to that occurred in August 1999 in the GPS inversion [Schmidt and Gao, 2010]. One SSE occurred beneath Port Angeles 30 days before another event occurred further north beneath Vancouver Island [Schmidt and Gao, 2010]. However, the detailed time-dependent slip pattern of the two-event sequence is not available from the above GPS inversion study. Another event in May 2008 is similar to the August 1999 event, except for the less observed slip (~ 1.5 cm) recorded beneath Vancouver Island [Schmidt and Gao, 2010]. These two segments (P1 and P2) in northern Cascadia may be regularly generating sequential SSEs, which may result from that effective stress perturbations in promoting the initiation of adjacent SSEs.

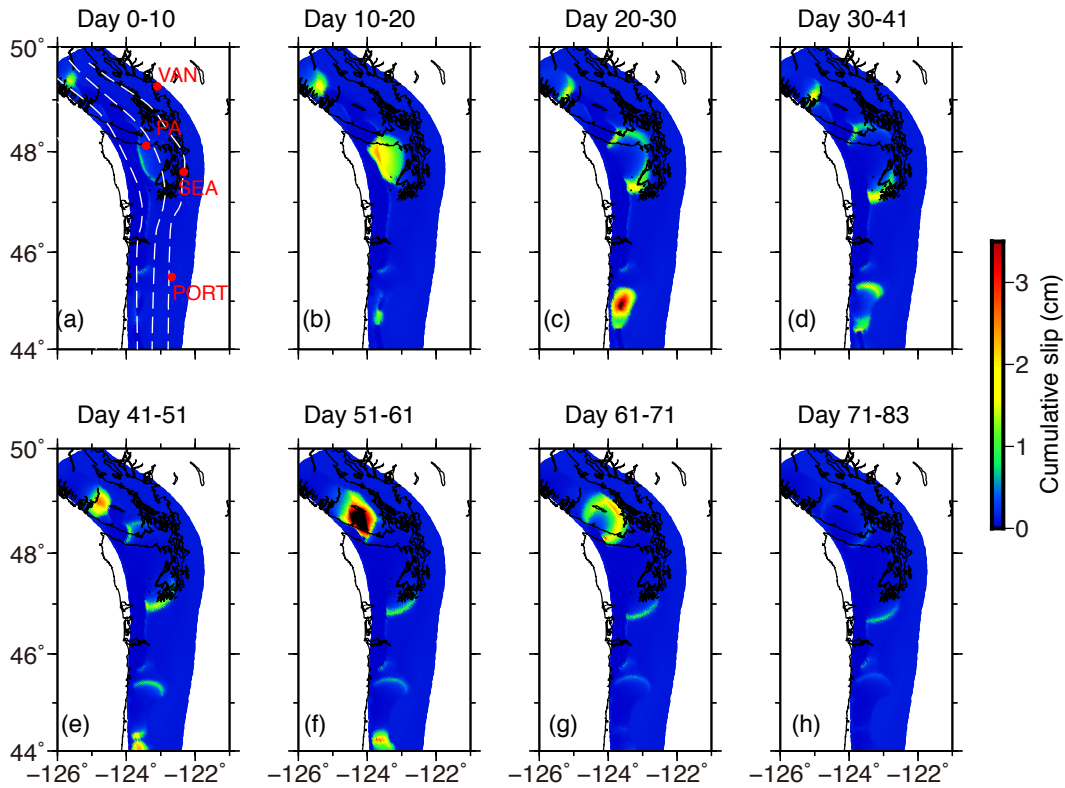


Figure 3–12: Snapshots of two sequential SSE adjacent to each other of the model with $\bar{\sigma}$ constrained by free-air anomaly. The first SSE initially appears beneath Port Angeles and propagates bilaterally for 30 days (a-c). Later at day 41, the second SSE occurs beneath southern Vancouver Island, migrates southward and finally stops at where the first SSE terminates (d-h). The maximum cumulative slips of these two episodes are about 2.5 and 3.0 cm. VAN: Vancouver. PA: Port Angeles. SEA: Seattle. PORT: Portland.

3.3.6 Source Parameter Scaling Relations

Here I intend to test the influence of the different slip criteria for choosing SSE source parameter on their inferred scaling relations. We use two types of velocities, the maximum rate and the average rate of each slip segment, in the definition of the start and ending times of one slow slip event. As an example, Figure 3–13a and c show the 7-year average and maximum slip velocity on segment P2, respectively, in a 10-year simulation with $\bar{\sigma}$ constrained by free-air anomaly. The average slip rate is proportional to the cumulative moment rate as shown in Figure 3–13e, and hence a

smoother representation of the energy release on the fault than the maximum slip rate history.

For an individual slow slip event, its duration is defined when the average velocity or the maximum velocity exceeds a certain threshold. The contrast in the resulting SSE duration of one event is obvious from Figure 3–13b and d. The duration defined by the average slip velocity is in the range 20-60 days, which is consistent with the GPS observations [Schmidt and Gao, 2010]. The maximum slip velocity, however, gives a duration of ~ 150 days, which is much longer than that from the observation. Thus I use the average slip velocity of each patch to define the duration of SSEs presented the paper.

Moment-area Scaling. I calculate the cumulative moment, the duration and the fault area with two selection criteria, 1) $V_{ave} > V_{pl}$ and 2) $V_{ave} > 0.5V_{pl}$, where V_{ave} is the average slip rate over each segment, for a total of 75 events. Plate convergence rate V_{pl} varies in the range 35-45 mm/yr, or 0.10-0.12 mm/day, along the strike. The cut-off velocity is chosen to approximate the GPS threshold 0.25-0.5 mm/day, given by Wech and Bartlow [2014].

The equivalent moment rate shown in Figure 3–13a is calculated as:

$$\dot{M} = \mu V_{ave} A \quad (3.9)$$

where \dot{M} is moment rate, A is area of SSE slip. We use shear modulus $\mu = 30$ GPa.

Figure 3–14a shows the moment-area scaling with the criterion $V_{ave} > V_{pl}$ for 75 events. The moment-area scaling represents a constant stress drop of 0.01 MPa, which is consistent with that inferred from GPS observations in Cascadia and the other subduction zones [Schmidt and Gao, 2010; Gao et al., 2012]. This stress drop is 1-2 orders of magnitudes smaller than those of regular earthquakes [Gao et al., 2012], which supports the hypothesis that the near-lithostatic pore fluid pressure reduce the

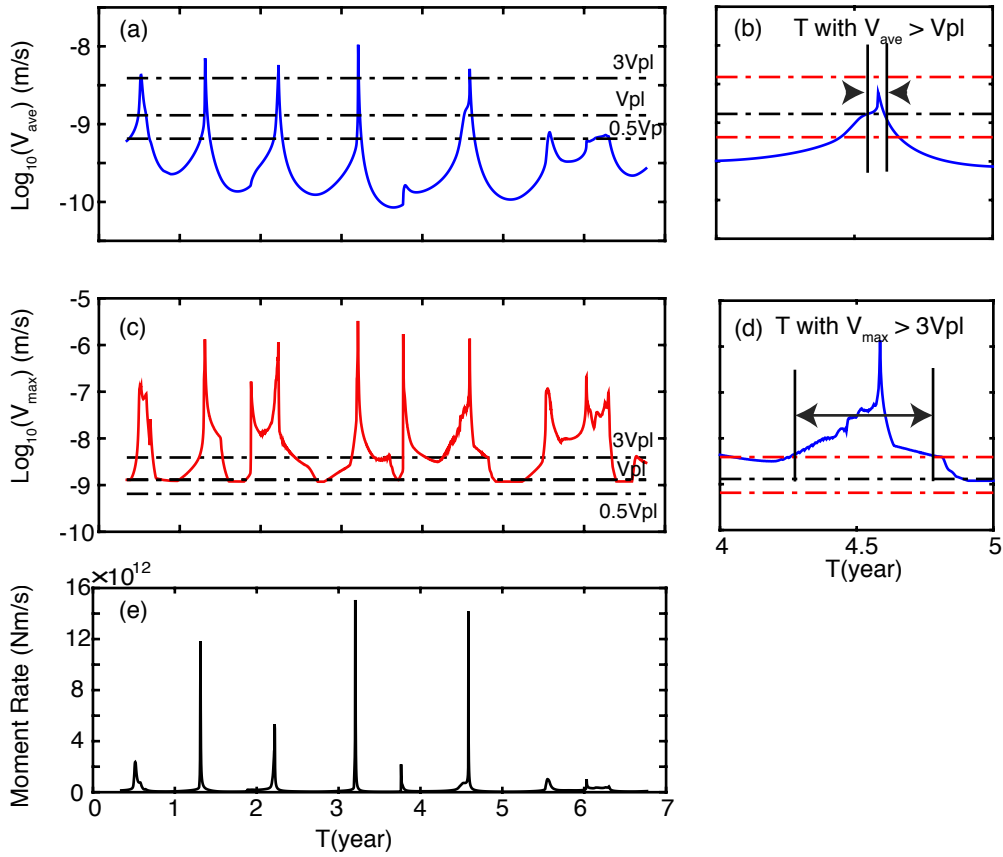


Figure 3–13: (a) Average slip velocity over the entire segments of P2 in 7 years. (b) Duration defined with velocity criterion $V_{ave} > V_{pl}$. The duration is ~ 20 days. (c) Maximum slip velocity of segment P2. (d) Duration defined with velocity criterion $V_{max} > 3V_{pl}$. The duration is ~ 200 days. (e) Cumulative moment rate (Nm/s) of slip patch P2. Each peak represents one episodic SSEs and well correlates to average slip velocity in (a). Dot-dashed lines are $3V_{pl}$, V_{pl} and $0.5V_{pl}$.

effective normal stress on the fault and facilitate the occurrence of slow slip and tremor. When the cut-off velocity is decreased from V_{pl} to $0.5V_{pl}$, the scaling relation and hence the stress drop estimate remains roughly constant (Figure 3–14c), which indicates the stress drop is not sensitive to the velocity criterion at least at the range I tested.

I notice that in the moment-area scaling, the SSEs of larger magnitude trend to have lower stress drops, compared with the smaller magnitude SSEs (Figure 3–14a and c), as a lowered cut-off velocity threshold involves a larger SSE area (or fault dimension)

while the cumulative slip remains relatively constant as it is more influenced by the choices of effective normal stress $\bar{\sigma}$ and characteristic slip distance d_c .

Moment-duration Scaling. Figure 2–14b shows the moment-duration scaling for the same 75 events, with the velocity criterion $V_{ave} > V_{pl}$. Most events have a duration between 0.02-0.2 years. The moment-duration scaling can be best fitted with an exponent of 1.75, although the broad trend roughly follows $M \sim T$. This is consistent with the 1.3-1.85 summarized from a planar-fault model for Cascadia [Liu, 2014] and slightly higher than the 1.3 exponent inferred for SW Japan SSE simulations [Shibazaki et al., 2012].

The moment-duration scaling changes obviously when the cut-off velocity is decreased from $V_{ave} > V_{pl}$ to $V_{ave} > 0.5V_{pl}$ (Figure 2–14b and d). The new criterion ($V_{ave} > 0.5V_{pl}$) makes the duration of each episode longer, due to the average SSE durations in general increase from ~ 0.1 to ~ 0.3 years, but the cumulative moment remains almost constant because majority of the SSE moment is already released at higher slip rates ($V > V_{pl}$). As a result, the scaling factor changes from 1.75 to 1.47 (Figure 2–14d). The general trend is still consistent with the linear scaling inferred from a wide range of slow earthquake phenomena [Ide et al., 2007; Gao et al., 2012].

3.4 Discussion

3.4.1 Effects of the Overlying Continental Lithosphere

The relation between the overlying continental plate and the source process of SSEs has been discussed in previous observational studies [Brudzinski and Allen, 2007; Audet and Burgmann, 2014]. In particular, Brudzinski and Allen [2007] proposed that the observed along-strike segmentation of SSE recurrence intervals in Cascadia may be spatially correlate with the gravity anomalies in Cascadia, due to the difference in density of the overlying plate of Waringellia, Siletzia and Klamath terranes from north to south.

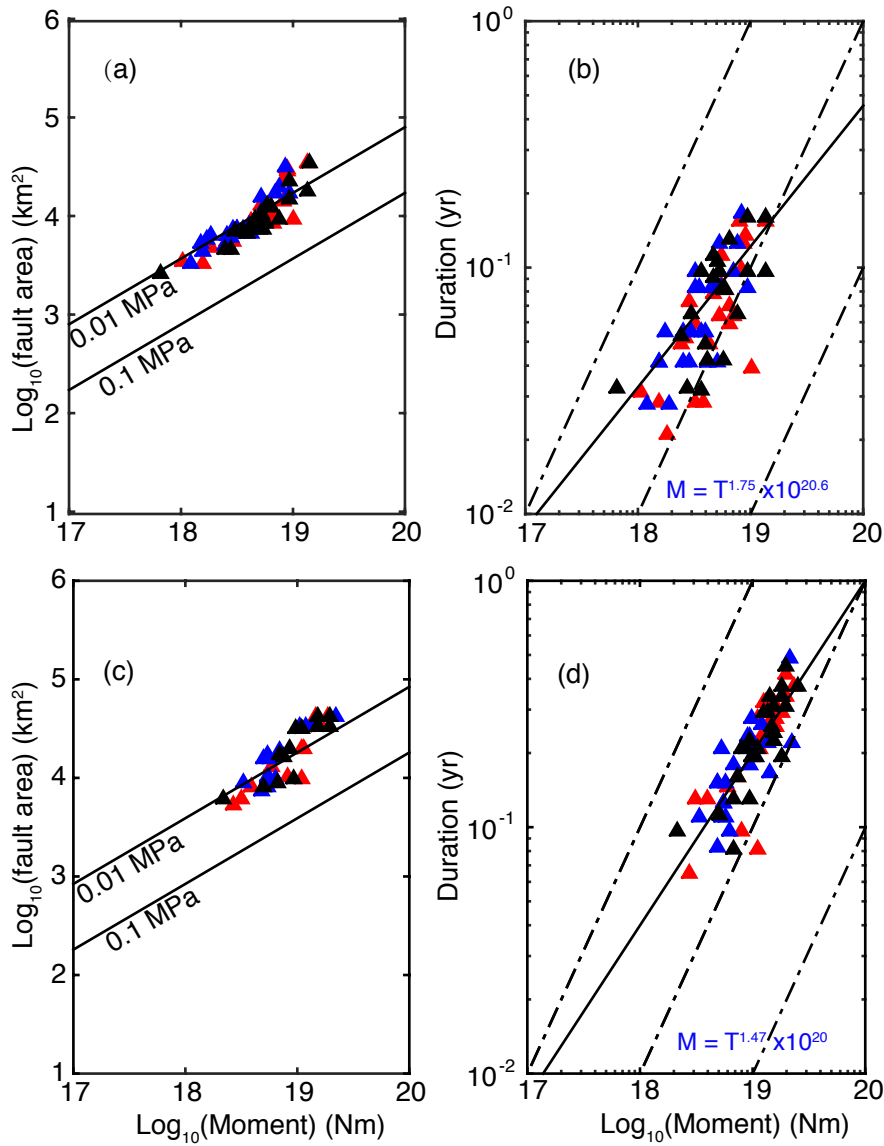


Figure 3–14: (a) Moment-area and (b) moment-duration scaling of 75 events in the three models with velocity criteria $V_{ave} > V_{pl}$. (c) Moment-area and (d) moment-duration scaling with velocity criteria $V_{ave} > 0.5V_{pl}$. Different triangles represent results from different models: Blue, uniform $\bar{\sigma} = 1.0$ MPa; Red: $\bar{\sigma}$ constrained by free-air anomaly and Black, $\bar{\sigma}$ constrained by Bouguer anomaly. Constant stress drops of 0.01 and 0.1 MPa are calculated with circular rupture model and also represent the range of stress drops estimated for Cascadia SSEs [Gao and Schmidt, 2012]. The dot-dashed lines in (b) and (d) shows the inferred linear scaling $M \sim T$ for slow earthquakes [Ide et al., 2007], while our modeling results show deviations from the linear trend at $M \sim T^{1.75}$ and $M \sim T^{1.47}$, respectively.

Our models with $\bar{\sigma}$ constrained by Bouguer and free-air anomalies, which mainly reflect heterogeneous of overlying crusts, demonstrate distinctive characteristics in the along-strike segmentation of SSEs. In Section 3.3.1, the model with free-air anomaly reproduces major cumulative slip beneath Port Angeles with gradual decrease along the strike, which is consistent with the geodetic observations of averaged SSE slip [Schmidt and Gao, 2010]. The model with Bouguer anomaly, however, generates the largest cumulative slip in northern Washington. In Section 3.3.3, both models show significantly smaller misfits to the recurrence intervals than the model with uniform $\bar{\sigma}$, while the model with free-air has a relatively smaller along-strike variation, among different segments. In addition, the synthetic GPS displacements calculated from the models with free-air anomaly also have smaller misfits than the ones with Bouguer anomaly (Figure 3–9 and 3–10). While the model with $\bar{\sigma}$ constrained by Bouguer anomaly can reproduce the varying recurrence intervals equally as well as that constrained by free-air anomaly, the uncertainty in the segmentation of recurrence interval can be large at individual GPS stations, as shown in both the numerical model and the observations Brudzinski and Allen [2007](Figure 4–4). Thus consideration of the cumulative slip pattern is important in analyzing the effect of gravity anomalies. Our numerical modeling results thus suggest free-air anomaly may be a better representation of the influence of the heterogeneities in the overlying continental plate on the source process of SSEs.

What characteristics of overlying plate are reflected in the gravity anomalies that affect the slow slip on the subduction fault? Brudzinski and Allen [2007] have correlated the recurrence intervals from both geodetic and seismic records with along-strike Bouguer anomaly, and suggested that the density and/or permeability in the overlying plate could affect ETS. The seismic imaging at the source depth of ETS have supported this hypothesis, as the V_p/V_s ratio in the fore-arc continent, rather than that

in low-velocity zone of oceanic crust, that is correlated to the recurrence trend of non-volcanic tremors [Audet and Burgmann, 2014]. The correlation is further attributed to the temperature-dependent solubility of silica, which can reduce the permeability in the vicinity of slow slip and tremor and thus elevate the pore pressure level [Audet and Burgmann, 2014]. It has been shown that the pore pressure evolution via long-term fluid-rock interaction [Audet and Burgmann, 2014] or short-term stress perturbations from, such as, near-by slip events [Frank et al., 2015b] or tidal forces [Shen et al., 2005] could affect the ETS recurrence.

Brudzinski and Allen [2007] have reported that the segmentation of ETS is correlated with gravity anomaly, but not quantitatively. Compared with free-air, Bouguer anomalies correct the topography and plate thickness above the equilibrium depth, and highlight the density of lithosphere, which is interpreted to affect the pore pressure via permeability at the ETS source depths [Brudzinski and Allen, 2007]. Our study, however, shows that effective normal stress constrained by free-air anomaly, which reflects the overall gravity including topography, is more related with the cumulative slip distribution of SSEs (Figure 3–6). The non-planar topographic features of the subduction fault not only results in heterogeneities in the normal stress, but also modulates pore pressure via affecting the pore fluid migration. The higher overloading in continent can compress the porosity and push the pore fluid away, resulting in higher effective normal stress and longer recurrence interval. Compared with pore fluid pressure, the fault normal stress is relatively stable over long-term period, and thus may control the first-order characteristics of the SSEs source parameters. The overloading variation along dip may be responsible for the difference between shallow and deep SSEs. Slow slip events inferred from GPS Observations in Hikurangi, New Zealand shows a general trend that shallow SSEs (<15 km) are smaller and shorter, while deep SSEs (20 km) are larger and longer [Wallace and Beavan, 2010].

What's more, it has been revealed that the paleo-earthquake "asperities" on the subduction interface are also correlated with offshore gravity anomalies. Brudzinski and Allen [2007] have pointed that these segments locate immediately landward of the fore-arc basins that interpreted as the manifests of megathrust earthquake asperities. Boyarko et al. [2015] have also reported the along-strike non-volcanic tremor segmentation is also related with megathrust "asperities". These evidences indicate that both the source properties of seismic and ETS zone are largely affected by the overlying continent. The segmentation of ETS downdip on the fault may be important in understanding the segmentation of seismogenic zone and evaluating the potential megathrust disaster.

In addition to the along-strike segmentation, some other characteristics of ETSs are related to the heterogeneities in the overlying continental plate. Audet and Burgmann [2014] propose the observed decreasing V_p/V_s ratio with slab depth is related to the reduction in the permeability controlled by the temperature-dependent solubility of the silica-rich fault gouges, rather than the sole effect of pore fluid supply. Specifically, the silica-rich fluid focusing above the mantle wedge corner and the concentration of quartz precipitation decrease the permeability in the continent fore-arc and may lead to ETS events [Hyndman et al., 2015]. These indicate that the rock composition can affect the recurrence of ETS via modulating the pore fluid. McCrory et al. [2014] show that the depths of fore-arc mantle corner are related with the tremor-distribution-center from Vancouver Island to Oregon, suggesting that fore-arc mantle corner may control the temperature structure and fluid migration at the depths of ETS events. However, compiling the velocity structure of SSE source region from teleseismic observations of six subduction zones, Audet and Kim [2016] suggest that the near-lithostatic pore pressure is a necessary but insufficient condition for slow slip phenomena. The environment in the vicinity of slow slip and non-volcanic tremors is complex and thus many other

factors, e.g., composition, dehydration rate, permeability and rheology of the overlying continent must be considered [Audet and Kim, 2016].

3.4.2 Creeping in Oregon

In Section 3.3.1, I have shown that there is a discrepancy between our modeled SSE cumulative slip and the GPS inversions in Oregon. This discrepancy persists in all the three models regardless of the along-strike variation in effective normal stress. However, a numerical test with a 20% reduction in the velocity-weakening value (changing $a - b$ from -0.003 to -0.0025) this discrepancy only results in a $\sim 6\%$ reduction in the cumulative slow slip, suggesting the discrepancy is not entirely due to the choice of rate-state frictional parameters (Section 3.3.2).

The along-strike variation in the fault locking along Cascadia margin has been realized for a long time [Hyndman and Wang, 1993]. Recently, Schmalzle et al. [2014] report the long-term plate locking model and total cumulative slip (from 2005.5 to 2011.0) of SSEs on the entire Cascadia margin, by incorporating the PBO (Plate Boundary Observatory) geodetic stations. They find that the long-term plate locking depth is shallower in Oregon (43° - 46° N), with a wider transition zone (Figure 3-2a), compared to Washington and Vancouver Island [Schmalzle et al., 2014]. There are reduced inter-seismic uplift and SSE cumulative slip in Oregon [Schmalzle et al., 2014]. Paleo-elevation study has revealed smaller coseismic subsidence during historical megathrust earthquakes in Oregon, than that in Washington [Leonard et al., 2010]. Schmalzle et al. [2014] attribute this reduced coseismic and aseismic slip to a fraction of partial creeping on the fault. They propose that the low permeability of the Siletzia terrane may prevent fluid migration and increase fluid supply, and hence may increase the partial creeping in Oregon. In addition, the segmentation of SSEs shown in Figure 4-4d exhibits an overlapping region between the two major segments reported by Schmalzle et al. [2014]. The range of this overlapping region is also where reduced slip

are observed and may indicate less firmly “locked” status during inter-SSE period, that slow slip of adjacent segments can propagate across the segmentation boundaries.

However, when the inter-SSE GPS displacement is decomposed into separate tectonic loading and strain release phases, Frank [2016] demonstrates that smaller SSEs with less than 1 mm of surface displacement occur more frequently than previously reported SSEs in Cascadia and Guerrero, Mexico. The plate coupling rate approaches 100% as various cycles of SSEs are removed from the GPS displacement time series, suggesting that the ETS depth range is likely to be strongly coupled, which is the prediction from our current model set up as the SSEs arise and maximum slip is accumulated in the velocity-weakening regime. Thus, the discrepancy in the slow slip distribution in Oregon needs to be further investigated by taking possible smaller, previously undetected, SSEs into the consideration of total slip budget.

3.4.3 Tremorless Slip

The synchronized occurrence of slow slip events and tremors in Cascadia and Nankai has been observed for more than a decade [Obara et al., 2004; Wech et al., 2009; Bartlow et al., 2011]. It has been hypothesized that tremor and slow slip are the seismic and geodetic manifestations of shear slip on the transitional fault [Shelly et al., 2006] and tremor can be used as a location proxy for slow slip currently below geodetic detection threshold [Wech and Creager, 2011]. However, this hypothesis about the spatial and temporal coincidence of slow slip and tremor may be challenged, as the appearance of tremorless slow slip between two adjacent ETSs in June and August 2011 in central Cascadia (between 46°N and 47°N) [Wech and Bartlow, 2014]. At this exact locus, where the tremorless slip appears, the previous 2009 ETS event initiates and migrates bilaterally [Bartlow et al., 2011]. Wech and Bartlow [2014] suggest that the synchronized appearance of tremor is actually sensitive to the slip rate of SSEs, and thus fluctuates among different episodes.

The deeper inter-ETS tremors are spatio-temporally related with the low-rate slip of the pre-SSE stage in the modeled SSEs, which indicates a down-to-up evolution prior to the major stage of SSEs [Li and Liu, 2016]. In this study, I further demonstrate that the low-rate slip can also appear at the position where W/h^* is small (46.5° - 47° N in Figure 3-4c), with tiny cumulative slip (~ 1 cm), when the nearby segments slip during major SSE episodes. These low-slip-rate segments act as 'bridges' between successive episodes, and may be corresponding to the tremorless slip with insufficient rate to drive tremors.

3.5 Conclusions

Along-strike segmentation of slow slip events (SSEs) and non-volcanic tremors in Cascadia may reflect heterogeneities of subduction slab or the overlying continental lithosphere. However, the nature behind this segmentation is not fully understood. I develop a 3-D episodic SSE model for northern and central Cascadia, incorporating both seismic and geodetic observations to constrain the heterogeneities in the megathrust fault properties. The 6-year automatically detected tremors are used to constrain the rate-state friction parameters. The effective normal stress at SSE depths is constrained by along-margin free-air and Bouguer gravity anomalies. The along-strike variation in long-term plate convergence rate is also taken into consideration. I present modeling results from three scenarios where the along-strike distribution of the effective normal stress is assumed to be (1) uniform, (2) constrained by the Bouguer anomaly and (3) constrained by the free-air anomaly observed along the margin. I calculate the recurrence interval and cumulative slip of the modeled SSEs in each scenario, and compare the modeled segmentation patterns of SSE recurrence interval and cumulative slip to GPS inversions. In this study, the major conclusions are:

- 1) Simulation results show five segments of \sim Mw6.0 SSEs spontaneously appear along the strike, correlated to the distribution of tremor epicenters. The cumulative

slip of each SSE segments are mainly controlled by the frictional property (velocity-weakening) on the fault.

2) The segmentations of recurrence intervals of models constrained by both types of gravity anomalies are equally comparable to recurrence in GPS observations. However, the model constrained by free-air anomaly does a better job in reproducing the cumulative slip as well as more consistent surface displacements with GPS observations.

3) Individual slow slip events can still propagate across the boundaries, which may cause interactions between adjacent SSEs, as observed in the time-dependent GPS inversions. The modeled along-strike segmentation only represents the averaged slip release over many SSE cycles, rather than permanent barriers. In addition, the moment-duration scaling is sensitive to selection velocity criteria. Hence the detection ability of the current GPS network should be considered in the interpretation of slow earthquake source parameter scaling relations.

4) The source parameter scaling is consistent with observations. However, the scaling relation is sensitive to the cutoff velocity, or current detection threshold.

Appendix A: A Hybrid Fitting of Bouguer Anomaly:

In the main text, I approximate the along-strike profile of Bouguer and free-air anomalies with polynomial and segmented-line fits, respectively (Figure). The polynomial fit is smoother than the segmented-line and results in smaller along-strike variations of recurrence interval (Figure 7). However, using polynomial fit cannot fit the main feature of free-air, but not Bouguer anomaly, as shown in Figure and b. Here I make another test, Model (4), with effective normal stress approximating a hybrid fit of Bouguer anomaly (Figure 3–15a and b). We fit Bouguer anomaly with 8th-order polynomial line and manually change the negative peak between 47.2°N and 48.1°N (solid line in Figure 3–15b). The effective normal stress is set between 1.0-1.5 MPa approximating this fit. We simulate 10 years for model (4) and compare the cumulative slip pattern along the strike in Figure S2a and S2b with those in Figure 5a and 5b, respectively.

The map view of cumulative slip and its profile along the strike are shown in Figure 3–15a and b . The maximum cumulative slip of P1-P5 is 1.9, 3.0, 4.0, 2.0, 1.8 cm, respectively. The maximum cumulative slips beneath Port Angeles (P2) and southern Washington (P3) are consistent with the result of model (2), shown in Figure 5a. The smaller cumulative slip in P2 comes from the negative peak in Bouguer anomaly. This result here support our conclusion in Section 3.1 that the model with the effective normal stress constrained by Bouguer anomaly cannot reproduce the slip pattern inferred from GPS inversion. The cumulative slips beneath Port Angeles (P2) and southern Washington (P3) are consistent with those from our segment-line fit, except for a slight southward shift of the center of P3. This shift is due to the more gradual effective normal stress changes between $\sim 46\text{N}$ and 47.3N . Additionally, maximum cumulative slips

in P4 and P4 are also reduced a little in hybrid-fit, as the effective normal stress level is lower in hybrid-fit (solid line in Figure S3c) than segment-fit (dashed line).

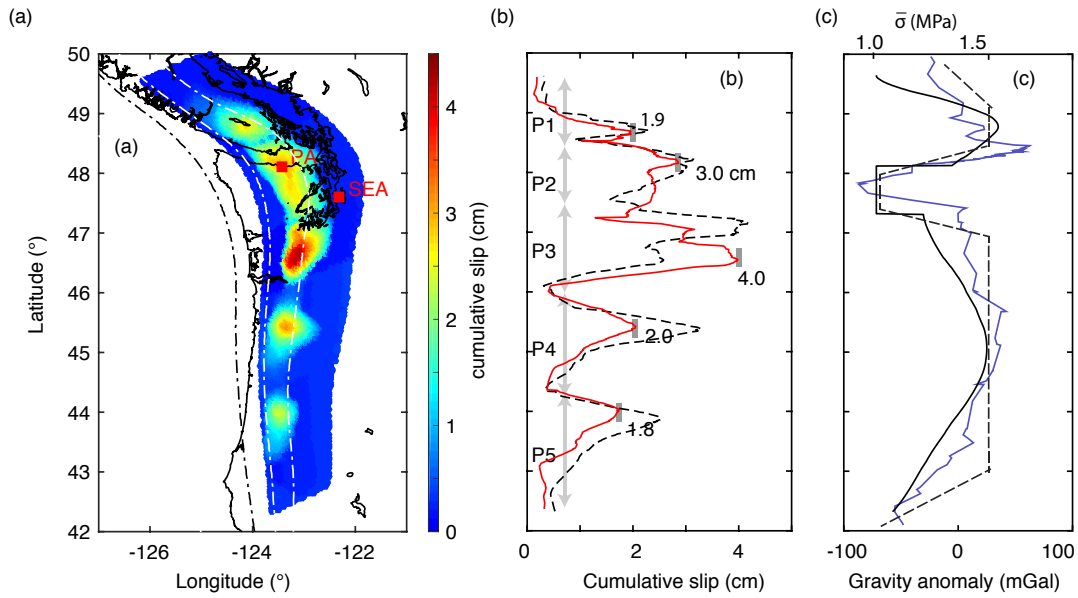


Figure 3–15: (a) Cumulative slip of model (4) with $\bar{\sigma}$ approximating a hybrid-fit of Bouguer anomaly. Five patches are defined as P1-P5 in (b). (b) Cumulative slip along the contour of $a - b = -0.0025$. The maximum cumulative slip in each of the five segments is 1.9, 3.0, 4.0, 2.0 and 1.8 cm, respectively. The dashed line is cumulative slip profile of segmented-line fit of Bouguer anomaly (c) Bouguer anomaly of 35 km depth contour (blue) and its hybrid-fit (solid black line). The dashed line is the segmented-line fit.

CHAPTER 4

Stress Rotation Across the Cascadia Megathrust Requires a Weak Subduction Plate Boundary at Seismogenic Depths

4.1 Introduction

The Cascadia subduction zone has experienced the repeated ruptures of large M8+ and M9+ earthquakes inferred from the geological records [Atwater et al., 1995; Goldfinger et al., 2012]. Yet since modern seismic networks have been installed the thrust interface is essentially seismically “quiet” except for a few small earthquakes [Tréhu et al., 2015]. The only significant thrust earthquake, a Mw7.1, occurred on April 1992 at Cape Mendocino near the triple junction, where the Gorda, North American and Pacific Plates meet each other. However, it ruptured a shallow dipping fault within the continental crust rather than on the subduction interface [Oppenheimer et al., 1993; Murray et al., 1996]. The nearly complete lack of moderate thrust earthquakes on the plate interface is surprising compared to the behavior seen in all other subduction zones. One explanation would be that despite the 300+ years since the last M9 rupture and the geodetic observations of current stress accumulation [Schmalzle et al., 2014], perhaps the stress levels are extremely uniform along the megathrust and still below the failure criteria.

Global surveys indicate that subduction interfaces are weak faults in a low-stress environment. In the shallowest regions, observations of high fluid pressures [Tobin and Saffer, 2009] and low friction coefficients of direct samples [Fulton et al., 2013] indicate extremely weak faults (effective friction coefficient <0.1). At the depths where great earthquakes usually rupture (5-40 km), global studies infer the direction of greatest compression generally lies at a moderate angle (45-60°) to the fault surface favouring

a “weak fault in a weak crust” model [Hardebeck, 2015]. However, the general increase in earthquake stress drop from 5 to 30 km depth [Bilek and Lay, 1999] and the strong high-frequency radiation from the deeper parts of large ruptures [Lay et al., 2012] indicates that stresses increase at least somewhat with depth along the fault compared to the shallowest regions. Further downdip, the fault is inferred to be extremely weak from various properties of Episodic Tremors and Slip events (ETS) [Liu and Rice, 2005; Rubinstein et al., 2007]. While the relative variation along the dip of the subduction zone is clear it has been difficult to place absolute constraints on the evolution of strength with depth along the interface.

The Gorda Plate subducts beneath North American Plate at ~ 5 cm/yr in the direction of N115°E. However, the megathrust region is unusual in that at regional scales the direction of the maximum compression is almost parallel to the trench, orthogonal to the subduction direction [Schwartz and Hubert, 1997; Wada et al., 2010]. The trench-parallel compression reflects the northward movement of the Pacific Plate and its collision with the Gorda Plate [Silver, 1971]. Slip along the subduction interface under these stress orientations implies that this interface is very weak [Schwartz and Hubert, 1997; Zoback and Townend, 2001]. The static force balance of the landward part of accretionary wedge also requires a small friction coefficient on the thrust interface [Wang and He, 1999]. Heat-flow measurement that represents coseismic friction averaged over the fault shows that the fault strength could peak as high as 70 MPa at 20-30 km depth [Wang et al., 1995; Gao and Wang, 2014]. Geodynamical modeling studies have found that the time-averaged shear stress on the thrust interface is quite low around 10-15 MPa [Geist and Yoshioka, 1996].

In contrast to the thrust interface, the Gorda Plate operates at high-stress levels with a high rate of seismicity, due to the high internal deformation [Chaytor et al.,

2004]. The North-South compressional stress field routinely generates Mw6.5+ strike-slip earthquakes rupturing either the Mendocino transform fault or within the Gorda lithosphere (Figure 4-1), and these events show the highest levels of radiated energy for their seismic moment (apparent stress) for shallow earthquakes globally [Choy and McGarr, 2002]. These high apparent stresses are consistent with the predictions of strength envelopes based on laboratory experiments which indicate the strength of the Gorda Plate mantle is at least 400 MPa [Choy and McGarr, 2002]. In the MTJ region, this intraplate seismicity continues into the subduction zone with high stress drop ruptures occurring in the subducting mantle just a few km below the thrust interface [Wei and McGuire, 2014; Chen and McGuire, 2016]. While no event is unambiguously associated with the thrust interface in this region, the small earthquakes within a few km of the interface exhibit stress drops a factor of 10 or more lower than those in the subducting mantle [Chen and McGuire, 2016].

Despite the great effort spent investigating subduction zones, there are very limited constraints on the stress state on the plate boundary fault at the depth of megathrust earthquakes. In this chapter, I present a high-resolution inversion for the principal stress orientations of both above and below the thrust interface in the southern Cascadia subduction zone, using focal mechanisms from historical catalogues and Cascadia Initiative OBS arrays. I find a significant rotation of the stress field over a distance of at most 10 km across the thrust interface. Unfortunately, inversions of focal mechanisms do not directly constrain the absolute magnitudes of the stress tensor and it is not possible to obtain borehole samples or stress measurements at seismogenic depths (~ 20 km). Instead, to constrain the absolute level of strength of the plate boundary, I present a new algorithm that utilizes the stress rotation and convex optimization techniques to constrain the range of possible stress tensors that may exist near the plate

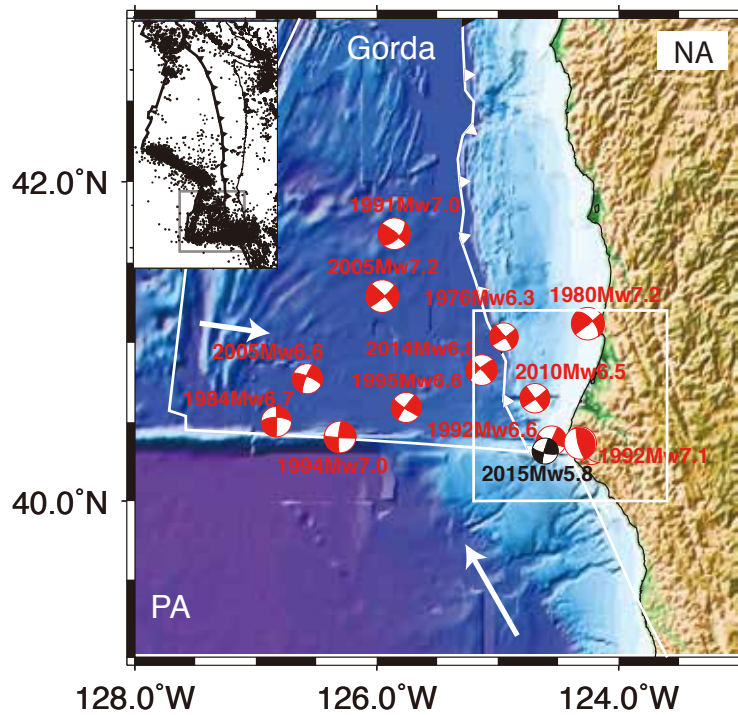


Figure 4–1: Map showing topography and seismicity distribution (insert) in Mendocino Triple Junction (MTJ). Historical events with magnitude $M_w 6.5+$ from US Geological Surveys (USGS) catalogue are shown in red. Plate boundaries, including the ridge of Gorda Plate, the Mendocino transform fault and the San Andreas Fault, are from the USGS. Relative plate motions are shown in arrows ($N27.5^\circ W$ between PA and NA). The only thrust event that has been recorded by the seismometers is the 1992 $M_w 7.1$ Cape Mendocino earthquake. Beachball in black shows the Jan 28th, 2015 $M_w 5.7$ earthquake that has been captured by the Cascadia Initiative OBS array. White box shows the study region.

boundary fault. My simplified three-layer model demonstrates that the plate boundary layer is a weak zone with differential stress no more than ~ 50 MPa and that the range of permissible stress tensors corresponds to effective friction coefficients between ~ 0 and 0.2, again demonstrating the weakness of the fault in an absolute sense. The low effective friction coefficients indicate either a present of near-lithostatic pore fluids or weak fault gouge materials.

4.2 Focal Mechanisms and Principal Stress Inversion

4.2.1 Catalogue

The Cascadia Initiative Expedition (CI) deployed an array of ocean bottom seismometers (OBSs) along the entire Cascadia margin from 2011 to 2015 [Toomey et al., 2014]. Both the CI year 2 (August 2012-April 2013) and year 4 (August 2014-July 2015) deployments included a dense OBS array (10 km spacing) covering the locked portion of the thrust interface in the Mendocino Triple Junction region (Figure 4-2). I created an earthquake catalog for moderate ($M_L \geq 2.0$) earthquakes using the CI year 4 data and also incorporated the earthquake catalog from the CI year 2 dataset built by [Chen and McGuire, 2016]. Both use manually picked P- and S-arrivals and P-wave polarities. The CI year 4 focused array deployed 21 OBSs in the MTJ region, including 10 from WHOI (Woods Hole Oceanographic Institution), 3 from SIO (Scripps Institution of Oceanography) and 8 from LDEO (Lamont-Doherty Earthquake Observatory), sampled at 50, 50 and 125 HZ, respectively. The inland stations of the Northern California Seismic Network (NCSN), the Plate Boundary Observatory (PBO) borehole and a temporary array using portable instruments the Portable Array Seismic Studies of the Continental Lithosphere (PASSCAL) network are also used. The distribution of the OBS and inland stations are shown in Figure 4-2.

To build the catalog, I first detect and locate the earthquakes based on STA/LTA ratios and the IASP91 velocity model in the Antelope software package. Then I manually adjust the arrivals and pick the P-arrival polarities for the earthquakes of $M_L \geq 2.0$ on waveforms filtered between 1-15 Hz. The hypocenters of the earthquakes are relocated using the *TomodD* software package [Zhang and Thurber, 2006] with the 3-D P-velocity model of Hole et al. [2000]. The uncertainty of the relocated epicenters is about 2-3 km for most events.

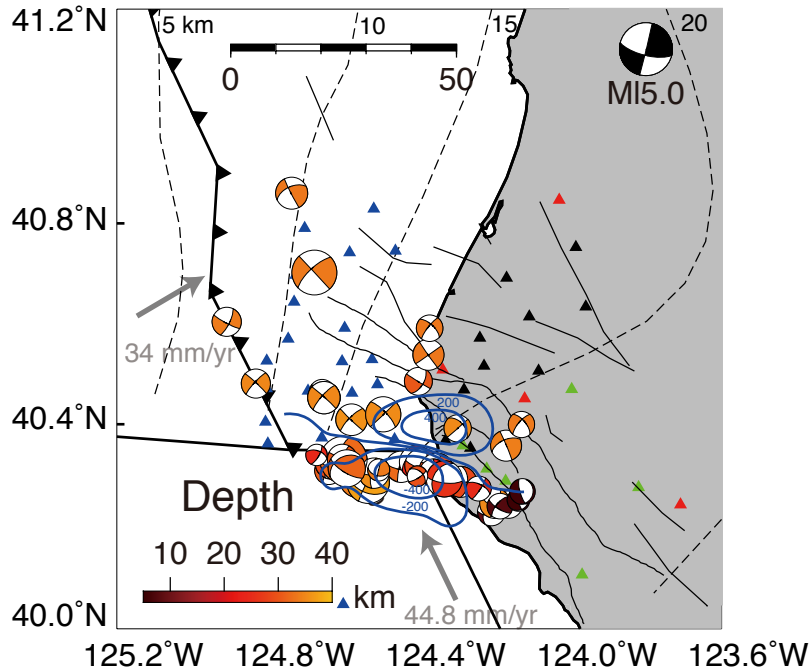


Figure 4-2: Map showing seismic stations used in this study and the aftershock sequences. The Cascadia Initiative expedition (CI) OBS array is shown in blue triangles. Inland seismic networks include the NCSN (red), PBO (green) and PASCAL (black). Coulomb stress changes of the $M_w 5.7$ mainshock on a 13° dipping thrust fault at 20km-depth is shown in contours (200 kPa interval), ranging from 0 to 400 kPa. Beachballs show focal mechanism of 40 earthquakes from January 29th, 2015 to July, 2015. The size of each earthquake is scaled by the upper-right focal mechanism of $M_L 5.0$. Quaternary faults in northern California are from USGS (<https://earthquake.usgs.gov/hazards/qfaults/>). Black dashed lines are depth contours from 5 km to 20 km.

4.2.2 Focal Mechanism

Fault-plane Solution. The fault-plane orientations and slip directions of earthquakes can provide important information about the fault structure at depth and the stress field in which the earthquakes occur [Hardebeck and Shearer, 2002]. The fault plane solutions were obtained using the grid-search method by minimizing the misfits

between the observed and theoretical first P-polarities. To invert for the best-fit fault plane solution, I use the grid-search program package, *HASH* [Hardebeck and Shearer, 2002]. *HASH* accounts for the possible errors from the velocity model, hypocenters, and P-wave polarity picks resulting in a set of accepted fault planes that are then averaged to get the best-fit focal mechanism [Hardebeck and Shearer, 2002].

Quality Estimation. *HASH* is based on the inversion algorithm, *FPFIT* software package, which was first built by Reasenber and Oppenheimer [1985]. [Reasenber and Oppenheimer, 1985] defined a weight based on the amplitude $A(j, k)$:

$$w_t^{j,k} = |A(j, k)|^{0.5} \quad (4.1)$$

Two indexes are used to estimate the qualification of focal mechanisms: *stdr* and *mfrac*. The *stdr* quantitatively estimates the station coverage in term of P-arrival-polarity radiation pattern [Reasenber and Oppenheimer, 1985]. *stdr* is defined as :

$$stdr = \frac{\sum_{k=1}^N (w_o^{j,k} w_t^{j,k})}{\sum_{k=1}^N w_o^{j,k}} \quad (4.2)$$

where N is number of P-arrival-arrival polarity. $w_o^{j,k}$ and $w_t^{j,k}$ are the observed and theoretical P-arrival-polarity of j th event at k th station. *stdr* is less robust when less than 0.5, as more stations lie near to the nodal planes.

The fraction of misfit *mfrac* shows the different between theoretical and observed P-arrival-polarity radiation. *mfrac* is defined by Reasenber and Oppenheimer [1985].

$$mfrac^j = \frac{\sum_{k=1}^N |p_o^{j,k} - p_t^{j,k}| w_t^{j,k} w_o^{j,k}}{\sum_{k=1}^N w_o^{j,k} w_t^{j,k}} \quad (4.3)$$

where $p_o^{j,k}$ and $p_t^{j,k}$ are the observed and theoretical P-polarity of j th event at k th station.

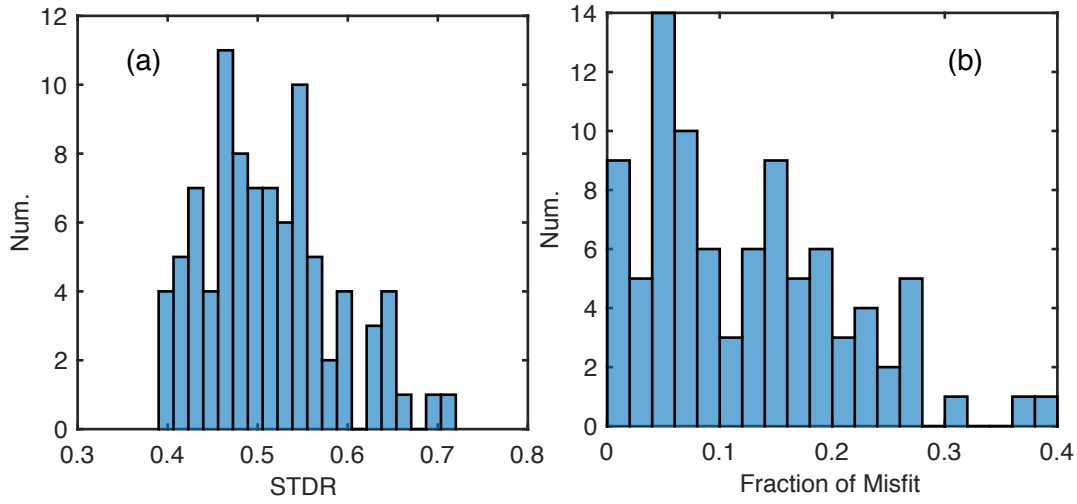


Figure 4–3: Graphs showing histogram of (a) station coverage index *stdr* and (b) fraction of misfit *mfrac* of the 91 earthquakes that are obtained in CI year 2 and year 4 .

I obtain 91 focal mechanisms of body magnitude between M_L 2.0 and 5.0 for CI year 2 and year 4 totally. The histograms of *stdr* and *mfrac* are shown in Figure 4–3. The CI OBS array complements the azimuthal coverage of the existing inland stations (Figure 4–2) and thus most of our events have *stdr* 0.5. There are 41 events that also appear in NCEDC catalogue. Our focal mechanisms show a consistency with the Northern California Earthquake Data Center (NCEDC) catalogue. The comparison of focal mechanisms is shown in Figure 4–4.

4.2.3 Principal Stress Inversion

Focal mechanisms constrain the range of orientations of the principal stress directions that would promote earthquake initiations on the two possible fault planes. The compression (P-) or extension (T-) axes of an individual focal mechanism are not sufficient to determine the background stress tensor, as the faults are not necessarily

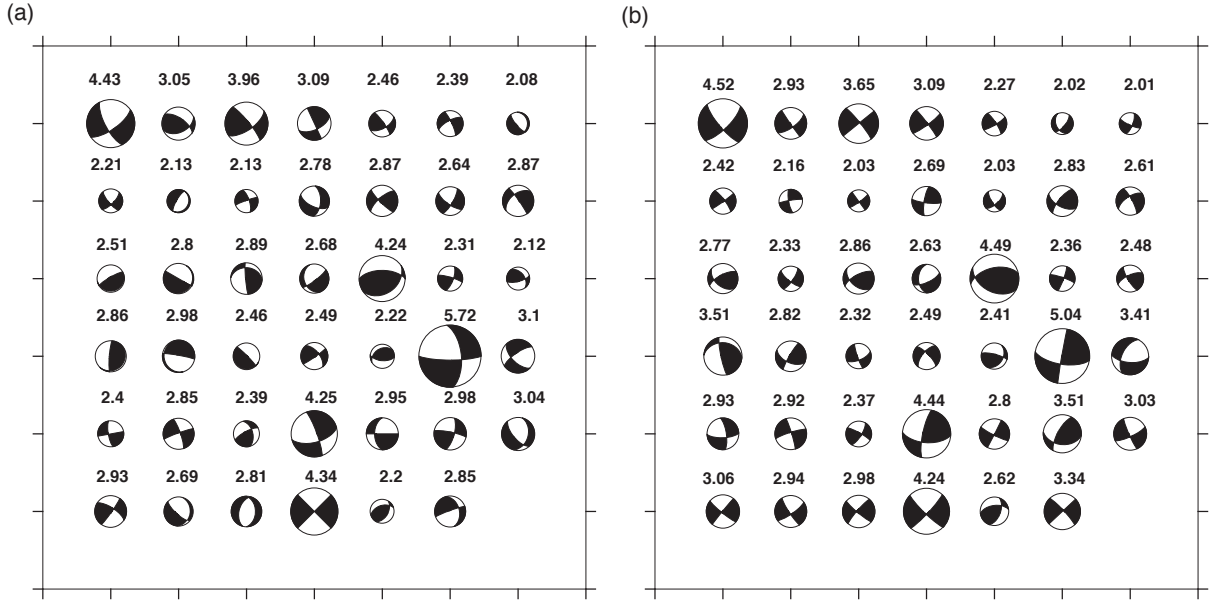


Figure 4-4: Graphs showing focal mechanisms from (a) NCEDC catalogue and (b) our OBS obtained catalogue, respectively. The Richter magnitude (M_L) is attached to each ball. The event list is shown in Table 4-3.

optimally orientated, especially at the shallow depth [McKenzie, 1969]. Michael [1984] established an algorithm to invert for the stress tensor by minimizing the difference between the unit shear tractions and slip vectors for a dataset of focal mechanisms in a region. As the magnitude of shear traction is not involved, only a relative magnitude ratio R , defined as $\frac{\sigma_1 - \sigma_2}{\sigma_1 - \sigma_3}$, is obtained along with the orientations of the three principal stresses.

For the j th event, the stress tensor satisfies the following relation from [Michael, 1984]:

$$|\tau|^j = \underline{\underline{A}}^j \underline{\underline{\Sigma}} = |s|^j \quad (4.4)$$

where τ^i and s^j are the unit shear traction and slip. $\underline{\Sigma}$ is a vector of the 5 independent stress components and \underline{A}^j is a matrix determined from the orientation of j th nodal plane. A damped linear inversion can be applied to a set of earthquakes to determine [Michael, 1987; Hardebeck and Michael, 2006]. The principal stress inversion is reliable when the dataset includes a diverse set of focal mechanism orientations [Michael, 1987].

To estimate the uncertainty of the stress inversion results, a bootstrap technique is used to account for the errors in the focal mechanisms [Michael, 1987; Hardebeck and Michael, 2006]. In each bootstrap trial, a subset of focal mechanisms is randomly resampled from the original dataset. To address the fault plane ambiguity of focal mechanism, each of the two nodal planes has a 50% chance to be picked in each trial. The closest 95% bootstrap results to the preferred solution, determined by the normalized scalar dot of two tensors $\frac{\sum_i^3 \sum_j^3 \hat{\sigma}_{ij} \sigma_{ij}^{boot}}{[\sum_i^3 \sum_j^3 (\hat{\sigma}_{ij})^2]^{0.5} [\sum_i^3 \sum_j^3 (\sigma_{ij}^{boot})^2]^{0.5}}$, are used to determine the confidential interval of the stress axes and R -ratio values. Basically, the bootstrap number should be 20 times the input data [Efron and Tibshirani, 1986].

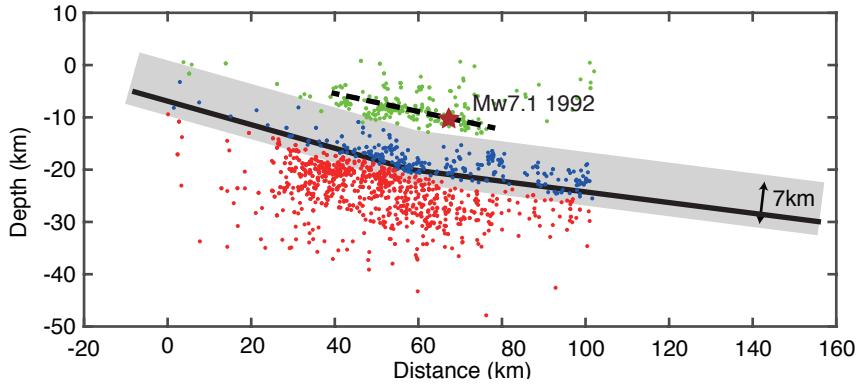


Figure 4-5: West-to-east cross-section of the hypocenters and assigned depth groups. The earthquake hypocenters are from NCEDC catalogue (1980-2015) and that obtained from OBS arrays (2012-2013 and 2014-2015). Events in the continental crust (green), plate boundary (blue) and oceanic mantle (red) are distinguished by perpendicular distances to the fault interface given by McCrory et al. [2012]. The dashed line is the assumed fault plane for the 1992 Mw7.1 Cape Mendocino event.

4.2.4 Binning Strategy

I use $M_L \geq 2.0$ earthquakes from both NCEDC focal mechanism catalogue (from 1980 to 2016) and OBS data (Figure 4–6) to invert for the principal stress in the MTJ region. Maps of the focal mechanisms in the different depth groups are shown in Figure 4–6. I use a MATLAB toolbox, *MSATSI*, which is built upon the foundation of the previous SATSI method [Hardebeck and Michael, 2006] to perform the inversion. To stabilize the inversion, each bin should contain at least 10 events (19-295 in the inversions actually).

In the principal stress inversions, a spatial binning strategy is used to account for the variation of the tectonic stress field [Hardebeck and Hauksson, 1999; Townend and Zoback, 2004]. The binning should consider both the tectonics features and spatial resolution. To avoid inappropriate gridding and obtain a reliable spatial resolution, I perform a grid-search for the bin boundaries and use the standard deviation of the bootstrap results to choose both the lateral and vertical binning sub-area in the study region.

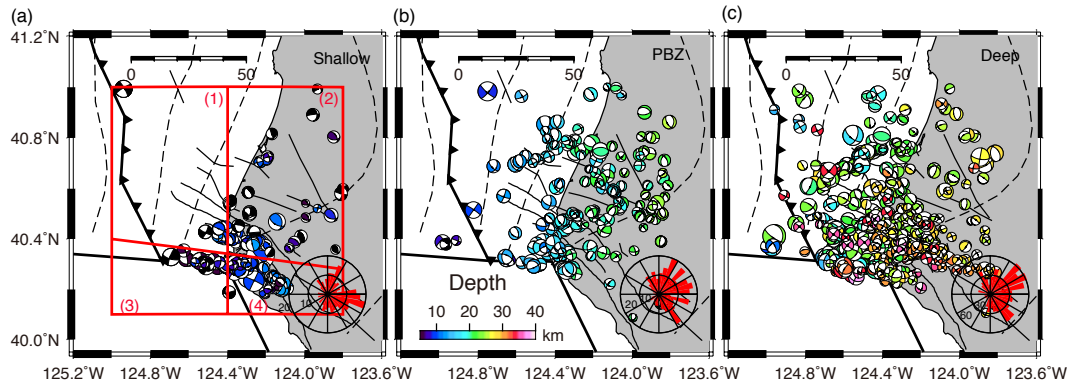


Figure 4–6: Mapview of distribution of focal mechanisms in (a) shallow crust, (b) PBZ and (c) deep mantle group, which are shown in Figure 4–5. Polar histogram shows the strike orientations of focal mechanisms.

Depth Group. In Cascadia, the plate interface is seismological “quite” [Tréhu et al., 2015]. In contrast to other subduction zones, there is no enough interplate earthquakes to precisely determine the slab geometry [Wang and Tréhu, 2016]. For example, in the northern Cascadia, there is a discrepancy up to 10 km of the plate interface inferred from earthquake relocations [McCrorry et al., 2012] and teleseismic reflection [Audet et al., 2009]. In Mendocino region, there is a shallow double-seismic zone that is believed to outline the oceanic crust [Wang and Rogers, 1994]. The slab interface that constrained by this double-seismic zone [McCrorry et al., 2012] is about 10 m deeper than the thrust fault inferred from Mw7.1 Cape Mendocino earthquake [Oppenheimer et al., 1993; Murray et al., 1996]. The velocity structure obtained from seismic reflection shows that there is a high-velocity layer that is below the thrust fault, indicating an oceanic crust [Henstock and Levander, 2003]. What’s more, a tightly clustered group of crustal earthquakes lies within the thrust fault [McCrorry et al., 2012] (Figure 4–5).

Thus, I define three depth groups adjust to the slab model given by McCrorry et al. [2012], with the goal of isolating the stress fields in the overriding plate and the seismically active part of the subducting slab without contaminating either with events close to the plate boundary. The three depth groups are (1) the Plate Boundary Zone (PBZ) <6 km above and <1 km below the McCrorry interface which likely includes some of the subducted oceanic crust (2) the overriding plate crust, >6 km to the plate interface and (3) the subducting mantle: >1 km below the interface (Figure 4–5). I tested several definitions of the slab groups defined at different depths and/or thicknesses. Alternative definitions other than the preferred one resulted in crustal stress tensors were contaminated by the deeper events (see Appendix A).

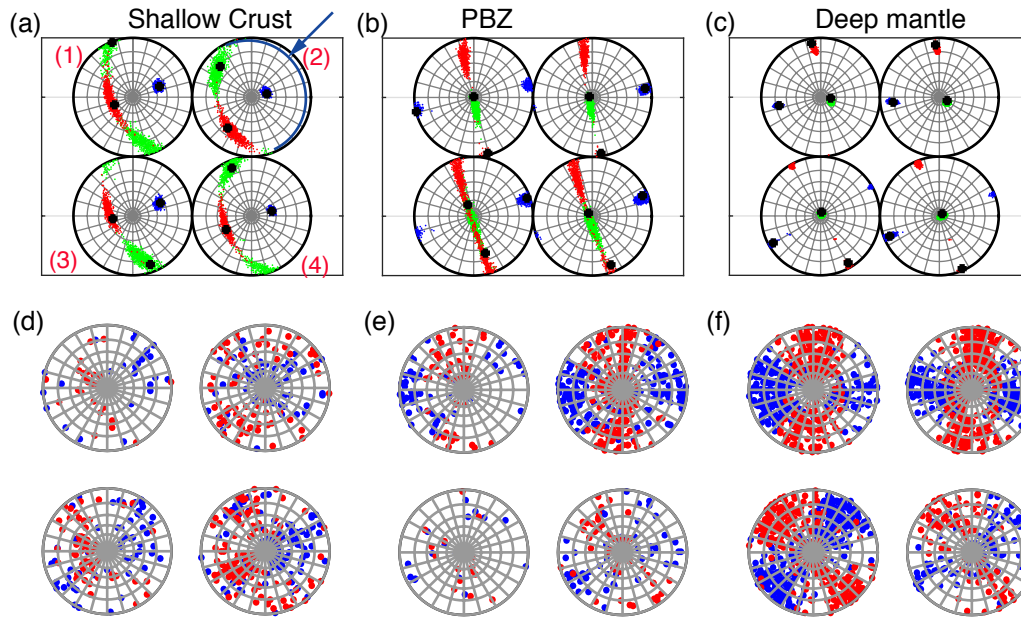


Figure 4-7: Stress inversion results for (a) shallow crust, (b) PBZ and (c) deep mantle are shown in lower-hemisphere projection. The cloud of dots shows the distribution of bootstrap resampling results. Red: σ_1 , green: σ_2 and blue: σ_3 . Subregion (1)-(4) are shown in Figure 4-6a. Blue arc is the subducting fault plane dipping at 13° . P-(red) and T-(blue) axes for focal mechanisms in (d) crust, (e) PBZ and (f) mantle are shown in lower-hemisphere projection.

In Figure 4-5, the majority of earthquakes in the overriding crust group cluster on a shallow dipping fault plane defined by the hypocenters and fault slip inversion of the 1992 Mw7.1 Cape Mendocino earthquake [Oppenheimer et al., 1993; Murray et al., 1996]. The deeper group has the highest rate of seismicity, most of which is likely located in the mantle of the subducted plate. The PBZ group includes earthquakes that are likely close to the thrust interface.

The focal mechanism distributions in the crust, the PBZ and the oceanic mantle are shown in Figure 4-6a-c. P-axes of the PBZ and the mantle focal mechanism are consistent with the direction of the Pacific movement, as shown in Figure 4-7d-f. The PBZ group has similar orientations of P- and T- to those in the subducted mantle group, possibly due to the uncertainty of earthquake depths (Figure 4-7e and f).

Lateral Subregions. Laterally, I use four sub-regions for each depth group (12 total inversion bins). Considering the geologic features, I separate the earthquakes close to the Mendocino transform fault from the subduction earthquakes to the north with a linear boundary from (125°W, 40.4°N) to (123.8°W, 40.26°N), as shown in Figure 4–8a. I apply a grid-search over the position of the NS bin boundary, from 124.5°W to 124.1°W (Figure 4–8a). I adopt 1000 bootstraps for each test (Figure 4–8b-f).

The bootstrap results of each test follow a normalized distribution, as shown in Figure 4–9a. To quantify the performance of each binning choice, I calculate the standard deviation for the trend (Figure 4–9b) and plunge of (Figure 4–9b) in each sub-region. Test 2, which put NS boundary at 124.4°W, has the smallest deviation for the four subregions. Thus the NS-trend boundary at 124.4°W ideally separates the dataset into two groups with well-constrained stress orientations.

4.2.5 Stress Orientations in Overlying Crust and Subducting Mantle

In the overriding continental crust, σ_1 orientates sub-parallel to the plate convergence direction, with the trend moderately varying between N140°W and N90°W in the four sub-regions ((1)-(4) in Figure 4–7a). σ_1 plunges vary slightly between 30° and 45° trenchward. σ_3 plunges landwards at an angle >30° and at 60° in sub-region (2). The continental stress is non-Andersonian as the shallow pre-existing faults can rupture in response to a non-optimally oriented driving force [McKenzie, 1969]. The bootstraps results for the R-ratio approximate a normal distribution of N(0.25, 0.1) (Figure 4–10a). The stress orientation in the continental crust is consistent with the fault slip model of the 1992 Mw7.1 earthquake [Murray et al., 1996; Oppenheimer et al., 1993], which indicates a P- (compression) axes with a trend and plunge of (N120°W, 30°).

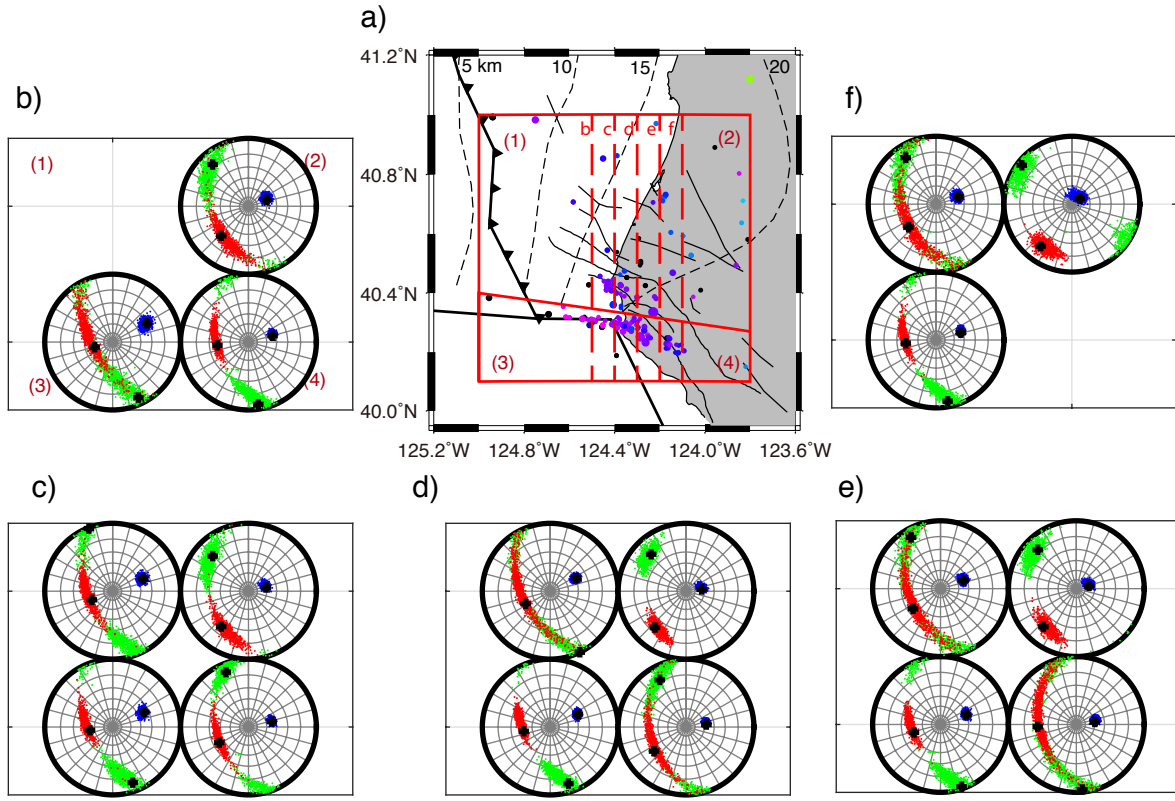


Figure 4–8: (a) Map showing grid-search test for the north-south trend boundary in each depth group. The position of north-south trend boundary is moving from 124.5W to 124.1W (red dashed lines). The solid red line separates the Mendocino transform fault and other intraplate earthquakes. Subfigure (b)–(f) show the inversion results of 1000 bootstraps for north-south boundary in (a). Black dashed lines are depth contours from 5 km to 20 km

In the mantle of the subducting plate, the stress tensor is quite uniform and well constrained (Figure 4–7c). The stress tensor is nearly aligned with the subduction geometry: σ_1 is essentially horizontal and trends along the strike of the slab in all four sub-regions (N15°W in sub-regions (1) and (2), and N30°W anti-clockwise in sub-regions (3) and (4)), σ_3 is horizontal and trends normal to the trench, and σ_2 is almost vertical. These results are consistent with earlier studies [Schwartz and Hubert, 1997; Wada et al., 2010]. The R ratio results approximate a normal distribution of $N(0.5,$

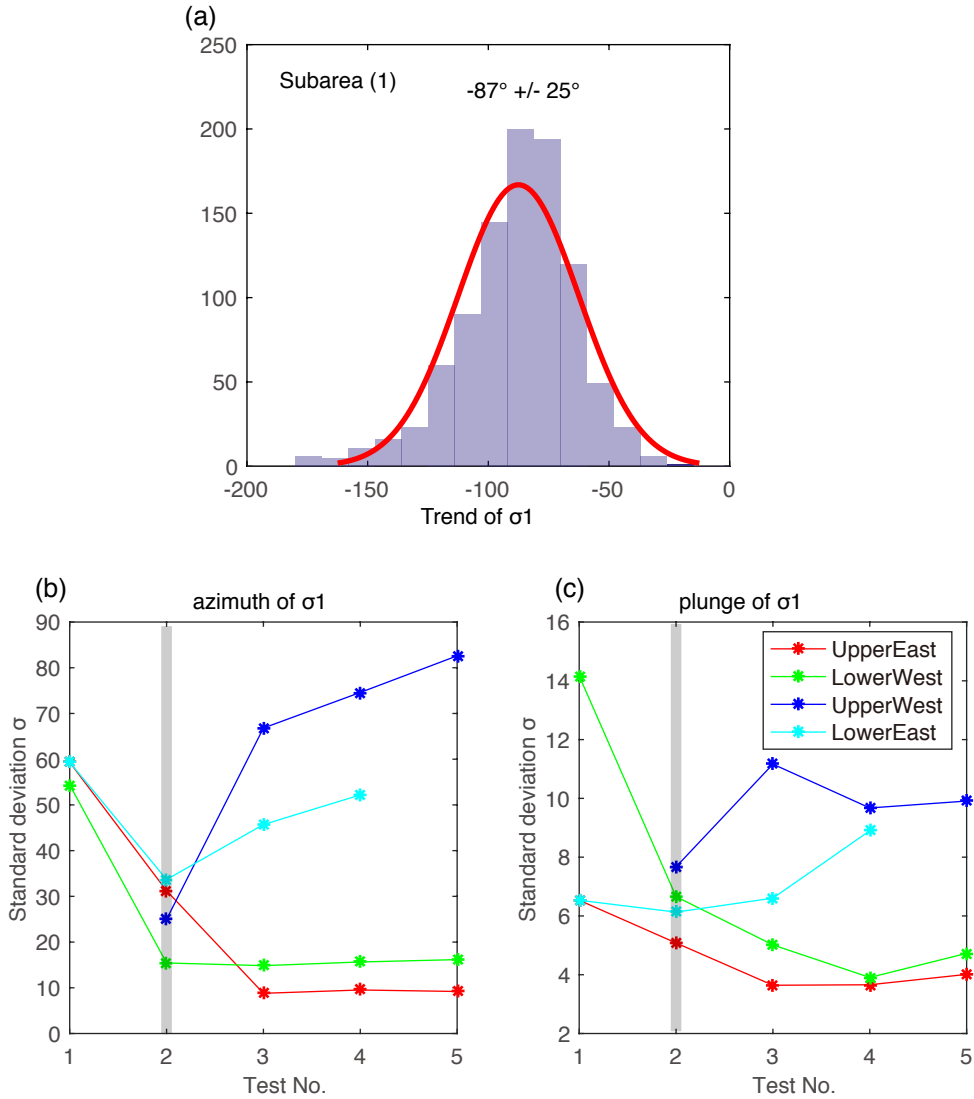


Figure 4-9: (a) Graph showing normalized distribution of the trend of σ_1 . Graphs of standard deviations of (b) trend and (c) plunge of σ_1 for the four sub-regions (1)-(4) in each test. X-axes shows the grid-search test for north-south boundary moving from *b* to *f* in Figure 4-8a. The preferred result has the smallest overall deviation (gray shaded bars).

0.04) (Figure 4-10b). The mantle earthquakes are occurring 20-30 km below the surface and immediately below the thrust interface (Figure 4-5). As one of the principal stress directions, σ_2 , makes an angle of 75° - 90° with the shallowly-dipping plate boundary, the plate interface must be a plane with relatively little shear stress acting on it. Due

to the earthquake location uncertainty and the lack of any thrust focal mechanisms at that depth range, I were not confidently able to invert focal mechanisms directly for the stress axes orientations in the Plate Boundary Zone (Figure 4–7b and Appendix A), but the results from the mantle inversion directly require that the thrust interface must be very weak relative to the subducting plate.

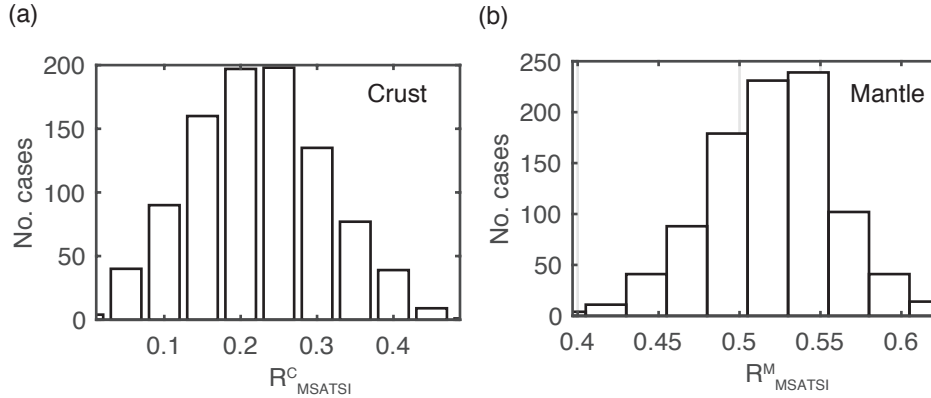


Figure 4–10: Graphs showing histograms of bootstrap inversion results of (a) R_{MSATSI}^C in crust and (b) R_{MSATSI}^M in mantle. The best estimations of R_{MSATSI}^C and R_{MSATSI}^M are 0.25 and 0.5, respectively. The standard deviations are ~ 0.1 and 0.04 , respectively.

4.3 Stress Inversion for PBZ

4.3.1 Method

I have shown that it is difficult to obtain the principal stress orientations in the PBZ from focal mechanisms, due to the “contamination” of earthquakes in the oceanic mantle. I developed an inversion to explore the range of absolute stress magnitudes in PBZ with the traction continuity condition across the plate boundary. I consider a three-layer model (Figure 4–11) and assume a uniform stress tensor in each layer. As I only focus on the average stress tensor within the PBZ, the thickness of the PBZ layer does not affect the inversion here. I assume the subducting slab dips at 13° consistent with a latitudinal cross-section at 40.2°W of the McCrory et al. [2012]

model in the depth range of 0-20 km. Thus, there are only 12 unknowns in the problem that I wish to solve for, the six unique stress tensor components in the plate boundary zone and the magnitudes of the principal stresses in the mantle and crust:

$$\underline{x} = [\sigma_{EE}^{PBZ}, \sigma_{EN}^{PBZ}, \sigma_{ED}^{PBZ}, \sigma_{NN}^{PBZ}, \sigma_{ND}^{PBZ}, \sigma_{DD}^{PBZ}, \sigma_1^C, \sigma_2^C, \sigma_3^C, \sigma_1^M, \sigma_2^M, \sigma_3^M]$$

where M denotes subducted mantle, C denotes overriding crust, P denotes PBZ, and E, N, D denote East, North, and Down.

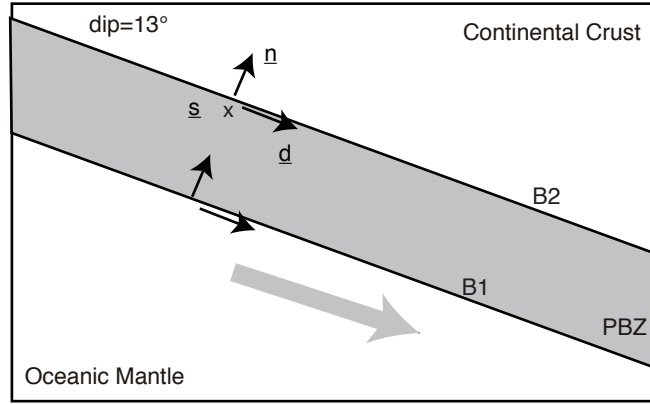


Figure 4-11: Schematic Diagram of the three-layer subduction zone model. PBZ represents the relatively weak region around the subduction fault interface. B1 and B2 denote the PBZ-mantle and crust-PBZ boundaries respectively. Normal- and dip-vector are shown in arrows and strike-vector in cross. The dip angle is 13° .

Linear Matrix Inversion (LMI) Syntax. I enforce the results of the focal mechanism inversions through a system of eight linear equations that must be satisfied by the solution vector \underline{x} . I enforce the continuity of traction at crust-PBZ (B2) and PBZ-mantle (B1) boundaries. The traction vectors are decomposed to fault normal- (\underline{n}), along dip- (\underline{d}) and along strike- (\underline{s}) components (Figure 4-11) for each boundary specifying the first six equations of the form:

$$\underline{T}^{PBZ}(\hat{n}) = \underline{\underline{\sigma}}^{PBZ} \hat{n} = \underline{T}^M(\hat{n}) \pm \underline{\epsilon}_1 \quad (4.5)$$

$$\underline{T}^{PBZ}(\hat{n}) = \underline{\underline{\sigma}}^{PBZ}\hat{n} = \underline{T}^C(\hat{n}) \pm \underline{\epsilon}_1 \quad (4.6)$$

where ϵ_1 is a tolerance for how tightly this constraint needs to be satisfied and $\hat{n} = [\sin \alpha \cos \theta, -\sin \alpha \sin \theta, -\cos \alpha]^T$. α is dip angle and θ is clockwise from north.

In the crust, the stress tensor has three eigenvalues σ^k and three eigenvectors \underline{V}^k . The rotation matrix between END and principle coordinates in the crust is $\underline{\underline{\Omega}}^C = \begin{bmatrix} V_E^1 & V_E^2 & V_E^3 \\ V_N^1 & V_N^2 & V_N^3 \\ V_Z^1 & V_Z^2 & V_Z^3 \end{bmatrix}$. Thus $\underline{\underline{\sigma}}^C$ in the END coordinates can be written as $\underline{\underline{\sigma}}^C = \underline{\underline{\Omega}}^C \underline{\underline{\sigma}}'^C \underline{\underline{\Omega}}^{CT}$.

where the principle tensor $\underline{\underline{\sigma}}'^C = \begin{bmatrix} \sigma_1^C & 0 & 0 \\ 0 & \sigma_2^C & 0 \\ 0 & 0 & \sigma_3^C \end{bmatrix}$. Similarly, we incorporate the principle stress orientations in the mantle from the previous section using $\underline{\underline{\sigma}}^M = \underline{\underline{\Omega}}^M \underline{\underline{\sigma}}'^M \underline{\underline{\Omega}}^{MT}$.

The traction continuity constraints of equations (4.5) and (4.6) at the mantle-PBZ interface (boundary 1) and at the crust-PBZ Inter-face (boundary 2) become (in END coordinates):

$$\underline{\underline{\Omega}}^M \underline{\underline{\sigma}}'^M \underline{\underline{\Omega}}^{MT} \hat{n} - \underline{\underline{\sigma}}^{PBZ} \hat{n} = 0 \pm \underline{\epsilon}_1 \quad (4.7)$$

$$\underline{\underline{\Omega}}^C \underline{\underline{\sigma}}'^C \underline{\underline{\Omega}}^{CT} \hat{n} - \underline{\underline{\sigma}}^{PBZ} \hat{n} = 0 \pm \underline{\epsilon}_1 \quad (4.8)$$

The constraints on the stress ratios are implemented as two additional equations (one for both the crust and mantle layers) as:

$$\sigma_1^C - \sigma_2^C + R^C(\sigma_1^C - \sigma_3^C) = 0 \pm \epsilon_2 \quad (4.9)$$

$$\sigma_1^M - \sigma_2^M + R^M(\sigma_1^M - \sigma_3^M) = 0 \pm \epsilon_2 \quad (4.10)$$

The linear equations of (4.7)-(4.10) can be written as a pair of linear matrix inequalities (LMIs):

$$\underline{\underline{A}}x > -\epsilon \quad (4.11)$$

$$\underline{\underline{A}}x < \epsilon \quad (4.12)$$

where the linear coefficient matrix $\underline{\underline{A}}$ is shown explicitly in the Appendix information.

I also enforce several physical constraints on the solution. Firstly, the stress tensor for each layer has only positive (compressional) principal stresses which is implemented as a three linear matrix inequality (LMI) constraints:

$$\underline{\underline{\sigma}}^{PBZ} \geq 0 \quad (4.13)$$

$$\underline{\underline{\sigma}}^M \geq 0 \quad (4.14)$$

$$\underline{\underline{\sigma}}^C \geq 0 \quad (4.15)$$

where \geq indicates positive semi-definite. I also require that the principal stress magnitudes be properly ordered to match the eigenvectors used in \underline{x} ; that the largest stress in the subducted mantle be greater than the largest stress in the PBZ; and that the maximum absolute stress is 1000 MPa.

$$\sigma_1^M \geq \sigma_2^M \geq \sigma_3^M \quad (4.16)$$

$$\sigma_1^C \geq \sigma_2^C \geq \sigma_3^C \quad (4.17)$$

$$\sigma_1^M \geq \sigma_1^{PBZ} \quad (4.18)$$

$$\sigma_i \leq 1000 MPa \quad (4.19)$$

The set of LMIs (equations 4.7-4.10) does not have any information in it to specify the scale of any of the stress tensors. I impose this by defining a least-square objective

function for the differential stress in the subducted mantle, S^M . Because the oceanic mantle is expected to be quite strong, I set this value, S^M , and use it to investigate the permissible values of the stresses in the three layers. The objective function is:

$$\text{Minimize} \|(\sigma_1^M - \sigma_3^M) - S^M\| \quad (4.20)$$

which I implement as a matrix inequality constraint using Schur complements [Vandenberghe and Boyd, 1996]. I then solve the system of LMI using the *mincx* function in MATLAB.

Tolerance. To explore the range of absolute stress magnitudes consistent with the principal stress rotation, I take each bootstrap result from the MSATSI inversion and use it to specify the LMI system (equations 4.11-4.20) and solve for \underline{x} . I found that there are no feasible solutions \underline{x} for any of the bootstrap results if I enforce the continuity and R-ratio equations exactly (e.g., $\epsilon_1 = 0$, $\epsilon_2 = 0$). Thus, a key choice is the tolerance values (ϵ_1) that I apply to allow the solution vector to deviate from exactly satisfying those constraints. ϵ_2 is kept to be 5 MPa in the inversions, thus only ϵ_1 affects the results. I perform the inversion with ϵ_1 ranging from 1 to 50 MPa, and varying S^M from 50 to 400 MPa.

Figure 4–12 shows results for S^M of 150 MPa. For each estimated parameter vector \underline{x} , I calculate the residual of R ratios, defined as to qualify the reliability of the results (superscript i denotes for C or M). R_{MSATSI} is the R ratios from MSATSI inversion using focal mechanisms and \hat{R} is calculated from \bar{x} . The averaged residual of the six continuity equations represents the difference of the stresses across these boundaries. When the tolerance increases, the mantle strength eventually approximates to the assumed value but ϵ_1 increases (Figure 4–12b). On the other hand, the R-residuals ($RESD$) in the crust and mantle decrease to zero at different rates. I choose as the

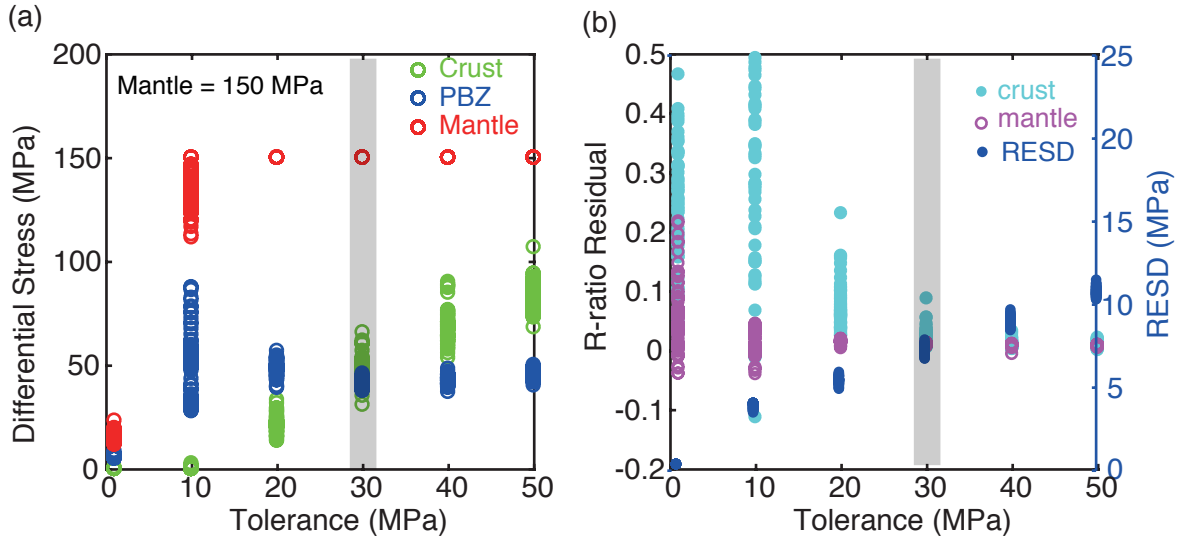


Figure 4–12: (a) Results with the subjective mantle strength $S^M = 150$ MPa under different tolerances ranging from 1 to 50 MPa are shown. Differential stress of mantle (red), crust (green) and PBZ (blue). (b) R-ratio residual is defined as $\hat{R}^i - R_{MSTASI}^i$ (left-axis). The averaged residuals in the traction continuity equations, $RESD$, are shown in right-axis. Gray shadowed bars denote the cut-off tolerance.

best solution, the smallest value of the tolerance where the assumed mantle strength is satisfied and both the crustal and mantle R ratios are below 0.1 (based on the uncertainty in bootstraps R_{MSATSI}^C in Figure 4–10). The tolerance that meets all the requirement is called cutoff tolerance.

The results of $S^M = 200$ MPa are comparable to $S^M = 150$ MPa, except for the value of strength (Figure 4–13). I then explore the cut-off tolerance for each assumed mantle strength from 50 to 400 MPa, at every 50 MPa step. The pair of mantle strength and cutoff tolerance is listed in Table 4–1.

Maximum and Minimum of PBZ. I also use a slightly modified formulation where I specifically optimize the differential stress in the PBZ. I run two additional inversions to either minimize or maximize the differential stress in the PBZ:

Table 4–1: The cutoff tolerance at each mantle S^M from 50 to 400 MPa.

Mantle (MPa)	Tolerance (MPa)
50	20
100	20
150	30
200	30
250	35
300	40
350	45
400	50

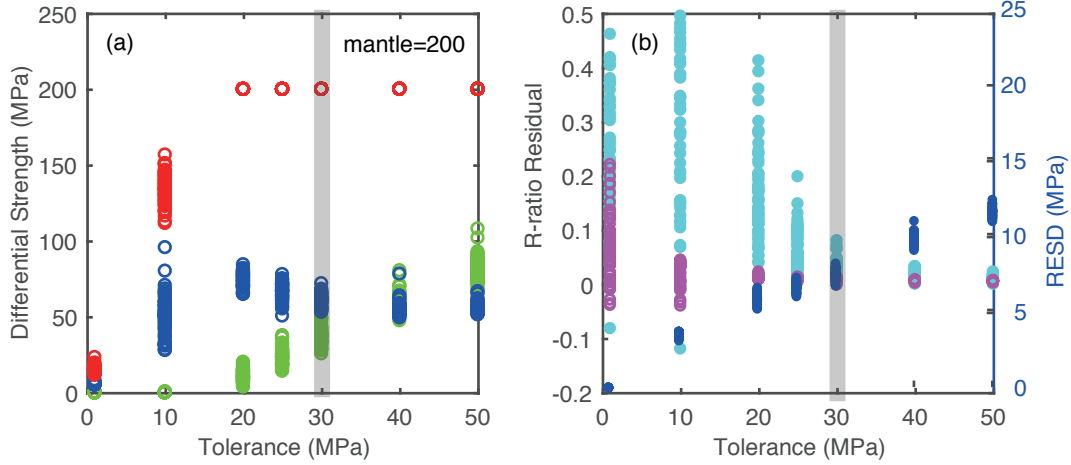


Figure 4–13: Same as Figure 4–12 except for $S^M = 200$ MPa.

$$\text{Maximize} \|\sigma_1^{PBZ} - \sigma_3^{PBZ}\| \quad (4.21)$$

$$\text{Minimize} \|\sigma_1^{PBZ} - \sigma_3^{PBZ}\| \quad (4.22)$$

To implement this, I modify the objective function to operate on the largest and smallest eigenvalues of $\underline{\underline{\sigma}}^{PBZ}$. I also use a slightly modified formulation where I specifically optimize the differential stress in the PBZ. I modify the objective function to operate on the largest and smallest eigenvalues of $\underline{\underline{\sigma}}^{PBZ}$. I add these eigenvalues to

the decision vector and include two additional *LMI* constraints to define them as the largest (Γ) and smallest (γ) eigenvalues of $\underline{\underline{\sigma}}^{PBZ}$ following Kovalsky et al. [2014].

$$\begin{bmatrix} \underline{\underline{\sigma}}^{PBZ} & \Gamma \underline{\underline{I}} \\ \Gamma \underline{\underline{I}} & \underline{\underline{\sigma}}^{PBZ} \end{bmatrix} \geq 0 \quad (4.23)$$

$$\frac{\underline{\underline{\sigma}}^{PBZ} + \underline{\underline{\sigma}}^{PBZ^T}}{2} \geq \gamma \underline{\underline{I}} \quad (4.24)$$

where I is a 3 by 3 identity matrix. When maximizing the differential stress in the PBZ (e.g., $\Gamma - \gamma$), I add an additional physical constraint that the differential stress in the subducted mantle is large than it is in the PBZ.

$$\sigma_1^M - \sigma_3^M \geq \sigma_1^{PBZ} - \sigma_3^{PBZ} \quad (4.25)$$

Solving the two optimization problems in Eq. 4.21 and 4.22 allows us to explore the entire permissible range of shear stresses on the PBZ for a set of principal stress orientations in the crust and mantle. In the optimization of Eq. 4.21 and 4.22, subjective mantle strength becomes an additional constraint $-0.1 \leq (\sigma_1^M - \sigma_3^M) - S^M \leq 0.1$ in the linear constrain matrix. For simplifying reference, I name Eq. 4.20 as version 1 and Eq. 4.21 and 4.22 to be version 2 and version 3, respectively.

4.3.2 Results

The assumed mantle strength constraint is used because of the considerable evidence that strength envelopes correctly characterize the behavior of oceanic plates [Boettcher et al., 2007] and are consistent with the properties of intra-plate earthquakes in our study region in particular [Choy and McGarr, 2002; Wei and McGuire, 2014]. Strength envelopes would predict a value of $\sigma_1 - \sigma_3 = 400$ MPa at the depth of the mantle earthquakes in our study region under hydrostatic conditions [Wei and McGuire, 2014], which is a maximum strength for the mantle. To explore the full

range of stress magnitude in the three-layer model, I varied the assumed strength of the mantle (S^M) from 50 to 400 MPa. I found no level at which that strength could be met and the continuity equations satisfied exactly for the three-layer model.

The three-layer model is an over simplification that attempts to represent a smooth stress rotation as an abrupt change at a boundary. I relaxed the stress continuity equations with a small misfit tolerance, ϵ_1 , on the order of 20-50 MPa. For each value of the assumed mantle strength (S^M), The minimum amount of misfit tolerance is required to be able to match the assumed strength and satisfy the continuity equations and R estimates (Figure 4–12 and 4–13). For example, in Figure 4–12, the reversed mantle strength reaches the assumed mantle 200 MPa at tolerance larger than 20 MPa (Figure 4–12a). But the residual, \hat{R}^C , drops below 0.1 only at tolerance no smaller than 30 MPa (Figure 4–12b). This makes 30 MPa be the cutoff tolerance for assumed mantle being 150 MPa. The same thing in Figure 4–13.

PBZ Strength. The strength of the PBZ at each assumed mantle S^M is shown in Figure 4–14. At each assumed mantle S^M , the cut-off tolerance is obtained (Table 4–1). The dots represent the results of bootstraps stress tensors and the line is the mean value. Each pair has a suitable tolerance that fits the acceptable residual requirement. The strength of PBZ scales with mantle strength at a ratio of 0.4. While the crustal strength remains almost constant at 50 MPa.

Then for each pair of S^M and tolerance, I perform another set of optimizations that specifically determine the maximum and minimum values of differential stress in the PBZ layer, $\sigma_1^{PBZ} - \sigma_3^{PBZ}$, using version 2 and version 3, respectively. These results in a range of differential stress for the PBZ that are consistent the assume mantle strength and observed stress rotation. Typically, the minimum acceptable PBZ strength is between about 0 and 50 MPa, while the maximum strength roughly scales

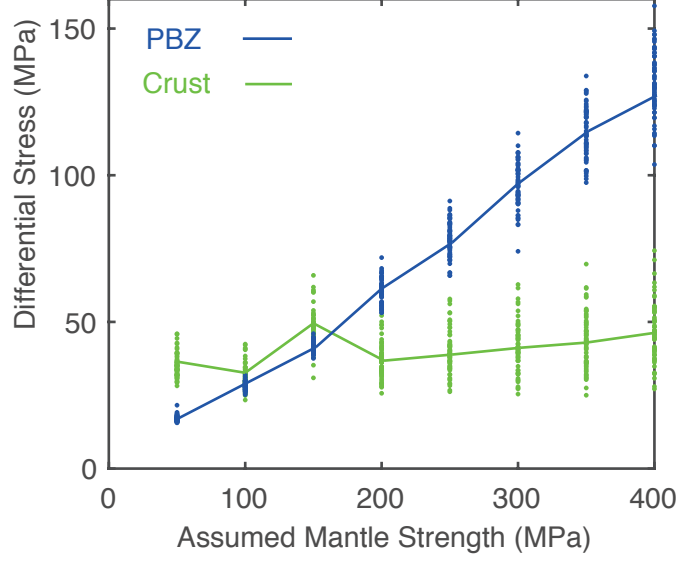


Figure 4–14: Graph showing the strength of PBZ (blue) and crust (green) at each pair of assumed mantle (S^M) from 50 to 400 MPa and tolerance when minimizing the assumed mantle strength $\|(\sigma_1^{PBZ} - \sigma_3^{PBZ}) - S^M\|$ (Version 1). The line shows the averaged of the bootstrap results (dots). The cutoff tolerance at each mantle strength is shown in Table 4–1.

with the assumed mantle strength, reaching ~ 150 MPa for a 400 MPa mantle strength (Figure 4–15). It is unrealistic that the PBZ could be stronger than the overlying crust, so I infer an upper limit on the PBZ strength of 50 MPa.). These values are all well below both the assumed differential stress in the mantle and what would be expected from typical strength envelopes at this depth (400 MPa at 20 km).

No scale constraint of the crust is used, as the crustal strength is determined by the traction across the boundary and PBZ stress. This is proved in Figure 4–15 that the crustal strength is larger in minimizing than maximizing PBZ. The crustal strength falls in the range of 20 to 80 MPa (green dots in Figure 4–15). This range seems consistent with the real observations so far. For example, the stress drop of crustal earthquakes is no larger than 100 MPa. With the stress drop of 2011 Tohoku-Oki earthquake, Hasegawa et al. [2011] estimated that the crustal strength in Japan

Trench should be around 20 MPa. Without more constraint, it seems that I cannot confirm the PBZ or mantle strength from crustal strength, as the wide range shown in Figure 4–15.

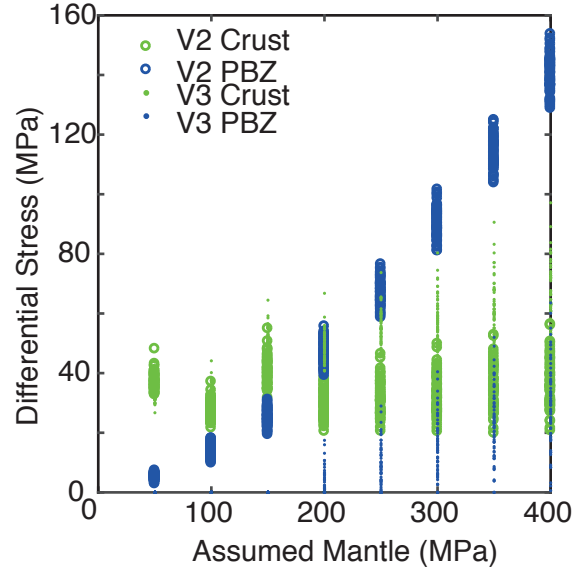


Figure 4–15: Graphs showing the range of the strength of PBZ (blue) and crust (green) at each pair of assumed mantle (S^M) from 50 to 400 MPa and tolerance when maximizing (Version 2) and minimizing (Version 3) $||\sigma_1^{PBZ} - \sigma_3^{PBZ}||$. Blue circles and dots are differential stress in PBZ using version 2 and version 3, respectively. Differential stress in the crust is reversely related with that in the PBZ in the maximization (green circles) and minimization (green dots).

Effective Friction Coefficient. Effective friction coefficient, μ_{eff} , reflects the frictional strength on the fault. It is unrealistic that the PBZ could be stronger than the overlying crust, so I infer an upper limit on the PBZ strength of ~ 50 MPa (Figure 4–15). These values are all well below both the assumed differential stress in the mantle and what would be expected from typical strength envelopes at this depth (~ 400 MPa at 20 km). The inversion results can also be represented as an effective friction coefficient in the PBZ which is slightly dependent on the assumed mantle strength but is generally

in the range of 0 to 0.2 (Figure 4–16). The histograms of μ_{eff} from bootstrap results, which follow normalized distributions, are shown in Figure 4–17.

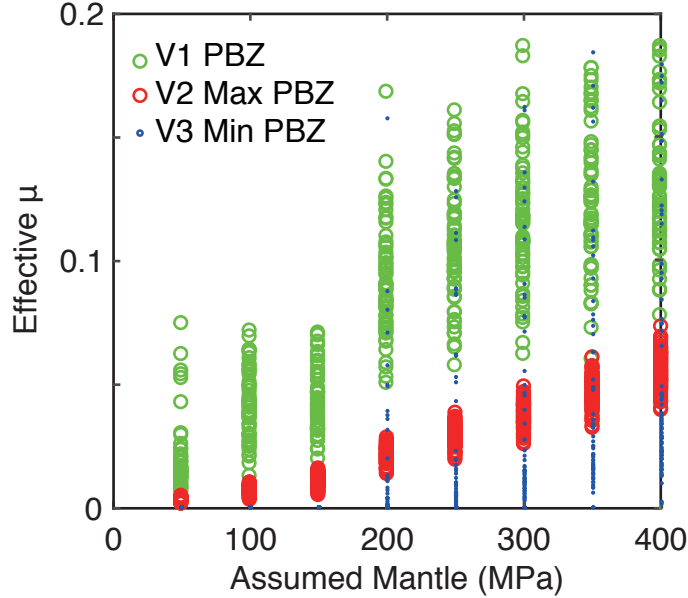


Figure 4–16: Effective friction coefficients at each pair of mantle and tolerance. Green circles are results when minimizing $\|(\sigma_1^M - \sigma_3^M) - S^M\|$ (Version 1) in the convex optimization LMIs. Red circles and blue dots are maximizing (Version 2) and minimizing (Version 3) $\|\sigma_1^{PBZ} - \sigma_3^{PBZ}\|$, respectively.

4.4 Discussions

4.4.1 Stress Rotation across PBZ

The stress orientations observed in the MTJ region are unique in imaging a difference in stress regime between the overlying and down-going plates (Figure 4–7). The compression in the shallow crust group orients NW-SE, parallel to plate convergence and changing to N-S direction in the oceanic mantle (Figure 4–7). This shallow dipping fault in the crust hosts the 1992 Mw7.1 Cape Mendocino event, which ruptures in the

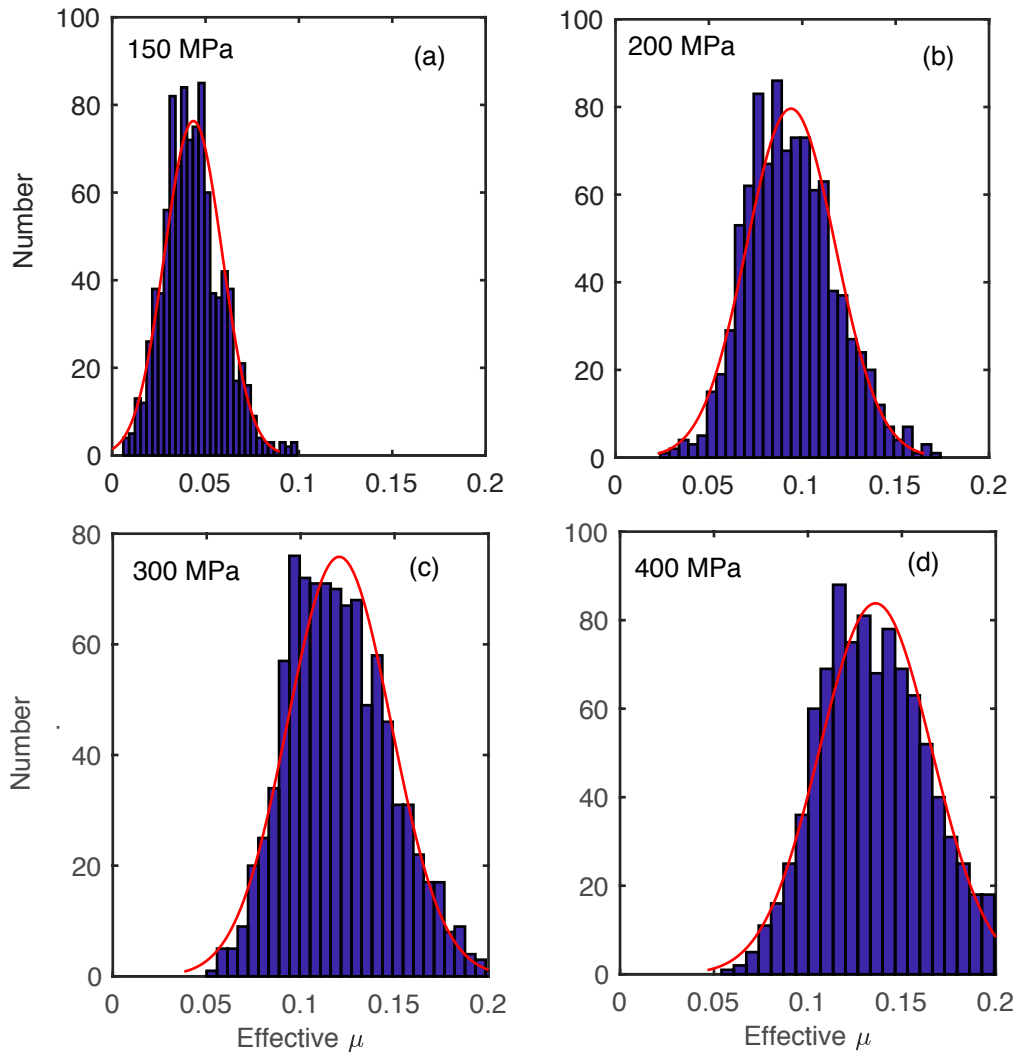


Figure 4–17: Histograms of bootstrap results of effective friction coefficient μ . μ is calculated as the ratio of shear/normal. The assumed mantle strength S^M is (a) 150, (b) 200, (c) 300 and (d) 400 MPa, respectively. Gaussian distributions are shown in red.

same direction of this compression. This stress transition is dominated by the northward movement of the Pacific Plate in the deeper plate, which has also been reported by Wada et al. [2010].

The non-Andersonian faulting regime in the continental crust is similar to the stress orientations typically found in subduction zones worldwide[Hardebeck, 2015].

The trenchward-plunging σ_1 axis makes an angle of $\sim 45\text{-}60^\circ$ to the plate interface, as in the global observations [Hardebeck, 2015], implying that the strength of the PBZ is on the order of the strength of the continental crust. However, the angles of $\sim 45^\circ\text{-}60^\circ$ are more typical of creeping subduction zones, rather than locked subduction zones [Hardebeck and Loveless, 2017].

The compression influences the seismicity in Cascadia. The northward movement of the Pacific Plate generates large internal deformation within the Gorda Plate [Gulick et al., 2001]. Most of the faults that originally generated in the mid-ocean ridge, with an orientation of $N20^\circ E$, are reactivated and rotate to $N75^\circ E$ [Gulick et al., 2001]. Thus most earthquakes in MTJ are strike-slip appearing in the Gorda lithosphere. The clockwise rotation at the southern Gorda may attribute to the northward compression. However, how the dominant compression affects the megathrust fault in Cascadia is not clear yet. More studies are required to understand the megathrust fault.

4.4.2 Weak Thrust Fault

The stress rotation with depth across the Cascadia thrust interface requires a low shear stress on the plate interface which is consistent with a number of related observations. Near lithostatic pore fluid pressures have been inferred in a layer about 5 km thick in the vicinity of the plate interface from metamorphic dehydration of oceanic slab [Peacock et al., 2011; Hyndman et al., 2015], receiver functions with land-based stations [Audet et al., 2009; Abers et al., 2009; Audet et al., 2010] and modeling studies in Cascadia [Liu and Rice, 2005; Wada et al., 2008]. However, high-quality receiver function studies have been limited to onshore areas more representative of the downdip ETS zone than the predominately offshore locked zones where $M8+$ earthquakes are expected to rupture. Modeling studies of the ETS events require the effective normal stress and hence strength of the ETS zone to be only a couple of MPa, hence significant

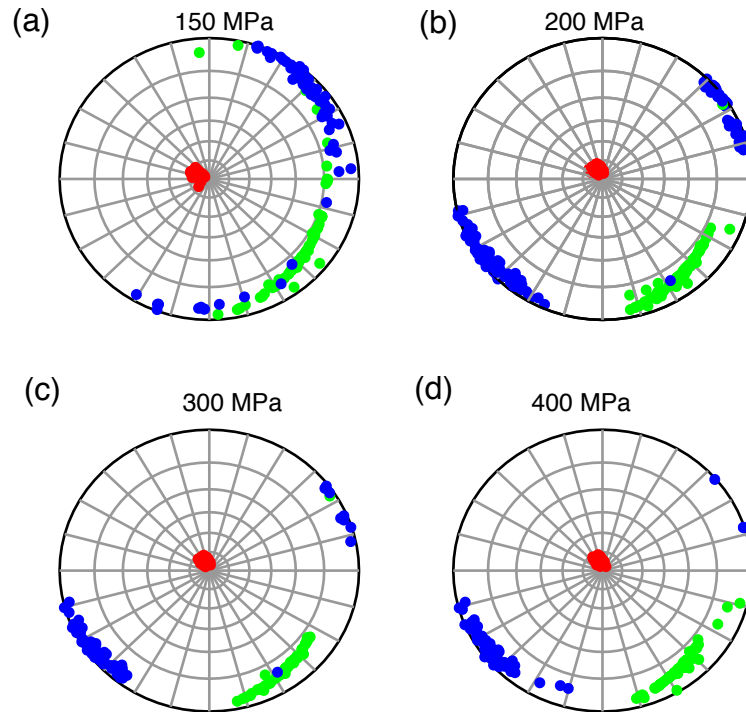


Figure 4–18: Graphs showing inverted stress orientation in PBZ in lower-hemispheric projection. Red: σ_1 , green: σ_2 , blue: σ_3 . The assumed mantle strength S^M is (a) 150, (b) 200, (c) 300 and (d) 400 MPa. σ_1 (compression) makes a high angle $\sim 75\text{-}80^\circ$ to the horizontal surface.

weaker than the locked zone [Liu and Rice, 2005; Segall and Bradley, 2012]. However, the absolute shear and normal stress levels of the locked zone were not well constrained and often assumed in the modeling studies to be an arbitrarily large value (~ 50 MPa) to satisfy the updip locking condition during ETS cycles. As downdip tremor is extremely sensitive to very small stress changes on the order of kPa [Rubinstein et al., 2007], our results indicate that the contrast in shear-stress levels between the ETS and mainshock zone could be as large as about 50 MPa. Smaller values are permissible (Figure 4–15) but the larger values (30-50 MPa) are comparable to what modeling studies require for the contrast between the ETS and the locked zone [Liu and Rice, 2005; Segall and Bradley, 2012].

While the permissible range of shear stress on the plate boundary is low in an absolute sense, the larger values (~ 50 MPa) exceed the stress drop in typical megathrust earthquakes indicating that it is possible that most of the stress drop in the last M9 earthquake has been recovered in this region. The failure threshold is unknown but the absence of moderate seismicity indicates that the stress level remains well below it. A local demonstration of this comes from a Mw5.7 earthquake on the Mendocino Transform Fault (Figure 4–2) that was recorded by the CI array and increased the Coulomb stress on the thrust interface by about +400 kPa. Despite this loading, I found no events in the 2-week aftershock sequence that have a clear thrust focal mechanism. While the fundamental explanation for the lack of Cascadia seismicity remains unknown, I have bracketed the range of possible shear stress levels on the thrust interface providing a constraint on this problem.

Future studies will be able to more precisely resolve the stress rotation as a function of depth. OBS arrays greatly improve the focal mechanism accuracy (Figure 4–3 and 4–4) and even a few quasi-permanent OBS offshore stations would greatly improve the catalog. Moreover, there remains up to 10 km of discrepancy in the depth of the thrust interface from different studies [McCroory et al., 2012; Henstock and Levander, 2003]. This is largely due to poorly known 3D velocity structure effecting earthquake depth uncertainties, particularly for the offshore regions. An improved 3D velocity model will help refine earthquake locations allowing a finer layering of the stress inversion in depth and a more precise understanding of the relationship between the rotation and the thrust interface. However, the unusual stress rotation in southern Cascadia can be a tool to compare to the stresses inferred from geodynamical models and improve our understanding of why the Cascadia thrust interface is so seismically quiet.

4.5 Conclusions

The Mendocino Triple Junction region is the most seismically active part of the Cascadia Subduction Zone. Previous studies show that the northward-moving Pacific Plate collides with the subducting Gorda Plate causing intense internal deformation within it. However, the stress status on the megathrust fault is unclear. Here I show that the stress field rotates rapidly with depth across the thrust interface from a strike-slip regime within the subducting plate, reflecting the Pacific Plate collision, to a thrust regime in the overriding plate. I utilize a dense focal mechanism dataset, including observations from the Cascadia Initiative ocean bottom seismograph experiment, to constrain the stress orientations. To quantify the implications of this rotation for the strength of the plate boundary, I designed an inversion that solves for the absolute stress tensors in a three-layer model subject to assumptions about the strength of the subducting mantle. The major conclusions in this chapter are:

- 1) The megathrust fault is seismologically quiet, throughout the entire Cascadia margin. There is no thrust earthquake found in neither CI year 2 nor year 4. Even after a M5.7 transform fault events near Cape Mendocino which generate +400 kPa Coulomb stress on the thrust fault. The absence of moderate seismicity indicates that the stress level remains well below the (unknown) failure threshold even though most of the stress drop of the last M9 megathrust earthquake may have recovered.

- 2) There is a stress variation across the plate boundary. In the continental crust, the compression is consistent with the plate convergence between the Gorda and North American Plate. In the mantle, the compression is dominated by the northward movement of Pacific Plate. The stress rotation in the southern Cascadia is unique around the world.

- 3) The shear stress on the plate boundary fault is likely no more than ~ 50 MPa at ~ 20 km depth when assumed mantle strength is from 50 to 400 MPa. Regardless of the

assumed mantle strength, I infer a relatively weak megathrust fault with an effective friction coefficient of ~ 0 to 0.2 at seismogenic depths. As effective friction coefficient $\mu' = \mu * (1 - \frac{P}{\sigma})$, such a low value requires a combination of high fluid pressures and/or fault-zone minerals with low inherent friction in the region where a great earthquake is expected in Cascadia.

Table 4–2: Test 1-9 for the depth and thickness of plate boundary zone (PBZ). The number of earthquakes in each group are shown. D: perpendicular distance to slab interface given by McCrory et al. [2012]. H: thickness of slab interface group.

Test	D (top, km)	D (bottom, km)	H (km)	No. of Crust	No. of PBZ	No. of Mantle
1	-2.5	2.5	5	384	322	852
2	-6	1	7	279	315	964
3	-4	3	7	327	421	810
4	-3	4	7	356	520	682
5	-2	5	7	406	631	521
6	-1	6	7	437	665	456
7	-2	2	4	406	263	889
8	2	6	4	669	452	437
9	-6	-2	4	279	127	1152

Table 4–3: List of focal mechanisms: event, latitude, longitude, depth, M_L magnitude

201209141153	40.473330	-124.181170	36.540000	4.520000
201209141157	40.463170	-124.167660	29.080000	2.930000
201209141819	40.456170	-124.171670	33.030000	3.650000
201209141821	40.465830	-124.182170	30.390000	3.090000
201209141825	40.453330	-124.175500	29.470000	2.270000
201209142011	40.459500	-124.174670	29.630000	2.020000
201210030114	40.385670	-124.299160	36.870000	2.010000
201210070752	40.481330	-124.103840	47.860000	2.420000
201210181340	40.730500	-123.957830	18.650000	2.160000
201211020330	40.456170	-124.171170	33.940000	2.030000
201212200817	40.680830	-123.924000	32.870000	2.690000
201212300739	40.397340	-124.154000	24.930000	2.030000
201301070142	40.221500	-124.115670	19.120000	2.830000
201301081046	40.337830	-123.908670	42.590000	2.610000
201302141826	40.326170	-124.320170	21.570000	2.770000
201302151832	40.389670	-124.297000	37.210000	2.330000
201302152258	40.396000	-124.296500	43.270000	2.860000
201302191020	40.382500	-124.302000	36.340000	2.630000
201410191424	40.262660	-124.364830	31.340000	4.490000
201410211905	40.260500	-124.341160	23.340000	2.360000
201410240901	40.481670	-124.222660	31.590000	2.480000
201501101012	40.379170	-124.267500	12.820000	3.510000
201501141038	40.303500	-124.614670	30.470000	2.820000
201501190255	40.470000	-124.479160	33.720000	2.320000
201501232109	40.365170	-124.129330	33.450000	2.490000
201501251653	40.198670	-124.186670	7.710000	2.410000
201501282108	40.281670	-124.601840	33.930000	5.040000
201501282111	40.254670	-124.332830	25.930000	3.410000
201501282123	40.248330	-124.289000	28.490000	2.930000
201501282234	40.321830	-124.170170	33.830000	2.920000
201501291727	40.235000	-124.242330	24.840000	2.370000
201501291913	40.293670	-124.600500	32.140000	4.440000
201501291947	40.294330	-124.603500	30.310000	2.800000
201502020301	40.275500	-124.591670	31.500000	3.510000
201502242328	40.831170	-124.737500	33.310000	3.030000
201503190210	40.419170	-124.652170	34.880000	3.060000
201503251453	40.505660	-124.375340	33.260000	2.940000
201505150920	40.374500	-124.578830	35.720000	2.980000
201505261017	40.671670	-124.677330	33.420000	4.240000
201506180827	40.187830	-124.208660	8.870000	2.620000
201507050208	40.385000	-124.495160	35.290000	3.340000

Appendix A: Tests on Depth Group

I create several tests, Test 2-9, by assigning different depth group with perpendicular distances to the slab interface, to compare with the preferred depth group in Test 1 (as shown in Table S1). The distances are from the top and bottom boundary of the PBZ group to the slab interface. In each test, I make three depth groups, each of which has four boxes.

Figure 4–19 shows the trends and plunges of σ_1 in box (1) in each test. σ_1 in Test 3-9 has an average trend of -14° and plunge of 5° . σ_1 from Test 3-9 are moderately the same, indicating the earthquake populations are from the same stress tensor in the oceanic crust. It should be noticed that a distinctive σ_1 occurs at Test 9, which has the shallowest plate boundary group among our tests. In Test 9, σ_1 trends $N15^\circ W$ and plunges at $\sim 45^\circ$ trenchward. Most of the focal mechanisms in the continental group in Test 9 are normal faults, and thus σ_1 shifts towards vertically. These normal-fault earthquakes may occur within either the accretionary prism or upper oceanic crust, due to the slab bending at the trench. If they appear on the accretionary prism, this depth range is the upper limit of the oceanic slab surface.

Figure 4–20a shows the results of Test 2. It has three depth groups: 1) plate boundary zone: perpendicular distance between -2.5 and 2.5 km, 2) continental crust: perpendicular distance < -2.5 km and 3) oceanic mantle: perpendicular distance > 2.5 km. The focal mechanisms and stress tensors in each depth group are shown in Figures 4–20b and c, respectively. Compared with Figure 4–7, the shallow crust has a compression that is similar with that in slab interface, due to the contamination of some deep events.

Appendix B: LMI Inversion Matrix

Traction should be continue across the boundary. Thus \underline{n} in the crust is denoted as:

$$\underline{T}^C(\underline{n}) = \underline{\underline{\sigma}}^C \underline{n} = \begin{bmatrix} \sigma_{EE}^C & \sigma_{EN}^C & \sigma_{EZ}^C \\ \sigma_{EN}^C & \sigma_{NN}^C & \sigma_{NZ}^C \\ \sigma_{EZ}^C & \sigma_{NZ}^C & \sigma_{ZZ}^C \end{bmatrix} \underline{n} = \begin{bmatrix} \sum_{i=1}^3 n_i \left[\sum_{k=1}^3 \lambda_k^M \Omega_{k1}^M \Omega_{ki}^M \right] \\ \sum_{i=1}^3 n_i \left[\sum_{k=1}^3 \lambda_k^M \Omega_{k2}^M \Omega_{ki}^M \right] \\ \sum_{i=1}^3 n_i \left[\sum_{k=1}^3 \lambda_k^M \Omega_{k3}^M \Omega_{ki}^M \right] \end{bmatrix} \quad (4.26)$$

where \underline{n} is normal vector, denoted as.

$\underline{n} = [\sin \alpha \cos \theta, -\sin \alpha \cos \theta, -\cos \alpha]^T$ where $+E, +N$ and $+Z$ are eastward, northward and downward, respectively. θ and α are dip angle of the plate at 20 km depth (20) and azimuth of the trench (0). Traction on the boundary \underline{n} in the PBZ is denoted as:

$$\underline{T}_n^P = \underline{\underline{\sigma}}^P \underline{n} = \begin{bmatrix} \sigma_{EE}^P & \sigma_{EN}^P & \sigma_{EZ}^P \\ \sigma_{EN}^P & \sigma_{NN}^P & \sigma_{NZ}^P \\ \sigma_{EZ}^P & \sigma_{NZ}^P & \sigma_{ZZ}^P \end{bmatrix} \underline{n} = \begin{bmatrix} \sum_{i=1}^3 n_i \sigma_{1i}^P \\ \sum_{i=1}^3 n_i \sigma_{2i}^P \\ \sum_{i=1}^3 n_i \sigma_{3i}^P \end{bmatrix} \quad (4.27)$$

Letting $\underline{T}_n^P = \underline{T}_n^C \pm \epsilon_1$ results in three linear equations. Similarly, we have $\underline{T}_n^{PBZ} = \underline{T}_n^M \pm \epsilon_1$

For each j -component, $j = E, N, Z$.

$$\sum_{i=1}^3 n_i \left[\sum_{k=1}^3 \lambda_k^M \Omega_{kj}^M \Omega_{ki}^M \right] - \sum_{i=1}^3 n_i \sigma_{ji}^{PBZ} = 0 \quad (4.28)$$

Finally, writing in the format of linear matrix $\underline{\underline{A}}\underline{\underline{x}} = 0 + \underline{\underline{\epsilon}}$, where $\underline{\underline{A}}$ is :

$$\left[\begin{array}{c}
 n_E, n_N, n_Z, 0, 0, 0, \sum_{i=1}^3 n_i \Omega_{11}^C \Omega_{1i}^C, \sum_{i=1}^3 n_i \Omega_{12}^C \Omega_{2i}^C, \sum_{i=1}^3 n_i \Omega_{13}^C \Omega_{3i}^C, 0, 0, 0 \\
 0, n_E, 0, n_N, n_Z, 0, \sum_{i=1}^3 n_i \Omega_{12}^C \Omega_{1i}^C, \sum_{i=1}^3 n_i \Omega_{22}^C \Omega_{2i}^C, \sum_{i=1}^3 n_i \Omega_{23}^C \Omega_{3i}^C, 0, 0, 0 \\
 0, 0, n_E, 0, n_N, n_Z, \sum_{i=1}^3 n_i \Omega_{31}^C \Omega_{1i}^C, \sum_{i=1}^3 n_i \Omega_{32}^C \Omega_{2i}^C, \sum_{i=1}^3 n_i \Omega_{33}^C \Omega_{3i}^C, 0, 0, 0 \\
 n_E, n_N, n_Z, 0, 0, 0, 0, 0, 0, \sum_{i=1}^3 n_i \Omega_{11}^M \Omega_{1i}^M, \sum_{i=1}^3 n_i \Omega_{12}^M \Omega_{2i}^M, \sum_{i=1}^3 n_i \Omega_{13}^M \Omega_{3i}^M \\
 0, n_E, 0, n_N, n_Z, 0, 0, 0, 0, \sum_{i=1}^3 n_i \Omega_{12}^M \Omega_{1i}^M, \sum_{i=1}^3 n_i \Omega_{22}^M \Omega_{2i}^M, \sum_{i=1}^3 n_i \Omega_{32}^M \Omega_{3i}^M \\
 0, 0, n_E, 0, n_N, n_Z, 0, 0, 0, \sum_{i=1}^3 n_i \Omega_{31}^M \Omega_{1i}^M, \sum_{i=1}^3 n_i \Omega_{32}^M \Omega_{2i}^M, \sum_{i=1}^3 n_i \Omega_{33}^M \Omega_{3i}^M \\
 0, 0, 0, 0, 0, 0, 1 - R^C, -1, R^C, 0, 0, 0 \\
 0, 0, 0, 0, 0, 0, 0, 0, 1 - R^M, -1, R^M
 \end{array} \right] \quad (4.29)$$

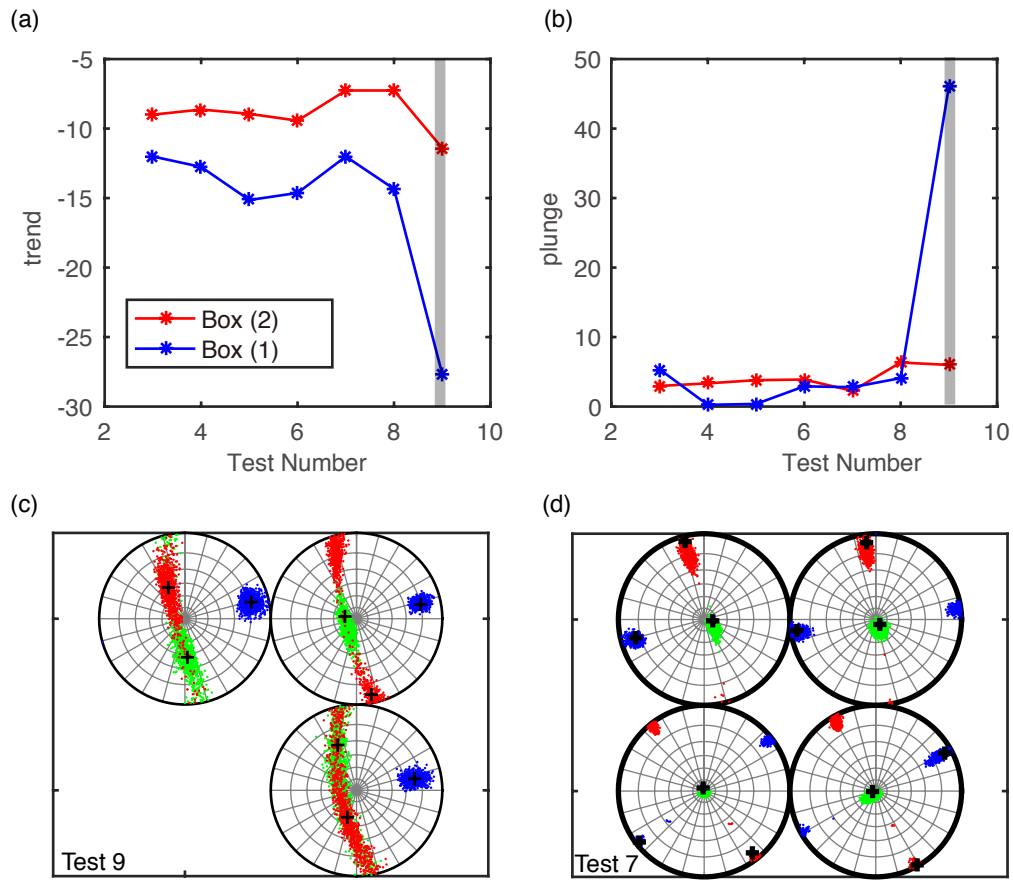


Figure A 4-19: Test on the depth and thickness of PBZ earthquakes in Table S1. (a) Trend and (b) plunge of σ_1 of two lateral sub-regions in different Test 3-9. Test 9 has the distinction in trend and plunge of compression. Stress tensor of (c) test 9 and (d) test 7. Red: σ_1 , green: σ_2 and blue: σ_3 .

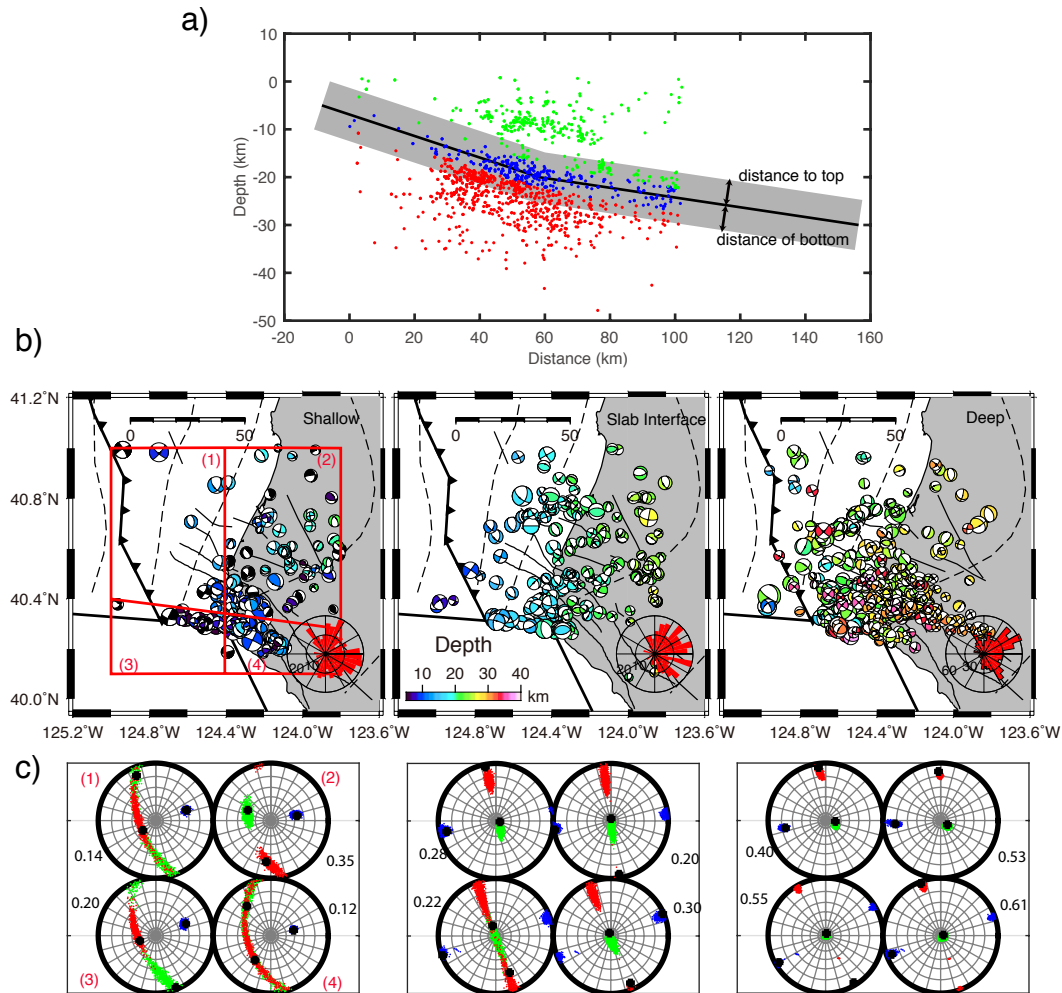


Figure A 4-20: (a) Three depth groups are defined as the continental crust (green), the plate boundary zone (blue) and the oceanic mantle (red). The perpendicular distance to the interface of top and bottom of slab interface is shown in arrows. (b) Distributions of focal mechanisms in three depth groups. Four sub-areas (1)-(4) are shown in red. (c) Stress inversion results of each depth group are shown in lower-hemisphere projection. Red: σ_1 , green: σ_2 and blue: σ_3 .

CHAPTER 5

Modeling Megathrust Earthquake Cycles Constrained by Geodetic Inversion of Fault Locking

5.1 Introduction

Earthquakes are usually recognized as frictional instabilities resulted from stick-slip events on the faults [Scholz, 1998]. On large-scale subduction faults, megathrust earthquakes always occur where elastic energy is continuously accumulated through convergent loading [Lay and Kanamori, 1981]. Geodetic inversions from long-term GPS records can reveal the fault locking coefficient, which is used as an index for the potential earthquake ruptures. In the young and warm subduction zones, geodetic fault locking is correlated with thermal structures [Hyndman and Wang, 1995]. Earthquakes cannot nucleate at depths deeper than a typical temperature as inferred from rock experiments (e.g., 350°C for granite gauges) [Hyndman and Wang, 1993]. Other than temperature, many factors also affect fault slip behaviors, including pressure, composition, and pore fluids [Blanpied et al., 1987; Scholz, 1998]. The very shallower parts of megathrust faults are unconsolidated, with abundant pore fluid and sediment clays, which usually prevent earthquake to nucleate [Hyndman and Wang, 1993].

Numerical models of earthquake cycles generally adopt the empirical rate-and-state friction to simulate the stress state on the fault [e.g. Rice, 1993; Lapusta et al., 2000; Lapusta and Liu, 2009]. Kaneko et al. [2010] have shown that inter-seismic fault coupling pattern is high related to the heterogeneous frictional properties on the fault, where frictionally unstable patches are separated by stable creeping “barriers”. This study proposed a guide for using geodetic observations to infer potential fault rupture: the regions of low coupling may serve as permanent barriers during coseismic slip. In

practice, however, the region of low coupling does not necessarily indicate the absence of potential coseismic ruptures. For example, the maximum slip of 1999 Mw7.6 Chi-Chi appeared on the northern fault that was inferred to be creeping before the earthquake [Ma et al., 2003]. The long-term creeping fault may be thermally weakened due to shear heating and thus generate large coseismic slip [Noda and Lapusta, 2013]. The 2011 Mw9.0 Tohoku-Oki earthquake also generated large slip in the shallower portion, 40 km landward from the trench, where no strong coupling is observed using the on-land GPS stations [Hashimoto et al., 2009; Ide et al., 2011a].

The great population along the Cascadia margin makes it important to investigate the potential hazard of megathrust earthquakes. Due to the lack of modern seismological records, our understanding of megathrust faults largely relies on the historical records from marine sedimental turbidities [Goldfinger et al., 2008] and coastal coseismic subsidence [Leonard et al., 2010]. Historically, several megathrust earthquakes have struck the margin [Atwater et al., 1995; Goldfinger et al., 2008] and generated great ground shaking and high tsunami waves across the Pacific ocean [Satake, 1993]. The estimated magnitude is approximately up to M9+[Goldfinger et al., 2008]. Coseismic rupture can also be estimated using the constraints from historical megathrust earthquake records. By comparing with the coastal subsidence data, Wang et al. [2013, and reference therein] construct a coseismic rupture model for the A.D. 1700 M9+ earthquake. They show five seismic segments with different downdip distances along the margin. Basically, the downdip extent of the segments is consistent with the thermal constraint for the downdip limit of coseismic rupture, with some minor differences [Hyndman et al., 2015; Wang and Tréhu, 2016].

In this chapter, I build a model for megathrust earthquake cycles in Cascadia, based on GPS observations and paleo-seismological data. As the entire fault is 1100 km long and 3-D curved geometry is computationally expensive, I build a planar fault

model to compare results from models constrained by geodetic locking pattern inferred from two different datasets 1) continuous GPS measurements [Schmalzle et al., 2014] (Model I) and 2) tidal gauge and leveling measurement [Burgette et al., 2009] (Model II) along the margin. The geodetic locking pattern is converted to be the friction parameter $a-b$ on the fault, as the relative amplitude of $a-b$ can reflect the degree of fault locking. The earthquake cycles reproduced by Model I and II are different, as the width of the seismogenic zone is heterogeneous along the strike. The coseismic subsidence data from coastal sediment measurements [Leonard et al., 2010; Wang et al., 2013] are used as constraints for ground motions. I find that the coastal subsidence pattern requires heterogeneous nucleation sizes (the minimum fault length for nucleating earthquakes) along the fault.

5.2 Method

5.2.1 Planar Fault

I use a planar fault model in this study, but the conceptual model can be applied to a 3-D curved model in the future. The planar fault model is advantageous in 1) saving computational time and 2) testing parameter space. The planar fault is 1100 km long in the strike and 492 km wide in the downdip (300 km when projected to the horizontal surface), as shown in Figure 5-1. Y-axis is set to north and X-axis is to east. The fault contains 1024 rectangles in strike and 384 in downdip direction, resulting in 393,216 totally. Thus each rectangle is 1.28 (trench-parallel) \times 1.07 (downdip) km^2 . The fault is loaded along-dip (X-axis) at a constant rate of 41 mm/yr. The shape of the trench is projected on the planar fault.

Two sets of fault locking coefficient patterns, ϕ , from the geodetic inversions are used: 1) Model I: using dense GPS arrays from 1991 to 2014, assuming ϕ is equal to 1 at the trench and follows a *Gamma* function of the landward distance from the

trench [Schmalzle et al., 2014] and 2) Model II: using coastal tidal gauges and sea-level measurements in Oregon and California [Burgette et al., 2009]. The fault locking patterns ϕ are shown in Figure 5–1. The major difference in the two pattern appears at the boundary of Washington and Oregon. In the result of Schmalzle et al. [2014], the fault locks further landward in Washington and northern California (Figure 5–1a). In the result of Burgette et al. [2009] shown in Figure 5–1b, the fault is only firmly locked offshore on southern Vancouver Island. From Washington to northern California, the fault locking decreases from about 1 to 0.5 and then increases to 0.9. The along-strike trend of ϕ in Oregon and northern California is constrained with tidal and sea-level data while with GPS inversions in Washington and southern Vancouver Island.

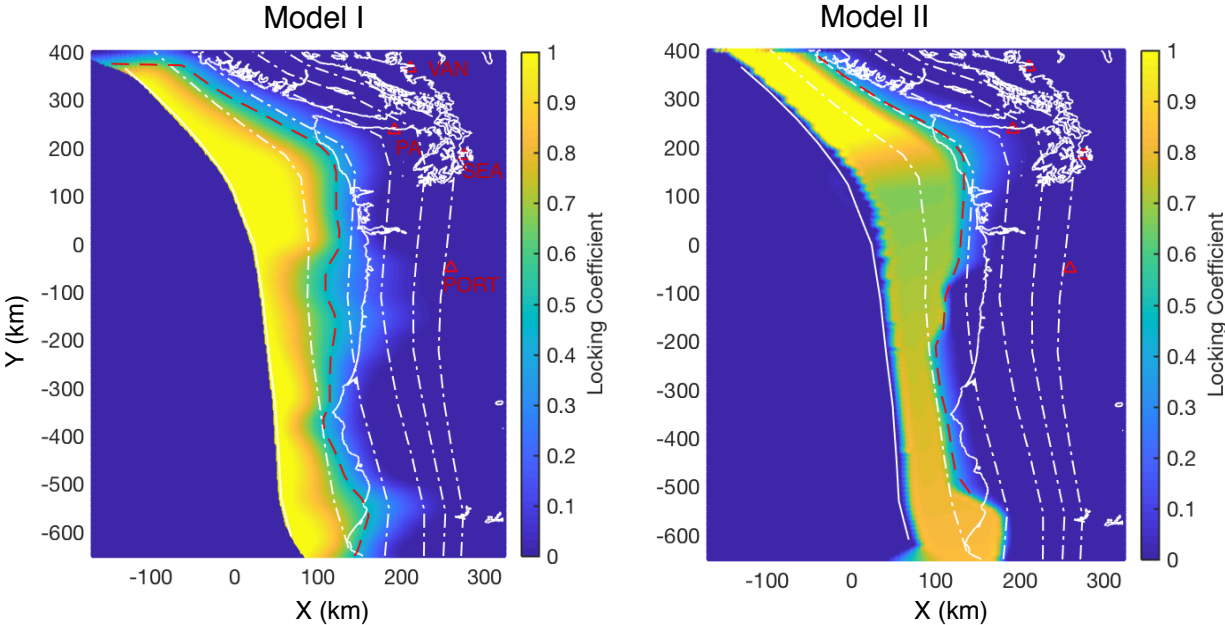


Figure 5–1: Maps showing fault locking coefficients ϕ of Model I: study of Schmalzle et al. [2014] and Model II: study of Burgette et al. [2009]. Red dashed lines are 50% fault locking contours. PORT: Portland, SEA: Seattle, PA: Port Angeles. VAN: Vancouver.

5.2.2 Parameter Choice

Parameter $a - b$. Physics of frictional parameter $a - b$ has been discussed in Chapter 2.2.1. In Chapter 2 and 3, parameter $a - b$ is constrained by isothermal contours and tremor epicenters, respectively, at the depth of SSEs. Here I assume the fault frictional stability is constrained by the fault locking pattern; non-dimensional parameter $a - b$ scales with fault locking ϕ . I choose the frictional instability, $a - b = 0$, at the contour of fault locking coefficient $\phi = 0.5$. Between $\phi = 1$ and $\phi = 0.5$, $a - b$ increases linearly from -0.0035 to 0 (Figure 5-2).

The slip behavior scales with W/h^* , where W is the length of velocity-weakening zone and h^* is the nucleation size (see Chapter 2.2.6). The range of W follows either thermal structure in Chapter 2 or tremor distribution in Chapter 3. In this chapter, however, W is constrained by the fault locking pattern (Figure 5-2). I make two models of different h^* along the strike. The definition of h^* is given by Rubin and Ampuero [2005] : $h_{RA}^* = \frac{2\mu b d_c}{\pi(1-\nu)(b-a)^2 \bar{\sigma}}$, where μ is shear modulus and ν is Poisson's ratio. Thus $d_c = \frac{h^* \pi(1-\nu)(b-a)^2 \bar{\sigma}}{2\mu b}$.

Uniform h^* . In this model, h^* is set to be 20 km everywhere on the fault. As W is between 50 and 180 km (Figure 5-2c), the W/h^* ratio is between 2.5 and 9. The peak W/h^* ratio appears at $Y = 200$ km while the smallest at $\sim Y = -400$ km. Between $Y = -100$ and -400 km, the average W is about 90 km.

Heterogeneous h^* . In contrast to the uniform h^* , I let the h^* to be 10 km in central Cascadia, where Y is in the range of [-300 0] km. The purpose for this is to keep W/h^* to be ≥ 5 along the fault, as W in central Cascadia is about half the size of that in northern or southern Cascadia (Figure 5-2c). The slip behaviors is highly affected by the choice of h^* , as shown later in section 5.3.4.

Effective normal stress. The effective normal stress, $\bar{\sigma}$, affects the recurrence behaviors of modeled slow slip events [Liu and Rice, 2007]. I set $\bar{\sigma}$ to be 50 MPa at

all depths on the fault. The uniform normal stress may be not realistic. Observations suggest that there should be stress heterogeneity as inferred from earthquake stress drop [Chen and McGuire, 2016] or influence from subducted seamounts [Yang et al., 2012]. Here using a uniform $\bar{\sigma}$ allows the focus on the influence of fault locking pattern on megathrust earthquake slip behaviors. Note that SSEs are not considered in this model.

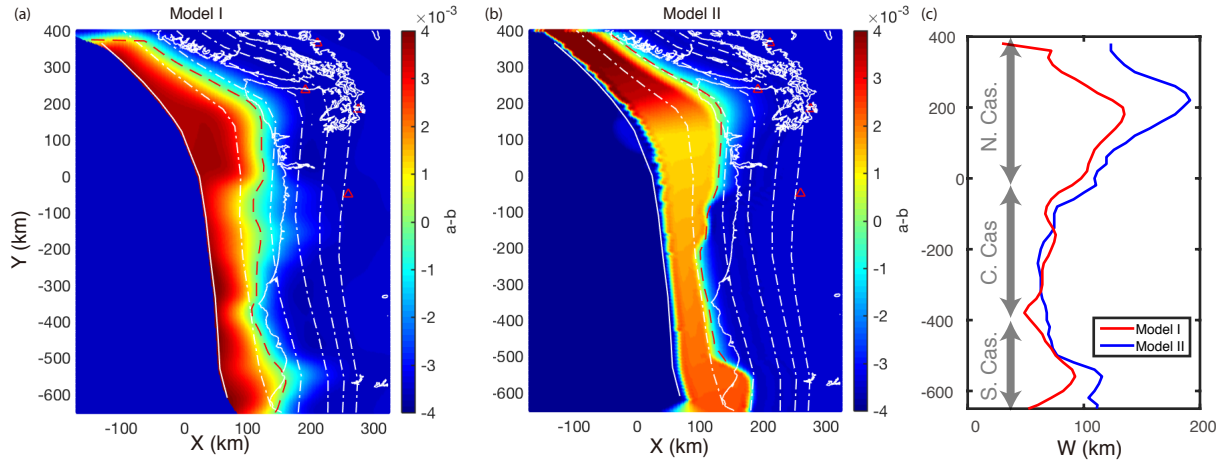


Figure 5–2: Maps showing non-dimensional frictional parameter $a - b$ of (a) Model I and (b) Model II. Parameter $a - b$ is linearly decreasing from -0.0035 to 0 from trench to downdip. 50% fault locking contours are shown by red dashed lines. (c) Along-strike length of velocity-weakening portion, W , on the fault interface. The range of the northern, central and southern Cascadia are denoted by gray bars.

5.2.3 Coastal Subsidence Data

Coastal deposits in the stratigraphic sequences can record the abrupt subsidence during coseismic ruptures [Atwater et al., 1995]. The coastal sediments will appear above a buried soil layer and thus can be dated with radiocarbon [Leonard et al., 2010]. Coastal subsidence records a 6500 yr earthquake deformation history in marsh sediments in Cascadia margin [Leonard et al., 2010]. The times and extents of the

historical coseismic ruptures that are inferred from the onshore marsh sediments are correlated with the marine turbidites data [Goldfinger et al., 2008]. Radiocarbon dating and thickness measurement of these deposits can constrain the surface deformation and estimate the magnitude of the seismic events [Leonard et al., 2010].

Tracing coastal deposits with microfossil features can narrow the uncertainty range of paleo-elevations before megathrust earthquakes [Leonard et al., 2010; Wang et al., 2013]. The measurements of subsidence at the coastal sediment sites from Washington to northern California are shown in Figure 5–4. The subsidence data are originally from Leonard et al. [2010]. Later Wang et al. [2013] refine the measurement using chronology techniques with microfossil assemblages. The uncertainty range is obtained by fitting the data with Gaussian probability distributions [Wang et al., 2013]. The synthetic subsidence is consistent with the observations, within the uncertainty range.

Both uniform and heterogeneous slip models inferred from coastal subsidence have been provided [Leonard et al., 2010; Wang et al., 2013]. The coastal subsidence can be used as a proxy for the downdip limit of seismogenic zone in Cascadia [Wang et al., 2013]. The most recent event was A.D. 1700 which was also recorded in the Japan coastal tsunami sediments [Atwater et al., 1995] and Cascadia marine turbidites [Goldfinger et al., 2008] and thus has a relatively precise timing. I use the coastal subsidence generated by the A.D. 1700 megathrust earthquake as a proxy for the modeled coseismic slip, analogous to the study of Wang et al. [2013].

The coseismic rupture is always followed by post-seismic slip, which is proposed to contaminate the subsidence records [Leonard et al., 2010; Wang et al., 2013]. Estimating the post-seismic deformation from historical data is difficult [Wang et al., 2013]. It has been assumed that post-seismic deformation within weeks can be relatively smaller compared with the coseismic subsidence in the marsh deposits [Wang et al., 2013].

The data error is estimated to be between 0.3 and 1.0 m, depending on the dating technology [Wang et al., 2013].

5.3 Results

In this section, I will show the fault cumulative slip through a simulation of 1500 years in each model. During the 1500 years, three segments: the northern, central and southern Cascadia slip patches appear along the margin. Coseismic slip is defined by a slip rate higher than 5 mm/s. The recurrence interval is about \sim 200-300 years. The cumulative slip is calculated by averaging the coseismic fault slip on each individual patch. In this section, I only focus on the cumulative slip and the total energy release, instead of time-dependent evolutions from episode to episode. The subsidence at coastal sites is calculated from the cumulative slip on the fault and is compared with observation data.

5.3.1 Modeled coseismic slip in northern Cascadia

Cumulative slip patterns during coseismic ruptures are shown in Figure 5–3. In Model I, two slip patches, the northern and southern Cascadia, appear in the simulation. The northern patch is about 450 km long in the trench-parallel direction. The maximum slip is 10 m and about 5 m at the coast of Washington. Model II also have a northern and southern patch. But the northern patch is only 400 km long with less northward extensions than Model I. The maximum slip of northern patch is 13 m and up to 6 m at the coast of Washington. The different fault slip is major constrained by the fault locking pattern, as shown in Figure 5–1 and listed in Table 5.3.1.

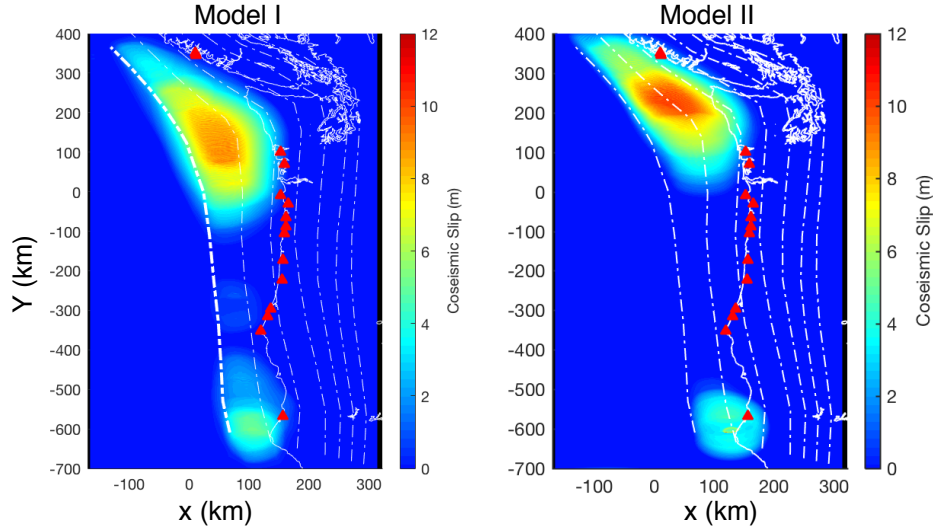


Figure 5–3: Maps showing coseismic fault slip in Model I and Model II. The cumulative slip is averaged over 1500 years with 3 or 4 earthquake cycles. The seismic moment magnitudes of the northern Cascadia slip patches in Model I and Model II are Mw8.7 and Mw8.6, respectively. Red triangles are sites of coastal sediment measurements that are shown in the study of Leonard et al. [2010].

Table 5–1: Recurrence intervals T and slips δ of coseismic ruptures in Model I and Model II

Model I		
Segment	T (yr)	δ_{max} (m)
N.	218	10
S.	140	5
Model II		
Segment	T (yr)	δ_{max} (m)
N.	240	13
S.	183	6

5.3.2 Synthetic coastal subsidence

The average cumulative slip is projected onto a 3-D curved fault model by using the depth contours from the study of McCrory et al. [2012]. Surface subsidence displacement is calculated using Okada’s dislocation method in a half-space homogeneous Earth [Okada, 1985]. The synthetic subsidence calculated from the northern Cascadia slip patch is shown in Figure 5–4. Comparing results from Model I and Model II, there

is a slight difference between $Y=0$ and 100 km. The difference in cumulative slip is resulting from the different geodetic fault locking patterns in Model I and II: a wider locked fault in Model I result in more coseismic rupture and larger subsidence (Figure 5-1).

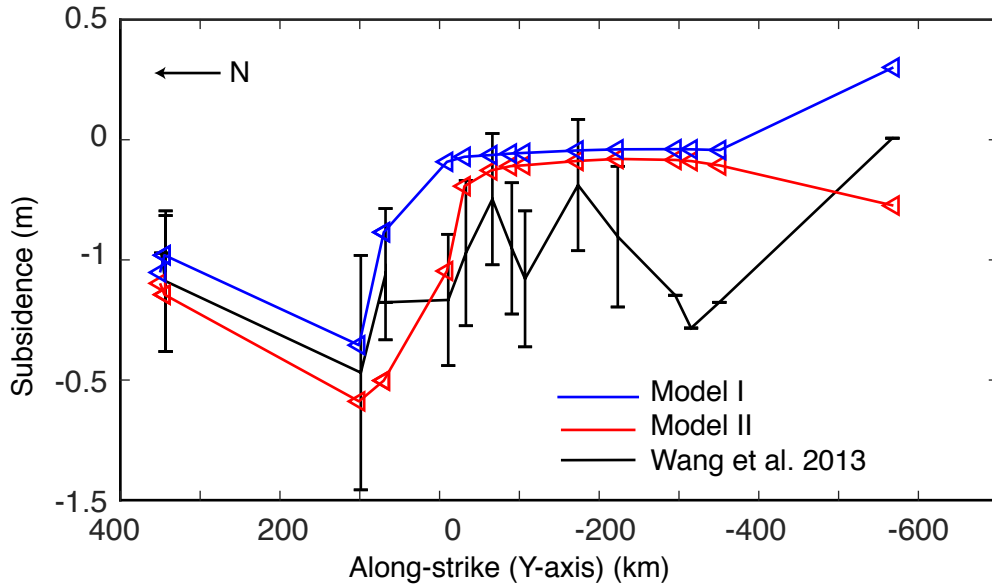


Figure 5-4: Graphs showing synthetic subsidence records of Model I (blue) and Model II (red). The paleoseismic subsidence data of the study of Wang et al. [2013] are shown in black. The error bars are uncertainty range estimated by Wang et al. [2013].

5.3.3 Aseismic slip in central Cascadia: uniform h^*

The central Cascadia fault cannot have coseismic ruptures (defined as $V_{slip} > 5$ mm/s) in the models with a uniform h^* distribution along the fault. Instead, there is distinctive aseismic slip (with slip rate of 10^{-7} m/s) lasting for ~ 10 years in central Cascadia. The total slip adds up to 4.5 m, which is about half of that in the northern Cascadia (Figure 5-5). The result for this small aseismic slip is that the W in central Cascadia is small (Figure 5-2c). As W in central Cascadia is about half the size of that in the northern and southern segment, the W/h^* is relatively smaller (Figure 5-5

and 5–2c). Thus W/h^* promotes the aseismic, instead of coseismic, fault slip in central Cascadia. In order to have the coseismic slip to match with paleo-seismic coastal subsidence in central Cascadia, I need to modify the frictional parameter W/h^* .

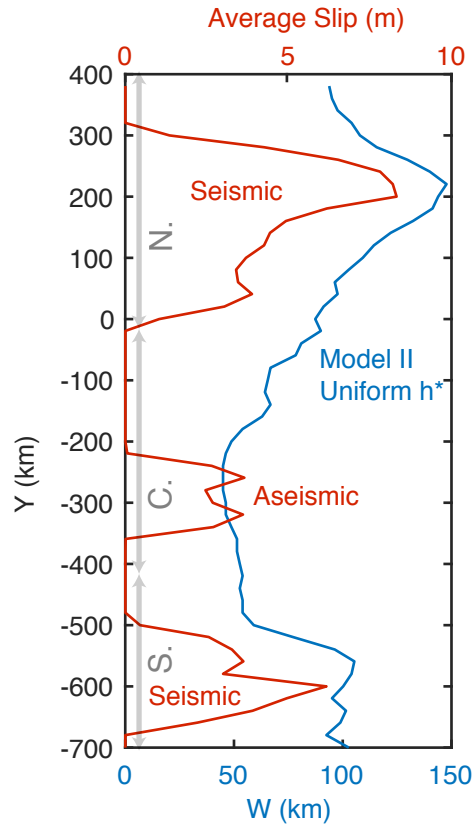


Figure 5–5: Graphs of down-dip distance of velocity-weakening, W (blue), and the modeled coseismic/aseismic slip (red) in Model II, with uniform h^* along the strike. Coseismic slip appears in the northern and southern while aseismic in the central Cascadia. The range of three segments are shown in gray.

5.3.4 Coseismic slip in central Cascadia: heterogeneous h^*

In Section 5.3.3, the model with uniform h^* cannot reproduce coseismic ruptures in central Cascadia, due to the smaller W/h^* . Here I use the heterogeneous h^* parameter setup to reproduce coseismic ruptures in Oregon. The ratio of W in northern and

central Cascadia in Model II is about 2. Thus I times h^* for central Cascadia by a factor of 0.5, resulting in a larger W/h^* there.

In this case, coseismic ruptures appear in central Cascadia (Oregon). The coseismic fault slip patterns are shown in Figure 5–6. The coseismic slip in central Cascadia is up to 7 m. This cumulative slip is relatively smaller than that in northern and southern Cascadia, which preserve the same pattern and magnitude as Model I, as W/h^* is not changed. The calculated coastal subsidence is shown and compared with the paleoseismic observations in the study of Wang et al. [2013] in Figure 5–7. The subsidence at northern and central Cascadia is quite comparable with the original data in terms of magnitudes. Even though the synthetic subsidence fits the general trend (blue line in Figure 5–7), the detailed variations between -300 and 0 km are not recovered. For example, there is -0.6 m subsidence at $Y=-100$ km in the observation data but not in the synthetic (Figure 5–7). It has also been shown that there are five coseismic patches along the strike required to fit the observations [Wang et al., 2013], which are more than the three patches I have here. The less along-strike segment in our model may be attributed to the simple assumption of no along-strike changes of friction parameters. However, there is no megathrust earthquake that ruptures the entire margin in our models. There patches rupture alternatively in the models.

5.4 Discussions

5.4.1 Various Nucleation Sizes

In numerical simulations, W/h^* largely affects aseismic and coseismic ruptures (see Chapter 2.2.6). The frictional behaviors that affected by W/h^* have been illustrated in earthquake [Rubin and Ampuero, 2005] and transient slow slip modeling [Rubin, 2008; Liu and Rice, 2009]. The downdip width of velocity-weakening, or W , is determined by

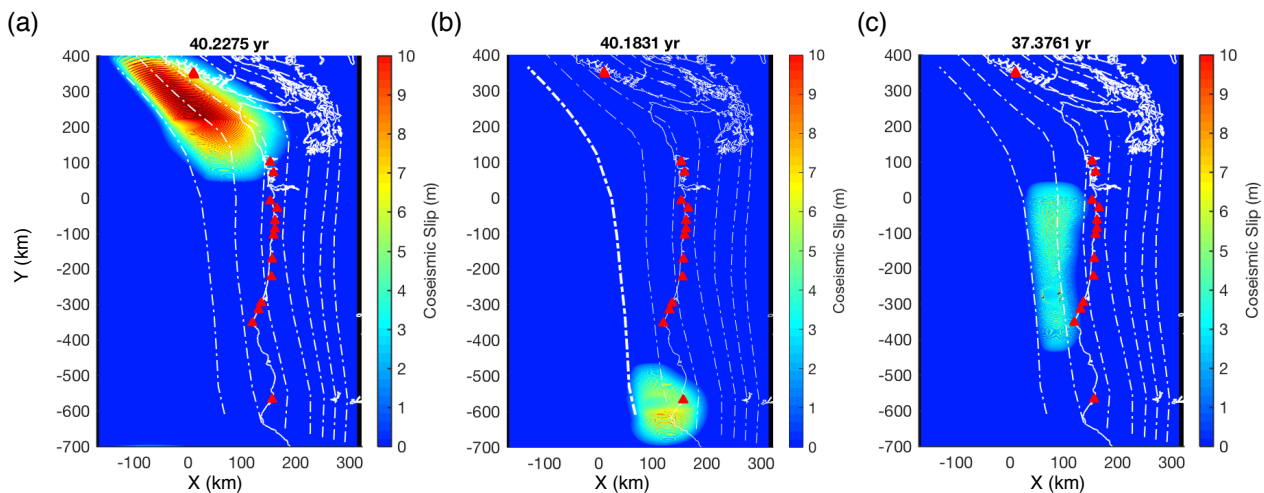


Figure 5–6: Modeled coseismic rupture on the fault for (a) northern, (b) southern and (c) central Cascadia in Model II, using heterogeneous h^* along the strike. The seismic moment magnitudes of the three patches are Mw8.7, Mw8.1 and Mw7.8, respectively. Red triangles show the sites of coastal sediment measurements.

the geodetic fault locking in our model. I assume in this model that the fault locking coefficient does not change with time. Thus, the along-strike heterogeneity of h^* affects the modeled earthquake nucleation process.

It has been shown the h^* needs to be (at least) half the size of that in northern/southern Cascadia, to fulfill the coseismic rupture in central Cascadia. In numerical models, the interpretation of parameter h^* is associated with d_c , though the fracture energy balance [Rubin, 2008]. d_c is usually in the range of mm as constrained by the meshing size, which is limited by computation capacity. In experiments, d_c reflects the frictional property of the gouge contact and is affected by many factors (e.g., roughness, thickness or porosity) [Marone, 1998]. For example, the rougher gouge contacts usually have larger d_c . However, extrapolating parameter d_c directly from the rock sliding experiments (in the range of μm) to pre-existing natural faults is difficult, as the scale-dependence of d_c is not yet understood [Marone, 1998]. For these reasons, I

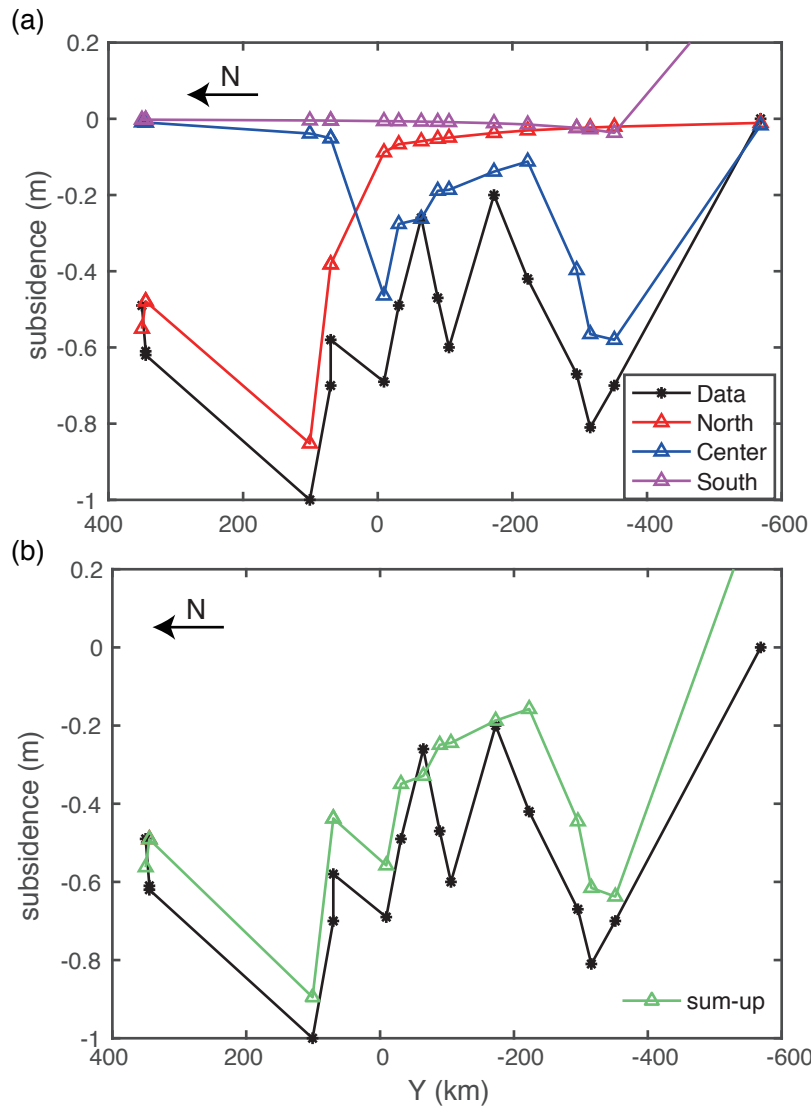


Figure 5-7: Graphs showing (a) synthetic subsidence records from three coseismic segments: northern (red), central (blue) and southern (magenta) and (b) sum of synthetic subsidences of three segments (green). Observational data from Wang et al. [2013] is in black.

am not trying to solve the exact value of h^* (or d_c). In this study, I am focusing on the effect of heterogeneous h^* on modeled fault ruptures and its geological implications.

Although the physics of d_c on the natural faults is not clear, the along-strike variation of fault properties (d_c) may reflect the heterogeneous geological characteristics of different terranes. The Cascadia margin is composed of the Wrangellia, Siletzia and

Klamath terrance from north to south. The Siletzia terrance (between 46°N and 43°N) is an accretion of Eocene age basalt with less permeability, which may increase the pore fluid and promote partial creeping on the megathrust fault [Schmalzle et al., 2014, and therein referred]. In this conceptual model, the less permeable overlying plate may lead to the smaller slip of both historical earthquakes and SSEs rather than elsewhere along the margin. This model can explain the wider transition zone between the fully locked and continuous creeping exists offshore Oregon. The hypothesis of along-strike variable permeability reconciled with the observed gravity anomalies, that is correlated with the SSE segmentation along the strike [Brudzinski and Allen, 2007]. Brudzinski and Allen [2007] proposed that the gravity anomalies reflect the density and porosity of the overlying plate, which may affect the fault hydrous condition through permeability.

Except for several historical megathrust earthquakes occurring along the entire margin, segmented ruptures appeared at parts of the margin [Goldfinger et al., 2008; Leonard et al., 2010]. For example, it is likely that several historical earthquakes only ruptured along Oregon and northern California margins [Leonard et al., 2010]. Why did those segmented earthquakes fail to rupture the entire fault? Is it possible that the entire rupture could occasionally result from several smaller segmented rupture via dynamic weakening on the fault in Cascadia? The questions are difficult to answer unless we have enough direct observations of fault materials or time-dependent rupture records. But there are pieces of evidence that earthquake ruptures may be driven by dynamic weakening within the long-term creeping portion [Noda and Lapusta, 2013]. For example, the 1999 Mw7.6 Chi-Chi rupture northern and southern fault, while the maximum slip appears in the previous creeping portion [Ma et al., 2003]. The obvious rupture pattern can be fulfilled by introducing dynamic weakening due to rapid shear heating during high slip rate in modeling [Noda and Lapusta, 2013]. To

fully investigate the detailed rupture process of megathrust earthquakes in Cascadia, dynamic earthquake models are needed in the future.

5.4.2 Current Fault Locking Models

The frictional parameters constrained by the fault locking pattern can reproduce coseismic ruptures throughout the entire margin (Figure 5–6), although the segmented coseismic ruptures are not synchronized in time. The synthetic subsidence is quite comparable with the observational data (Figure 5–7b). One possible reason is that the quasi-dynamic model simplifies the inertial effect and may underestimate the coseismic slip, although larger slip is expected with larger W/h^* in quasi-dynamic models.

Fault locking models are important in estimating the potential hazards. But the models are less accurate without near-trench geodetic observations as constraints [Wang and Tréhu, 2016]. The lack of near-trench observations leaves the shallow fault status not well constrained. For example, in Tohoku offshore region, the fault locking inversions with inland GPS stations show no strong coupling within 100 km landward from the trench [Hashimoto et al., 2009]. However, the 2011 Mw9.2 Tohoku-Oki earthquake initiated at 40 km landward from the trench where the fault is expected to be low-coupled [Hashimoto et al., 2009; Simons et al., 2011]. Additionally, Wallace et al. [2016] found several shallow slow slip events (within in 7 km) in the Hikurangi subduction zone using pore pressure gauges. The existence of shallow SSEs suggests that the shallow part of megathrust fault may undergo conditionally stable slip. The conditionally-stable shallower portion can still have coseismic ruptures and generate large tsunami waves [Ide et al., 2011b].

Most current models need to assume that the fault locking is strong (about 100%) at the trench and decreases with landward distance [e.g. Schmalzle et al., 2014]. The fault locking models will be different when using different mathematical formation to constrain the downdip variation [Schmalzle et al., 2014]. The estimation of fault

locking pattern can affect potential hazard assessments. Unless we have enough offshore observations, the width of seismogenic zones is not well constrained. In addition, taking into viscoelastic stress relaxation also generate a significant difference in the geodetic inversion [Wang and Tréhu, 2016]. In the future, more observations are needed to improve our knowledge of the fault locking model.

5.5 Conclusions

Due to the lack of modern seismological records, the downdip extent of seismogenic zone in Cascadia is still obscure. Thus coastal sediment data is significant in understanding the rupture of historical megathrust earthquakes. To understand the historical seismic records, I model the earthquake cycle with seismogenic zone constrained by different fault locking patterns ϕ in Cascadia margin. The frictional parameter $a - b$ is set to be proportional to ϕ : $a - b$ is negative between $\phi = 1$ and $\phi = 0.5$ while positive elsewhere. To match the synthetic surface subsidence with the coastal subsidence data, along-strike heterogeneous nucleation sizes h^* are required. I setup two models: uniform h^* and heterogeneous h^* . In these models, I investigate how the coseismic rupture is related with the fault locking pattern. As the model is relatively simple, I only have three preliminary conclusions:

- 1) The coseismic rupture is controlled by the model parameters constrained by fault locking ϕ . As the fault is locked to different depths along the strike, there are three rupture segments: northern, central and southern Cascadia. The northern patch has the largest along-dip width and consequently the largest coseismic slip.

- 2) Only if the nucleation size h^* is reduced, or W/h^* is amplified, coseismic slip appears in central Cascadia. For example, the maximum coseismic fault slip becomes 7 m, when h^* is reduced to half of that in northern Cascadia. In the uniform h^* model, the central Cascadia is accommodated by an aseismic slip of about 5 m.

3) The synthetic subsidence is comparable to the paleo-seismic coastal measurements. The along-strike variation of coastal subsidence can be reproduced with the coseismic fault slip. However, due to the uncertainty in the data, I am not able to distinguish which fault locking pattern is “better” in terms of reproducing coastal subsidence that comparable with observations. More future observations are needed to refine the fault locking inversion.

CHAPTER 6

Conclusions and Perspectives

6.1 Thesis Conclusions

The subduction zones generate the most devastating earthquakes and related hazards in the world. So far we have limited knowledge of the physics of earthquakes and fault properties that control/influence it. The current numerical models can reproduce the diverse source parameters of SSEs, by tuning frictional properties or hydrous conditions. But the relation between the physics of SSEs and the structures of subduction zones, especially the geometry and overlying plate, is still unclear. In contrast to major subduction zones, Cascadia margin is seismologically quiet. The fault stress status is important as it controls earthquake nucleations. In this thesis, I have investigated the Cascadia megathrust fault through the physics of SSEs and stress state. These studies can help us 1) to understand the geometric effect on the physics of SSEs, 2) to understand the effect of overlying plates on the segments of SSEs and 3) to evaluate the subduction fault shear strength and stress rotation in the plate boundary at a depth of megathrust earthquakes.

Subduction Geometric Effect on the Physics of SSEs. The relationship between SSE source parameters and subduction geometry has been explored in Chapter 2. I investigate the geometric effect in a numerical model for the 3-D curved model of SSEs in northern Cascadia. I incorporate a realistic fault geometry of northern Cascadia in the framework of rate- and state-dependent friction law, to simulate the spatiotemporal evolution of SSEs. The geometry of the subduction fault not only controls the modeled segmentation SSEs but also affects the source parameters of SSEs.

The along-strike segmentation of slow slip is inversely related to the fault local dip and strike angle of the SSE zone. The unique geometric feature, especially the along-strike variation of dip angle, may significantly affect the nucleation and segmentation of SSEs.

SSEs in the curved fault model capture the major characteristics of observed SSEs. The SSE patch beneath Port Angeles is comparable with that in the GPS inversions in terms of magnitude and along-strike extent. The SSE slip release about 50% of the total plate convergence beneath Port Angeles, which is consistent with the observations. This indicates that SSEs accommodate a significant fraction of the plate convergence below seismogenic zones. The cumulative slip at a single GPS site is also consistent with the GPS records. The curved model is effective in reproducing the characteristics of SSEs that are observed in Cascadia.

Influence of Gravity Anomalies on Slow Slip Segmentation. Along-strike segmentation of slow slip events (SSEs) and non-volcanic tremors in Cascadia may reflect the geological heterogeneities of subduction slab or overlying continental lithosphere. However, the nature behind this segmentation is not fully understood. I develop a 3-D episodic SSE model for the northern and central Cascadia, incorporating both seismic and geodetic observations to constrain the heterogeneities of the megathrust fault properties (Chapter 3). The 6-year automatically detected tremors are used to constrain the rate-state friction parameters. The effective normal stress at SSE depths is constrained by along-margin free-air and Bouguer gravity anomalies. The along-strike variation in long-term plate convergence rate is also taken into consideration.

Simulation results show that five segments of \sim Mw6.0 SSEs spontaneously appear along the strike. This segmentation is correlated to the distribution of tremor epicenters. The cumulative slip of each SSE segments is mainly controlled by the width of velocity-weakening on the fault. The segmentation of recurrence intervals of models

constrained by both types of gravity anomalies is equally comparable to recurrence that inferred from GPS observations. However, the model constrained by free-air anomaly does a better job in reproducing the cumulative slip as well as more consistent surface displacements with GPS observations.

Free-air anomalies correct the elevations from the raw data while Bouguer anomalies correct the topography and plate thickness above the equilibrium depth, and highlight the density of lithosphere. Brudzinski and Allen [2007] has interpreted the SSE segments to the pore pressure via permeability at the ETS source depths. The non-planar topographic features of subduction faults not only result in heterogeneities in the normal stress, but also modulate pore pressure via affecting the pore fluid migrations. The higher overloading in continents can compress the porosity and push the pore fluid away, resulting in higher effective normal stress and longer recurrence intervals. Compared with pore fluid pressure, the fault normal stress is relatively stable over long-term periods. Thus the fault normal stress may control the first-order characteristics of the SSEs source parameters.

The segmentation of SSEs also affects the propagation. Individual slow slip events can still propagate across the boundaries, which may cause interactions between adjacent SSEs, as observed in the time-dependent GPS inversions. The modeled along-strike segmentation only represents the averaged slip release over many SSE cycles, rather than permanent barriers.

Limitation of Current Geodetic Observations. The current GPS detection ability is not able to capture the whole SSE process (Chapter 2). I find that each SSE cycle consists of deep pre-SSE and post-SSE phases, besides the GPS-detectable fast-spreading phase. The fast-spreading phase is distinguished by the high moment rate release. The pre-SSE is likely correlated with the inter-ETS tremor appearance observed in Cascadia. The pre-SSE and post-SSE phases are similar as the fault slip

release during dynamic rupture. The finding helps us to understand the energy process of SSEs.

I also find the dependence of source parameter scaling on the geodetic detection limit (Chapter 3). The source parameter scaling is consistent with observations. However, the scaling relation is sensitive to the cut-off velocity, or current detection threshold. For example, a reduced cut-off slip rate, from V_{pl} to $0.5V_{pl}$, will change the index of moment-duration scaling from 1.75 to 1.47. Hence the detection ability of the current GPS network should be considered in the interpretation of slow earthquake source parameter scaling relations.

Stress Rotation and Weak Plate Boundary. The Mendocino Triple Junction region is the most seismically active part of the Cascadia Subduction Zone. Previous studies have shown that the northward-moving Pacific Plate collides with the subducting Gorda Plate causing intense internal deformation within it. However, the megathrust fault is seismologically quiet, throughout the entire Cascadia margin. There is no thrust earthquake found in either CI year 2 or year 4. Even after a M5.7 transform fault event near Cape Mendocino which generate +400 kPa Coulomb stress on the thrust fault (Chapter 4). This indicates that the fault is firmly locked or the stress has not recovered from the last megathrust earthquake.

There is a stress variation across the plate boundary (Chapter 4). In the continental crust, the compression is consistent with the plate convergence between the Gorda and North American Plate. In the mantle, the compression is dominated by the northward movement of Pacific Plate. The stress variation is unique among the world, as shown by the stress inversion in the Japan Trench with the same binning strategy. The shear stress on the plate boundary fault is likely no more than about ~ 50 MPa at ~ 20 km depth. Regardless of the assumed mantle strength, I infer a relatively weak megathrust fault with an effective friction coefficient of ~ 0 to 0.2 at seismogenic

depths. Such a low value for the effective friction coefficient requires a combination of high fluid pressures and/or fault-zone minerals with low inherent friction in the region where a great earthquake is expected in Cascadia.

6.2 Scope for Future Work

In my opinion, there are several perspectives concerning to the physics of megathrust faults and earthquakes that can be pursued: 1) development of dynamic earthquake cycles in continuum-mechanical models, 2) the interaction between SSEs and megathrust earthquakes in numerical modeling and 3) the rheological property of subduction faults and its influence on the occurrence of SSEs. Each of these will be discussed briefly below.

Investigating Earthquake Cycles in Continuum-mechanical Models. Our model is based on quasi-dynamic shear stress evolution related with the fault slip, which simplifies the wave mediated transfer and has been shown to be effective in modeling the coseismic fault slip pattern [Ben-Zion and Rice, 1997; Lapusta et al., 2000]. The fully-dynamic model considers the seismic wave related stress transfers and generally has a more rapid seismic rupture front [Lapusta et al., 2000; Lapusta and Liu, 2009]. For example, the coseismic slip rate of a fully-dynamic model is about twice higher than that of quasi-dynamic [Lapusta and Liu, 2009]. As computational ability improves, using fully-dynamic method for simulating earthquake cycles on fault of realistic geometry and rheological properties will be possible for future researches.

So far most earthquake cycle models adopt an infinitely thin fault assumption and neglect the shear localization during fault ruptures. A newly developed model, seismo-thermal-mechanical code [van Dinther et al., 2013, 2014], could handle a more physical complex system. van Dinther [2013] has developed the continuum-mechanical modeling tool to simulate both off- and on-megathrust seismicity in subduction zones in the convergent stress loading. As the rapid development of high-performance computers,

large-scale 3-D continuum mechanical simulations will also be practical in the near future.

Interactions between Megathrust Earthquakes and SSEs. Slow slip has been observed to trigger nearby seismicity. For example, an increasing seismicity swarm appears closely to a 2011 Cape Turnagain SSE, Hikurangi, New Zealand [Bartlow et al., 2014]. The swarm appears at <15 km depth and thus has large uncertainty in the hypocenters. However, the swarm tightly distributed in a small region close to the interface, indicating a potential triggering by the stress that loaded of the SSE [Bartlow et al., 2014]. SSEs can trigger not only seismicity swarms but also megathrust earthquakes. Before the 2011 Tohoku-Oki earthquake, there is an along-strike migration of small seismicity. Even though there is no offshore GPS observation, it is believed that a shallow SSE is related with the migration and promote the nucleation of the foreshocks, on March 9th, and the mainshock on March 11th. Before the 2014 Papanoa earthquake in Mexico, a slow slip appears just adjacent to the epicenter. The positive Coulomb stress that generated by the SSEs is believed to trigger the mainshock [Radiguet et al., 2016].

Another significant aspect is the relation between shallow SSEs near the trench and tsunamigenic earthquakes. Tsunamigenic earthquakes can be generated on near-trench faults [Kanamori, 1972]. Shallow SSEs can release quite a fraction plate convergence and thus suppress potential earthquake nucleations. In the Nankai Trough, records of two near-trench borehole strainmeters between 2011 and 2016 suggest that the regular shallow SSEs and LFEs are sensitive to small stress perturbations like a few kPa [Araki et al., 2017, and references therein]. About 30-55% percentages of the plate convergence are accommodated through SSEs and slow earthquakes. The occurrence of SSE indicates that the accretionary prism faults are weak and not able sustain high

strain energy accumulation. The shallow SSEs may be pervasive phenomena in subduction zones, like Cascadia. Thus near-trench observations are important for estimating potential hazards.

Rheological Heterogeneity of Subduction Faults. A new conceptual model concerning the rheological origins of SSE regions has been proposed [Gao and Wang, 2017, and references therein]. They have shown that both the thermal-petrological controlled frictional-viscous transition and high pore fluid pressures released at depth influence the genesis of ETS. In this model, an isolated frictional ETS zone can appear below the seismogenic portion of faults under the influence of metamorphic dehydrations around fore-arc mantle wedges. The fault between “locked” and ETS zone can be either semi-frictional or viscous during continuous convergent loading, mainly depending on the petrological parameters in that range. Although this conceptual model is subject to parameter choices, it provides a rheological foundation for many observations of ETSs around the world. For example, the semi-frictional portion between the “locked” and ETS zone is suitable for long-term SSEs in Nankai but too narrow for those to occur in Cascadia.

References

- Abers, G. A., MacKenzie, L. S., Rondenay, S., Zhang, Z., Wech, A. G., and Creager, K. C. (2009). Imaging the source region of cascadia tremor and intermediate-depth earthquakes. *Geology*, 37(12):1119–1122.
- Ampuero, J.-P. and Rubin, A. M. (2008). Earthquake nucleation on rate and state faults: Aging and slip laws. *J. Geophys. Res.*, 113(B01302).
- Araki, E., Saffer, D. M., Kopf, A. J., Wallace, L. M., Kimura, T., Machida, Y., Ide, S., and Davis, E. a. (2017). Recurring and triggered slow-slip events near the trench at the nankai trough subduction megathrust. *Science*, 356:1157–1160.
- Atwater, B. F., Nelson, A. R., Clague, J. J., Carver, G. A., Yamaguchi, D. K., Brothersky, P. T., Bourgeois, J., Darienzo, M. E., Grant, W. C., and Hemphill-Haley, E. (1995). Summary of coastal geologic evidence for past great earthquakes at the cascadia subduction zone. *Earthquake spectra*, 11(1):1–18.
- Audet, P., Bostock, M. G., Boyarko, D. C., Brudzinski, M. R., and Allen, R. M. (2010). Slab morphology in the cascadia fore arc and its relation to episodic tremor and slip. *Journal of Geophysical Research: Solid Earth*, 115(B4).
- Audet, P., Bostock, M. G., Christensen, N. I., and Peacock, S. M. (2009). Seismic evidence for overpressured subducted oceanic crust and megathrust fault sealing. *Nature*, 457:76–78.
- Audet, P. and Burgmann, R. (2014). Possible control of subduction zone slow-earthquake periodicity by silica enrichment. *Nature*, 510:389–393.

- Audet, P. and Kim, Y. (2016). Teleseismic constraints on the geological environment of deep episodic slow earthquakes in subduction zone forearcs: A review. *Tectonophysics*, 670:1–15.
- Bartlow, N. M., Miyazaki, S., Bradley, A. M., and Segall, P. (2011). Space-time correlation of slip and tremor during the 2009 cascadia slow slip event. *Geophysical Research Letters*, 38(18). L18309.
- Bartlow, N. M., Wallace, L. M., Beavan, R. J., Bannister, S., and Segall, P. (2014). Time-dependent modeling of slow slip events and associated seismicity and tremor at the hikurangi subduction zone, new zealand. *Journal of Geophysical Research: Solid Earth*, 119(1):734–753.
- Beeler, N. M., Tullis, T. E., Blanpied, M. L., and Weeks, J. D. (1996). Frictional behavior of large displacement experimental faults. *J. Geophys. Res.*, 101(B4):8697–8715.
- Beeler, N. M., Tullis, T. E., and Weeks, J. D. (1994). The roles of time and displacement in the evolution effect in rock friction. *Geophys. Res. Lett*, 21(18):1987–1990.
- Ben-Zion, Y. and Rice, J. R. (1997). Dynamic simulations of slip on a smooth fault in an elastic solid. *J. Geophys. Res.*, 102(B8):17771.
- Bilek, S. L. and Lay, T. (1999). Rigidity variations with depth along interplate megathrust faults in subduction zones. *Nature*, 400(6743):443–446.
- Blanpied, M., Tullis, T., and Weeks, J. (1987). Frictional behavior of granite at low and high sliding velocities. *Geophysical Research Letters*, 14(5):554–557.
- Blanpied, M. L., Marone, C. J., Lockner, D. A., Byerlee, J. D., and King, D. P. (1998). Quantitative measure of the variation in fault rheology due to fluid-rock interactions. *J. Geophys. Res.*, 103(B5):9691–9712.
- Boettcher, M. S., Hirth, G., and Evans, B. (2007). Olivine friction at the base of oceanic seismogenic zones. *J. Geophys. Res.*, 112(B1):n/a–n/a.

- Boyarko, D., Brudzinski, M., Porritt, R., Allen, R., and Tréhu, A. (2015). Automated detection and location of tectonic tremor along the entire cascadia margin from 2005 to 2011. *Earth and Planetary Science Letters*, 430:160–170.
- Brudzinski, M. R. and Allen, R. M. (2007). Segmentation in episodic tremor and slip all along cascadia. *Geology*, 35(10):907–910.
- Burgette, R. J., Weldon, R. J., and Schmidt, D. A. (2009). Interseismic uplift rates for western oregon and along-strike variation in locking on the cascadia subduction zone. *Journal of Geophysical Research: Solid Earth*, 114(B1):n/a–n/a.
- Chaytor, J. D., Goldfinger, C., Dziak, R. P., and Fox, C. G. (2004). Active deformation of the gorda plate: Constraining deformation models with new geophysical data. *Geology*, 32(4):353–356.
- Chen, X. and McGuire, J. J. (2016). Measuring earthquake source parameters in the mendocino triple junction region using a dense obs array: Implications for fault strength variations. *Earth Planet. Sci. Lett.*, 453:276–287.
- Choy, G. L. and McGarr, A. (2002). Strike-slip earthquakes in the oceanic lithosphere: observations of exceptionally high apparent stress. *Geophys. J. Int.*, 150(2):506–523.
- Clarke, G. K. C. (1987). Subglacial till: A physical framework for its properties and processes. *J. Geophys. Res.*, 92:9023–9036.
- Colella, H. V., Dieterich, J. H., Richards-Dinger, K., and Rubin, A. M. (2012). Complex characteristics of slow slip events in subduction zones reproduced in multi-cycle simulations. *Geophysical Research Letters*, 39(20).
- Collela, H. V., Dieterich, J. H., and Richards-Dinger, K. B. (2011). Multi-event simulations of slow slip events for a Cascadia-like subduction zone. *Geophys. Res. Lett.*, 38(L16312).
- Dieterich, J. H. (1972). Time-dependent friction in rocks. *Journal of Geophysical Research*, 77(20):3690–3697.

- Dieterich, J. H. (1978). Time-dependent friction and the mechanics of stick-slip. *pure and applied geophysics*, 116(4-5):790–806.
- Dieterich, J. H. (1979). Modeling of rock friction 1. Experimental results and constitutive equations. *J. Geophys. Res.*, 84(B5):2161–2168.
- Dieterich, J. H. (1981). Mechanical behavior of crustal rocks. pages 103–102. Geophysical Monograph Series, No. 24, American Geophys. Union.
- Dragert, H., Wang, K., and James, T. S. (2001). A silent slip event on the deeper Cascadia subduction interface. *Science*, 292(5521):1525–1528.
- Efron, B. and Tibshirani, R. (1986). Bootstrap methods for standard errors, confidence intervals, and other measures of statistical accuracy. *Statistical science*, pages 54–75.
- Frank, W., Shapiro, N., Husker, A., Kostoglodov, V., Bhat, H., and Campillo, M. (2015a). Along-fault pore-pressure evolution during a slow-slip event in Guerrero, Mexico. *Earth and Planetary Science Letters*, 413:135–143.
- Frank, W. B. (2016). Slow slip hidden in the noise: The intermittence of tectonic release. *Geophysical Research Letters*, 43(19).
- Frank, W. B., Radiguet, M., Rousset, B., Shapiro, N. M., Husker, A. L., Kostoglodov, V., Cotte, N., and Campillo, M. (2015b). Uncovering the geodetic signature of silent slip through repeating earthquakes. *Geophys. Res. Lett.*, page 2774?2779.
- Fu, Y., Liu, Z., and Freymueller, J. T. (2015). Spatiotemporal variations of the slow slip event between 2008 and 2013 in the southcentral Alaska subduction zone. *Geochemistry, Geophysics, Geosystems*, 16(7):2450–2461.
- Fulton, P., Brodsky, E. E., Kano, Y., Mori, J., Chester, F., Ishikawa, T., Harris, R., Lin, W., Eguchi, N., and Toczko, S. (2013). Low coseismic friction on the Tohoku-oki fault determined from temperature measurements. *Science*, 342(6163):1214–1217.
- Gao, H., Schmidt, D. A., and Wells, R. J. (2012). Scaling relationships of source parameters for slow slip events. *Bulletin of the Seismological Society of America*, 102(1).

- Gao, X. and Wang, K. (2014). Strength of stick-slip and creeping subduction megathrusts from heat flow observations. *Science*, 345(6200):1038–1041.
- Gao, X. and Wang, K. (2017). Rheological separation of the megathrust seismogenic zone and episodic tremor and slip. *Nature*.
- Geist, E. and Yoshioka, S. (1996). Source parameters controlling the generation and propagation of potential local tsunamis along the cascadia margin. *Natural Hazards*, 13(2):151–177.
- Ghosh, A., Huesca-Pérez, E., Brodsky, E., and Ito, Y. (2015). Very low frequency earthquakes in cascadia migrate with tremor. *Geophysical Research Letters*, 42(9):3228–3232. 2015GL063286.
- Ghosh, A., Vidale, J. E., and Creager, K. C. (2012). Tremor asperities in the transition zone control evolution of slow earthquakes. *Journal of Geophysical Research: Solid Earth*, 117(B10):n/a–n/a. B10301.
- Goldfinger, C., Grijalva, K., Bürgmann, R., Morey, A. E., Johnson, J. E., Nelson, C. H., Gutiérrez-Pastor, J., Ericsson, A., Karabanov, E., Chaytor, J. D., et al. (2008). Late holocene rupture of the northern san andreas fault and possible stress linkage to the cascadia subduction zone. *Bulletin of the Seismological Society of America*, 98(2):861–889.
- Goldfinger, C., Nelson, C., Morey, A., Johnson, J., Patton, J., Karabanov, E., Gutiérrez-Pastor, J., Eriksson, A., Gràcia, E., Dunhill, G., Enkin, R., Dallimore, A., and Vallier, T. (2012). Turbidite event history-methods and implications for holocene paleoseismicity of the cascadia subduction zone. *U.S. Geological Survey Professional Paper*, 1661-F:170.
- Gulick, S. P., Meltzer, A. S., Henstock, T. J., and Levander, A. (2001). Internal deformation of the southern gorda plate: Fragmentation of a weak plate near the mendocino triple junction. *Geology*, 29(8):691–694.

- Hardebeck, J. L. (2015). Stress orientations in subduction zones and the strength of subduction megathrust faults. *Science*, 349(6253):1213–1216.
- Hardebeck, J. L. and Loveless, J. P. (2017). Creeping subduction zones are weaker than locked subduction zones. *Nature Geosci.*
- Hardebeck, J. L. and Michael, A. J. (2006). Damped regional-scale stress inversions: Methodology and examples for southern california and the coalinga aftershock sequence. *J. Geophys. Res.*, 111(B11).
- Hardebeck, J. L. and Shearer, P. M. (2002). A new method for determining first-motion focal mechanisms. *Bull. Seismol. Soc. Am.*, 92(6):2264–2276.
- Hasegawa, A., Yoshida, K., and Okada, T. (2011). Nearly complete stress drop in the 2011 mw 9.0 off the pacific coast of tohoku earthquake. *Earth Planets Space*, 63(7):35.
- Hashimoto, C., Noda, A., Sagiya, T., and Matsu'ura, M. (2009). Interplate seismogenic zones along the kuril-japan trench inferred from gps data inversion. *Nature Geosci*, 2(2):141–144.
- Hawthorne, J. C. and Rubin, A. M. (2013). Tidal modulation and back-propagating fronts in slow slip events simulated with a velocity-weakening to velocity-strengthening friction law. *Journal of Geophysical Research: Solid Earth*, 118(3):1216–1239.
- He, C., Wang, Z., and Yao, W. (2007). Frictional sliding of gabbro gouge under hydrothermal conditions. *Tectonophys.*, 445:353–362.
- He, C., Yao, W., Wang, Z., and Zhou, Y. (2006). Strength and stability of frictional sliding of gabbro gouge at elevated temperatures. *Tectonophysics*, 427(1):217–229.
- Henstock, T. J. and Levander, A. (2003). Structure and seismotectonics of the mendocino triple junction, california. *J. Geophys. Res.*, 108(B5):n/a–n/a.

- Hirose, H., Hirahara, K., Kimata, F., Fujii, N., and Miyazaki, S. (1999). A slow thrust slip event following the two 1996 Hyuganada earthquakes beneath the Bungo Channel, southwest Japan. *Geophys. Res. Lett.*, 26(21):3237–3240.
- Hirose, H., Kimura, H., Enescu, B., and Aoi, S. (2012). Recurrent slow slip event likely hastened by the 2011 tohoku earthquake. *Proceedings of the National Academy of Sciences*, 109(38):15157–15161.
- Hole, J., Beaudoin, B., and Klemperer, S. (2000). Vertical extent of the newborn san andreas fault at the mendocino triple junction. *Geology*, 28(12):1111–1114.
- Hutchison, A. A. and Ghosh, A. (2016). Very low frequency earthquakes spatiotemporally asynchronous with strong tremor during the 2014 episodic tremor and slip event in cascadia. *Geophysical Research Letters*, 43(13):6876–6882. 2016GL069750.
- Hyndman, R. D. (2013). Dwindip landward limit of cascadia great earthquake rupture. *Journal of Geophysical Research: Solid Earth*, 118(10):5530–5549.
- Hyndman, R. D., McCrory, P., Wech, A., Kao, H., and Ague, J. (2015). Cascadia subducting plate fluids channelled to fore-arc mantle corner: Ets and silica deposition. *Journal of Geophysical Research: Solid Earth*, 120(6):4344–4358.
- Hyndman, R. D. and Wang, K. (1993). Thermal constraints on the zone of major thrust earthquake failure: The cascadia subduction zone. *J. Geophys. Res.*, 98(B2):2039.
- Hyndman, R. D. and Wang, K. (1995). The rupture zone of cascadia great earthquakes from current deformation and the thermal regime. *J. Geophys. Res.*, 100(B11):22133–22154.
- Ide, S., Baltay, A., and Beroza, G. C. (2011a). Shallow dynamic overshoot and energetic deep rupture in the 2011 mw 9.0 tohoku-oki earthquake. *Science*, 332(6036):1426–1429.

- Ide, S., Baltay, A., and Beroza, G. C. (2011b). Shallow dynamic overshoot and energetic deep rupture in the 2011 mw 9.0 tohoku-oki earthquake. *Science*, 332(6036):1426–1429.
- Ide, S., Beroza, G. C., Shelly, D. R., and Uchide, T. (2007). A scaling law for slow earthquakes. *Nature*, 447.
- Ide, S., Imanishi, K., Yoshida, Y., Beroza, G. C., and Shelly, D. R. (2008). Bridging the gap between seismically and geodetically detected slow earthquakes. *Geophys. Res. Lett.*, 35(L10305).
- Ito, Y., Hino, R., Kido, M., Fujimoto, H., Osada, Y., Inazu, D., Ohta, Y., Iinuma, T., Ohzono, M., and Miura, S. (2013). Episodic slow slip events in the japan subduction zone before the 2011 tohoku-oki earthquake. *Tectonophysics*, 600:14–26.
- Iverson, R. M., Reid, M. E., Iverson, N. R., LaHusen, R. G., Logan, M., Mann, J. E., and Brien, D. L. (2000). Acute sensitivity of landslide rates to initial soil porosity. *Science*, 290:513–516.
- Kanamori, H. (1972). Mechanism of tsunami earthquakes. *Physics of the Earth and Planetary Interiors*, 6(5):346 – 359.
- Kaneko, Y., Avouac, J., and Lapusta, N. (2010). Towards inferring earthquake patterns from geodetic observations of interseismic coupling. *Nature Geoscience*, 3.
- Kao, H., Shan, S., Dragert, H., Rogers, G., Cassidy, J. F., and Ramachandran, K. (2005). A wide depth distribution of seismic tremors along the northern Cascadia margin. *Nature*, 436(7052):841–844.
- Kato, A., Obara, K., Igarashi, T., Tsuruoka, H., Nakagawa, S., and Hirata, N. (2012). Propagation of slow slip leading up to the 2011 mw 9.0 tohoku-oki earthquake. *Science*, 335(6069):705–708.
- Kovalsky, S. Z., Aigerman, N., Basri, R., and Lipman, Y. (2014). Controlling singular values with semidefinite programming. *ACM Trans. Graph.*, 33(4):68:1–68:13.

- Lapusta, N. and Liu, Y. (2009). Three-dimensional boundary integral modeling of spontaneous earthquake sequences and aseismic slip. *J. Geophys. Res.*, 114(B09303).
- Lapusta, N. and Rice, J. R. (2003). Nucleation and early seismic propagation of small and large events in a crustal earthquake model. *J. Geophys. Res.*, 108(B4).
- Lapusta, N., Rice, J. R., Ben-Zion, Y., and Zheng, G. (2000). Elastodynamic analysis for slow tectonic loading with spontaneous rupture episodes on faults with rate- and state-dependent friction. *J. Geophys. Res.*, 105(B10):23765–23789.
- Lay, T., Ammon, C. J., Kanamori, H., Xue, L., and Kim, M. J. (2011). Possible large near-trench slip during the 2011 mw 9.0 off the pacific coast of tohoku earthquake. *Earth, Planets and Space*, 63(7):32.
- Lay, T. and Kanamori, H. (1981). An asperity model of large earthquake sequences. *Earthquake Prediction*, pages 579–592.
- Lay, T., Kanamori, H., Ammon, C. J., Koper, K. D., Hutko, A. R., Ye, L., Yue, H., and Rushing, T. M. (2012). Depth-varying rupture properties of subduction zone megathrust faults. *J. Geophys. Res.*, 117(B4):n/a–n/a.
- Leeman, J. R., Saffer, D. M., Scuderi, M. M., and Marone, C. (2016). Laboratory observations of slow earthquakes and the spectrum of tectonic fault slip modes. *Nature communications*, 7.
- Leonard, L. J., Currie, C. A., Mazzotti, S., and Hyndman, R. D. (2010). Rupture area and displacement of past cascadia great earthquakes from coastal coseismic subsidence. *Geological Society of America Bulletin*, 122(11-12):2079–2096.
- Li, D. and Liu, Y. (2016). Spatiotemporal evolution of slow slip events in a non-planar fault model for northern cascadia subduction zone. *Journal of Geophysical Research: Solid Earth*, 63(3):959–968.
- Liu, Y. and Rice, J. R. (2005). Aseismic slip transients emerge spontaneously in three-dimensional rate and state modeling of subduction earthquake sequences. *J.*

- Geophys. Res.*, 110(B08307).
- Liu, Y. and Rice, J. R. (2007). Spontaneous and triggered aseismic deformation transients in a subduction fault model. *J. Geophys. Res.*, 112(B09404).
- Liu, Y. and Rice, J. R. (2009). Slow slip predictions based on granite and gabbro friction data compared to GPS measurements in northern Cascadia. *J. Geophys. Res.*, 114(B09407).
- Liu, Y., Rice, J. R., and Larson, K. M. (2007). Seismicity variations associated with aseismic transients in Guerrero, Mexico, 1995–2006. *Earth and Planetary Science Letters*, 262(3–4):493 – 504.
- Liu, Y. and Rubin, A. M. (2010). Role of fault gouge dilatancy on aseismic deformation transients. *J. Geophys. Res.*, 115(B10414).
- Liu, Y. J. (2013). Numerical simulations on megathrust rupture stabilized under strong dilatancy strengthening in slow slip region. *Geophys. Res. Lett.*, 40:1311–1316.
- Liu, Y. J. (2014). Source scaling relations and along-strike segmentation of slow slip events in a 3-D subduction fault model. *J. Geophys. Res.*, 119.
- Ma, K.-F., Brodsky, E. E., Mori, J., Ji, C., Song, T.-R. A., and Kanamori, H. (2003). Evidence for fault lubrication during the 1999 Chi-Chi, Taiwan, earthquake (M_w7.6). *Geophysical Research Letters*, 30(5):n/a–n/a. 1244.
- Marone, C. (1998). Laboratory-derived friction laws and their application to seismic faulting. *Annual Review of Earth and Planetary Sciences*, 26(1):643–696.
- Marone, C., Raleigh, C. B., and Scholz, C. H. (1990). Frictional behavior and constitutive modeling of simulated fault gouge. *J. Geophys. Res.*, 95(B5):7007–7025.
- Marone, C. J. and Blanpied, M. L. (1994). Faulting, friction, and earthquake mechanics .1. introduction. *Pure. Appl. Geophys.*, 142(3-4):413–416.

- Matsuzawa, T., Shibasaki, B., and Hirose, H. (2013). Comprehensive model of short- and long-term slow slip events in the Shikoku region of Japan, incorporating a realistic plate configuration. *Geophys. Res. Lett.*, 40(19).
- McCaffrey, R., Qamar, A. I., King, R. W., Wells, R., Khazaradze, G., Williams, C. A., Stevens, C. W., Vollick, J. J., and Zwick, P. C. (2007). Fault locking, block rotation and crustal deformation in the pacific northwest. *Geophysical Journal International*, 169(3):1315–1340.
- McCaffrey, R., Wallace, L. M., and Beavan, J. (2008). Slow slip and frictional transition at low temperature at the Hikurangi subduction zone. *Nature, Geosci.*, 1:316–320.
- McCausland, W., Malone, S., and Johnson, D. (2005). Temporal and spatial occurrence of deep non-volcanic tremor: From Washington to northern California. *Geophys. Res. Lett.*, 32(L24311).
- McCrorry, P., Blair, J., Oppenheimer, D., and Walter, S. (2006). Depth to the juan de fuca slab beneath the cascadia subduction margin; a 3-d model for sorting earthquakes us geological survey.
- McCrorry, P., Blair, J. L., Waldhauser, F., and Oppenheimer, D. H. (2012). Juan de Fuca slab geometry and its relation to Wadati-Benioff zone seismicity. *J. Geophys. Res.*, 117(B09).
- McCrorry, P. A. (2000). Upper plate contraction north of the migrating mendocino triple junction, northern california: Implications for partitioning of strain. *Tectonics*, 19(6):1144–1160.
- McCrorry, P. A., Hyndman, R. D., and Blair, J. L. (2014). Relationship between the cascadia fore-arc mantle wedge, nonvolcanic tremor, and the downdip limit of seismogenic rupture. *Geochemistry, Geophysics, Geosystems*, 15(4):1071–1095.
- McGuire, J. J. and Segall, P. (2003). Imaging of aseismic fault slip transients recorded by dense geodetic networks. *Geophys. J. Int.*, 155(3):778–788.

- McKenzie, D. P. (1969). Speculations on the consequences and causes of plate motions. *Geophys. J. R. Astron. Soc.*, 18:1–32.
- McLaskey, G. C. and Yamashita, F. (2017). Slow and fast ruptures on a laboratory fault controlled by loading characteristics. *J. Geophys. Res.*, 122(5):3719–3738.
- Meade, B. J. (2007). Algorithms for the calculation of exact displacements, strains, and stresses for triangular dislocation elements in a uniform elastic half space. *Computers and Geosciences*, 33(8):1064–1075.
- Michael (1984). Determination of stress from slip data: Faults and folds. *J. Geophys. Res.*, 89(B13):11517–11526.
- Michael (1987). Use of focal mechanisms to determine stress: A control study. *J. Geophys. Res.*, 92(B1):357.
- Miller, S. A. (2002). Properties of large ruptures and the dynamical influence of fluids on earthquakes and faulting. *J. Geophys. Res.*, 107(B9).
- Murray, M. H., Marshall, G. A., Lisowski, M., and Stein, R. S. (1996). The 1992 m = 7 cape mendocino, california, earthquake: Coseismic deformation at the south end of the cascadia megathrust. *Journal of Geophysical Research: Solid Earth*, 101(B8):17707–17725.
- Noda, H. and Lapusta, N. (2013). Stable creeping fault segments can become destructive as a result of dynamic weakening. *Nature*, 493(7433):518–521.
- Obana, K., Scherwath, M., Yamamoto, Y., Kodaira, S., Wang, K., Spence, G., Riedel, M., and Kao, H. (2015). Earthquake activity in northern cascadia subduction zone off vancouver island revealed by ocean-bottom seismograph observations. *Bulletin of the Seismological Society of America*, 105(1):489–495.
- Obara, K. (2002). Nonvolcanic deep tremor associated with subduction in southwest Japan. *Science*, 296(5573):1679–1681.

- Obara, K. (2010). Phenomenology of deep slow earthquake family in southwest Japan: Spatiotemporal characteristics and segmentation. *J. Geophys. Res.*, 115(B00A25).
- Obara, K. (2011). Characteristics and interactions between non-volcanic tremor and related slow earthquakes in the Nankai subduction zone, southwest Japan. *Journal of Geodynamics*, 52(3):229–248.
- Obara, K., Hirose, H., Yamamizu, F., and Kasahara, K. (2004). Episodic slow slip events accompanied by non-volcanic tremors in southwest Japan subduction zone. *Geophys. Res. Lett.*, 31(L23602).
- Ohta, Y., Freymueller, J. T., Hreinsdottir, S., and Suito, H. (2006). A large slow slip event and the depth of the seismogenic zone in the south central Alaska subduction zone. *Earth. Planet. Sci. Lett.*, 247(1-2):108–116.
- Okada, Y. (1985). Surface deformation due to shear and tensile faults in a half-space. *Bulletin of the seismological society of America*, 75(4):1135–1154.
- Okada, Y. (1992). Internal deformation due to shear and tensile faults in a half-space. *Bull. Seismol. Soc. Amer.*, 82(2):1018–1040.
- Oppenheimer, D. Fau Eaton, J., Eaton J Fau Jayko, A., Jayko A Fau Lisowski, M., Lisowski M Fau Marshall, G., Marshall G Fau Murray, M., Murray M Fau Simpson, R., Simpson R Fau Stein, R., Stein R Fau Beroza, G., Beroza G Fau Magee, M., Magee M Fau Carver, G., Carver G Fau Dengler, L., Dengler L Fau McPherson, R., McPherson R Fau Gee, L., Gee L Fau Romanowicz, B., Romanowicz B Fau Gonzalez, F., Gonzalez F Fau Li, W. H., Li Wh Fau Satake, K., Satake K Fau Somerville, P., Somerville P Fau Valentine, D., and Valentine, D. (1993). The Cape Mendocino, California, earthquakes of April 1992: subduction at the triple junction. (0036-8075 (Print)).
- Outerbridge, K. C., Dixon, T. H., Schwartz, S. Y., Walter, J. I., and Protti, M. (2010). A tremor and slip event on the Cocos-Caribbean Subduction zone as measured by

- a global positioning system (GPS) and seismic network on the Nicoya Peninsula, Costa Rica. *J. Geophys. Res.*, 115(B10408).
- Peacock, S. M. (2009). Thermal and metamorphic environment of subduction zone episodic tremor and slip. *J. Geophys. Res.*, 114(B00A07).
- Peacock, S. M., Christensen, N. I., Bostock, M. G., and Audet, P. (2011). High pore pressures and porosity at 35 km depth in the cascadia subduction zone. *Geology*, 39(5):471–474.
- Peacock, S. M., Wang, K., and McMahon, A. M. (2002). Thermal structure and metamorphism of subducting oceanic crust: Insight into cascadia intraslab earthquakes. In Kirby, S., Wang, K., and Dunlop, S., editors, *The Cascadia subduction zone and related subduction systems: Seismic structure, Intraslab earthquakes and processes, and earthquake hazards*, pages 123–126. U. S. Geol. Surv. Open-File Rep., 02-328 and Geol. Surv. Canada Open-File, 4350.
- Peng, Y. and Rubin, A. M. (2017). Intermittent tremor migrations beneath guerrero, mexico, and implications for fault healing within the slow slip zone. *Geophys. Res. Lett.*, pages n/a–n/a.
- Peng, Z. and Chao, K. (2008). Non-volcanic tremor beneath the central range in taiwan triggered by the 2001 mw 7.8 kunlun earthquake. *Geophys. J. Int.*, 175(2):825–829.
- Peng, Z. and Gomberg, J. (2010). An integrated perspective of the continuum between earthquakes and slow-slip phenomena. *Nature Geoscience*, 3:599–607.
- Peng, Z., Vidale, J. E., Wech, A. G., Nadeau, R. M., and Creager, K. C. (2009). Remote triggering of tremor along the san andreas fault in central california. *J. Geophys. Res.*, 114(B7):n/a–n/a.
- Peterson, C. L. and Christensen, D. H. (2009). Possible relationship between nonvolcanic tremor and the 1998–2001 slow slip event, south central alaska. *Journal of Geophysical Research: Solid Earth*, 114(B6).

- Radiguet, M., Perfettini, H., Cotte, N., Gualandi, A., Valette, B., Kostoglodov, V., Lhomme, T., Walpersdorf, A., Cabral Cano, E., and Campillo, M. (2016). Triggering of the 2014 mw7.3 papanoa earthquake by a slow slip event in guerrero, mexico. *Nature Geosci*, advance online publication.
- Reasenber, P. and Oppenheimer, D. (1985). Fpfit, fpplot and fppage; fortran computer programs for calculating and displaying earthquake fault-plane solutions. Report 2331-1258, US Geological Survey.
- Rice, J. R. (1993). Spatiotemporal complexity of slip on a fault. *J. Geophys. Res.*, 98(B6):9885–9907.
- Rice, J. R. and Ruina, A. L. (1983). Stability of steady frictional slipping. *J. Appl. Mech.*, 50(2):343–349.
- Rogers, G. and Dragert, H. (2003). Episodic tremor and slip on the Cascadia subduction zone: The chatter of silent slip. *Science*, 300(5627):1942–1943.
- Rubin, A. M. (2008). Episodic slow slip events and rate-and-state friction. *J. Geophys. Res.*, 113(B11414).
- Rubin, A. M. and Ampuero, J.-P. (2005). Earthquake nucleation on (agine) rate and state faults. *J. Geophys. Res.*, 110(B11312).
- Rubinstein, J. L., Vidale, J. E., Gomberg, J., Bodin, P., Creager, K. C., and Malone, S. D. (2007). Non-volcanic tremor driven by large transient shear stresses. *Nature*, 448(7153):579–82.
- Ruina, A. L. (1983). Slip instability and state variable friction laws. *J. Geophys. Res.*, 88(B12):10359–10370.
- Saffer, D. M. and Wallace, L. M. (2015). The frictional, hydrologic, metamorphic and thermal habitat of shallow slow earthquakes. *Nature Geoscience*, 8(8):594–600.

- Satake, K. (1993). Depth distribution of coseismic slip along the Nankai Trough, Japan, from joint inversion of geodetic and tsunami data. *J. Geophys. Res.*, 98(B3):4553–4565.
- Satake, K., Shimazaki, K., Tsuji, Y., and Ueda, K. (1996). Time and size of a giant earthquake in Cascadia inferred from Japanese tsunami records of January 1700. *Nature*, 379(6562):246.
- Satake, K., Wang, K., and Atwater, B. F. (2003). Fault slip and seismic moment of the 1700 Cascadia earthquake inferred from Japanese tsunami descriptions. *J. Geophys. Res.*, 108(B11).
- Schmalzle, G. M., McCaffrey, R., and Creager, K. C. (2014). Central Cascadia subduction zone creep. *Geochemistry, Geophysics, Geosystems*, 15(4):1515–1532.
- Schmidt, D. A. and Gao, H. (2010). Source parameters and time-dependent slip distributions of slow slip events on the Cascadia subduction zone from 1998 to 2008. *J. Geophys. Res.*, 115(B00A18).
- Scholz, C. and Engelder, J. (1976). The role of asperity indentation and ploughing in rock friction?i: Asperity creep and stick-slip. 13(5):149–154.
- Scholz, C. H. (1998). Earthquakes and friction laws. *Nature*, 391.
- Schwartz, S. Y. and Hubert, A. (1997). The state of stress near the Mendocino triple junction from inversion of earthquake focal mechanisms. *Geophys. Res. Lett.*, 24(10):1263–1266.
- Schwartz, S. Y. and Rokosky, J. M. (2007). Slow slip events and seismic tremor at circum-Pacific subduction zones. *Reviews of Geophysics*, in review.
- Segall, P. and Bradley, M. (2012). Slow-slip evolves into megathrust earthquakes in 2D numerical simulations. *Geophys. Res. Lett.*, 39(L18308).
- Segall, P., Desmarais, E. K., Shelly, D. R., Miklius, A., and Cervelli, P. (2006). Earthquakes triggered by silent slip events on Kilauea volcano, Hawaii. *Nature*,

442(7098):71–74.

Segall, P., Rubin, A. M., Bradley, M., and Rice, J. R. (2010). Dilatant strengthening as a mechanism for slow slip events. *J. Geophys. Res.*, 115(B12305).

Shelly, D. R., Beroza, G. C., and Ide, S. (2007). Non-volcanic tremor and low-frequency earthquake swarms. *Nature*.

Shelly, D. R., Beroza, G. C., Ide, S., and Nakamura, S. (2006). Low-frequency earthquakes in Shikoku, Japan, and their relationship to episodic tremor and slip. *Nature*, 442(7099):188–191.

Shelly, D. R. and Hardebeck, J. L. (2010). Precise tremor source locations and amplitude variations along the lower-crustal central San Andreas Fault. *Geophys. Res. Lett.*, 37(L14301).

Shen, Z., Wang, Q., Burgmann, R., Wan, Y., and Ning, J. (2005). Pole-tide modulation of slow slip events at circum-pacific subduction zones. *Bull. Seismol. Soc. Amer.*, 95(5):2009–2015.

Shibazaki, B., Bu, S., Matsuzawa, T., and Hirose, H. (2010). Modeling the activity of short-term slow slip events along deep subduction interfaces beneath shikoku, southwest japan. *Journal of Geophysical Research: Solid Earth*, 115(B4).

Shibazaki, B. and Iio, Y. (2003). On the physical mechanism of silent slip events along the deeper part of the seismogenic zone. *Geophys. Res. Lett.*, 30(9).

Shibazaki, B., Obara, K., Matsuzawa, T., and Hirose, H. (2012). Modeling of slow slip events along the deep subduction zone in the Kii Peninsula and Tokai regions, southwest Japan. *J. Geophys. Res.*, 117.

Shimamoto, T. (1986). Transition between frictional slip and ductile flow for halite shear zones at room temperature. *Science*, 231(4739):711–714.

Silver, E. A. (1971). Tectonics of the mendocino triple junction. *Geol. Soc. Am. Bull.*, 82(11):2965–2978.

- Simons, M., Minson, S. E., Sladen, A., Ortega, F., Jiang, J., Owen, S. E., Meng, L., Ampuero, J.-P., Wei, S., Chu, R., Helmberger, D. V., Kanamori, H., Hetland, E., Moore, A. W., and Webb, F. H. (2011). The 2011 magnitude 9.0 tohoku-oki earthquake: Mosaicking the megathrust from seconds to centuries. *Science*, 332:1421–1425.
- Skarbek, R. M. and Rempel, A. W. (2016). Dehydration-induced porosity waves and episodic tremor and slip. *Geochemistry, Geophysics, Geosystems*, 17(2):442–469.
- Stuart, W. D., Hildenbrand, T. G., and Simpson, R. W. (1997). Stressing of the New Madrid Seismic Zone by a lower crust detachment fault. *J. Geophys. Res.*, 102(B12).
- Sun, T., Wang, K., Fujiwara, T., Kodaira, S., and He, J. (2017). Large fault slip peaking at trench in the 2011 tohoku-oki earthquake. *Nature communications*, 8:14044.
- Szeliga, W., Melbourne, T. I., Santillan, V. M., and Miller, M. M. (2008). GPS constraints on 34 slow slip events within the Cascadia subduction zone, 1997-2005. *J. Geophys. Res.*, 113(B04404).
- Tobin, H. J. and Saffer, D. M. (2009). Elevated fluid pressure and extreme mechanical weakness of a plate boundary thrust, nankai trough subduction zone. *Geology*, 37(8):679–682.
- Toomey, D. R., Allen, R. M., Barclay, A. H., Bell, S. W., Bromirski, P. D., Carlson, R. L., Chen, X., Collins, J. A., Dziak, R. P., and Evers, B. (2014). The cascadia initiative: A sea change in seismological studies of subduction zones.
- Tréhu, A. M., Braunmiller, J., and Davis, E. (2015). Seismicity of the central cascadia continental margin near 44.5 n: A decadal view. *Seismol. Res. Lett.*
- Uchida, N. and Matsuzawa, T. (2013). Pre-and postseismic slow slip surrounding the 2011 tohoku-oki earthquake rupture. *Earth Planet. Sci. Lett.*, 374:81–91.
- van Dinther, Y. (2013). seismo-thermo-mechanical modeling of subduction zone seismicity. *Ph.D. Thesis*.

- van Dinther, Y., Gerya, T. V., Dalguer, L. A., Mai, P. M., Morra, G., and Giardini, D. (2013). The seismic cycle at subduction thrusts: Insights from seismo-thermo-mechanical models. *Journal of Geophysical Research: Solid Earth*, 118(12):6183–6202.
- van Dinther, Y., Mai, P. M., Dalguer, L. A., and Gerya, T. V. (2014). Modeling the seismic cycle in subduction zones: The role and spatiotemporal occurrence of off-megathrust earthquakes. *Geophysical Research Letters*, 41(4):1194–1201.
- Vandenberghe, L. and Boyd, S. (1996). Semidefinite programming. *SIAM review*, 38(1):49–95.
- Veedu, D. M. and Barbot, S. (2016). The parkfield tremors reveal slow and fast ruptures on the same asperity. *Nature*, 532(7599):361–365.
- Wada, I., Mazzotti, S., and Wang, K. (2010). Intraslab stresses in the cascadia subduction zone from inversion of earthquake focal mechanisms. *Bull. Seismol. Soc. Am.*, 100(5A):2002–2013.
- Wada, I., Wang, K., He, J., and Hyndman, R. D. (2008). Weakening of the subduction interface and its effects on surface heat flow, slab dehydration, and mantle wedge serpentization. *Journal of Geophysical Research: Solid Earth*, 113(B4):n/a–n/a. B04402.
- Wallace, L. M. and Beavan, J. (2010). Diverse slow slip behavior at the Hikurangi subduction margin, New Zealand. *Journal of Geophysical Research*, 115(B12).
- Wallace, L. M., Beavan, J., Bannister, S., and Williams, C. (2012). Simultaneous long-term and short-term slow slip events at the Hikurangi subduction margin, New Zealand: Implications for processes that control slow slip event occurrence, duration, and migration. *Journal of Geophysical Research*, 117(B11).

- Wallace, L. M., Webb, S. C., Ito, Y., Mochizuki, K., Hino, R., Henrys, S., Schwartz, S. Y., and Sheehan, A. F. (2016). Slow slip near the trench at the hikurangi subduction zone, new zealand. *Science*, 352(6286):701–704.
- Wang, K. and He, J. (1999). Mechanics of low-stress forearcs: Nankai and cascadia. *J. Geophys. Res.*, 104(B7):15191–15205.
- Wang, K., Hyndman, R. D., and Yamano, M. (1995). Thermal regime of the southwest japan subduction zone - effects of age history of the subducting plate. *Tectonophysics*, 248(1-2):53–69.
- Wang, K. and Rogers, G. C. (1994). An explanation for the double seismic layers north of the mendocino triple junction. *Geophys. Res. Lett.*, 21(2):121–124.
- Wang, K. and Tréhu, A. M. (2016). Invited review paper: Some outstanding issues in the study of great megathrust earthquakes?the cascadia example. *Journal of Geodynamics*, 98:1 – 18.
- Wang, P.-L., Engelhart, S. E., Wang, K., Hawkes, A. D., Horton, B. P., Nelson, A. R., and Witter, R. C. (2013). Heterogeneous rupture in the great cascadia earthquake of 1700 inferred from coastal subsidence estimates. *Journal of Geophysical Research: Solid Earth*, 118(5):2460–2473.
- Wech, Creager, K. C., and Melbourne, T. I. (2009). Seismic and geodetic constraints on cascadia slow slip. *Journal of Geophysical Research: Solid Earth*, 114(B10).
- Wech, A. and Bartlow, N. M. (2014). Slip rate and tremor genesis in Cascadia. *Geophys. Res. Lett.*, 41.
- Wech, A. and Creager, K. C. (2011). A continuum of stress, strength and slip in the Cascadia subduction zone. *Nature Geoscience*, 4.
- Wech, A. G. and Creager, K. C. (2008). Automated detection and location of cascadia tremor. *Geophysical Research Letters*, 35(20).

- Wei, M., Kaneko, Y., Liu, Y., and McGuire, J. J. (2013). Episodic fault creep events in California controlled by shallow frictional heterogeneity. *Nature Geoscience*, 6.
- Wei, M. and McGuire, J. J. (2014). The Mw6.5 offshore northern California earthquake of 10 January 2010: Ordinary stress drop on a high-strength fault. *Geophys. Res. Lett.*, 41(18):6367–6373.
- Wei, M., McGuire, J. J., and Richardson, E. (2012). A slow slip event in the south central Alaska subduction zone and related seismicity anomaly. *Geophys. Res. Lett.*, 39(L15309).
- Wells, R. E., Blakely, R. J., Sugiyama, Y., Scholl, D. W., and Dinterman, P. A. (2003). Basin-centered asperities in great subduction zone earthquakes: A link between slip, subsidence, and subduction erosion? *Journal of Geophysical Research: Solid Earth*, 108(B10). 2507.
- Wessel, P. and Smith, W. H. (1998). New, improved version of generic mapping tools released. *Eos, Transactions American Geophysical Union*, 79(47):579–579.
- Yang, H., Liu, Y., and Lin, J. (2012). Effects of subducted seamounts on megathrust earthquake nucleation and rupture propagation. *Geophysical Research Letters*, 39(24).
- Yue, H. and Lay, T. (2011). Inversion of high-rate (1 sps) gps data for rupture process of the 11 March 2011 Tohoku earthquake (Mw9.1). *Geophys. Res. Lett.*, 38(7):n/a–n/a.
- Zhang, H. and Thurber, C. (2006). Development and applications of double-difference seismic tomography. *Pure and Applied Geophysics*, 163(2):373–403.
- Zoback, M. D. and Townend, J. (2001). Implications of hydrostatic pore pressures and high crustal strength for the deformation of intraplate lithosphere. *Tectonophysics*, 336(1):19–30.